

STRUCTURE-PROPERTY RELATIONSHIPS OF PEMs USING FLUOROUS-IONIC COPOLYMERS

by

Ming Wai Emily Tsang
B. Sc., Simon Fraser University, 2005

THESIS SUBMITTED IN PARTIAL FULFILLMENT OF
THE REQUIREMENTS FOR THE DEGREE OF

DOCTOR OF PHILOSOPHY

In the
Department of Chemistry

© Ming Wai Emily Tsang 2011

SIMON FRASER UNIVERSITY

Summer 2011

All rights reserved. However, in accordance with the *Copyright Act of Canada*, this work may be reproduced, without authorization, under the conditions for *Fair Dealing*. Therefore, limited reproduction of this work for the purposes of private study, research, criticism, review and news reporting is likely to be in accordance with the law, particularly if cited appropriately.

Approval

Name: Ming Wai Emily Tsang
Degree: Doctor of Philosophy
Title of Thesis: Structure-Property Relationships of PEMs using Fluorous-Ionic Copolymers

Examining Committee:

Chair: Dr. Paul C. H. Li
Professor, Department of Chemistry

Dr. Steven Holdcroft
Senior Supervisor
Professor, Department of Chemistry

Dr. Charles J. Walsby
Supervisor
Associate Professor, Department of Chemistry

Dr. Peter D. Wilson
Supervisor
Associate Professor, Department of Chemistry

Dr. Robert A. Britton
Internal Examiner, Department of Chemistry
Assistant Professor

Dr. Kenji Miyatake
External Examiner
Professor, Fuel Cell Nanomaterials Center
University of Yamanashi, Japan

Date Defended/Approved: June 20, 2011



SIMON FRASER UNIVERSITY
LIBRARY

Declaration of Partial Copyright Licence

The author, whose copyright is declared on the title page of this work, has granted to Simon Fraser University the right to lend this thesis, project or extended essay to users of the Simon Fraser University Library, and to make partial or single copies only for such users or in response to a request from the library of any other university, or other educational institution, on its own behalf or for one of its users.

The author has further granted permission to Simon Fraser University to keep or make a digital copy for use in its circulating collection (currently available to the public at the "Institutional Repository" link of the SFU Library website <www.lib.sfu.ca> at: <<http://ir.lib.sfu.ca/handle/1892/112>>) and, without changing the content, to translate the thesis/project or extended essays, if technically possible, to any medium or format for the purpose of preservation of the digital work.

The author has further agreed that permission for multiple copying of this work for scholarly purposes may be granted by either the author or the Dean of Graduate Studies.

It is understood that copying or publication of this work for financial gain shall not be allowed without the author's written permission.

Permission for public performance, or limited permission for private scholarly use, of any multimedia materials forming part of this work, may have been granted by the author. This information may be found on the separately catalogued multimedia material and in the signed Partial Copyright Licence.

While licensing SFU to permit the above uses, the author retains copyright in the thesis, project or extended essays, including the right to change the work for subsequent purposes, including editing and publishing the work in whole or in part, and licensing other parties, as the author may desire.

The original Partial Copyright Licence attesting to these terms, and signed by this author, may be found in the original bound copy of this work, retained in the Simon Fraser University Archive.

Simon Fraser University Library
Burnaby, BC, Canada

Abstract

Proton exchange membranes (PEMs) are a key component in PEM fuel cells, serving as both a fuel separator and an electrolyte. The goal of this thesis work is to investigate structure-property relationships in PEMs. Specifically, the role of polymer microstructure on membrane morphology and physicochemical properties is examined. This is achieved by the design, synthesis, and characterization of model polymers with controlled chain architectures and chemical composition, leading to membranes with controlled nanophase-separated morphologies, from which the influence of morphology upon proton transport and other membrane properties is investigated.

Two classes of model polymer systems were devised and studied: diblock copolymers of sulfonated poly([vinylidene difluoride-*co*-hexafluoropropylene]-*b*-styrene) [P(VDF-*co*-HFP)-*b*-SPS]; and graft copolymers of sulfonated poly([vinylidene difluoride-*co*-chlorotrifluoropropylene]-*g*-styrene) [P(VDF-*co*-CTFE)-*g*-SPS]. These model polymer systems are of interest due to chemical dissimilarity between the hydrophobic fluoropolymer segments and the hydrophilic sulfonated polystyrene segments, which promote phase separation into ionic and non-ionic domains. In addition, controlled radical polymerization techniques were employed to grow the polystyrene segments, which provide high degrees of structural control. Macromolecular structural parameters, such as block ratio, graft length and degree of sulfonation, were systematically varied to

determine the effects of polymer microstructure on morphology and proton conductivity.

One of the key findings obtained from this work is that block ionomers, whether linear or graft structure, with a lower content of the acid-bearing constituent block (i.e., polystyrene block) gave enhanced proton conductivity at a given ion content. This is attributed to the relatively high degree of sulfonation required and therefore, closer spatial proximity between sulfonic acid groups, which allows for the formation of purer and more percolated ionic aggregates within the proton-conducting domains. Additionally, direct comparison between the diblock and the graft copolymers revealed that the formation of smaller-scale ionic domains is preferable for PEMs because of reduced water swelling which mitigates acid dilution at high ion contents. Furthermore, membranes with small-scale ionic domains provided enhanced water retention and proton conduction under low humidity and high temperature conditions. The knowledge gained from this thesis work provides useful insights into aspects of membrane design and preferred structures.

Keywords: Proton Exchange Membranes; Fuel Cells; Morphology; Structure-Property Relationships; Polymer Synthesis; Proton Conductivity

To my parents, Michelle & Chak Lam,

and to my family

Acknowledgements

I would like to express my gratitude and thanks to:

My senior supervisor Prof. Steven Holdcroft for giving me the opportunity to work under his supervision and for his valuable guidance, support and assistance throughout my studies.

My supervisory committee, Prof. Charles Walsby and Prof. Peter Wilson, for their supervision and for providing useful comments to improve my thesis.

My examining committee, Prof. Kenji Miyatake and Prof. Robert Britton for taking the time to review this thesis.

Drs. Zhaobin Zhang, Zhiqing Shi and Timothy Peckham for their mentorship and meaningful discussions on this research project.

Mr. Rasoul Narimani and Prof. Barbara Frisken of Department of Physics, SFU, for the fruitful discussion and the collaborative research project.

Ms. Ami Yang for acquiring some of the conductivity data presented in Chapter 4.

Dr. Tatyana Soboleva for her assistance with the through-plane conductivity measurements.

Drs. Colin Zhang and Andrew Lewis for collecting ^{19}F NMR data.

Dr. Timothy Peckham for proof-reading this thesis.

Past and present members of the Holdcroft group for their great friendship, support and useful discussions.

My family and friends for their love, support and encouragement throughout my studies.

Simon Fraser University and the Natural Sciences and Engineering Research Council of Canada for financial support.

Table of Contents

Approval.....	ii
Abstract.....	iii
Dedication.....	v
Acknowledgements.....	vi
Table of Contents.....	viii
List of Figures.....	xi
List of Tables.....	xvi
List of Abbreviations.....	xvii
List of Symbols.....	xx
Chapter 1. Introduction.....	1
1.1 Fuel cells.....	1
1.2 Proton Exchange Membrane Fuel Cells.....	4
1.3 Proton Exchange Membrane.....	6
1.4 Alternate Proton Exchange Membranes.....	9
1.4.1 Perfluorinated Ionomers.....	9
1.4.2 Partially Fluorinated Ionomers.....	12
1.4.3 Non-fluorinated Hydrocarbons.....	16
1.4.4 Polymer blends and composite membranes.....	22
1.5 Proton Conduction in PEMs.....	23
1.6 Morphological Studies of Nafion Membranes.....	27
1.7 Importance of Structure-Property Relationships.....	34
1.7.1 Copolymer Microstructure.....	36
1.7.2 Structure-Property Relationships in PEMs.....	38
1.8 Research Outline.....	44
Chapter 2. Polymer Synthesis and Characterization.....	48
2.1 Free-Radical Polymerization.....	48
2.2 Atom Transfer Radical Polymerization.....	51
2.3 Gel Permeation Chromatography.....	55
2.4 Sulfonation.....	58
2.5 Membrane Preparation and Characterization.....	60
2.5.1 Membrane Casting and Pre-treatment.....	60
2.5.2 Water Sorption.....	61
2.5.3 Ion Exchange Capacity and Acid Concentration.....	62
2.5.4 Proton Conductivity.....	64
2.5.5 Proton Mobility.....	69
2.5.6 Transmission Electron Microscopy (TEM).....	72
2.5.7 Wide-angle X-ray Scattering (WAXS).....	75

Chapter 3. Ionic Purity and Percolation of Proton-Conducting Channels in Fluorous-Ionic Diblock Copolymers	79
3.1 Introduction	79
3.2 Experimental	85
3.2.1 Materials	85
3.2.2 Synthesis of P(VDF- <i>co</i> -HFP)- <i>b</i> -SPS Diblock Ionomers	86
3.2.3 Membrane Preparation and Characterization	89
3.2.4 Instrumentation and Techniques	90
3.3 Results and Discussion	91
3.3.1 Synthesis of P(VDF- <i>co</i> -HFP)- <i>b</i> -SPS Diblock Ionomers	91
3.3.2 TEM	103
3.3.3 Water Sorption	106
3.3.4 Proton Conductivity	110
3.3.5 Proton Mobility	114
3.3.6 Conductivity Anisotropy	117
3.4 Conclusion	118
Chapter 4. Nanostructure, Morphology, and Properties of Fluorous Copolymers Bearing Ionic Grafts	120
4.1 Introduction	120
4.2 Experimental Section	125
4.2.1 Materials	125
4.2.2 Synthesis of Fluorous Macroinitiator [P(VDF- <i>co</i> -CTFE)]	125
4.2.3 Grafting ATRP of Styrene onto P(VDF- <i>co</i> -CTFE) Macroinitiator	126
4.2.4 Sulfonation of Polystyrene Graft Chains	127
4.2.5 Membrane Preparation and Characterization	128
4.2.6 Instrumentation and Techniques	129
4.3 Results and Discussion	132
4.3.1 Synthesis of P(VDF- <i>co</i> -CTFE)- <i>g</i> -SPS Graft Copolymers	132
4.3.2 TEM	140
4.3.3 Water Sorption	146
4.3.4 Wide-Angle X-ray Scattering	151
4.3.5 Proton Conductivity	154
4.3.6 Conductivity as a Function of Temperature and Humidity	159
4.4 Conclusion	163
Chapter 5. Fluorous-Ionic Copolymers: Diblocks versus Grafts	165
5.1 Introduction	165
5.2 Experimental Section	168
5.2.1 Materials	168
5.2.2 Membrane Preparation and Characterization	169
5.2.3 Instrumentation and Techniques	170
5.3 Results and Discussion	172
5.3.1 Preparation of Diblock and Graft Ionic Copolymers	172
5.3.2 TEM	176
5.3.3 Water Sorption	177
5.3.4 Proton Conductivity	179
5.3.5 Conductivity Anisotropy	183

5.4 Conclusion	184
Chapter 6. Research Summary and Outlook.....	186
References.....	191

List of Figures

Figure 1.1	Schematic drawing of a proton exchange membrane fuel cell.....	4
Figure 1.2	Chemical structures of (a) sulfonated polystyrene-divinylbenzene (cross-linked polystyrene sulfonic acid, PSSA) and (b) Nafion [®] membranes.....	7
Figure 1.3	Chemical structures of commercially available perfluorosulfonic acid (PFSA) membranes.....	10
Figure 1.4	Chemical structure of BAM [®] membranes.....	12
Figure 1.5	Chemical structures of representative radiation-grafted PEMs: a) poly(tetrafluoroethylene-co-hexafluoropropylene)- <i>g</i> -PSSA (FEP- <i>g</i> -PSSA), b) poly(ethylene- <i>alt</i> -tetrafluoroethylene)- <i>g</i> -PSSA (ETFE- <i>g</i> -PSSA) and c) poly(vinylidene fluoride)- <i>g</i> -PSSA (PVDF- <i>g</i> -PSSA).....	14
Figure 1.6	Schematic preparation of radiation-grafted membranes.....	15
Figure 1.7	Degradation mechanisms of sulfonated polystyrene-based membranes by (a) benzylic hydrogen atom abstraction and (b) radical addition.....	17
Figure 1.8	Chemical structures of representative sulfonated polystyrene-based block ionomer membranes: (a) partially sulfonated poly(styrene- <i>b</i> -[ethylene-co-butylene]- <i>b</i> -styrene) (S-SEBS), (b) partially sulfonated poly(styrene- <i>b</i> -isobutylene- <i>b</i> -styrene) (S-SIBS), (c) partially sulfonated hydrogenated poly(butadiene- <i>b</i> -styrene) (S-HPBS), (d) partially sulfonated poly(styrene- <i>b</i> -ethylene- <i>alt</i> -propylene) (S-SEP) and (e) partially sulfonated poly(styrene- <i>b</i> -[ethylene- <i>alt</i> -propylene]- <i>b</i> -styrene) (S-SEPS).....	19
Figure 1.9	Chemical structures of (a) sulfonated poly(<i>p</i> -phenylene oxide) (S-PPO), (b) sulfonated poly(<i>p</i> -phenylene sulfide) (S-PPS), (c) sulfonated poly(ether ether ketone) (S-PEEK), (d) sulfonated polysulfone (S-PSF), (e) sulfonated polybenzimidazole (S-PBI) and (f) sulfonated polyimide (S-PI).....	21
Figure 1.10	Schematic representation of ionic cross-linking in acid-base blend membranes.....	23
Figure 1.11	Simplified schematic representation of proton transport in hydrated PEMs. A comparison of the surface mechanism, Grotthuss mechanism, and vehicle mechanism.....	25
Figure 1.12	Schematic of proton transport by the Grotthuss mechanism.....	26
Figure 1.13	Cluster network model for the morphology of hydrated Nafion [®] membrane.....	28

Figure 1.14	Schematic representation of the structural evolution of Nafion [®] as a function of water content.....	29
Figure 1.15	Parallel water-channel model of Nafion [®] : a) Cross-sectional and side views of a water channel (inverted-micelle cylinder), with hydrophobic polymer backbone on the outside and ionic side chains lining the water channel. b) Near-hexagonal packing of several water channels. c) Cross-sections through the cylindrical water channels (white) and the Nafion crystallites (black) in the non-crystalline Nafion matrix. d) Effect of hydration on water channel size.....	31
Figure 1.16	TEM image of an ultrathin section (~60 nm) of Nafion membrane (IEC = 0.91 mmol/g), stained with Cs ⁺	32
Figure 1.17	Tapping-mode AFM images of Nafion 117 (K ⁺ -form) ionomer membrane after exposure to: a) room temperature humidity and b) liquid water. Scan boxes are 300 x 300 nm.....	33
Figure 1.18	Microstructures of copolymers.	36
Figure 1.19	Schematic representation of chemical structures (top), TEM micrographs (bottom left and right) and proton conductivity (bottom center) of PS- <i>g</i> -PSSA and PS- <i>r</i> -PSSA copolymers.	39
Figure 1.20	Schematic representation of the microstructures of Nafion and sulfonated poly(ether ether ketone) (S-PEEK).	40
Figure 1.21	Chemical structures of sulfonated poly(arylene ether sulfone)s with various hydrophobic components.	41
Figure 1.22	Chemical structures of a) superacid-bearing FSPE, b) conventional sulfonatedSPE and c) multiblock FSPE.	42
Figure 1.23	Chemical structures of midblock-sulfonated triblock copolymers of PHMA- <i>b</i> -SPS- <i>b</i> -PHMA and PFMA- <i>b</i> -SPS- <i>b</i> -PFMA.	43
Figure 2.1	Mechanism of free-radical polymerization.	49
Figure 2.2	Termination reactions in free-radical polymerization by a) bimolecular radical coupling and b) disproportionation.....	50
Figure 2.3	General scheme of controlled/living radical polymerization systems.	52
Figure 2.4	General mechanism of transition-metal catalyzed atom transfer radical polymerization (ATRP).	53
Figure 2.5	Schematic representation of the formation of a) diblock, b) ABA triblock and c) graft copolymers using macroinitiator approach.....	55
Figure 2.6	Schematic diagram showing the separation of analytes of varied size using a gel permeation chromatography (GPC) column.....	56
Figure 2.7	Typical calibration curve of a gel permeation chromatography instrument.....	57
Figure 2.8	Mechanism of a) formation of acetyl sulfate from acetic anhydride and sulfuric acid and b) sulfonation of polystyrene using acetyl sulfate.....	59

Figure 2.9	In-plane impedance electrochemical cell.....	65
Figure 2.10	Typical Nyquist plot for the in-plane impedance of a membrane: open circles represent experimental data and solid line represents the fitted data.	66
Figure 2.11	Randles equivalent circuit model used to fit in-plane impedance data.	66
Figure 2.12	Through-plane impedance electrochemical cell.	67
Figure 2.13	Typical Nyquist plot for the through-plane impedance of a membrane: empty squares represent experimental data and solid line represents the fitted data.....	68
Figure 2.14	Randles equivalent circuit model used to fit through-plane impedance data.	68
Figure 2.15	Schematic representation of the effects of connectivity and tortuosity of ionic channels on proton mobility (red = ionic domains).	71
Figure 2.16	Schematic representation of the effects of spatial proximity of neighboring acid groups on proton mobility.....	71
Figure 2.17	Schematic diagram of an electron transmission microscope (TEM).	74
Figure 2.18	Reflection of X-rays from atoms in different layers of a crystal lattice with interplanar spacing of d	76
Figure 2.19	Schematic representation of the microstructure of semi-crystalline polymer possessing crystalline phases and amorphous phases.	77
Figure 2.20	WAXS diffractogram of a P(VDF- <i>co</i> -HFP) copolymer showing the resolved crystalline and amorphous peaks (dashed line).	78
Figure 3.1	Morphological phase diagram for polystyrene- <i>b</i> -polyisoprene (PS- <i>b</i> -PI) diblock copolymers.....	80
Figure 3.2	Synthetic Scheme for P(VDF- <i>co</i> -HFP)- <i>b</i> -SPS.....	83
Figure 3.3	Structural relationship between the various series of P(VDF- <i>co</i> -HFP)- <i>b</i> -SPS membranes.	85
Figure 3.4	Mechanism of chain transfer polymerization initiated by $\text{CCl}_3\cdot$ radicals (I = initiator; M = monomer).....	93
Figure 3.5	^1H NMR spectra (d_6 -acetone) of (a) P(VDF- <i>co</i> -HFP), (b) P(VDF- <i>co</i> -HFP)- <i>b</i> -PS, and (c) partially sulfonated P(VDF- <i>co</i> -HFP)- <i>b</i> -SPS (DS = 37%).	94
Figure 3.6	^{19}F NMR spectrum (d_6 -acetone) of P(VDF- <i>co</i> -HFP) macroinitiator.....	95
Figure 3.7	GPC traces of (a) P(VDF- <i>co</i> -HFP) macroinitiator, and (b) P(VDF- <i>co</i> -HFP)- <i>b</i> -PS diblock copolymer.....	96
Figure 3.8	TEM images of selected P(VDF- <i>co</i> -HFP)- <i>b</i> -SPS membranes from: the 6 – 17 vol% PS series with IECs (mmol/g) of (A) 0.46, (B) 0.70, (C) 1.20; the 35 vol% PS series with IECs of (D) 0.42, (E) 0.68, (F) 0.73; the 45 vol% PS series with IECs of (G) 0.62, (H) 0.89, (I) 1.31; and the 50 vol% PS with IEC of (J) 1.09.	104

Figure 3.9	(a) Water content vs. IEC and (b) λ vs. IEC for P(VDF- <i>co</i> -HFP)- <i>b</i> -SPS membranes with 6 – 17 (Δ), 35 (\bullet), 45 (\blacksquare) and 50 vol% (\blacktriangledown) polystyrene. Note: open symbols represent fully sulfonated membranes; filled symbols, partially sulfonated.	107
Figure 3.10	Schematic representation of the hierarchical microstructure in P(VDF- <i>co</i> -HFP)- <i>b</i> -SPS: a) The large scale morphology consists of stacks of alternating fluorocarbon and sulfonated polystyrene domains. b) Within the sulfonated polystyrene domains, formation of ionic aggregates of sulfonated polystyrene (PSSA) in a matrix of host polystyrene.....	108
Figure 3.11	(a) Proton conductivity vs. IEC, (b) proton conductivity vs. λ , and (c) $[-SO_3H]$ vs. IEC for P(VDF- <i>co</i> -HFP)- <i>b</i> -SPS membranes with 6 – 17 (Δ), 35 (\bullet), 45 (\blacksquare) and 50 vol% (\blacktriangledown) polystyrene. Note: open symbols represent fully sulfonated membranes; filled symbols, partially sulfonated.	112
Figure 3.12	(a) <i>Effective</i> proton mobility (μ_{eff}) vs. IEC and (b) μ_{eff} vs. water volume fraction (X_v) for P(VDF- <i>co</i> -HFP)- <i>b</i> -SPS membranes with 6 – 17 (Δ), 35 (\bullet), 45 (\blacksquare) and 50 vol% (\blacktriangledown) polystyrene. Note: open symbols represent fully sulfonated membranes; filled symbols, partially sulfonated.	116
Figure 4.1	Synthetic scheme of partially sulfonated P(VDF- <i>co</i> -CTFE)- <i>g</i> -SPS graft copolymers.	121
Figure 4.2	Structural relationship between the various series of P(VDF- <i>co</i> -CTFE)- <i>g</i> -SPS.	124
Figure 4.3	GPC traces of (a) P(VDF- <i>co</i> -CTFE) macroinitiator and the resulting P(VDF- <i>co</i> -CTFE)- <i>g</i> -PS graft copolymers at various reaction time: (b) 8 h, (c) 16 h and (d) 24 h (Note: the original negative peak in (a) is inverted for convenience).	133
Figure 4.4	1H NMR spectra of (a) P(VDF- <i>co</i> -CTFE) macroinitiator (d_6 -acetone), (b) P(VDF- <i>co</i> -CTFE)- <i>g</i> -PS graft copolymer (d_6 -acetone), and (c) partially sulfonated P(VDF- <i>co</i> -CTFE)- <i>g</i> -SPS graft copolymers (d_6 -DMSO).	135
Figure 4.5	^{19}F NMR spectra of (a) P(VDF- <i>co</i> -CTFE) macroinitiator (d_6 -acetone) and (b) P(VDF- <i>co</i> -CTFE)- <i>g</i> -PS graft copolymer (d_6 -acetone).	135
Figure 4.6	TEM images of selected P(VDF- <i>co</i> -CTFE)- <i>g</i> -SPS membranes from the short series with IECs (mmol/g) of 0.64 (A) and 2.48 (B); the medium series with IECs of 0.73 (C) and 2.46 (D) mmol/g; and the long series with IECs of 0.73 (E) and 2.53 (F) mmol/g.	141
Figure 4.7	Distributions of the ionic cluster sizes in selected membranes from (a) short, (b) medium, and (c) long graft copolymer series.	142
Figure 4.8	Schematic representation for the formation of a percolated ionic network: (a) increasing ionic cluster size but constant number of ionic clusters and (b) increasing number of ionic clusters but constant ionic cluster size.	144

Figure 4.9	(a) Water content (wt %) vs. IEC and (b) λ vs. IEC for P(VDF-co-CTFE)- <i>g</i> -SPS having short (●), medium (□), and long (▲) graft chains.	147
Figure 4.10	Schematic representation of the postulated ionic aggregation in P(VDF-co-CTFE)- <i>g</i> -SPS membranes with (a) short and (b) long graft length at different ion contents.	150
Figure 4.11	(a) WAXS spectra for membranes of P(VDF-co-CTFE) macroinitiator and P(VDF-co-CTFE)- <i>g</i> -PS of various graft lengths (measured under ambient conditions, intensity scale is in arbitrary units). (b) Fitting of the scattering data with two Gaussians for identifying of the amorphous peak and the crystalline peak (note: lower curve shows the residuals from the fit).	152
Figure 4.12	WAXS spectra for short graft membranes of various degrees of sulfonation (measured under ambient conditions, intensity scale is in arbitrary units).	154
Figure 4.13	(a) Proton conductivity vs. IEC and (b) proton conductivity. vs λ for P(VDF-co-CTFE)- <i>g</i> -SPS membranes having short (●), medium (□), and long (▲) graft lengths.....	155
Figure 4.14	(a) Analytical [-SO ₃ H] in hydrated membranes vs. IEC, (b) <i>effective</i> proton mobility (μ_{eff}) vs. IEC and (c) μ_{eff} vs. water volume fraction (X_v) for P(VDF-co-CTFE)- <i>g</i> -SPS membranes having short (●), medium (□), and long (▲) graft lengths.....	157
Figure 4.15	(a) Proton conductivity vs. relative humidity, at 30 °C; (b) water uptake vs. relative humidity, at 25 °C; and (c) proton conductivity vs. temperature, at 95 % RH, for selected P(VDF-co-CTFE)- <i>g</i> -SPS membranes from long graft series and Nafion [®] 117.	161
Figure 4.16	Plots of natural logarithm of proton conductivity vs 1000/T (K ⁻¹) for P(VDF-co-CTFE)- <i>g</i> -SPS membranes and Nafion [®] 117.	163
Figure 5.1	Chemical structures of (a) P(VDF-co-HFP)- <i>b</i> -SPS diblock and (b) P(VDF-co-CTFE)- <i>g</i> -SPS graft copolymers.....	168
Figure 5.2	TEM micrographs of (a) P(VDF-co-HFP)- <i>b</i> -SPS diblock (IEC = 0.72 mmol/g) and (b) P(VDF-co-CTFE)- <i>g</i> -SPS Graft (IEC = 1.03 mmol/g) membranes.....	176
Figure 5.3	(a) Water content vs. IEC and (b) λ vs. IEC of P(VDF-co-HFP)- <i>b</i> -SPS diblock (○) and P(VDF-co-CTFE)- <i>g</i> -SPS graft (■) membranes.	178
Figure 5.4	(a) In-plane proton conductivity vs. IEC, (b) analytical [-SO ₃ H] vs. IEC, and (c) <i>effective</i> proton mobility (μ_{eff}) vs. IEC of P(VDF-co-HFP)- <i>b</i> -SPS diblock (○) and P(VDF-co-CTFE)- <i>g</i> -SPS graft (■) membranes.....	180
Figure 5.5	Effective proton mobility (μ_{eff}) vs. water volume fraction of P(VDF-co-HFP)- <i>b</i> -SPS diblock (○) and P(VDF-co-CTFE)- <i>g</i> -SPS graft (■) membranes.....	182

List of Tables

Table 1.1	Common Types of Fuel Cells.....	3
Table 3.1	Chemical Compositions of Macroinitiator, P(VDF- <i>co</i> -HFP)- <i>b</i> -PS and Sulfonated P(VDF- <i>co</i> -HFP)- <i>b</i> -SPS.....	97
Table 3.2	Chemical Compositions of P(VDF- <i>co</i> -HFP)- <i>b</i> -SPS Membranes Studied.....	101
Table 3.3	Properties of Various Series of P(VDF- <i>co</i> -HFP)- <i>b</i> -SPS Diblock Copolymer Membranes.....	102
Table 3.4	In-plane and Through-plane Conductivity of P(VDF- <i>co</i> -HFP)- <i>b</i> -SPS Membranes Possessing Different Morphologies.....	118
Table 4.1	Chemical Compositions of P(VDF- <i>co</i> -CTFE)- <i>g</i> -PS Parent Graft Copolymers.....	133
Table 4.2	Chemical Compositions of P(VDF- <i>co</i> -CTFE)- <i>g</i> -SPS Graft Membranes.....	138
Table 4.3	Properties of P(VDF- <i>co</i> -CTFE)- <i>g</i> -SPS Membranes.....	139
Table 4.4	Ionic Cluster Size and Number Density.....	143
Table 4.5	Extrapolated Proton Mobility Values at Infinite Dilution ($X_v = 1.0$).....	159
Table 5.1	Chemical Compositions of P(VDF- <i>co</i> -HFP)- <i>b</i> -PS Diblock and P(VDF- <i>co</i> -HFP)- <i>g</i> -PS Graft Copolymers.....	174
Table 5.2	Properties of P(VDF- <i>co</i> -HFP)- <i>b</i> -SPS Diblock and P(VDF- <i>co</i> -CTFE)- <i>g</i> -SPS Graft Copolymer Membranes.....	175
Table 5.3	Proton Conductivity Anisotropy ($\sigma_{\parallel,\perp}$) of Selected P(VDF- <i>co</i> -HFP)- <i>b</i> -SPS Diblock and P(VDF- <i>co</i> -CTFE)- <i>g</i> -SPS Graft Membranes.....	184

List of Abbreviations

AFC	alkaline fuel cell
AFM	atomic force microscopy
ATRP	atom transfer radical polymerization
CTFE	chlorotrifluoroethylene
DMF	dimethyl formamide
DMFC	direct methanol fuel cell
DMAc	<i>N,N</i> -dimethylacetamide
DP	degree of polymerization
DS	degree of sulfonation
DVB	divinylbenzene
ETFE	poly(ethylene- <i>alt</i> -tetrafluoroethylene)
ETFE- <i>g</i> -PSSA	poly([ethylene- <i>alt</i> -tetrafluoroethylene]- <i>g</i> -styrenesulfonic acid)
FEP	poly(tetrafluoroethylene- <i>co</i> -hexafluoropropylene)
FEP- <i>g</i> -PSSA	poly([tetrafluoroethylene- <i>co</i> -hexafluoropropylene]- <i>g</i> -styrenesulfonic acid)
<i>g</i> -ATRP	<i>graft</i> -atom transfer radical polymerization
GPC	gel permeation chromatography
HFP	hexafluoropropylene
IEC	ion exchange capacity

MEA	membrane-electrode-assembly
MCFC	molten carbonate fuel cell
P4VP	poly(4-vinylpyridine)
PAFC	phosphoric acid fuel cell
PDI	polydispersity index
PEM	proton exchange membrane
PEMFC	proton exchange membrane fuel cell
PFA	poly(tetrafluoroethylene-co-perfluoropropyl vinyl ether)
PFSA	perfluorosulfonic acid
PS	polystyrene
PS- <i>b</i> -PI	poly(styrene- <i>b</i> -isoprene)
PS- <i>g</i> -PSSA	poly(styrene- <i>g</i> -styrenesulfonic acid)
PS- <i>r</i> -PSSA	poly(styrene- <i>r</i> -styrenesulfonic acid)
PSSA	polystyrenesulfonic acid
PTFE	polytetrafluoroethylene
PVDF	polyvinylidene difluoride
P(VDF- <i>co</i> -CTFE)	poly(vinylidene difluoride- <i>co</i> -chlorotrifluoroethylene)
P(VDF- <i>co</i> -CTFE)- <i>g</i> -SPS	partially sulfonated poly([vinylidene fluoride- <i>co</i> -chlorotrifluoroethylene]- <i>g</i> -styrene)
P(VDF- <i>co</i> -HFP)	poly(vinylidene difluoride- <i>co</i> -hexafluoropropylene)
P(VDF- <i>co</i> -HFP)- <i>b</i> -SPS	partially sulfonated poly([vinylidene difluoride- <i>co</i> -hexafluoropropylene]- <i>b</i> -styrene)
PVDF- <i>g</i> -PSSA	poly(vinylidene difluoride- <i>g</i> -styrenesulfonic acid)
ROMP	ring opening metathesis polymerization

SANS	small-angle neutron scattering
SAXS	small angle X-ray scattering
SFRP	stable free radical polymerization
SOFC	solid oxide fuel cell
S-HPBS	sulfonated hydrogenated poly(butadiene- <i>b</i> -styrene)
S-PBI	sulfonated polybenzimidazole
S-PEEK	sulfonated poly(ether ether ketone)
S-PI	sulfonated polyimide
S-PPO	sulfonated poly(<i>p</i> -phenylene oxide)
S-PPS	sulfonated poly(<i>p</i> -phenylene sulphide)
S-PSF	sulfonated polysulfone
S-SEBS	partially sulfonated poly(styrene- <i>b</i> -[ethylene- <i>co</i> -butylene]- <i>b</i> -styrene)
S-SEP	partially sulfonated poly(styrene- <i>b</i> -ethylene- <i>alt</i> -propylene)
S-SEPS	partially sulfonated poly(styrene- <i>b</i> -[ethylene- <i>alt</i> -propylene]- <i>b</i> -styrene)
S-SIBS	partially sulfonated poly(styrene- <i>b</i> -isobutylene- <i>b</i> -styrene)
SC-SBS	sulfonated cross-linked poly(styrene- <i>b</i> -butadiene- <i>b</i> -styrene)
TEM	transmission electron microscopy
TFE	tetrafluoroethylene
THF	tetrahydrofuran
VDF	vinylidene difluoride
WAXS	wide-angle X-ray scattering

List of Symbols

A	cross-sectional area of membrane (in-plane conductivity); area of platinum electrode (through-plane conductivity)
α_{H^+}	proton activity
C_{dl}	double-layer capacitance
C_{m}	bulk membrane capacitance
χ	Flory-Huggins segmental interaction parameter
F	Faraday's constant
k_{act}	rate constant of activation reaction
k_{ct}	rate constant of chain transfer reaction
k_{d}	rate constant of initiator dissociation reaction
k_{deact}	rate constant of deactivation reaction
k_{i}	rate constant of initiation reaction
k_{p}	rate constant of propagation reaction
k_{t}	rate constant of termination reaction
L	distance between platinum electrodes (in-plane conductivity); membrane thickness (through-plane conductivity)
λ	molar ratio of water to ion exchange sites
M	monomer
μ_{eff}	<i>effective</i> proton mobility
M_{n}	number-average molecular weight

M_w	weight-average molecular weight
N	degree of polymerization
P_n	terminated polymer
ρ	density
σ_{\perp}	<i>through-plane</i> proton conductivity
σ_{\parallel}	<i>in-plane</i> proton conductivity
$\sigma_{\parallel/\perp}$	proton conductivity anisotropy
T_g	glass transition temperature
V_{dry}	volume of dry membrane
V_{wet}	volume of hydrated membrane
W_{dry}	mass of dry membrane
W_{wet}	mass of hydrated membrane
x_{cr}	degree of crystallinity
X_v	water volume fraction
YZ	transfer agent

Chapter 1. Introduction

1.1 Fuel cells

Fuel cells, offering high energy efficiency, high power density, and minimal pollution, represent a clean and sustainable alternative to conventional energy conversion technologies. They are promising candidates to replace the internal combustion engines in automotive applications, and thus may provide a feasible solution to the anticipated, world-wide, oil crisis. The concept of the fuel cell was first demonstrated by Sir William Robert Grove in 1839; however, it was not until the early 1960s that fuel cells gained prominence after their first major application as power sources for spacecraft in the Gemini space program.¹

Fuel cells are electrochemical devices that convert the chemical energy of a fuel and an oxidant directly into electrical energy. They generally consist of three components: the anode, the electrolyte and the cathode (see, for example, Figure 1.1). During operation, the fuel (i.e., hydrogen) and the oxidant (i.e., oxygen, air) flow separately to their respective electrodes: oxidation of the fuel occurs at the anode while reduction of the oxidant occurs at the cathode. The electrons flow through an external circuit to power a load. The electrolyte serves as a separator of the reactant and oxidant, and as an ion-conductor to balance the charge and complete the electrochemical circuit. Fuel cells based on a hydrogen/oxygen system generate electricity with water and heat as the by-products, and thus can reduce the emission of greenhouse and toxic gases that

are produced by conventional energy conversion technologies (i.e., fossil fuel combustion). In addition, fuel cells provide much higher fuel efficiencies (typically, 50 - 60%) compared to internal combustion engines (~30% fuel efficiency).²

In principle, fuel cells operate like conventional cell batteries as they both convert chemical energy directly into electrical energy through electrochemical processes. However, unlike conventional cell batteries, which are thermodynamically closed systems with reactants being stored inside, fuel cells are thermodynamically open systems in which reactants are supplied from an external source. As a result, fuel cells do not run down or require recharging, and they can operate continuously as long as the necessary reactant and oxidant flows are supplied.

As summarized in Table 1.1, several types of fuel cells exist today, and they can be categorized by their electrolyte material. The choice of electrolyte materials governs several important characteristics of a fuel cell including the fuel/oxidant type, the electrochemical reactions, and the operating temperature range.

Table 1.1 Common Types of Fuel Cells

Fuel Cell Type	Electrolyte	Fuel/Oxidant Type	Operating Temperature (°C)	Charge carrier	Electrochemical Reactions
Proton Exchange Membrane Fuel Cell (PEMFC)	Solid polymer electrolyte membrane	H ₂ /O ₂ Methanol/O ₂	30 - 200	H ⁺	Anode: H ₂ → 2H ⁺ + 2e ⁻ Cathode: ½O ₂ + 2H ⁺ + 2e ⁻ → H ₂ O Overall: H ₂ + ½O ₂ → H ₂ O Anode: CH ₃ OH + H ₂ O → 6H ⁺ + 6e ⁻ + CO ₂ Cathode: ¾O ₂ + 6H ⁺ + 6e ⁻ → 3H ₂ O Overall: CH ₃ OH + ¾O ₂ → 2H ₂ O + CO ₂
Phosphoric Acid Fuel Cell (PAFC)	Liquid phosphoric acid soaked in a matrix	H ₂ /O ₂	150 – 220	H ⁺	Anode: H ₂ → 2H ⁺ + 2e ⁻ Cathode: ½O ₂ + 2H ⁺ + 2e ⁻ → H ₂ O Overall: H ₂ + ½O ₂ → H ₂ O
Alkaline Fuel Cell (AFC)	Solution of potassium hydroxide soaked in a matrix	H ₂ /O ₂	90 - 100	OH ⁻	Anode: H ₂ + 2OH ⁻ → 2H ₂ O + 2e ⁻ Cathode: ½O ₂ + H ₂ O + 2e ⁻ → 2OH ⁻ Overall: H ₂ + ½O ₂ → H ₂ O
Molten Carbonate Fuel Cell (MCFC)	Molten mixture of alkaline carbonates	H ₂ /O ₂	650 – 1000	CO ₃ ²⁻	Anode: H ₂ + CO ₃ ²⁻ → H ₂ O + CO ₂ + 2e ⁻ Cathode: ½O ₂ + CO ₂ + 2e ⁻ → CO ₃ ²⁻ Overall: H ₂ + ½O ₂ + CO ₂ (ca.) → H ₂ O + CO ₂ (an.)
Solid Oxide Fuel Cell (SOFC)	Solid zirconium oxide doped with a small amount of yttria	H ₂ /O ₂	850 - 1000	O ²⁻	Anode: H ₂ + O ²⁻ → H ₂ O + 2e ⁻ Cathode: ½O ₂ + 2e ⁻ → O ²⁻ Overall: H ₂ + ½O ₂ → H ₂ O

1.2 Proton Exchange Membrane Fuel Cells

Proton exchange membrane (also known as “polymer electrolyte membrane”) fuel cells (PEMFCs) are currently the focus of fuel cell research, as they are considered the most promising candidate for automotive power applications.^{1, 3} The PEMFC employs a solid polymer film (a proton exchange membrane, PEM) as the electrolyte, as illustrated in Figure 1.1. This membrane is sandwiched between two gas diffusion electrodes, each incorporating a porous gas diffusion layer (GDL) and a catalyst electrode layer (CL). The whole construction forms a membrane-electrode-assembly (MEA), which is situated in the heart of the fuel cell.

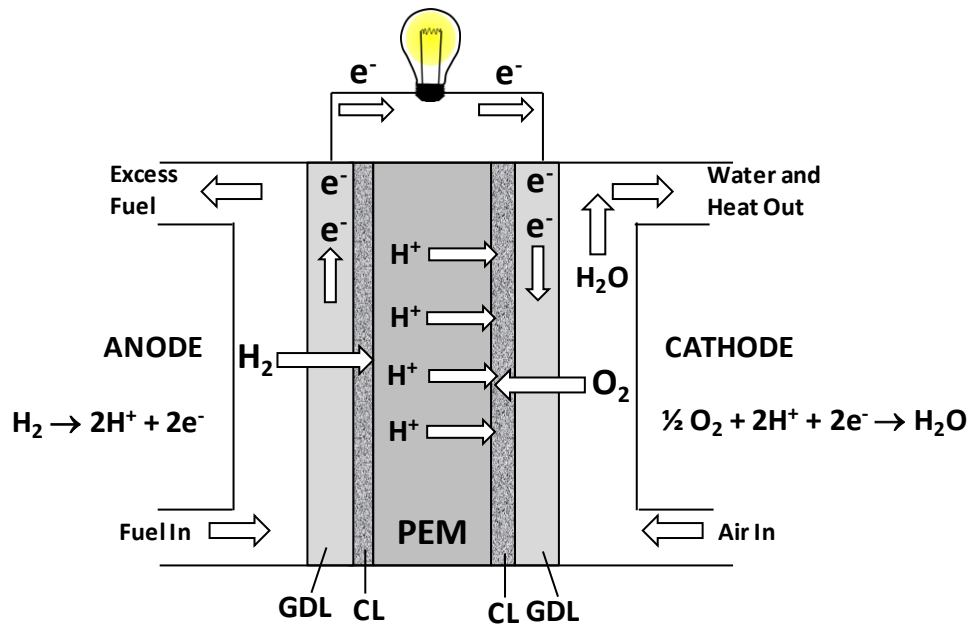
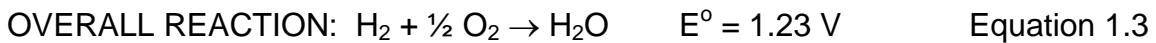


Figure 1.1 Schematic drawing of a proton exchange membrane fuel cell.

During operation, the fuel of choice (typically hydrogen) is oxidized at the anode generating protons and electrons (Equation 1.1). The protons migrate

through the PEM to the cathode, whereas the electrons travel through an external circuit to power a load and subsequently terminate at the cathode. At the cathode, oxygen reacts with protons and electrons to form water (Equation 1.2). Overall, the by-products of the electrochemical reaction between hydrogen and oxygen are water and electrical energy (Equation 1.3).



PEMFCs offer many practical advantages over other fuel cell systems. The solid polymer electrolyte eliminates electrolyte leakage issues and the requirement of handling corrosive acids/bases, thus leading to longer cell life. PEMFCs can operate at very high power densities and relatively low temperatures (30 – 200 °C), allowing for quick start-up under diverse conditions, which is a key requirement for automotive applications. Their ability to utilize various hydrogen-containing fuels (i.e., H₂, methanol, ethanol, propane) and quiet operation makes them attractive for small portable electronic devices as well as large-scale stationary power generation.

Indeed, PEMFC technology has been successfully used to power automobiles, buses, backup power generators, boats and laptop computers.⁴ However, the widespread commercialization of PEMFCs has been challenging primarily due to high material cost, performance and durability issues under operating conditions, as well as the need for improvements in hydrogen production and storage.

1.3 Proton Exchange Membrane

The proton exchange membrane (PEM) is a crucial component in a PEMFC, serving as a separator to prevent mixing of the fuel and oxidant, as a structural support for the electrodes and catalyst layers, and as an electrolyte for transporting protons from the anode to the cathode. PEMs generally consist of ionomers – polymers with covalently bonded ionic functionalities – that are capable of exchanging protons. The bound ion is typically a strong acid, such as sulfonic acid. Incorporation of acidic groups into a polymer can be achieved by direct polymerization of monomers functionalized with ionic groups, or alternatively, by attaching ionic groups onto a base polymer backbone via post-polymerization reaction (i.e., post-sulfonation reaction).

The material requirements for an ideal PEM include:^{3, 5, 6}

- High proton conductivity
- Low electronic conductivity
- Long-term chemical, electrochemical and thermal stability
- Adequate mechanical properties in both the dry and hydrated states
- Low permeability to fuel and oxidant
- Low production cost

The performance of a membrane depends heavily on its proton conductivity and water uptake, which in turn depends on the concentration of ionic groups, i.e., $-\text{SO}_3\text{H}$, in the polymer membrane. The ion content of a PEM is often represented by the ion exchange capacity (IEC) with units of millimoles of ion exchange sites per gram of dry polymer (mmol/g). Intuitively, it might seem

desirable to maximize the proton conductivity of the membrane by merely increasing its ion content. However, other physical properties are also affected by the ion content and must be carefully considered. The incorporation of large amounts of ionic groups can lead to excessive water swelling, which compromises mechanical stability and durability. Furthermore, high water content can cause increased water transport across the membrane leading to flooding at the cathode. Thus, devising a polymer system that can conduct protons while maintaining low levels of water content is the ultimate goal for PEM research.

The PEMFCs first deployed in the Gemini space program in the early 1960s were developed by General Electric Research Laboratory. These fuel cells, employing membranes based on cross-linked polystyrene sulfonic acid (PSSA), Figure 1.2a, had very short lifetimes (300 - 1000 hr at 60 °C) due to oxidative degradation of the hydrocarbon backbone of PSSA.^{7, 8} In the late 1960s, DuPont developed a class of perfluorosulfonic acid (PFSA) membranes under the trademark Nafion[®]. Although Nafion[®] membranes were originally developed as permselective separators in chlor-alkali electrolyzers,⁹ their excellent chemical stability and proton conductivity render them highly suitable for use as fuel cell membranes.

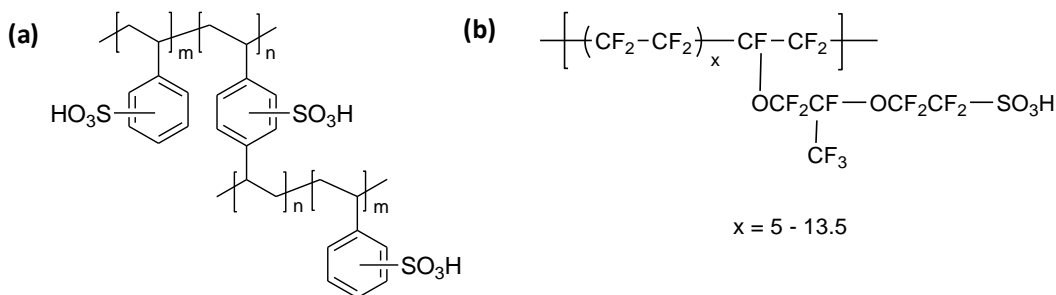


Figure 1.2 Chemical structures of (a) sulfonated polystyrene-divinylbenzene (cross-linked polystyrene sulfonic acid, PSSA) and (b) Nafion[®] membranes.

Indeed, Nafion[®] is currently the material of choice and the technology standard in fuel cell research, offering to date an adequate combination of performance, durability, and reliability.^{3, 6} As illustrated in Figure 1.2b, the chemical structure of Nafion[®] consists of a tetrafluoroethylene backbone sequence with pendent perfluorinated vinyl ether side chains terminated by sulfonic acid groups. The Teflon[®]-like molecular backbone imparts to these membranes long-term stability in both oxidative and reductive environments. In addition, Nafion[®] membranes exhibit excellent mechanical strength and protonic conductivities in the order of 0.10 S cm^{-1} under fully hydrated conditions.⁵

Although Nafion[®] membranes provide good performance under normal conditions, they suffer several critical drawbacks: Their operating condition is usually limited to $< 90 \text{ }^\circ\text{C}$ and $> 50\%$ relative humidity (RH) due to their tendency for dehydration.⁶ The high cost of production renders them unsuitable for automotive applications. For direct methanol fuel cell (DMFC) applications, where a liquid methanol fuel highly diluted in water is used as the source of protons, Nafion[®] membranes provide a poor barrier to methanol crossover leading to reduced fuel efficiency. In H_2/O_2 systems, they allow for a high electro-osmotic drag coefficient that leads to detrimental dehydration of the anode and/or flooding at the cathode. Recycling and disposal of the fluorinated polymer are other issues. In the ionic form, they are difficult to process and cannot be easily dissolved, melted, or extruded, and thus are often precluded from being used in novel cell designs with complex geometries. For these and other reasons, there

is a growing need to develop alternative PEM materials at lower cost and with improved properties over those currently offered by Nafion membranes.¹⁰⁻¹²

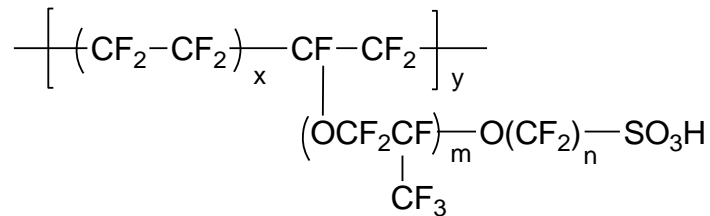
1.4 Alternate Proton Exchange Membranes

Over the last two decades, a wide array of proton conducting polymers have been developed and explored as PEM materials. These membrane materials are generally classified according to their chemical class as follows:

- Perfluorinated ionomers
- Partially fluorinated polymers
- Non-fluorinated hydrocarbons
- Polymer blends and composite membranes

1.4.1 Perfluorinated Ionomers

In addition to providing an attractive combination of performance and reliability, perfluorosulfonic acid (PFSA) membranes also demonstrate excellent durability due to their strong C-F bonds, which are highly resistant to radically induced chemical degradation. The chemical structures of common PFSA membranes are shown in Figure 1.3.



Nafion [®]	m = 1; n = 2; x = 5 – 13.5
Flemion [®]	m = 0, 1; n = 1 – 5
Aciplex [®]	m = 0, 3; n = 2 – 5; x = 1.5 – 14
Dow [®] , Hyflon-Ion [®]	m = 0; n = 2; x = 3 – 10
3M [®]	m = 0; n = 3
Asahi-Kasei [®]	m = 0, n = 4

Figure 1.3 Chemical structures of commercially available perfluorosulfonic acid (PFSA) membranes.

Nafion[®] is a free-radical initiated random copolymer derived from hydrophobic tetrafluoroethylene (TFE) and a perfluorovinylether comonomer in its sulfonyl fluoride form. The sulfonyl fluoride group (-SO₂F) may be converted to a sulfonate by alkaline hydrolysis, and subsequent acidification provides the acid form (-SO₃H). The ion content of Nafion[®] membranes can be varied by changing the ratio of the two monomer components (i.e., varying x in Figure 1.3). Like many fluoropolymers, Nafion[®] possesses exceptional oxidative and chemical stability, but it is primarily the presence of the strong perfluorosulfonic acid groups (-CF₂SO₃H, pK_a ~ -6)¹³ that imparts many of its desirable properties as a proton exchange membrane. The highly hydrophobic, crystallizable, perfluorinated backbone provides excellent morphological and mechanical stability. Nafion[®] is the most extensively studied PEM in terms of its conductivity and microstructure.¹⁴ As a result of its commercial availability and superior

performance, Nafion[®] is currently considered as the technology standard to which new alternative membranes are compared.

Other perfluorosulfonic acid ionomers based on the Nafion structure have also been developed by the Asahi Glass Company (Flemion[®]) and the Asahi Chemical Company (Aciplex[®]), in which the length of the perfluorinated ether side chains and the ionic contents are varied to some extent, as shown in Figure 1.3.⁶ Both alternative membranes exhibit similar fuel cell performance to that of Nafion. The Dow Chemical Company also developed a similar material (Dow[®] membrane) in which the side chain is reduced to only two CF₂ units in addition to the ethereal oxygen.¹⁵ Due to its shorter side chains, the Dow[®] membrane can be prepared with relatively higher IECs (1.25 mmol/g for Dow vs. 0.9 – 1.0 mmol/g for Nafion). The proton conductivity of the Dow[®] membrane has been demonstrated to exceed that of Nafion due to its higher ion content.¹⁶ It has also been suggested that a shorter side chain might be favourable for proton transport under low humidity conditions.¹⁷ Solvay-Solexis has recently developed a new and cheaper route for the synthesis of short side chain PFSA (Hyflon-Ion[®]).¹⁸ Variations on the Dow structure have also been extended to three CF₂ units (3M[®])¹⁹ as well as four CF₂ units (Asahi-Kasei[®])²⁰ in the side chain.

More recently, perfluorinated ionomers in which the sulfonic acid groups have been replaced with sulfonamide groups (e.g., -SO₂NHSO₂CF₃) for proton conduction have also been developed.²¹ These materials have been reported to possess better thermal stability (up to 400 °C in the acid form) than Nafion, excellent chemical and electrochemical stability, as well as being less susceptible

to dehydration and oxidative degradation than perfluorosulfonic acid based PEMs.²² These systems are presumed to have similar membrane microstructure to their sulfonic acid counterparts. At relative humidity < 70%, sulfonamide-based materials show higher proton conductivity than the analogous Nafion membrane, suggesting that sulfonamide groups are less sensitive to water content than sulfonic acid groups.²³

1.4.2 Partially Fluorinated Ionomers

Due to the cost and difficulty in synthesizing the perfluorovinylether comonomers of perfluorosulfonic acid membranes, partially fluorinated materials have been developed to provide a better balance between cost and performance. Partially fluorinated membranes can generally be prepared at a much lowered cost while retaining many of the advantages of fully fluorinated systems (i.e., good durability, mechanical and morphological stability).

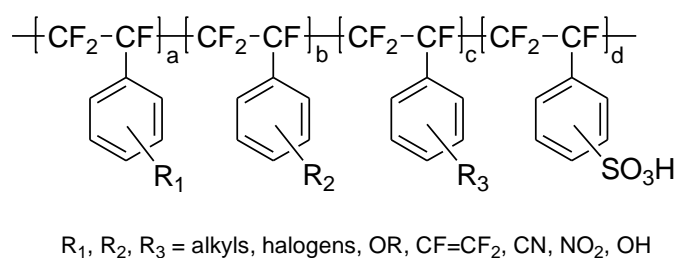


Figure 1.4 Chemical structure of BAM[®] membranes.

One of the major classes of partially fluorinated PEM materials is based on random copolymers incorporating α,β,β -trifluorostyrene and substituted α,β,β -trifluorostyrene comonomers, as shown in Figure 1.4. These membranes were

prepared by Ballard Advanced Materials in the mid to late 1990s, and are commonly known by their trademark name, BAM[®] (also known as BAM 3G).^{24, 25} The unsulfonated random copolymers are reportedly synthesized by a radical emulsion copolymerization of the substituted and un-substituted trifluorostyrene monomers.²⁵ The copolymer is then dissolved in an appropriate solvent and sulfonated using reagents such as chlorosulfonic acid or a sulfur trioxide complex. The ion content in these materials can be controlled by varying the ratios of monomers and/or manipulating the post-sulfonation conditions. The fluorinated main chain mitigates radical-induced chemical degradation while the presence of a substituent (R) on the non-ionic styrene units serves as an internal plasticizer to reduce brittleness and thereby enhance the mechanical properties.

Radiation-grafted PEMs are an important family of partially fluorinated membranes prepared by radiation-induced grafting of a suitable monomer (i.e., styrene, trifluorostyrene) onto a base fluoropolymer film, followed by subsequent sulfonation of the graft chains.²⁶⁻²⁸ The base polymer is typically a commercially-available fluoropolymer film including poly(tetrafluoroethylene) (PTFE),²⁹⁻³³ poly(vinylidene fluoride) (PVDF),³⁴⁻³⁸ poly(tetrafluoroethylene-co-perfluoropropyl vinyl ether) (PFA),³⁹⁻⁴² poly(tetrafluoroethylene-co-hexafluoropropylene) (FEP),⁴³⁻⁴⁷ and poly(ethylene-alt-tetrafluoroethylene) (ETFE).^{45, 46} The chemical structures of some representative radiation-grafted PEMs are shown in Figure 1.5.

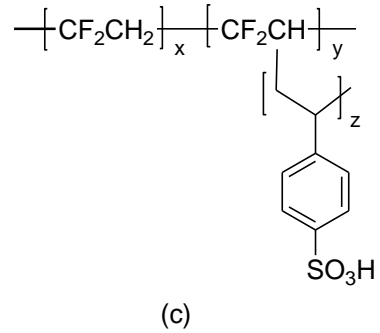
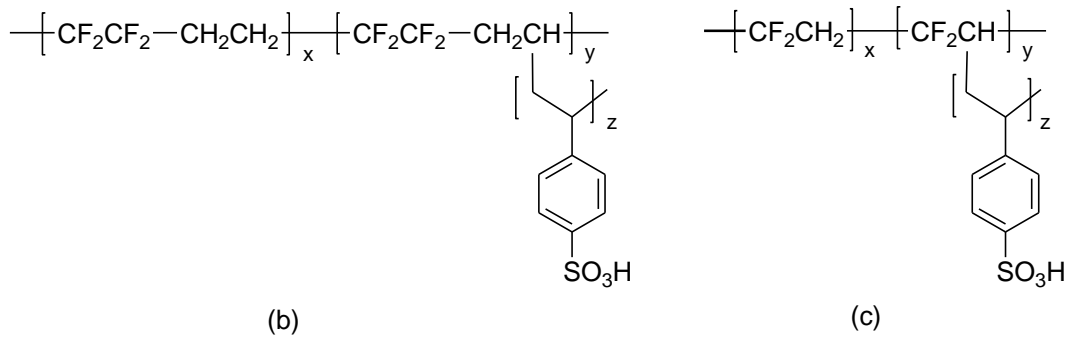
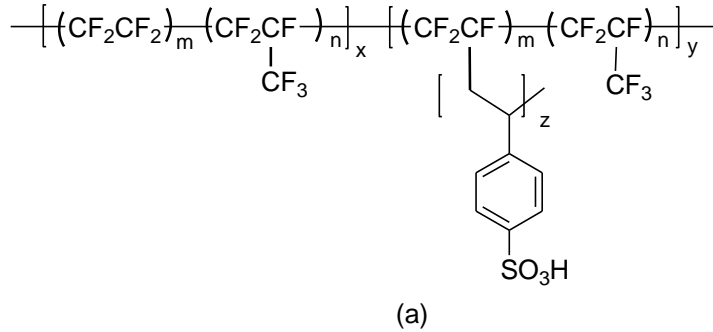


Figure 1.5 Chemical structures of representative radiation-grafted PEMs: a) poly(tetrafluoroethylene-co-hexafluoropropylene)-*g*-PSSA (FEP-*g*-PSSA), b) poly(ethylene-*alt*-tetrafluoroethylene)-*g*-PSSA (ETFE-*g*-PSSA) and c) poly(vinylidene fluoride)-*g*-PSSA (PVDF-*g*-PSSA).

The preparation of radiation-grafted membranes is illustrated in Figure 1.6. Irradiation of the base fluoropolymer film can take place in the presence of monomer – i.e., direct radiation grafting, or alternatively, the base substrate can be pre-irradiated prior to the introduction of monomer – i.e., pre-irradiation grafting. In both cases, radicals generated in the base polymer react with the monomer leading to the growth of polymer chains affixed to the irradiated film. The grafting and sulfonation processes introduce ionic conductivity while maintaining the desirable mechanical integrity associated with the base polymer.

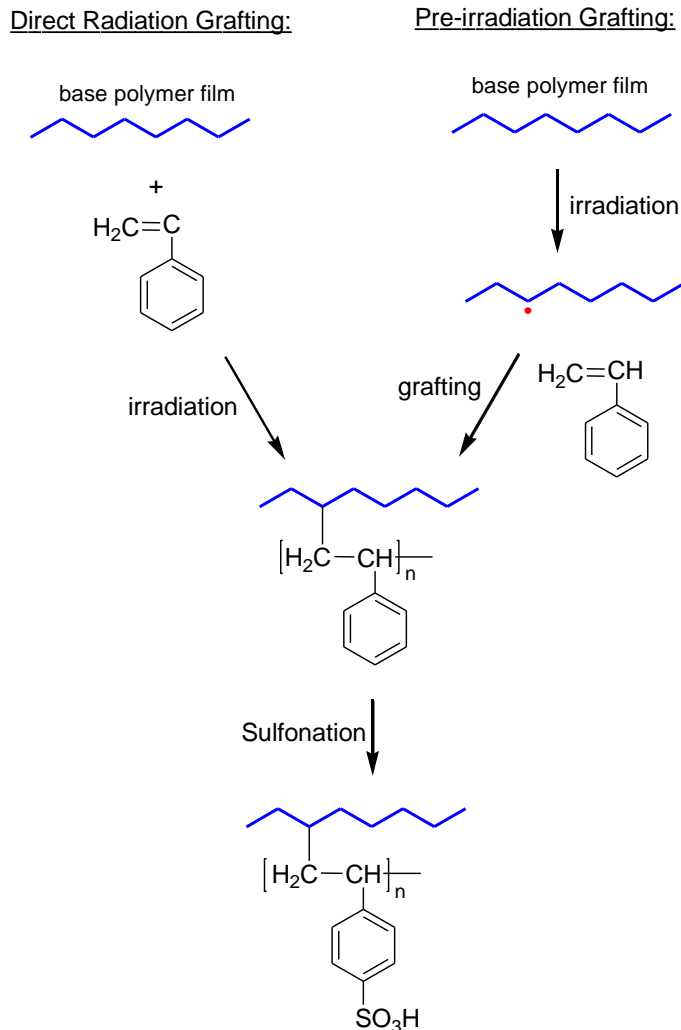


Figure 1.6 Schematic preparation of radiation-grafted membranes.

This radiation-grafting technique offers several advantages such as the use of prefabricated commercial films, which mitigates the cost and difficulties associated with film formation processes. Furthermore, material properties can be readily modified by selecting the base polymer on the basis of its mechanical properties and the monomers on the basis of their proton conducting ability. The durability and mechanical strength of these membranes can also be significantly improved by the introduction of cross-linkers, such as divinylbenzene (DVB) and

triallyl cyanurate, during the graft copolymerization of styrene.⁴⁸ However, it is postulated that membranes generated using radiation grafting may not be homogeneous since most of the radiation polymerization occurs on the surface of the base fluoropolymer film.⁴⁹ Although the proton conductivity of radiation-grafted membranes has been reported to be comparable to other perfluorinated sulfonic acid membranes (i.e., Nafion),⁵⁰ the lack of chemical structural control remains a significant drawback.

1.4.3 Non-fluorinated Hydrocarbons

Hydrocarbon-based membranes have been extensively investigated and explored over the last two decades as alternative membrane materials. They offer several important advantages over perfluorosulfonic acid membranes: they are less expensive, the base polymers are usually commercially available, and their structure often permits the introduction of polar sites as pendant groups, which enhances their water retention property allowing high temperature operations (>120 °C).⁵ Increasing the operating temperature of fuel cells is desirable because of improved tolerance of the anode catalyst to carbon monoxide poisoning, which enables the use of hydrogen produced by reforming natural gas, methanol or gasoline. Higher operating temperature also offers improved electrode kinetics, increased proton conductivity, simplification of the cooling system, and the possible use of co-generated heat.

Polystyrene-based membranes represent an important family of hydrocarbon membranes. As discussed in Section 1.3, the first generation of proton exchange membranes were based on sulfonated polystyrene where

divinylbenzene was used as a cross-linker for extra mechanical stability, Figure 1.2a. These membranes were inexpensive and easy to manufacture; however, they suffer from poor chemical stability and short lifetime due to the weaker C-H bond compared to the C-F bond, as well as the vulnerability of the benzylic α -hydrogen atoms to radical abstraction.⁵¹ Oxygen crossover to the anode side of the membrane and subsequent reaction with hydrogen can lead to the formation of peroxy ($\text{HOO}\cdot$) and hydroxyl ($\text{HO}\cdot$) radicals. Another source of these radicals is the formation of H_2O_2 due to incomplete reduction of oxygen at the cathode; the H_2O_2 subsequently reacts with trace metal ions (i.e., Fe^{2+} , Cu^{2+}) in the membrane to generate $\text{HOO}\cdot$ and $\text{HO}\cdot$ radicals.⁵² For sulfonated polystyrene-based PEMs, these highly reactive radicals are believed to deteriorate the membrane by attacking the benzylic α -hydrogen atoms, which can lead to chain scission (“reverse polymerization”, Figure 1.7a).⁵³ Radical addition to the aromatic rings, preferentially in the ortho position, can also generate benzylic radicals for subsequent oxidative degradation of polymer chains (Figure 1.7b).⁵⁴

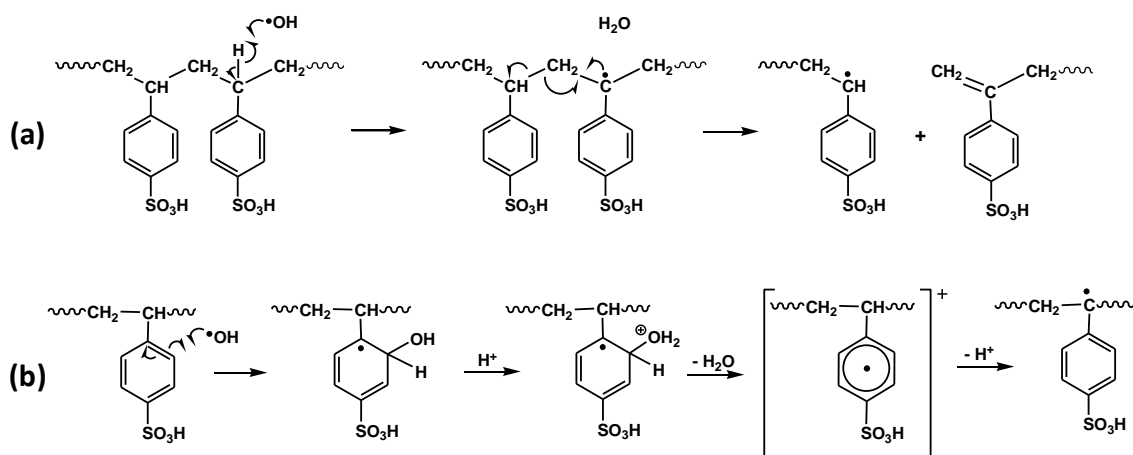
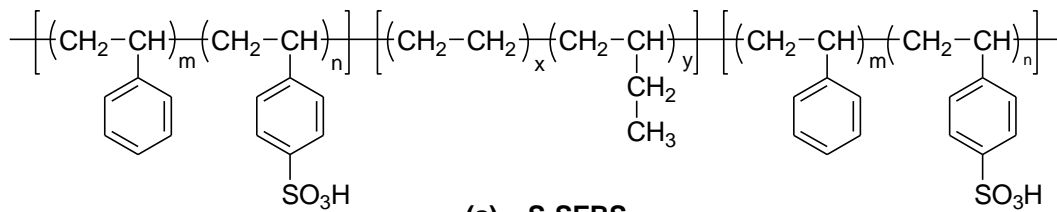
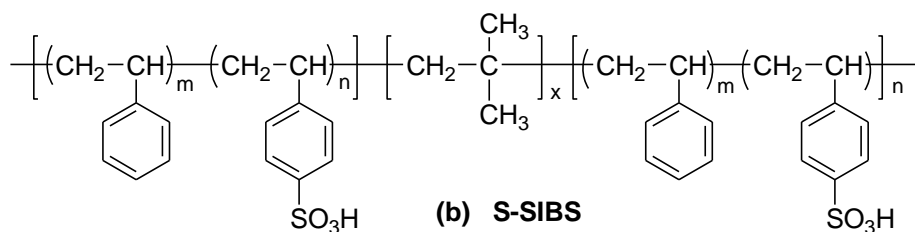


Figure 1.7 Degradation mechanisms of sulfonated polystyrene-based membranes by (a) benzylic hydrogen atom abstraction and (b) radical addition.

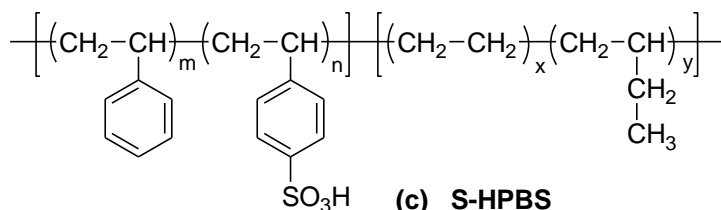
Although durability is a significant issue in polystyrene-based membranes, they are still extensively studied since the styrene monomers are widely available and easy to modify, and their polymers are readily synthesized via conventional free radical and other polymerization techniques, often with controlled macromolecular architectures. Well-defined polystyrene-containing block ionomers may be obtained via living polymerization routes, i.e., anionic, atom transfer radical polymerization (ATRP), and TEMPO-assisted stable free radical polymerization (SFRP), followed by post-sulfonation. Alternatively, they can be obtained by the incorporation of macromonomers of sulfonated polystyrene into growing polymer chains. Representative membranes based on sulfonated polystyrene-containing block ionomers are illustrated in Figure 1.8. These include partially sulfonated poly(styrene-*b*-[ethylene-*co*-butylene]-*b*-styrene) (S-SEBS),⁵⁵⁻⁶⁹ partially sulfonated poly(styrene-*b*-isobutylene-*b*-styrene) (S-SIBS),^{63, 64, 70-74} partially sulfonated hydrogenated poly(butadiene-*b*-styrene) (S-HPBS),^{75, 76} partially sulfonated poly(styrene-*b*-ethylene-*alt*-propylene) (S-SEP),^{77, 78} and partially sulfonated poly(styrene-*b*-ethylene/propylene-*b*-styrene) (S-SEPS).⁷⁷ These block ionomers are intensively studied for deducing structure-property relationships in PEMs since they often yield membranes with controlled microstructure and morphology.



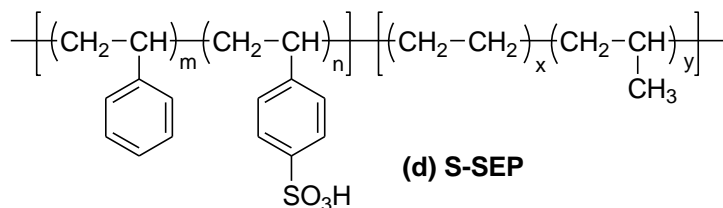
(a) S-SEBS



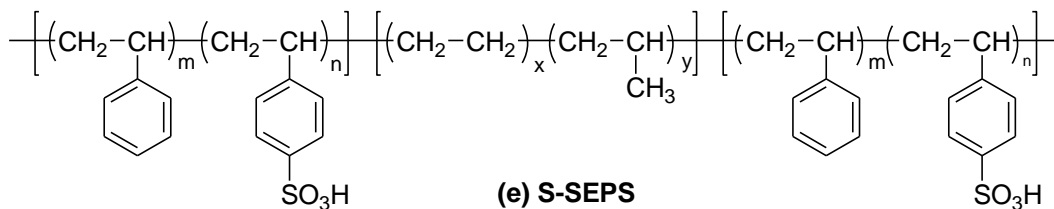
(b) S-SIBS



(c) S-HPBS



(d) S-SEP



(e) S-SEPS

Figure 1.8 Chemical structures of representative sulfonated polystyrene-based block ionomer membranes: (a) partially sulfonated poly(styrene-*b*[ethylene-co-butylene]-*b*-styrene) (S-SEBS), (b) partially sulfonated poly(styrene-*b*-isobutylene-*b*-styrene) (S-SIBS), (c) partially sulfonated hydrogenated poly(butadiene-*b*-styrene) (S-HPBS), (d) partially sulfonated poly(styrene-*b*-ethylene-*alt*-propylene) (S-SEP) and (e) partially sulfonated poly(styrene-*b*-[ethylene-*alt*-propylene]-*b*-styrene) (S-SEPS).

Sulfonated polyaromatic membranes are currently considered as one of the more promising routes to high performance PEMs due to their attractive thermal and chemical stability, processability, low cost and commercial availability of the base aromatic polymers. As illustrated in Figure 1.9, sulfonated poly(*p*-phenylene)s (S-PPO, S-PPS), sulfonated poly(ether ether ketone)s (S-PEEK), sulfonated polysulfones (S-PSF), sulfonated polyimides (S-PI), and sulfonated polybenzimidazoles (S-PBI), are the focus of many investigations.^{5, 79} High thermal and oxidative stability in polyaromatic materials are believed to be due to the fact that the C-H bonds of the aromatic moieties have higher bond energies than aliphatic C-H bonds.⁵ The inflexible and bulky aromatic backbone often leads to high temperature rigid polymers with glass transition temperatures (T_g) typically > 200 °C, rendering them suitable for high temperature applications. Furthermore, the aromatic rings offer the possibility of electrophilic as well as nucleophilic substitution, thus providing great versatility for tuning of material properties to those desirable for fuel cell application.

Aromatic polymers are commonly synthesized by step-growth/condensation polymerization of bifunctionalized monomers (i.e., dialcohols, diamines, dihalogens, and dicarboxylic acids). Introduction of active proton exchange sites to these materials can be accomplished by post-sulfonation using concentrated sulfuric acid, fuming sulfuric acid, chlorosulfonic acid or sulfur trioxide. Post-sulfonation reactions are usually restricted due to their lack of precise control over the degree and location of functionalization, the possibility of side reactions, and degradation of the polymer backbone.^{80, 81} Thus,

recent efforts in the synthesis of sulfonated aromatic polymers have focused on the direct copolymerization of sulfonated monomers⁸²⁻⁹² or coupling reactions of sulfonated compounds with functional groups attached to a polymer backbone.⁹³

Although a number of sulfonated polyaromatic membranes have recently found applications in PEM fuel cells, their poor mechanical strength, resulting from high water swelling when high IEC membranes are prepared for high proton conductivity, remains an important issue that requires further attention.

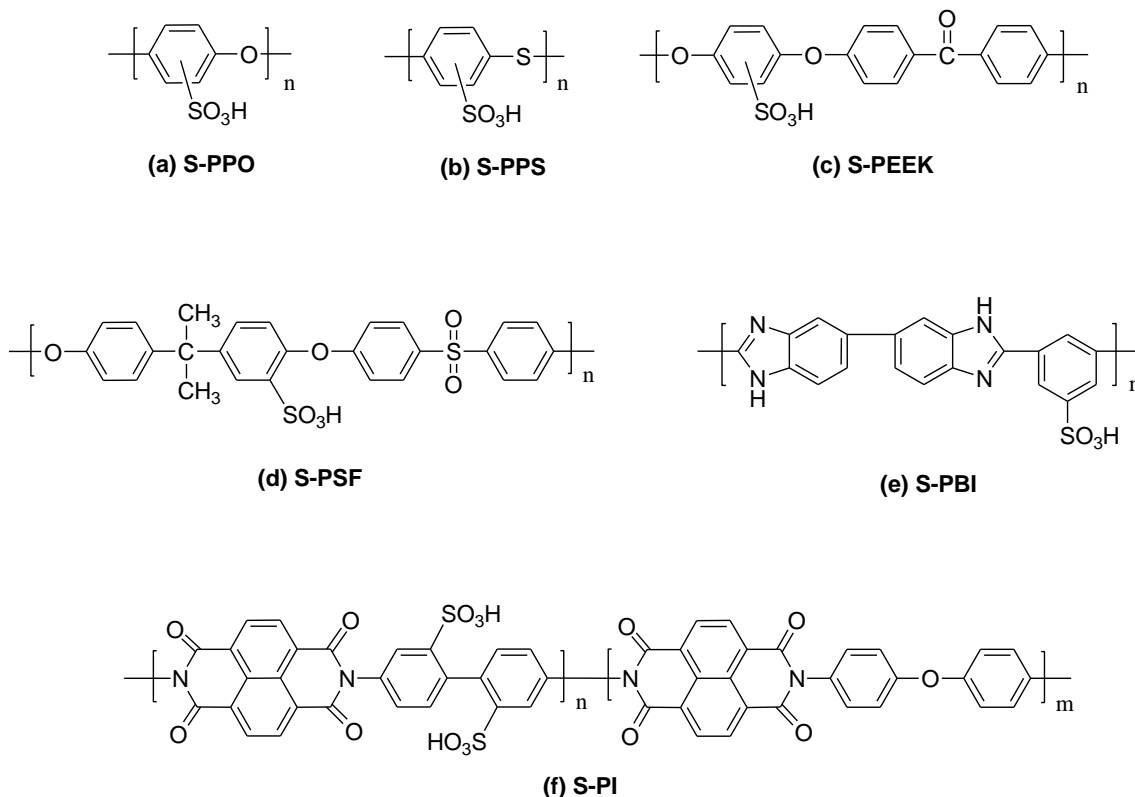


Figure 1.9 Chemical structures of (a) sulfonated poly(*p*-phenylene oxide) (S-PPO), (b) sulfonated poly(*p*-phenylene sulfide) (S-PPS), (c) sulfonated poly(ether ether ketone) (S-PEEK), (d) sulfonated polysulfone (S-PSF), (e) sulfonated polybenzimidazole (S-PBI) and (f) sulfonated polyimide (S-PI).

1.4.4 Polymer blends and composite membranes

Polymer blending provides a convenient method to combine the desirable properties from two or more distinct polymer systems. Nafion have been blended with non-ionic polymers, such as polyvinylidene fluoride (PVDF) and polyphenylene oxide, to yield membranes with improved mechanical properties and lower methanol permeability; however, these blend membranes often show significantly lower proton conductivity presumably due to the increase in hydrophobicity and thereby lower water uptake.^{94, 95} To improve component compatibility and interfacial adhesion, blend membranes containing different sulfonated polymers have also been investigated. Blend membranes comprised of sulfonated polystyrene and sulfonated poly(phenylene oxides) are reported to show higher proton conductivity than either of the separate components.⁹⁶ Blending of Nafion with sulfonated poly(aryl ether sulfone) provides membranes with reduced methanol permeability compared to pure Nafion membranes.⁹⁷

Blends of acidic polymers and basic polymers have also been investigated. As illustrated in Figure 1.10, proton donation from acidic to basic sites leads to ionic cross-linking, and thereby improving mechanical and thermal stabilities.⁹⁸ Examples of acid-base blend membranes include sulfonated poly(ether ether ketone) (S-PEEK), sulfonated polysulfone (S-PSF) or sulfonated polyimides (S-PI) as the acidic component while poly(benzimidazole) (PBI), poly(4-vinylpyridine) (P4VP) or aminated polyimides as the basic component.⁹⁹⁻

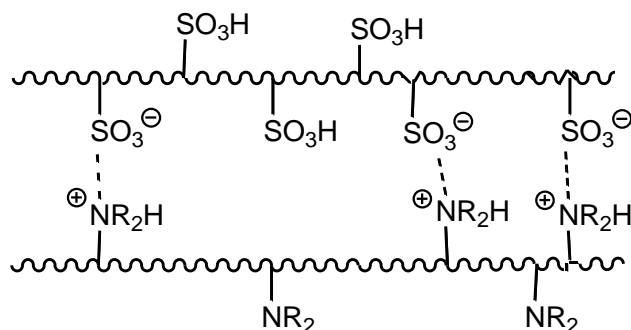


Figure 1.10 Schematic representation of ionic cross-linking in acid-base blend membranes.

Composite membranes, typically formed by incorporating hydrophilic inorganic species into an existing membrane, have been studied in an effort to provide PEMs that operate at high temperature and low humidity conditions.¹⁰² Composite membranes of Nafion or other sulfonated polymers (i.e., S-PEEK) with inorganic particles (i.e., SiO_2 , TiO_2 , ZrO_2 , Al_2O_3), inorganic acids (i.e., calcium phosphate, zirconium phosphate, heteropolyacids), and heterocyclic compounds (i.e., imidazoles) have been investigated and showed some promising results.^{103, 104} Introduction of inorganic particles into PEMs has been achieved by: mixing the particles with an ionomer solution prior to casting, impregnation of the particles inside a preformed membrane through sol-gel techniques, and growing inorganic nanoparticles within the membrane.¹⁰⁵

1.5 Proton Conduction in PEMs

One of the key requirements of a PEM is adequate proton transport from anode to cathode. High proton conductivity is essential for achieving high fuel cell current densities, as Ohmic losses are minimized. Proton conductivity is directly

related to the constituent polymer's chemical structure (i.e., its composition, microstructure, sequence distribution, nature of the acid group, and ion content), as well as the resulting membrane's nanostructure and morphology.^{106, 107} Proton conductivity is also influenced by the water content of the membrane and external factors such as temperature and humidity. Rationalizing proton conductivity in the context of these properties is crucial for obtaining insights into proton transport in PEMs and for the design of next generation membranes.

In Nafion[®] and the majority of PEMs, interconnected nanometer-sized ionic channels are believed to form due to phase separation between the incompatible hydrophobic polymer backbone and hydrophilic sulfonic acid groups. Proton conduction generally occurs within the continuity of these hydrated ionic domains – protons dissociate from their conjugate base, are solvated, and mobilized by water. The mechanisms for the transport of protons within the water-containing ionic channels of PEMs can be similar to those found in bulk water (Figure 1.11).¹⁰⁷⁻¹⁰⁹ Protons in bulk water do not exist as bare ions, but instead, are strongly associated with surrounding water molecules to form dynamic aggregates such as the hydronium ion (H_3O^+), the Zundel ion (H_5O_2^+), and the Eigen ion (H_9O_4^+). Proton transport can take place by a molecular diffusion process in which a hydrated proton aggregate moves through the aqueous channel as a single entity – the *vehicular* mechanism. Alternatively, protons can move via a structural diffusion process in which protons are transferred across a chain of hydrogen bonds followed by reorientation of the water dipoles. This structural diffusion is commonly referred to as the *Grotthuss*

mechanism.¹⁰⁸ The processes have been demonstrated by molecular dynamics simulation,^{110, 111} and supported by NMR analysis,¹¹² to involve a periodic series of isomerization between the Zundel and Eigen ions (Figure 1.12). The Grotthuss mechanism relies on the formation and breaking of hydrogen bonds;¹⁰⁸ thus, any factor that leads to an increase in the average hydrogen bond energy or a disruption in the network of hydrogen bonding will be detrimental to this process. In addition to the vehicular and Grotthuss mechanism, proton transport can also occur via a surface mechanism, wherein protons “hop” between the sulfonic acid groups that line the pore wall, mediated by intermediate water molecules (Figure 1.11).¹¹³

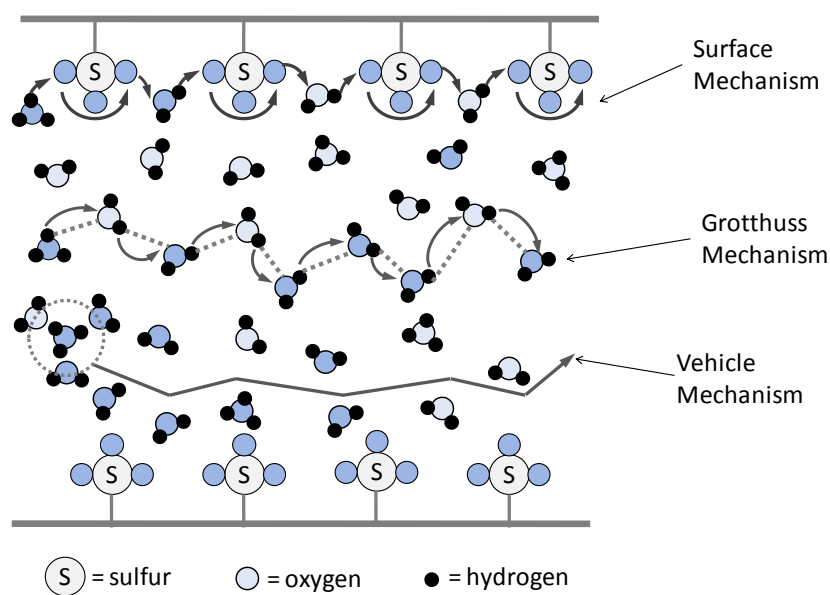


Figure 1.11 Simplified schematic representation of proton transport in hydrated PEMs. A comparison of the surface mechanism, Grotthuss mechanism, and vehicle mechanism.

[Adapted with permission from *Journal of Polymer Science Part B-Polymer Physics*. Choi, P.; Jalani, N. H.; Thampan, T. M.; Datta, R. *44*, 2183, © 2006, John Wiley & Sons, Inc.]

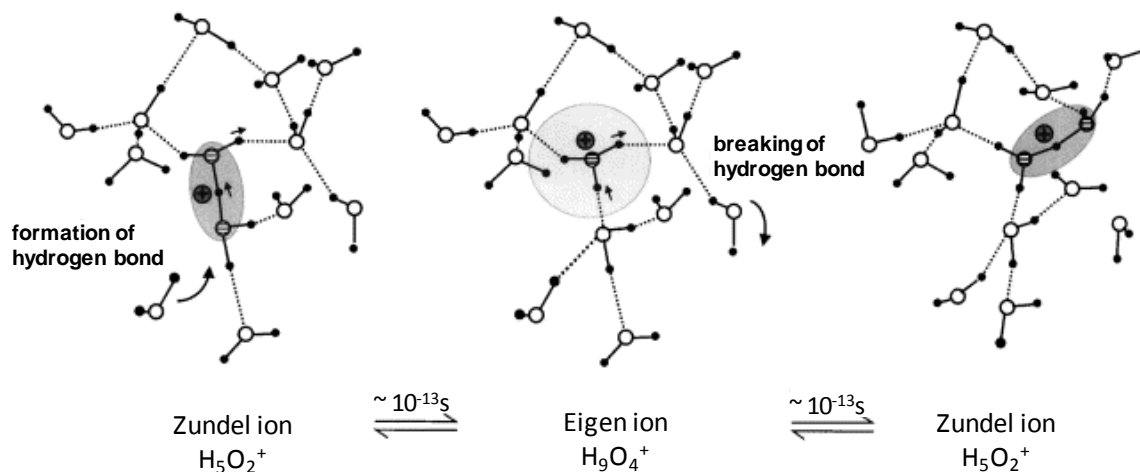


Figure 1.12 Schematic of proton transport by the Grotthuss mechanism.

[Reprinted with permission from *Solid State Ionics*. Kreuer, K.D. 136-137, 149, © 2000, Elsevier.]

All three of the above transport mechanisms (i.e., vehicular, Grotthuss, and surface mechanism) can contribute to proton conduction in PEMs; however, it has been suggested that one transport mechanism might dominate over another depending on the water content of the membrane. By comparing the diffusion coefficients of H_2O and H^+ , Zawodzinski and co-workers¹¹⁴ suggested that at high water contents, both the vehicular and Grotthuss mechanisms participate in proton transport, but the Grotthuss mechanism is dominant. They have proposed that as water content decreases, the contribution of the vehicle mechanism increases while that of the Grotthuss mechanism decreases. For low water contents, the number of hydrogen bonding interactions is small, which causes the remaining hydrogen bonds to be shortened and tightened. This leads to an increased average hydrogen bond energy, which results in a reduced rate of the bond breaking-forming processes necessary for structural diffusion in the Grotthuss mechanism.

Eikerling and Kornyshev¹¹³ calculated that under conditions of minimal hydration, i.e., 1 – 2 water molecules per sulfonic acid group (λ), proton transport occurs between the sulfonic acid groups along the surface of the pore wall via a proton “hopping” mechanism. It is suggested that the activation enthalpy of the surface mechanism increases considerably with increasing distance between sulfonic acid groups.¹¹³ Other factors that affect the rate of proton transport along the pore surface include the conformation of the polymer backbone, flexibility of the side chains, and degree of aggregation of sulfonic acid groups.

1.6 Morphological Studies of Nafion Membranes

Given its position as a technological standard for fuel cell research, the Nafion[®] membrane has been investigated in depth. As shown in Figure 1.2b, the chemical structure of Nafion[®] consists of a perfluorinated backbone with perfluorovinyl ether side chains terminated with sulfonic acid groups. The chemical incompatibility between the hydrophobic Teflon[®]-like main chain and the hydrophilic side chains leads to a nanophase-separated morphology. The nanostructure and morphology of Nafion membranes have been extensively studied using various scattering techniques including small-angle X-ray (SAXS) and small-angle neutron (SANS) scattering.¹¹⁵⁻¹¹⁸ A variety of structural models have been proposed to fit the calculated and observed scattering profiles of Nafion[®] membranes and to interpret the transport and mechanical properties.^{115, 119-124} Common to these models is that ionic groups aggregate in the perfluorinated polymer matrix to form a network of ionic clusters. In the presence of water, the ionic clusters swell significantly to provide nanometer-scale,

hydrated channels for proton transport whereas the hydrophobic domains impart mechanical stability and resistance against dissolution to the hydrated membranes.

Hsu and Gierke¹²⁰ established the formation of ionic clustering in Nafion[®] membranes. As illustrated in Figure 1.13, a “cluster network model” was proposed to describe the formation of inverted micelles consisting of spherical ionic clusters (4 – 5 nm in diameter) of sulfonic acid groups. These ionic clusters are interconnected by narrow ionic channels (1 nm in width) to form a cluster network embedded in a fluorocarbon matrix. Each ionic cluster was estimated to contain approximately 70 sulfonic acid groups when fully hydrated.

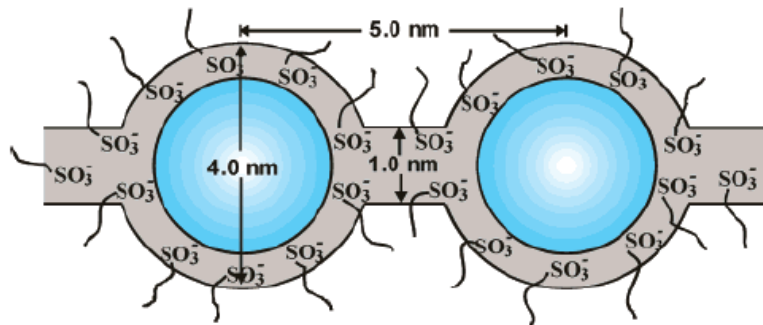


Figure 1.13 Cluster network model for the morphology of hydrated Nafion[®] membrane.

[Reprinted with permission from *Journal of Membrane Science*. Hsu, W. Y.; Gierke, T. D. 13, 307, © 1983, Elsevier.]

Later, Gebel *et al.*¹¹⁵ proposed a conceptual description for structural evolution and morphological reorganization of Nafion[®] as a function of water content (Figure 1.14). Dry Nafion[®] membranes possess isolated spherical ionic clusters with diameters of 15 Å and an inter-cluster spacing of 27 Å. The lack of connectivity between the ionic domains leads to low levels of proton conductivity in dry Nafion[®] membranes. With absorption of water, the ionic clusters begin to

swell to 20 Å in diameter, with sulfonic acid groups located at the polymer-water interface. With a relatively large inter-cluster distance of ~30 Å, the hydrated ionic clusters are still isolated and hence, conductivity remains low. As water content increases further, the ionic clusters swell to diameters of 40 Å while the inter-cluster distance increases only marginally. At a water volume fraction (X_v) > 0.2, a significant increase in ionic conductivity is observed indicating a percolation threshold is reached. The percolation threshold represents the critical transition at which interconnected water channels are formed between previously isolated ionic clusters leading to a sharp increase in the proton conductivity. Between $X_v = 0.3$ and 0.5, the ionic domains continue to swell from 40 Å to 50 Å, and the proton conductivity increases steadily with water content. At $X_v > 0.5$, morphological inversion occurs and the structure consists of a connected network of polymer rods surrounded by water. At very high water content ($X_v > 0.75$), membrane dissolution occurs and the structure is characterized by a colloidal dispersion of rod-like polymer aggregates.

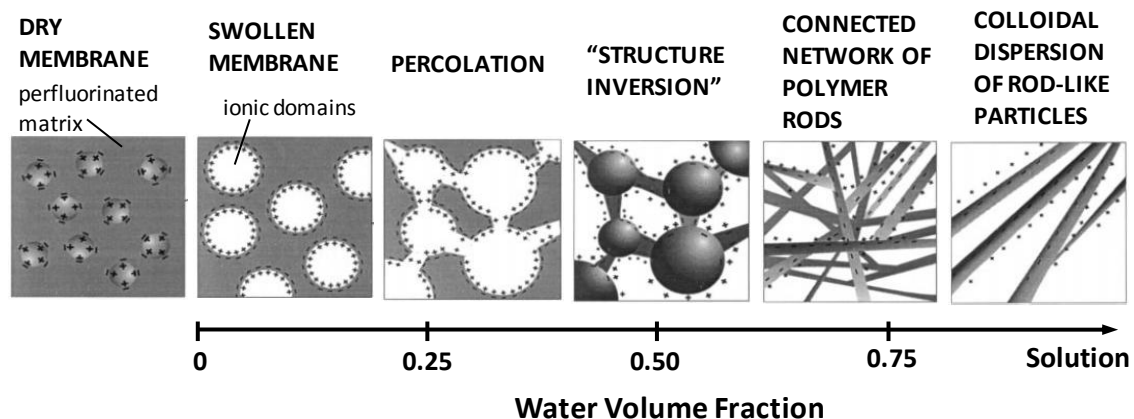


Figure 1.14 Schematic representation of the structural evolution of Nafion® as a function of water content.

[Reprinted with permission from *Polymer*. Gebel, G. 41, 5829, © 2000, Elsevier.]

More recently, Schmidt-Rohr and Chen¹²⁵ have proposed a “parallel water-channel model” which quantitatively simulated the experimental small-angle scattering profiles of hydrated Nafion[®] membranes. As illustrated in Figure 1.15a, this model features parallel water channels lined with ionic side groups, forming inverted-micelle cylinders (~2.4 nm in diameter). These densely packed water channels are stabilized by a shell of relatively stiff hydrophobic polymer backbones, and are expected to have a persistence length of tens of nanometres (Figure 1.15a, b). Elongated and nearly-cylindrical Nafion crystallites (~5 nm in cross-sections, shown in black in Figure 1.15c) are parallel to the water channels, and form physical cross-links to account for the mechanical properties of Nafion[®]. With increasing water content, the water-channels swell accordingly while their number remains constant (Figure 1.15d). With a relatively large channel diameter (~2.4 nm at 20 vol% water), this model is able to account for the low temperature proton conductivity and high water and methanol permeability of Nafion.¹²⁵

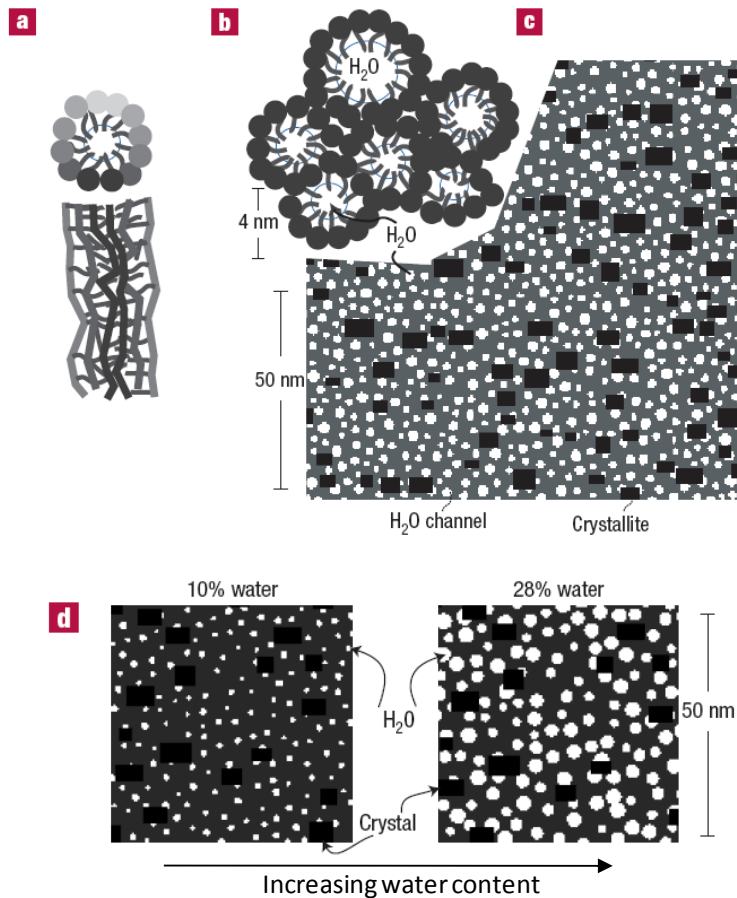


Figure 1.15 Parallel water-channel model of Nafion[®]: a) Cross-sectional and side views of a water channel (inverted-micelle cylinder), with hydrophobic polymer backbone on the outside and ionic side chains lining the water channel. b) Near-hexagonal packing of several water channels. c) Cross-sections through the cylindrical water channels (white) and the Nafion crystallites (black) in the non-crystalline Nafion matrix. d) Effect of hydration on water channel size.

[Reprinted with permission from *Nature Materials*. Schmidt-Rohr, K.; Chen, Q. 7, 75, © 2008, Nature Publishing Group.]

The morphologies of Nafion[®] have also been observed and studied using imaging techniques such as transmission electron microscopy (TEM) and atomic force microscopy (AFM). These techniques provide direct visualization of phase separation and geometric details of ionic clusters in the membrane. TEM analyses are typically performed on ultrathin sections of membranes prepared either by ultra-microtome¹²⁶⁻¹²⁸ or by casting a thin film from solution.^{127, 129-131} To

enhance scattering contrast, the membranes are often stained with reagents such as RuO_4 ,¹²⁹ Cs^+ ,^{127, 128} and Pb^{2+} ¹²⁶ prior to imaging. Generally, TEM images of dehydrated Nafion[®] membranes show the presence of nearly spherical ionic clusters, typically 3 – 10 nm in diameter.^{129, 130, 132} A TEM image¹²⁸ of Nafion[®] showing a typical ion cluster morphology is revealed in Figure 1.16. The ion clusters, represented as the darker regions, are uniformly distributed and found to be a few nanometers in size.

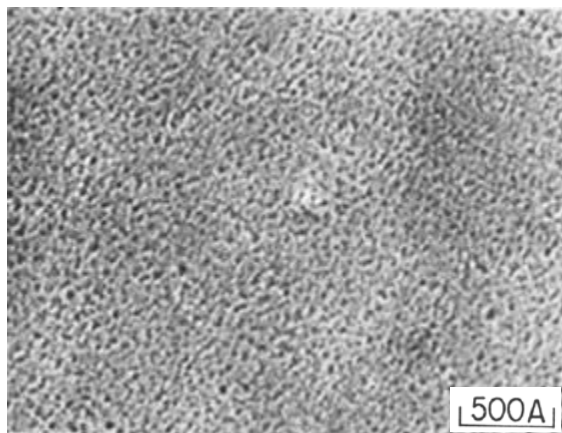


Figure 1.16 TEM image of an ultrathin section (~60 nm) of Nafion membrane (IEC = 0.91 mmol/g), stained with Cs^+ .

[Reproduced with permission from *Macromolecules*, Fujimura, M.; Hashimoto, T.; Kawai, H. 15, 136, © 1982, American Chemical Society.]

Given that TEMs are necessarily obtained on dehydrated membranes due to the high vacuum requirement, AFM has also been employed for structural studies since this technique offers the advantage of studying membrane samples at different humidity. McLean *et al.*¹³³ used tapping mode AFM to characterize the morphological positions of both ionic domains and fluorine-rich crystal aggregates in Nafion membranes. The low-energy AFM images of Nafion[®] 117 (K^+ form) exposed to various hydrating conditions are shown in Figure 1.17. The

white regions in the images represent ionic domains. For membranes exposed to ambient humidity only (Figure 1.17a), the ionic clusters (4 – 10 nm in diameter) exhibit a uniform distribution. For samples exposed to liquid water (Figure 1.17b), the ionic regions appear to coalesce into channels with dimensions ranging from 15 – 30 nm. The authors speculated that when the ionic clusters swell with water, a channel-like morphology results from the constraints placed upon the ionic domains by the crystalline regions.¹³³ It is worth noting that AFM techniques are limited to surface studies; a morphology observed at the polymer/air interface may not necessarily resemble that in the interior of the membrane.

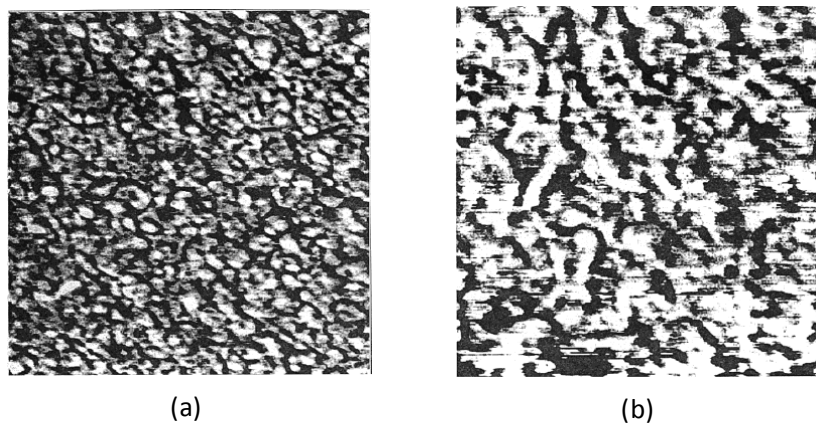


Figure 1.17 Tapping-mode AFM images of Nafion 117 (K⁺-form) ionomer membrane after exposure to: a) room temperature humidity and b) liquid water. Scan boxes are 300 x 300 nm.

[Reprinted with permission from *Macromolecules*, McLean, R. S.; Doyle, M.; Sauer, B. B. 33, 6541, © 2000, American Chemical Society.]

The processing conditions (i.e., solution casting, molding, extrusion) and thermal history can also have a profound influence on the resulting membrane morphology. A morphology observed at low temperature may significantly

change upon annealing, and different morphologies for the same material may be observed in response to shear forces,^{134, 135} stretching,¹³⁶ solvents,^{137, 138} rate of solvent evaporation,¹³⁹ and film thickness.¹⁴⁰

Although a true morphological model of Nafion is still under debate, it is generally agreed that the excellent proton conductivity and mechanical integrity in Nafion are directly related to its ability to undergo nanophase separation. The importance of nanostructure and morphology on the properties of PEMs is clearly demonstrated by the observation that Nafion when dissolved and recast exhibits an ionic conductivity much lower than “as-received” membranes.¹⁴¹ Furthermore, conductivity anisotropy in Nafion has been reported to be dependent on the method of membrane preparation (i.e., melt extrusion vs. solution casting).¹⁴²⁻¹⁴⁴ Anisotropic conductivity is typically observed in extruded membranes due to the orientation of the ionic clusters along the direction of membrane extrusion. In contrast, relatively isotropic conductivity is observed in solution-cast Nafion in which an isotropic morphology with no particular orientation of ionic clusters is expected.¹⁴⁴

1.7 Importance of Structure-Property Relationships

As overviewed in Section 1.4, over the past decade, a wide array of polymer systems have been developed and explored in the search for an advanced alternative material to Nafion[®]. Several review articles have reported various aspects of membrane development for PEM fuel cells.^{3, 5, 11, 14, 79, 107, 108, 145-155} Although significant progresses have been made in this area and a few novel membranes have shown promises in fuel cells for specific applications,

there is not yet a suitable candidate material that can sufficiently meet all of the material requirements for a successful technology commercialization.

During the early period of PEM research, new membranes have been generally developed using a random “hit or miss” approach: a new polymer backbone system is targeted for the incorporation of acid groups, after which the effects of polymer backbone and acid content on fuel cell relevant properties are investigated. Such random approach to membrane development has been proven to be inefficient and unsuccessful, and is thus becoming unpopular. More recently, however, a more systematic approach has been undertaken, which involves the study of fundamental structure-property relationships, with the intentions of obtaining insights for rational membrane design.

From the preceding discussions, it is clear that the nanostructure and morphology of membranes are important factors in determining their proton conducting ability. The formation of hydrophilic ionic domains, due to phase separation between incompatible components within the membrane, provides ionic pathways for proton transport. However, it is still unclear as to how polymer microstructure (i.e., chain architecture, acid content, chemical composition) influences the aggregation and interaction of ionic groups, and thereby influences membrane morphology and proton conductivity. In order to design new membranes with improved levels of proton conduction, it is crucial to obtain a better understanding of the fundamental relationships between polymer microstructure, morphology and physicochemical properties. Therefore, there exists a need to develop and investigate model polymer systems, with controlled

polymer microstructure leading to controlled morphology, for the elucidation of structure-property relationships and preferred structures in membrane design.

1.7.1 Copolymer Microstructure

In PEM research, the elucidation of architectural preference is currently a subject of much research interests. The preference for having random, diblock, triblock, multiblock or graft ionic copolymers for proton conducting media is not fully clear and requires further study.

A polymer's microstructure includes aspects of chemical composition, polymer architecture, and chain conformation. Proton exchange membranes are often fabricated from copolymers of an acid-bearing and a hydrophobic monomer. Depending on the arrangement of the different repeating units in the polymer chain, a wide range of architectural structures are possible, as illustrated in Figure 1.18.

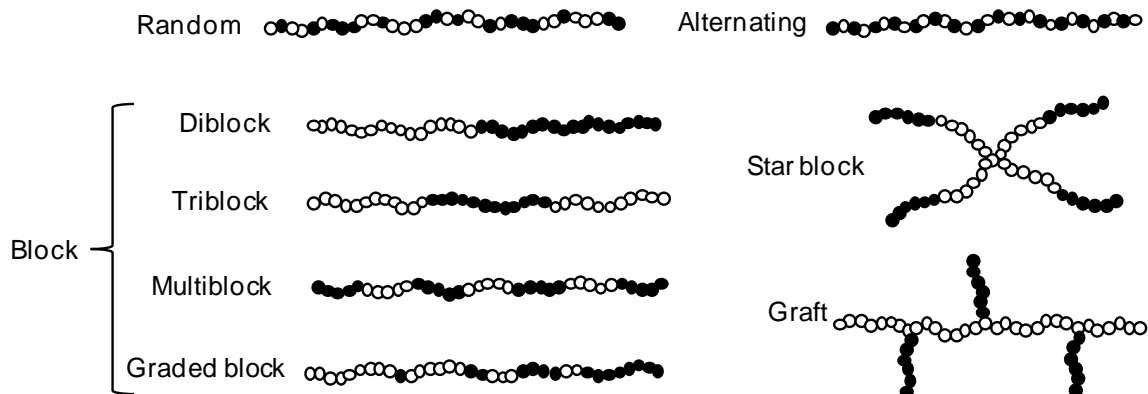


Figure 1.18 Microstructures of copolymers.

Random copolymers have monomers distributed randomly. However, most of the random copolymers reported are not truly random, but rather 'statistical' for which the monomer sequential distribution depends on the reactivity of specific monomers and the method of synthesis.¹⁵⁶ Alternating copolymers are characterized by sequences of alternating monomer units. Block copolymers are linear polymers possessing one or more uninterrupted segments of each monomer unit. These can be further sub-categorized into di-blocks, triblocks, multiblocks, graded blocks and star blocks, etc. Graft copolymers are a special class of block copolymer in which graft chains of a different type of monomer are attached to the main chain.

A single-phase morphology is often displayed in random and alternating copolymers because the sequences of each monomer unit are generally too short to induce phase separation.¹⁵⁷ In contrast, block and graft copolymers are able to self-assemble into a variety of two-phase morphologies, often with scalable periodicities. Microphase separation in block/graft copolymers is driven by the enthalpy of de-mixing of the constituent components, whereas macrophase separation is prohibited by chemical connectivity of the components. The degree of microphase separation is primarily controlled by three segmental features: composition dissimilarity, molecular weight, and crystallizability. Two-phase morphologies are often observed when the segments are chemically incompatible and/or of high molecular weight. Crystallizability in one or both segment(s) often results in microphase separation even when the segments possess similar chemical composition and low molecular weights.

1.7.2 Structure-Property Relationships in PEMs

Recently, intensive research effort has been devoted to the investigation of structure-property relationships in PEMs.^{158, 159} These studies are often performed using model polymers with controlled chemical compositions and chain architectures, leading to membranes with tailored morphologies. Thus, a study of model polymer systems may allow researchers to elucidate the morphological effects on the physicochemical properties of membranes. A few of the more recent studies are briefly highlighted here.

Ding *et al.*¹⁶⁰⁻¹⁶² reported a novel class of well-defined graft copolymers comprised of styrenic main chain and styrenesulfonic acid graft chains (PS-*g*-PSSA) (Figure 1.19 top). Comparison between the more structurally ordered PS-*g*-PSSA and random copolymers of styrene and styrenesulfonic acid (PS-*r*-PSSA) revealed that structural order gave rise to significantly higher proton conductivity. TEM analysis revealed that PS-*g*-PSSA membranes exhibited clear signs of nanophase separation and a continuous network of ionic channels, whereas PS-*r*-PSSA was lacking in phase separation (Figure 1.19 bottom). These results clearly demonstrated that proton conductivity can be greatly influenced by a polymer's microstructure and morphology, and that polymers with more controlled chemical structures in which acid groups are directed to certain segments can provide enhanced phase separation leading to higher proton conductivity.

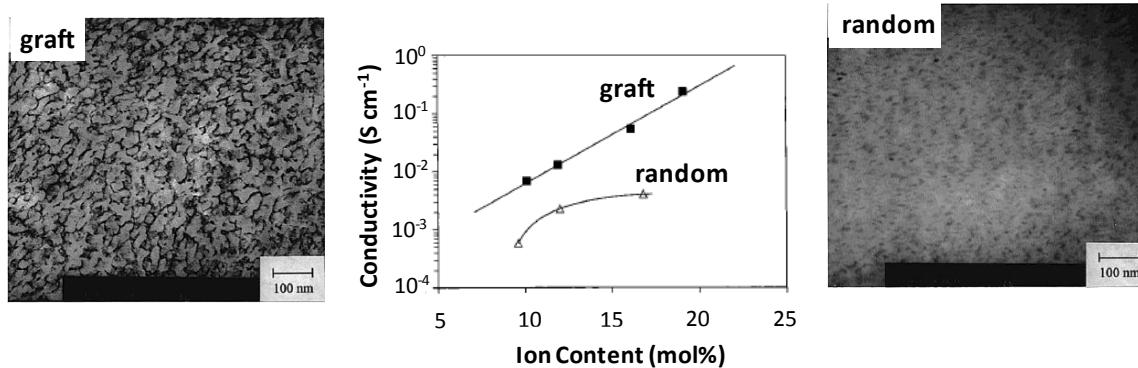
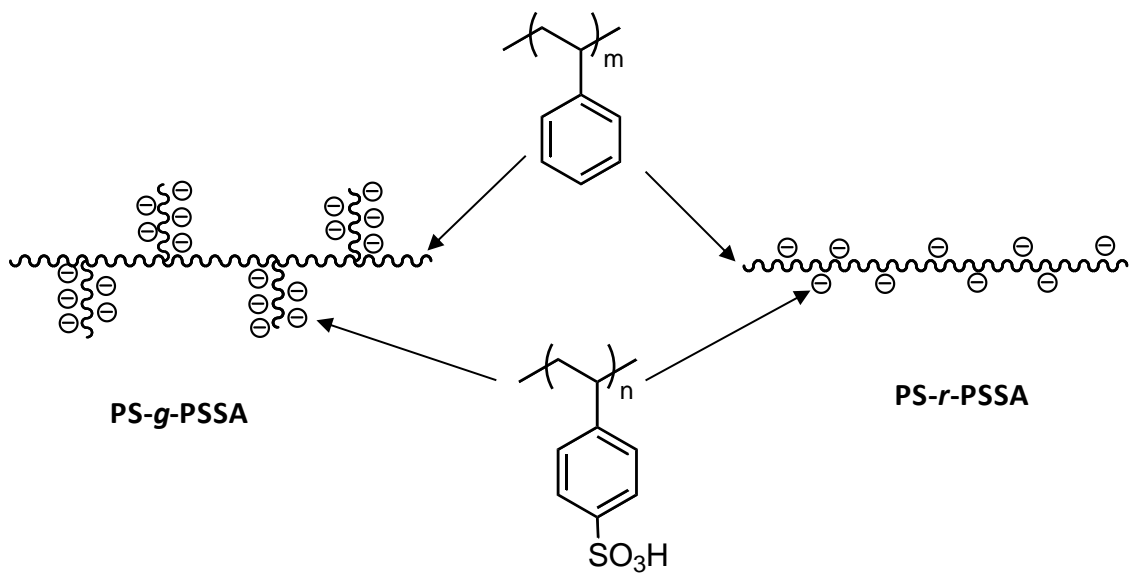


Figure 1.19 Schematic representation of chemical structures (top), TEM micrographs (bottom left and right) and proton conductivity (bottom center) of PS-g-PSSA and PS-r-PSSA copolymers.

[Reprinted with permission from *Chemistry of Materials*, Ding, J.; Chuy, C.; Holdcroft, S. 13, 2231, © 2001, American Chemical Society.]

Miyatake, Watanabe and coworkers¹⁶³ have investigated the effect of the size of hydrophobic moieties on the properties of sulfonated poly(arylene ether sulfone)s (SPAES a – d, Figure 1.21). Based on semi-empirical molecular orbital calculations, the volume dimensions of the hydrophobic components were estimated to decrease in the order: a > b > c > d. TEM analysis revealed that the size of the ionic domains increases with decreasing size of the hydrophobic components (i.e., larger ionic domains in c – d than in a – b). It was postulated that the smaller, hydrophobic components facilitate the aggregation of both hydrophobic and hydrophilic domains, leading to well-developed ionic clusters, which, in turn, provides higher proton conductivity and proton diffusion coefficients.

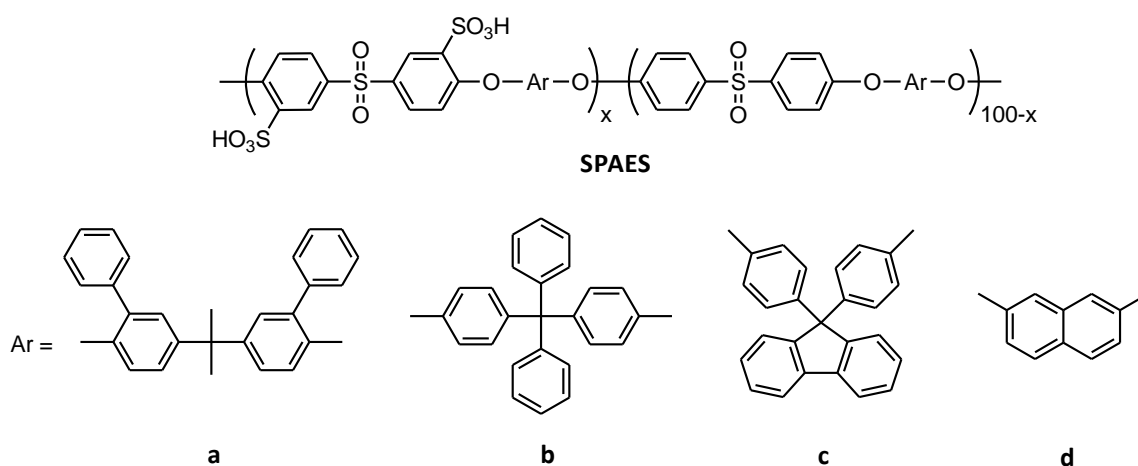


Figure 1.21 Chemical structures of sulfonated poly(arylene ether sulfone)s with various hydrophobic components.

More recently, Miyatake, Watanabe and coworkers¹⁶⁴⁻¹⁶⁶ have also prepared and studied poly(arylene ether)s containing superacidic perfluorosulfonic acid groups (FSPEs, Figure 1.22a). Compared to conventional

sulfonated poly(arylene ether)s, in which $-\text{SO}_3\text{H}$ groups are directly attached to aromatic rings (SPEs, Figure 1.21b), the superacid-bearing FSPE membranes possessed significantly higher proton conductivity. This is attributed to the much stronger acidity of the perfluorosulfonic acid group ($\text{p}K_{\text{a}} < -6$, compared to ca. -1 for ArSO_3H), which promotes proton dissociation and phase-separation between hydrophilic and hydrophobic domains. In a related work, multiblock poly(arylene ether)s containing superacid groups were reported (Figure 1.22c).¹⁶⁷ Compared to random copolymers with a similar chemical composition, the multiblock copolymers exhibited higher water uptake and proton conductivity, which is believed to be due to their unique morphology, in which well-developed phase separation with relatively large hydrophilic clusters was observed.

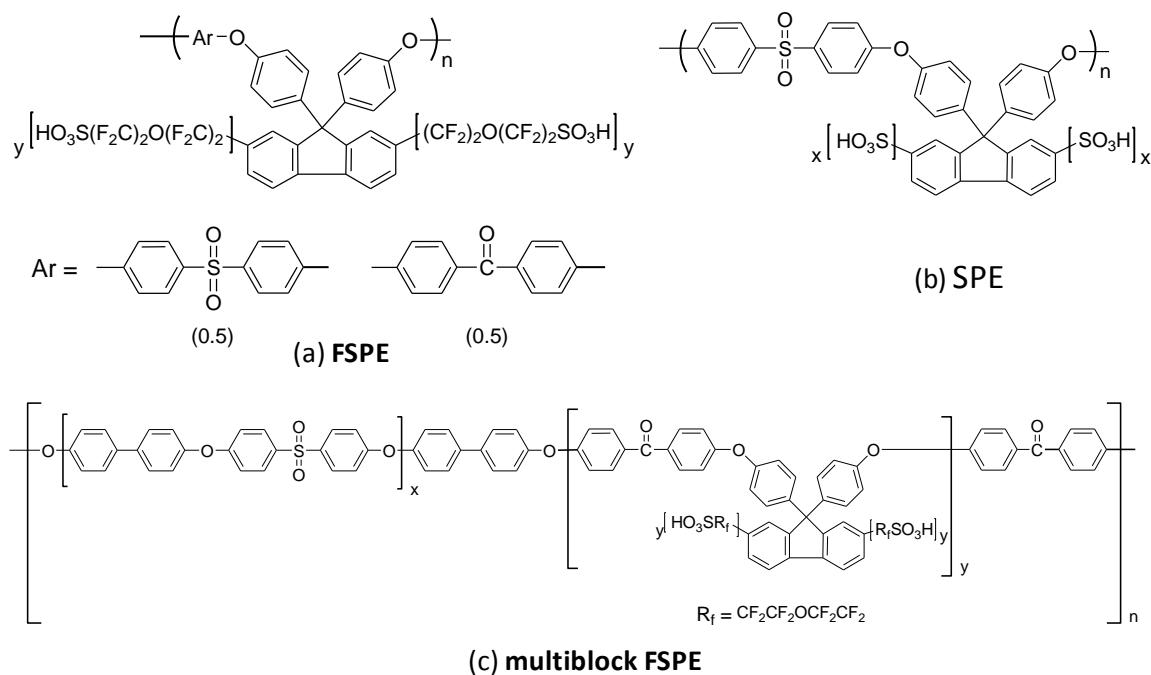


Figure 1.22 Chemical structures of a) superacid-bearing FSPE, b) conventional sulfonated SPE and c) multiblock FSPE.

Hickner *et al.*¹⁶⁸ have prepared midblock-sulfonated triblock copolymers to investigate how the location of the sulfonated block as well as the composition and properties of the unsulfonated blocks influence membrane transport properties. As shown in Figure 1.23, ABA triblock copolymers with a hydrophilic center block comprising of sulfonated polystyrene (SPS) and hydrophobic outer blocks comprising of either a hydrocarbon (poly(hexyl methacrylate), PHMA) or a partially fluorinated (poly(perfluorooctyl methacrylate), PFMA) segment were synthesized and studied. Differential scanning calorimetry analyses indicated that phase separation occurs in both the PHMA- and PFMA- based membranes. Interestingly, the proton conductivity of the non-fluorinated PHMA-based film is greater than that of the fluorinated PFMA-based film. This has been attributed to the lower glass transition temperature (T_g) and greater solubility of the PHMA-block in the casting solvent, which led to a greater degree of morphological order in the PHMA-*b*-SPS-*b*-PHMA film.¹⁶⁸

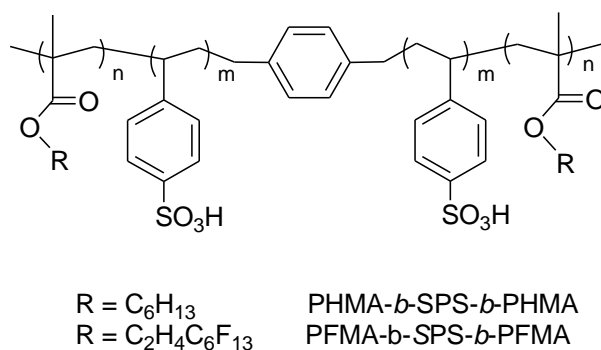


Figure 1.23 Chemical structures of midblock-sulfonated triblock copolymers of PHMA-*b*-SPS-*b*-PHMA and PFMA-*b*-SPS-*b*-PFMA.

1.8 Research Outline

Perfluorosulfonic acid membranes, in particular Nafion, are still the material of choice in proton exchange membrane fuel cell technology, offering to date an adequate combination of performance, durability, and reliability. However, as the technological requirements for a mass commercialization of PEM fuel cells become increasingly stringent, Nafion membranes, having high cost, methanol fuel cross-over and limited operating conditions, are becoming less attractive. Therefore, novel advanced membrane materials with lower cost and improved properties are actively being sought after.

It is believed that the nanostructure and morphology of membranes play a crucial role on their proton conduction. Phase-separation between incompatible components within a membrane leads to the formation of hydrophilic ionic domains, within which proton conduction occurs. However, it is not fully clear how polymer microstructure - i.e., chain architecture, chemical composition, ion content - influences the aggregation and connectivity of ionic domains and in turn, influences proton transport and water sorption. Questions concerning the preferences of diblock, multiblock, graft, or random acid-bearing polymers for proton exchange membranes remain a subject of much research interest. In this thesis research, model polymer systems, in which polymer architectures and chemical compositions are systematically controlled, are devised and studied for elucidating relationships between polymer microstructure, morphology and physicochemical properties. The goal is to broaden our understanding of these

relationships and thus, obtain useful insights into preferred structures for future membrane design.

The synthetic approaches employed to obtain the various model polymer systems used in this work are described in Chapter 2. In particular, an overview of conventional free-radical polymerization and atom transfer radical polymerization (ATRP), which allows control of polymer architectures and polydispersity, is given. Descriptions of the various instruments and techniques employed for membrane characterization are also given. These include gel permeation chromatography (GPC), water sorption measurements, acid-base titration, AC impedance spectroscopy and transmission electron microscopy (TEM).

In Chapter 3, the use of fluorosulfonated diblock copolymers, sulfonated poly([vinylidene difluoride-*co*-hexafluoropropylene]-*b*-styrene) [P(VDF-*co*-HFP)-*b*-SPS], as model polymers for studying structure-property relationships in proton exchange membranes is described. These diblock copolymers are attractive model systems due to the chemical incompatibility between the two block segments which ensures ionic aggregation and phase-separation. Based on the knowledge that morphological control in block copolymers can be achieved by varying the block ratios, several series of P(VDF-*co*-HFP)-*b*-SPS diblock membranes possessing different block ratios and thereby, different membrane morphologies, were synthesized and compared. The degree of sulfonation of the ionic polystyrene block and the percolation of the ionic channels in the membranes were found to play an important role in their proton conduction.

Chapter 4 is based on published work that reports the nanostructure, morphology and properties of fluororous-ionic graft copolymers of partially sulfonated poly([vinylidene difluoride-co-chlorotrifluoroethylene]-*g*-styrene) [P(VDF-co-CTFE)-*g*-SPS]. These fluororous-ionic graft copolymers serve as suitable model systems for deducing structure-property relationships because their composition and microstructure can be systematically varied by control of graft length, graft density and degree of sulfonation. Three series of P(VDF-co-CTFE)-*g*-SPS graft copolymers, with similar graft density but different sulfonated polystyrene (SPS) graft length, were systematically synthesized to elucidate the effects of ionic graft lengths on membrane morphology and properties. The correlations between graft length, morphology, and properties such as proton conductivity, proton mobility, acid concentration, water sorption, and crystallinity were investigated and revealed interesting trends that may be useful in the design of future membranes.

Chapter 5 is based on published work that reports a direct comparison between the two classes of copolymer systems – diblock vs. graft ionic copolymers – that are described in Chapters 3 and 4, respectively. These two copolymer systems possess similar chemical compositions, but distinct macromolecular architecture. Diblock copolymers of P(VDF-co-HFP)-*b*-SPS possessed a hydrophobic fluororous segment linearly attached to an ionic sulfonated polystyrene segment. In contrast, the graft analogue of P(VDF-co-CTFE)-*g*-SPS consisted of a hydrophobic fluororous backbone with ionic sulfonated styrene side chains. Two series of diblock and graft copolymers

containing a similar ratio of fluorinated to styrene components were directly compared for the purpose of obtaining insights into aspects of preferred polymer architecture. It was found that the morphologies and properties of the membranes are heavily dependent upon the polymer architecture.

Lastly, a summary of the key findings obtained from this thesis work as well as some research outlooks are described in Chapter 6.

Chapter 2. Polymer Synthesis and Characterization

In this thesis work, conventional free-radical polymerization as well as controlled radical polymerization, which allows the synthesis of polymers with controlled molecular weight and chain architecture, were employed to obtain the various model polymer systems. A general overview of these polymerization techniques will be given below, followed by an overview of the various polymer characterization techniques used in this work.

2.1 Free-Radical Polymerization

Compared to other polymerization methods, free-radical polymerizations are relatively facile and easy to carry out; rigorous removal of moisture is generally unnecessary, and the reaction can be carried out in the bulk, solution, or dispersed phase (i.e., emulsion and suspension). The active species in radical polymerizations often involve organic free radicals. Stabilization of radicals can be achieved by resonance, inductive, and polar effects. The high reactivity of free radical chemical interactions renders radical polymerization a versatile form of polymerization.

As shown in Figure 2.1, free-radical polymerizations proceed via four elementary steps: initiation, propagation, chain transfer, and termination.

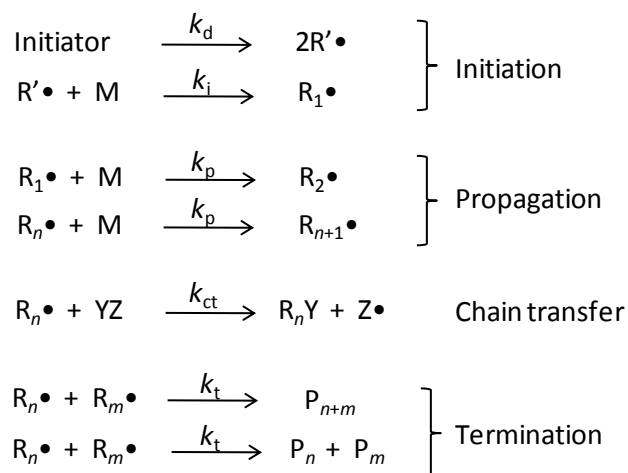


Figure 2.1 Mechanism of free-radical polymerization.

Initiation involves the formation of initiating radicals, $R'\bullet$, from an initiator; the $R'\bullet$ radical then reacts with a monomer, M , to initiate chain growth. Initiators for free-radical polymerization are typically compounds that dissociate into free radicals by thermal decomposition, photolysis or redox reaction. Common initiators include organic peroxides, azo compounds, organometallic compounds, and redox systems. Initiating radicals can also be generated from the monomer itself by heat or irradiation with light or high-energy sources (i.e., X-ray, γ -rays, and high-energy electrons).

Propagation occurs when monomers are added sequentially to the active radical chain ends, accompanied by regeneration of the radical sites after each addition. Chain transfer involves the transfer of the radical site to a chain transfer agent, YZ , which may be a solvent, monomer, initiator, or polymer. The molecule that loses the radical site is terminated while the one that accepts the radical site can initiate a new chain. Chain transfer requires higher activation energy than

propagation and becomes a competitive pathway only at higher temperatures. As illustrated in Figure 2.2, termination may occur by cross-coupling between two polymer radicals (“combination”, Figure 2.2a) or by atom transfer from one polymer radical to another (“disproportionation”, Figure 2.2b). Combination can bring a considerable increase in the molecular weight of the final polymer; while disproportionation generates two chemically different types of polymer molecules: one polymer with a saturated end-group whereas the other, unsaturated. In order to grow high molecular weight polymers, the termination rate must be much slower than propagation. Given that termination is a 2nd-order reaction with respect to radical concentration whereas propagation is 1st-order, the radical concentration must be kept low, typically in the range of ppm or ppb, to achieve high molecular weight.

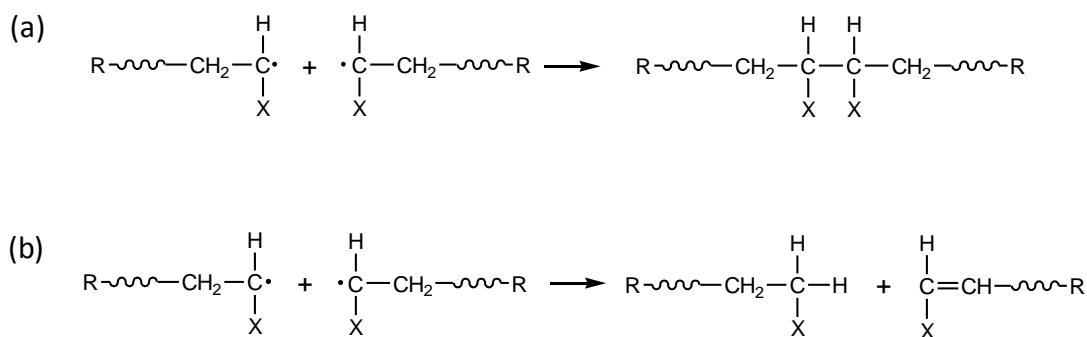


Figure 2.2 Termination reactions in free-radical polymerization by a) bimolecular radical coupling and b) disproportionation.

In free-radical polymerization, a steady-state concentration of radicals is established by balancing the rate of initiation to that of termination (typically, 10³ times slower than the propagation rate). Slow initiations can be achieved using radical initiators with long half lifetimes (> several hours) and low decomposition

rates ($< 10^{-5} \text{ s}^{-1}$). Initiating radicals, and thus new chains, are constantly generated throughout a polymerization. Slow initiations and irreversible termination steps often lead to uncontrolled molecular weight and broad molecular weight distribution (i.e., polydispersities). Furthermore, the average lifetime of a propagating chain is relatively short ($< 10 \text{ s}$) with respect to the time of polymer synthesis such that virtually all chains are “dead” at any given instant; therefore, block copolymers and polymers with controlled architectures cannot typically be produced by conventional free-radical polymerization. These limitations are overcome through controlled radical polymerization techniques, as discussed below.

2.2 Atom Transfer Radical Polymerization

Conventional free-radical polymerization is inherently limited in its ability to synthesize polymers with well-defined architectural and structural parameters. This is primarily because radical polymerizations are generally susceptible to irreversible termination and chain transfer processes, leading to unwanted chain termination and broad polydispersity. However, at present, it is known that these irreversible chain-terminating processes can be effectively suppressed to generate controlled radical polymerization systems that afford well-defined polymers.¹⁶⁹

Controlled radical polymerization provides the ability to prepare tailored polymers with low polydispersities, controlled molecular weights, compositions, and macromolecular architectures. Generally, a controlled/living radical polymerization is characterized by the following experimental features:¹⁷⁰

propagate (k_p) or terminate (k_t), as in conventional radical polymerization, but it can also be reversibly deactivated (k_{deact}) by coupling with X-Y to regenerate the dormant species ($M_n\text{-X}$). Since k_{deact} is typically much larger than k_{act} ($k_{\text{deact}}/k_{\text{act}} \sim 10^4 - 10^{10}$), the equilibrium is predominantly shifted towards the dormant species and the concentration of active radical species at any given time is very low (usually, $\sim 10^{-8}$ M). Thus, the rate of chain propagation is reduced and the probability of radical-radical termination and chain transfer are effectively suppressed. Consequently, pseudo-living polymer chains with controlled molecular weight and macromolecular structure can be obtained.

Atom transfer radical polymerization (ATRP), first developed by Wang and Matyjaszewski in 1995,¹⁷⁴ is among the most extensively developed controlled/living radical polymerization systems. ATRP can be carried out in bulk, solution, or heterogeneous phases (i.e., suspension, emulsion, or dispersion) and has been applied successfully to a wide range of monomers including styrene, (meth)acrylates, (meth)acrylamides, and acrylonitrile.¹⁷⁵ As a multicomponent system, ATRP is composed of monomer, an initiator with a transferable halogen (RX), and a transition metal catalyst. A general mechanism of ATRP is shown in Figure 2.4.¹⁷⁶

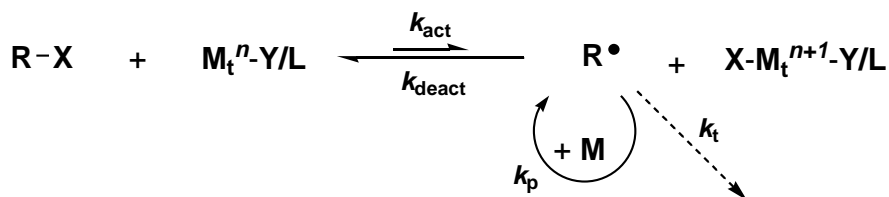


Figure 2.4 General mechanism of transition-metal catalyzed atom transfer radical polymerization (ATRP).

The transition metal catalyst (M_t^n -Y/L, where Y is a counterion and L is a complexing ligand) causes homolytic cleavage of an alkyl halogen (R-X) bond (k_{act}) which generates $X-M_t^{n+1}$ -Y/L and an active radical (R^\bullet).^{176, 177} The R^\bullet active radical can then propagate (k_p), terminate (k_t), or be reversibly deactivated (k_{deact}) by $X-M_t^{n+1}$ -Y/L to form a halide-capped dormant chain. With k_{deact} being typically much larger than k_{act} , a dynamic equilibrium is achieved between an excess of dormant species and a trace amount of active growing radicals. The rapid reversible deactivation of active radical chains reduces the stationary concentration of growing radicals and thereby minimizes the contribution of termination by radical-radical coupling and disproportionation.¹⁷⁴ This leads to the uniform growth of all the chains and allows control of molecular weight and structure.

The dynamic equilibrium between active and dormant species, and thus the rate of propagation, can be readily manipulated by modifying the ligand of the metal catalyst.¹⁷⁶ Nitrogen-based ligands are commonly employed in Cu-mediated ATRP catalyst system such as bipyridine and diethylenetriamine.

Alkyl halides (RX) with activating substituents on the α -carbon, such as aryl, carbonyl, or allyl groups, are typically used as initiators in ATRP. When the initiating moiety X (i.e., Br or Cl) is attached to macromolecular species, macroinitiators are formed which can be used to synthesize block/graft copolymers,¹⁷⁸ as demonstrated in Figure 2.5. If the initiating moieties are present at the chain ends of the macroinitiator, diblock or triblock copolymers may result (Figures 2.5a and 2.5b); alternatively, if they are present on the side

chains of the macroinitiator, graft copolymers may be produced (Figure 2.5c). In addition to the macroinitiator approach, block copolymers can also be obtained by sequential addition of different types of monomers.

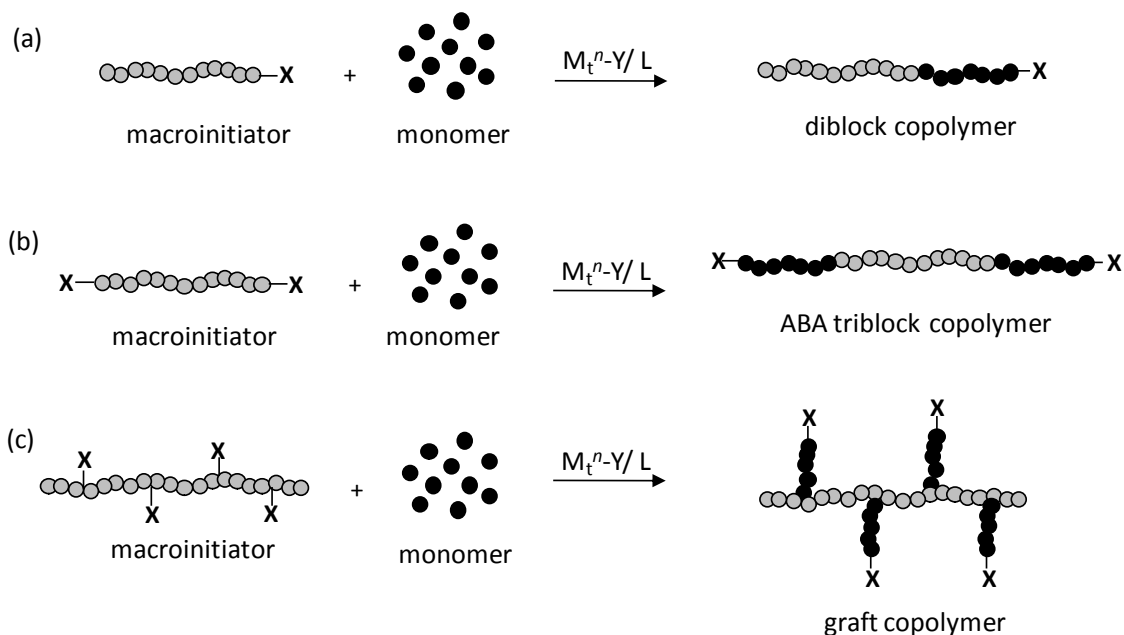


Figure 2.5 Schematic representation of the formation of a) diblock, b) ABA triblock and c) graft copolymers using macroinitiator approach.

2.3 Gel Permeation Chromatography

Gel permeation chromatography (GPC) is a separation technique which separates analytes on the basis of size. The GPC method is commonly used to determine the molecular weight and molecular weight distribution of polymers. In GPC, polymers are separated according to their size or hydrodynamic volume and therefore, molecular weight. Separation occurs via the use of a column that is typically packed with porous particles of a polystyrene gel. The surface pore sizes are determined by the amount of crosslinking in the polystyrene gel, since

the pores are formed by the solvent-swollen cavities that exist between the crosslinks. As demonstrated in Figure 2.6, when a solution containing a broad molecular weight distribution of polymers flows through the column, the smaller polymer molecules can enter the pores more easily and therefore, are delayed in their elution through the column. Conversely, larger polymer molecules are unable to penetrate the pores, and are swept along with the solvent front and eluted more quickly. Consequently, the larger molecules have shorter retention time and are separated from the smaller molecules. For an effective separation, the surface pore sizes of the stationary particles should be similar to that of the polymer analytes. Often, several GPC columns, each of which contains stationary particles with a different pore size, are connected in series to increase the resolution of the separation.

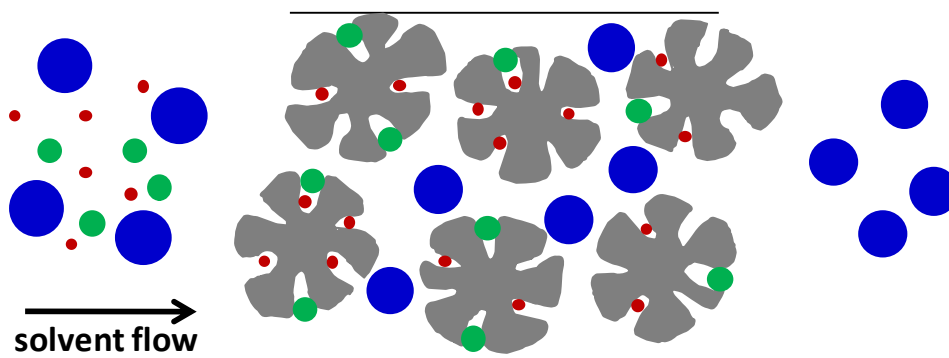


Figure 2.6 Schematic diagram showing the separation of analytes of varied size using a gel permeation chromatography (GPC) column.

After passage through the column system, the eluents are monitored by a detector. Common detection methods used in GPC include differential refractive index measurements and ultraviolet absorption. A differential refractometer

measures the difference in refractive index between the eluted solution and the pure solvent. When ultraviolet detection is used, the spectrometer is set to a particular wavelength and the absorbance is monitored. A plot of the detector signal as a function of retention time provides directly a plot of the molecular weight distribution. In order to assess the molecular weight of the polymer samples, the GPC apparatus is calibrated with a set of polymer standards of known molecular weights. A calibration curve is obtained by plotting the logarithm of molecular weights against the retention times for the polymer standards, as shown in Figure 2.7.

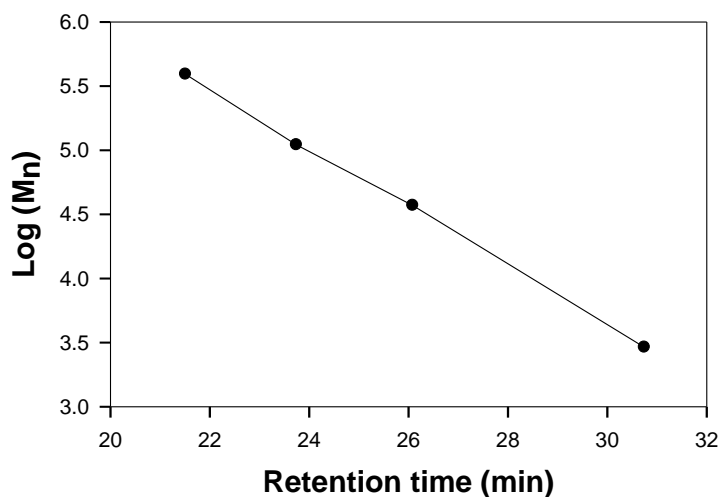


Figure 2.7 Typical calibration curve of a gel permeation chromatography instrument.

The retention time of the sample is then calibrated against the polymer standards to determine the molecular weight. Often, the GPC is calibrated using standard polymers that are chemically different from the polymer of interest and thus, in this case, the estimated molecular weight is merely a relative molecular

weight. The molecular weight of the polymers are commonly characterized as the number average molecular weight (M_n) and weight average molecular weight (M_w), as calculated by Equation 2.1 and 2.2, respectively.

$$M_n = \frac{\sum n_i M_i}{\sum n_i} \quad \text{Equation 2.1}$$

$$M_w = \frac{\sum n_i M_i^2}{\sum n_i M_i} \quad \text{Equation 2.2}$$

where n_i is the number of molecules of molecular weight M_i . The molecular weight distribution is often measured by the polydispersity index (PDI), which is defined as the ratio of M_w to M_n (Equation 2.3). A PDI of unity indicates a mono-dispersed polymer (i.e., all polymers have a uniform molecular weight).

$$PDI = \frac{M_w}{M_n} \quad \text{Equation 2.3}$$

2.4 Sulfonation

A large majority of proton exchange membranes are based on sulfonated polymers. Sulfonic acid ($-\text{SO}_3\text{H}$) groups may be incorporated onto the polymer structure by direct polymerization of sulfonated monomers or by post-sulfonation of pristine polymers. In direct polymerization of sulfonated monomers, the acid content in the resulting polymer can be controlled by varying the ratio of sulfonated to non-sulfonated monomers. However, direct polymerization of sulfonated monomers can be challenging due to intolerance of the sulfonate moiety ($-\text{SO}_3^-\text{M}^+$) during polymerization.¹⁵⁹ Alternatively, post-sulfonation may provide a facile and versatile route to sulfonated polymers.

Polystyrene-based polymers may be sulfonated using sulfonating reagents such as concentrated sulfuric acid, sulfur trioxide, acetyl sulfate, and chlorosulfonic acid.¹⁷⁹ In this thesis work, acetyl sulfate is used as the sulfonating reagent due to its mild reaction conditions (i.e., 40 – 50 °C in 1,2-dichloroethane), as well as its relatively slower sulfonation kinetics, which allow better control of the degree of sulfonation by varying the reaction time.¹⁷⁹ Sulfonation of polystyrene-based polymers using acetyl sulfate has been reported to provide a random distribution of –SO₃H groups along the PS chain and minimal chain-to-chain heterogeneity.⁵⁶ Acetyl sulfate can be prepared by the reaction between acetic anhydride and sulfuric acid (Figure 2.8a). The mechanism of the sulfonation reaction is described by an electrophilic aromatic substitution, in which the electrophilic acetyl sulfate reacts with the delocalized π-electron system of the aromatic ring (Figure 2.8b).

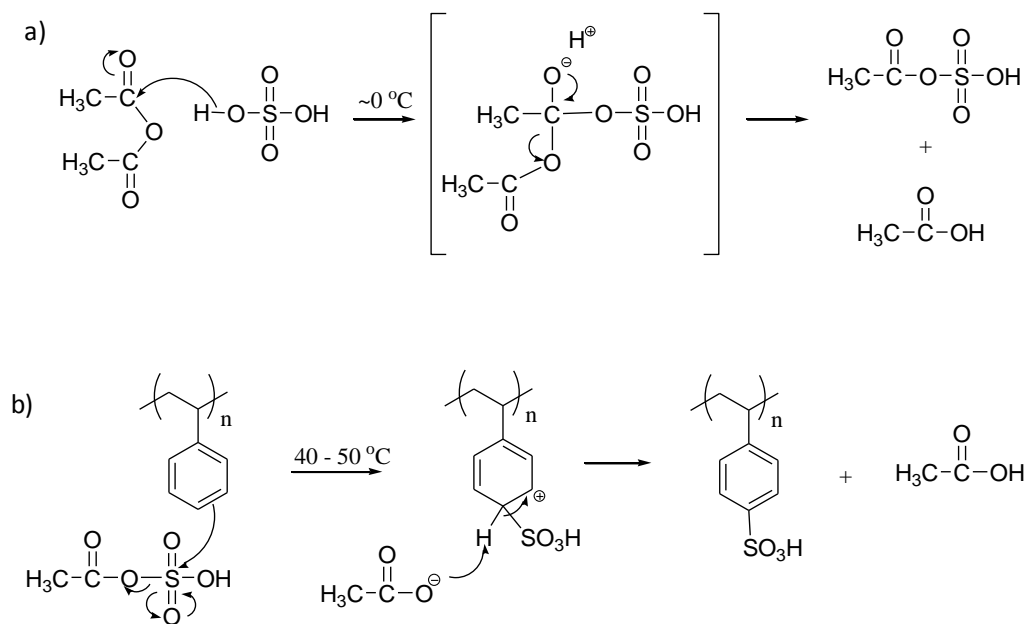


Figure 2.8 Mechanism of a) formation of acetyl sulfate from acetic anhydride and sulfuric acid and b) sulfonation of polystyrene using acetyl sulfate.

The electrophile is added at the position with the highest electron density, which is controlled by the position and nature of other substituents located around the aromatic ring. Electron-donating substituents (i.e., alkyl, NH₂, halogen, OR, OH) are both *ortho*- and *para*-directors, however, the *para*-isomers are generally more predominant due to steric effect and electronic repulsion of the SO₃H groups. On the other hand, electron-withdrawing substituents (i.e., NR₃⁺, NO₂, CN, SO₃H, COOR) are *meta*-directing groups. In the case of polystyrene, the electron-donating alkyl substituent (i.e., polymer backbone) on the aromatic ring directs the reaction to the *ortho* and *para* positions. However, sulfonation of polystyrene is reported to be predominantly occurring at the *para* position due to steric hinderance caused by the polymer backbone.¹⁷⁹ Furthermore, di-sulfonation on the same styrene unit is difficult because the first sulfonic acid group causes a reduction in the electron density of the aromatic ring and therefore, deactivates the ring towards further sulfonation.

2.5 Membrane Preparation and Characterization

2.5.1 Membrane Casting and Pre-treatment

In this thesis work, the membranes were prepared by dissolving the acid-bearing polymers in their respective solvents and drop-casting on a levelled Teflon[®] sheet. The polymer membranes were dried at room temperature for 2 – 12 h, depending on the solvent used, and then at 60 °C under vacuum for 24 h. To ensure complete protonation, the dried membranes (typically, 100 μm thick) were immersed in aqueous hydrochloric acid (HCl, 2 M) for 24 h. The protonated membranes were washed several times with Milli-Q deionized water for 30 min

periods, and then stored in water for 24 h to remove excess acid on the surfaces and the interior of the membranes.

2.5.2 Water Sorption

Water-saturated membranes were obtained by equilibration in Milli-Q deionized water for 24 h at ambient temperature. Prior to determining the wet weight, the membranes were blotted with a Kimwipe to remove surface water. The dry weights were obtained after the membranes were dried at 80 °C for minimum of 12 h under vacuum. The water uptake was calculated as the percentage increase in mass over the dry weight according to Equation 2.4:

$$\text{water uptake} = \frac{W_{\text{wet}} - W_{\text{dry}}}{W_{\text{dry}}} \times 100\% \quad \text{Equation 2.4}$$

where W_{wet} (g) and W_{dry} (g) are the wet and dry weights of the membrane, respectively.

Water content was calculated both as a mass and a volume percentage of water in the wet membrane and given by Equations 2.5 and 2.6:

$$\text{water content (wt \%)} = \frac{W_{\text{wet}} - W_{\text{dry}}}{W_{\text{wet}}} \times 100\% \quad \text{Equation 2.5}$$

$$\text{water content (vol \%)} = X_v = \frac{V_{\text{wet}} - V_{\text{dry}}}{V_{\text{wet}}} \quad \text{Equation 2.6}$$

where V_{wet} and V_{dry} are the wet and dry volumes of the membrane, respectively.

The membrane's thickness was measured with Series 293 Mitutoyo Quickmike

thickness micrometer while the length and width were measured with Mitutoyo Digimatic caliper.

Another parameter commonly used to represent water content is the molar ratio of water molecules to ion exchange sites. Essentially, this value provides a measure of the average number of water molecules per ion exchange site ($[\text{H}_2\text{O}]/[\text{SO}_3^-]$, often referred to as λ value), and was calculated by Equation 2.7:

$$[\text{H}_2\text{O}]/[\text{SO}_3^-] = \lambda = \frac{\text{water uptake}(\%) \times 10}{18 \times \text{IEC (mmol/g)}} \quad \text{Equation 2.7}$$

where IEC is the ion exchange capacity (mmol/g), as determined by titration and discussed below.

2.5.3 Ion Exchange Capacity and Acid Concentration

Ion exchange capacity (IEC) was used to quantify the sulfonic acid content of the membrane, and was expressed as the number of millimoles (mmol) of ion exchange sites per gram of dry polymer. The IEC was determined by acid-base titration. Membranes were converted to their protonic form by immersing in 2 M HCl for 24 h, followed by rinsing repeatedly in deionized water. The pretreated membranes were then immersed in an aqueous solution of sodium chloride (NaCl, 2 M) for a minimum of 4 h to release the protons, which were subsequently titrated with a standardized solution of sodium hydroxide (NaOH) to the phenolphthalein end-point. Control acid-base titrations were performed on NaCl solutions with no membranes present to determine the “blank” titration volume. After titration, the membranes were immersed in 2 M hydrochloric acid (HCl) for a minimum of 4 h to reprotonate the sulfonic sites. After drying at 80 °C

in vacuo, the membranes' dry weight was measured. The ion exchange capacity, IEC (mmol/g), of the membrane was calculated by Equation 2.8:

$$\text{IEC (mmol/g)} = \frac{V_{\text{NaOH}} M_{\text{NaOH}}}{W_{\text{dry}}} \quad \text{Equation 2.8}$$

where V_{NaOH} and M_{NaOH} are the blank-corrected volume (mL) and molar concentration (mol/L) of the NaOH titrant, respectively; W_{dry} is the dry weight (g) of the membrane.

From the IEC data, the analytical acid concentration, $[-\text{SO}_3\text{H}]$ (mol/L), in a hydrated membrane, can be calculated by Equation 2.9:

$$[-\text{SO}_3\text{H}] = \frac{W_{\text{dry}} (\text{g})}{V_{\text{wet}} (\text{cm}^3)} \times \text{IEC (mmol/g)} \quad \text{Equation 2.9}$$

where W_{dry} (g) is the membrane's dry weight; V_{wet} (cm^3) is the volume of the hydrated membrane; and IEC is the ion exchange capacity (mmol/g).

The acid-base titration technique, used to determine IEC, provides a quantitative measure of the amount of tethered sulfonic acid groups, $-\text{SO}_3\text{H}$, in a membrane, rather than the actual amount of free dissociated protons, H^+ . Therefore, $[-\text{SO}_3\text{H}]$, as derived from IEC titration data, represents the *overall* concentration of protons in the membrane – i.e., it does not distinguish between free dissociated protons and bound protons that are associated with the sulfonic acid groups.

2.5.4 Proton Conductivity

Proton conductivities were measured using ac impedance spectroscopy with a Solartron 1260 frequency response analyzer employing a two-probe electrode configuration, according to a procedure described in the literature.^{144, 180} Data analysis and fitting were performed using commercial Z plot/Z view[®] software (Scribner Associates).

To measure in-plane proton conductivity, a strip of hydrated membrane (~10 mm x 5 mm) was placed between two platinum foil electrodes that were ~5 mm apart and fixed in place by attaching them to an inert Teflon block (Figure 2.9). Another Teflon block was placed on top and tightened to immobilize the membrane during measurements. The electrochemical cell was connected to the frequency response analyzer using two wires that were fitted with alligator clips (not shown). A sinusoidal ac voltage (amplitude of 100 mV over a frequency range of 10 MHz to 100 Hz) was applied across the two platinum electrodes and the ac impedance was measured. To prevent the membrane from losing water to the atmosphere before completion of the measurement, the electrochemical cell was covered with wet tissue paper. All measurements were carried out on fully hydrated membranes at room temperature, under ambient atmosphere

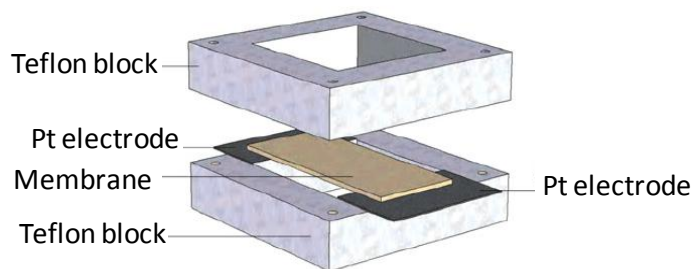


Figure 2.9 In-plane impedance electrochemical cell.

[Reprinted with permission from *Journal of Electroanalytical Chemistry*, Soboleva, T.; Xie, Z.; Shi, Z.; Tsang, E.; Navessin, T.; Holdcroft, S. 622, 145, © 2008, Elsevier B.V.]

A typical Nyquist plot (complex-plane plot of the imaginary impedance, Z'' , versus real impedance, Z') for in-plane impedance is shown in Figure 2.10. To obtain the ionic resistance from the impedance data, the Nyquist plot was fitted to a Randles equivalent circuit model consisting of an interfacial contact resistance (R_c) acting in series with a parallel combination of a membrane bulk capacitance (C_m) and a membrane bulk resistance (R_m) (Figure 2.11). In essence, an approximation of the membrane bulk resistance (R_m) can be obtained by taking the difference between the high frequency and low frequency x-intercepts (i.e., the diameter of the semi-circle).

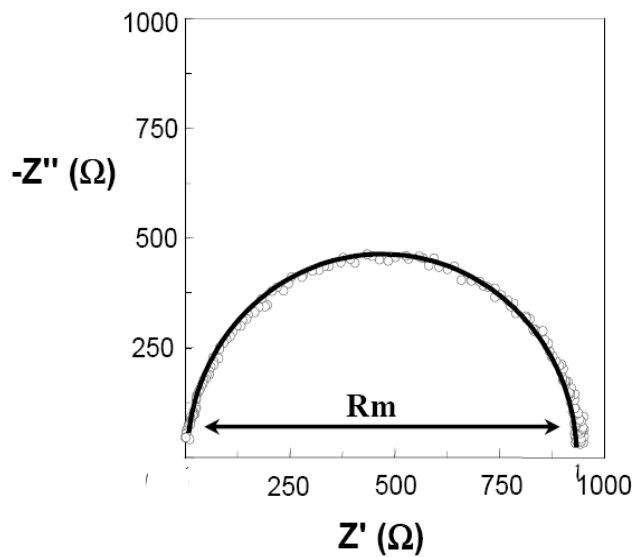


Figure 2.10 Typical Nyquist plot for the in-plane impedance of a membrane: open circles represent experimental data and solid line represents the fitted data.

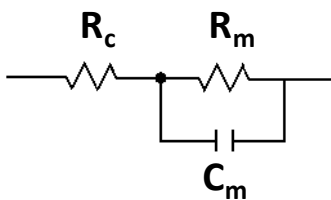


Figure 2.11 Randles equivalent circuit model used to fit in-plane impedance data.

The membrane resistance, R_m , was used to calculate the in-plane proton conductivity (σ) using Equation 2.10:

$$\sigma = \frac{L}{R_m A} \quad \text{Equation 2.10}$$

where L (cm) is the distance between platinum electrodes; R_m is the membrane resistance; and A (cm^2) is the cross-sectional area of the membranes, measured as the product of the width (cm) and the thickness (cm) of the membrane.

For through-plane proton conductivity measurements, a piece of membrane (5 mm x 5 mm) was sandwiched between two platinum electrodes, and the electrochemical cell was tightened with screws to minimize interfacial contact resistance (Figure 2.12). The through-plane electrochemical cell was connected to the frequency response analyzer by means of pins (not shown). Impedance data were collected in the frequency range of 10 MHz to 100 Hz with an ac voltage of 100 mV. Prior to conducting the measurements, the cell was calibrated to determine the high frequency inductance of the cell by measuring the impedance of the shorted cell and subtracting this as the background from the subsequent measurements.

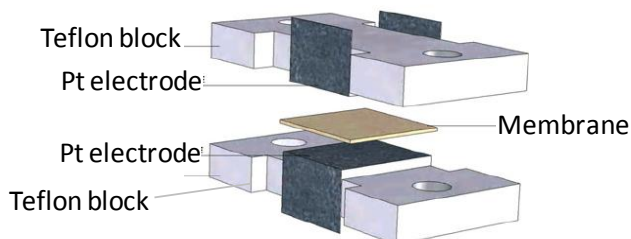


Figure 2.12 Through-plane impedance electrochemical cell.

[Reprinted with permission from *Journal of Electroanalytical Chemistry*, Soboleva, T.; Xie, Z.; Shi, Z.; Tsang, E.; Navessin, T.; Holdcroft, S. 622, 145, © 2008, Elsevier B.V.]

A typical Nyquist plot for through-plane impedance is shown in Figure 2.13. Only a partial semi-circle was resolved due to the experimental frequency limitation of the frequency response analyzer. Membrane resistance was obtained by fitting the Nyquist plot into a Randles equivalent circuit model consisted of an interfacial double-layer capacitance (C_{dl}) acting in series with a

parallel combination of membrane bulk capacitance (C_m) and membrane bulk resistance (R_m) (Figure 2.14).

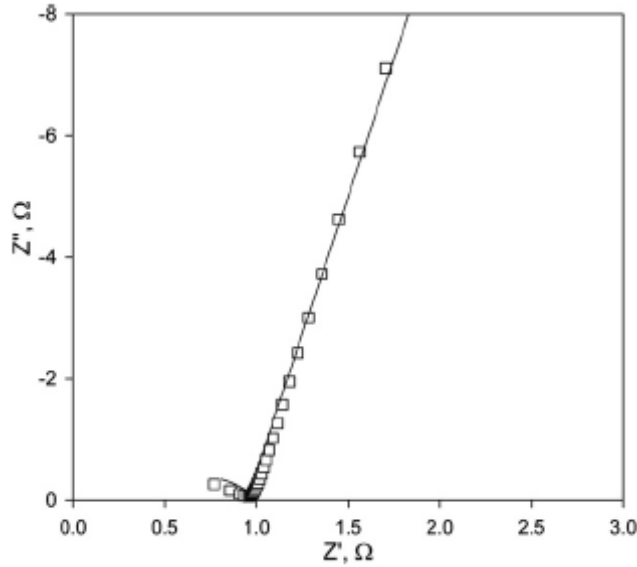


Figure 2.13 Typical Nyquist plot for the through-plane impedance of a membrane: empty squares represent experimental data and solid line represents the fitted data.

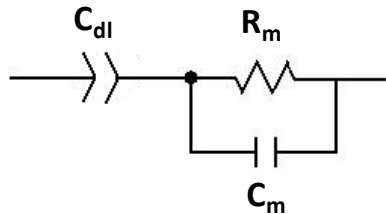


Figure 2.14 Randles equivalent circuit model used to fit through-plane impedance data.

The through-plane proton conductivity was also calculated using Equation 2.7 except that L (cm), corresponding to the electrode separation, is the thickness of the membrane; and A (cm^2) is the surface area of the platinum electrode.

The degree of conductivity anisotropy was calculated as follows:

$$\sigma_{\parallel/\perp} = \frac{\sigma_{\parallel}}{\sigma_{\perp}} \quad \text{Equation 2.11}$$

where $\sigma_{\parallel/\perp}$ is the proton conductivity anisotropy; σ_{\parallel} is the in-plane proton conductivity (average of the two perpendicular in-plane directions, X and Y); and σ_{\perp} is the through-plane proton conductivity (Z direction).

2.5.5 Proton Mobility

Proton conductivity (σ_{H^+}) is related, through the Nernst-Einstein equation,¹⁸¹ to the concentration ($[H^+]$) and mobility (μ_{H^+}) of protons, as shown in Equation 2.12.¹⁸²

$$\sigma_{H^+} = F [H^+] \mu_{H^+} \quad \text{Equation 2.12}$$

where F is the Faraday's constant. A more correct description of Equation 2.12 can be obtained by replacing $[H^+]$ with the activity of H^+ (a_{H^+}). As shown in Equation 2.13, a_{H^+} is governed by the proton concentration as well as the degree of dissociation of the acid group (f), which itself, is dependent upon the acid strength (pK_a) and the water content.^{182, 183}

$$a_{H^+} = f [H^+] \quad \text{Equation 2.13}$$

However, in PEMs, a_{H^+} is an unattainable value since IEC titration only measures the analytical *acid* concentration $[-SO_3H]$ (i.e., combining both dissociated and undissociated protons), rather than the actual free *proton* concentration. In addition, the mobility of protons in the hydrated ionic channels of a membrane deviates from the classical picture of mobility of free protons in an acid solution: In a membrane, the $-SO_3^-$ counter-anions, being tethered to the

polymer chain, are immobile and thus, may impede the mobility of protons; whilst in an acid solution, the SO_3^{2-} anions are mobile. Thus, proton mobility in PEMs can only be described as an *effective* proton mobility (μ_{eff}) (Equation 2.14),^{182, 183} which incorporates the tethering effects of the $-\text{SO}_3^-$ anion and the uncertainties of the degree of acid dissociation. For instance, in the case that all the protons in the membrane remain undissociated, then μ_{eff} would be zero.

$$\sigma_{\text{H}^+} = F [-\text{SO}_3\text{H}] \mu_{eff} \quad \text{Equation 2.14}$$

$$\mu_{eff} = \frac{\sigma_{\text{H}^+}}{F [-\text{SO}_3\text{H}]} \quad \text{Equation 2.15}$$

From Equation 2.15 (rearrangement of Equation 2.14), it can be seen that μ_{eff} essentially represents a “normalized” proton conductivity (i.e., acid concentration effects removed). Thus, calculation of μ_{eff} allows the determination of the relative contributions of both proton mobility and acid concentration to the proton conductivity.

In addition to acid dissociation and water content, the mobility of protons in a membrane is also influenced by other factors. For instance, the effective mean-free path and connectivity of the ionic conduction pathway may play a role in proton mobility. As demonstrated in Figure 2.15, the conduction pathways in membrane A are more tortuous and possess a series of dead-ends, while those in membrane B are more linear. Thus, all other things being equal, proton mobility will be greater in B relative to A. Furthermore, the spatial proximity between the acid groups can also influence the mobility of protons. Figure 2.16 demonstrates ionic channels having different distances between acid groups. As

the protons are transported between the tethered $-\text{SO}_3^-$ anions, it is expected that the larger distances between $-\text{SO}_3^-$ groups in A will require greater activation energy compared to B, and thus lower proton mobility is expected in A.^{107, 113} In short, the effective proton mobility is a useful parameter for providing insights into the degree of acid dissociation, ionic channel tortuosity and spatial proximity of neighbouring acid groups.¹⁸²

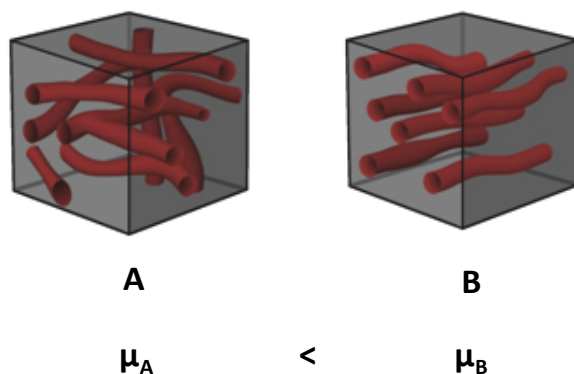


Figure 2.15 Schematic representation of the effects of connectivity and tortuosity of ionic channels on proton mobility (red = ionic domains).

[Reprinted with permission from *Advanced Materials*, Peckham, T. J.; Holdcroft, S. 22, 4667, © 2010, Wiley-VCH Verlag GmbH & Co. KGaA.]

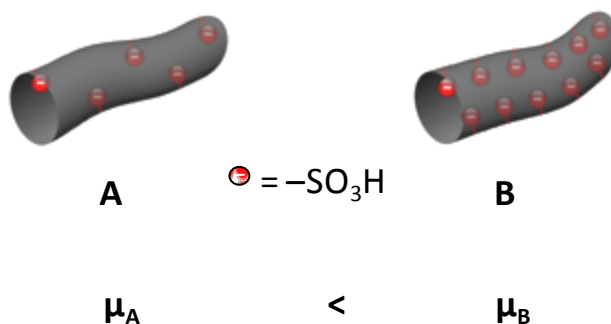


Figure 2.16 Schematic representation of the effects of spatial proximity of neighboring acid groups on proton mobility.

[Reprinted with permission from *Advanced Materials*, Peckham, T. J.; Holdcroft, S. 22, 4667, © 2010, Wiley-VCH Verlag GmbH & Co. KGaA.]

2.5.6 Transmission Electron Microscopy (TEM)

Transmission electron microscopy (TEM) is a microscopy technique which utilizes electrons to produce images at nanometer-scale resolution. The TEM was originally developed to overcome the limited resolving power of the conventional optical microscope. In an optical microscope, the resolving power (i.e., smallest resolvable distance, d) is governed by the wavelength of the radiation source (λ) and the numerical aperture of the microscope system (NA), as given by Equation 2.16.

$$d \approx \frac{\lambda}{2NA} \quad \text{Equation 2.16}$$

Due to the relatively large wavelength of visible light (400 – 700 nm), an optical microscope is limited to image resolutions of only a few micrometers. Although TEM operates under the same basic principles as the optical microscope, it uses electrons instead of visible light as the radiation source. The wavelength of an electron (λ_e) is related to their energy, as given by the de Broglie's equation (Equation 2.17):

$$\lambda_e = \frac{h}{\sqrt{2m_oE}} \quad \text{Equation 2.17}$$

where h is Planck's constant, m_o is the rest mass of an electron and E is the energy of the accelerated electron. For a TEM operating at an accelerating voltage of 100kV, the electrons have a wavelength of ~0.004 nm, which is five orders of magnitude smaller than visible light. Due to the much smaller

wavelength of the electrons, TEMs are capable of imaging at significantly higher resolution than optical microscopes, and can be used to probe structures at near atomic levels (i.e., nanometer-scale resolution).

A simplified schematic diagram of a TEM is shown in Figure 2.17. At the top of the microscope, an electron source, typically a tungsten filament or lanthanum hexaboride crystals (LaB_6), is heated to generate electrons which travel down the TEM column. The entire microscope column is under vacuum to prevent the absorption of electrons by gas molecules. The emitted electrons are manipulated by electromagnetic lens into a very fine beam. The electron beam then travels through the specimen. Interactions between the electrons and the specimen cause some of the electrons to be scattered and disappear from the beam, while others are transmitted through the specimen unchanged. Factors affecting the scattering of electrons include the atomic number/weight of the scattering atom, the thickness, density, and crystallinity of the specimen. The transmitted portion of the electron beam is then focused and magnified by various electromagnetic lenses down the column. At the bottom of the microscope, the transmitted electron beam hits a fluorescent screen which translates the electron intensity to light intensity, giving rise to a two-dimensional shadow image of the specimen with varied contrast. The most common mode of operation for a TEM is the bright field imaging mode, in which contrast formation is formed directly by occlusion and scattering of electrons. The darker areas of the image represent the regions of the specimen at which more electron scattering occurred (i.e., heavier atom, thicker, higher material density); whereas

the lighter areas represent the regions at which more electrons were transmitted through (i.e., lighter atom, thinner, lower density).

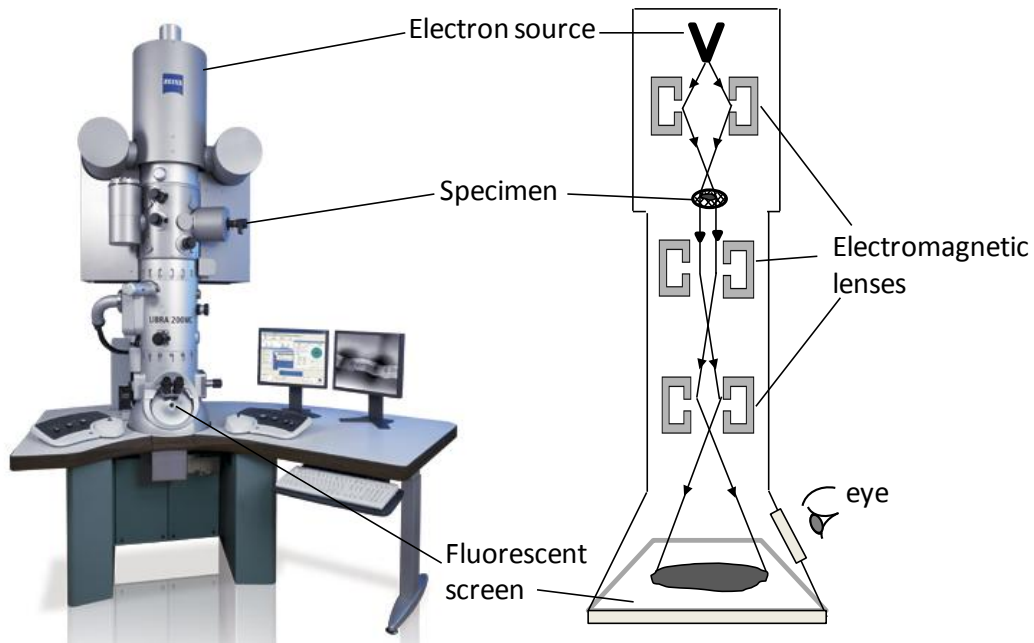


Figure 2.17 Schematic diagram of an electron transmission microscope (TEM).

TEM can be used to study phase separation and morphology in polymeric materials. This often requires the preparation of very thin specimens in order to transmit sufficient electrons so that enough intensity falls on the imaging screen to afford an interpretable image. In the case of polymeric materials, common methods for the preparation of ultra thin specimens include spin-casting from dilution polymer solutions or sectioning with an ultramicrotome. Staining of samples prior to imaging allows for enhanced image contrast. In the case of proton exchange membranes, the H^+ of the sulfonic acid groups are often

exchanged with heavier cations such as Pb^{2+} , Cs^+ and Ag^+ to increase the electron scattering of the ionic domains, and thus the contrast of the image.

2.5.7 Wide-angle X-ray Scattering (WAXS)

X-ray diffraction is commonly used to study the crystallographic structure of materials. The technique is based on the elastic scattering of X-rays with the electron clouds of atoms. When the atoms form a crystal lattice with an inter-planar spacing that is comparable to the wavelength of the incident X-ray beam, diffraction occurs. Diffraction is caused by constructive interference when the reflected beams from different atomic planes are in phase and reinforce each other to form an enhanced wave front (Figure 2.18). The relation by which diffraction occurs is given by the Bragg's law:

$$2d \sin(\theta) = n\lambda \quad \text{Equation 2.18}$$

where d is the inter-planar lattice spacing, θ is the angle of the incident X-ray, n is an integer and λ is the wavelength of the X-rays. An X-ray diffractometer typically consists of a monochromatized X-ray source (i.e., Cu K_α source, $\lambda = 1.5418 \text{ \AA}$), a sample holder, and an X-ray detector (typically, a scintillation counter). A goniometer mechanically couples the rotation of the sample holder and the detector in a 1:2 relationship – i.e., the sample rotates by the angle θ and the detector simultaneously rotates by the angle 2θ .

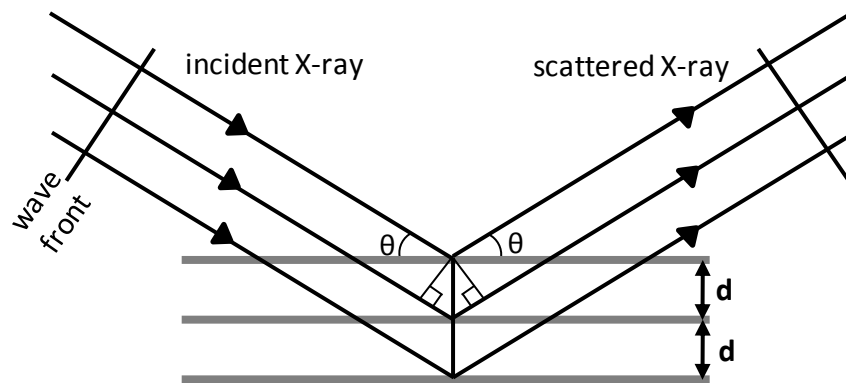


Figure 2.18 Reflection of X-rays from atoms in different layers of a crystal lattice with interplanar spacing of d .

X-ray scattering techniques can be categorized into two main areas: small- and wide-angle X-ray scattering, which provide structural information at length scales on the order of nano-meter and sub-nanometer, respectively. Wide-angle X-ray scattering (WAXS), with a typical angular range of $5^\circ < 2\theta < 50^\circ$, are commonly employed to study the crystallinity of polymers. Semi-crystalline polymers contain both crystalline and amorphous phases, as illustrated in Figure 2.19. The crystalline phases are comprised of ordered, regularly aligned polymer chains while the intervening amorphous phases contain randomly arranged chains. The degree of crystallinity represents the fraction of the material that is crystalline, and can be determined from the X-ray diffraction pattern by comparing the scattering due to the crystalline phases to the total scattering intensity.¹⁸⁴ A WAXS profile, reported by Abbrent *et al*,¹⁸⁵ of a semi-crystalline poly(vinylidene difluoride-co-hexafluoropropylene) copolymer is shown in Figure 2.20. Three sharp crystalline peaks ($2\theta = 18.4^\circ, 20.0^\circ, 26.7^\circ$) are distinguished from the broad amorphous peak with centre at $= 18.0^\circ$. The degree of crystallinity (x_{cr}) can be estimated by the ratio of the integrated

intensities of the crystalline peaks to the sum of the integrated intensities of the crystalline and amorphous peaks:¹⁸⁴

$$x_{cr} = \frac{\int_0^{\infty} I_{cr}(q)q^2 dq}{\int_0^{\infty} I_{total}(q)q^2 dq} \quad \text{Equation 2.19}$$

where I_{cr} is the intensity scattered by the crystalline domains, I_{total} is the overall scattered intensity, and q is the magnitude of the scattering vector ($q = (4\pi/\lambda) \sin \theta$).

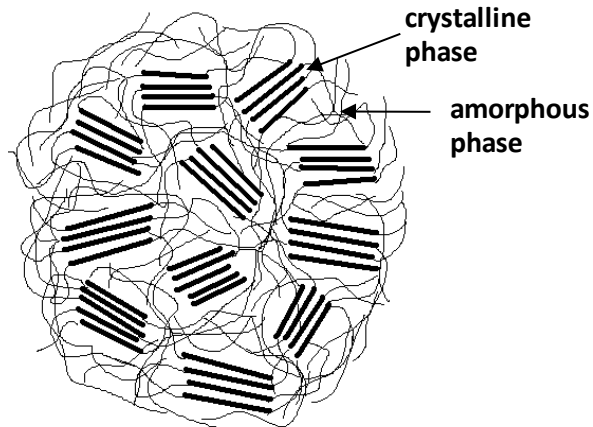


Figure 2.19 Schematic representation of the microstructure of semi-crystalline polymer possessing crystalline phases and amorphous phases.

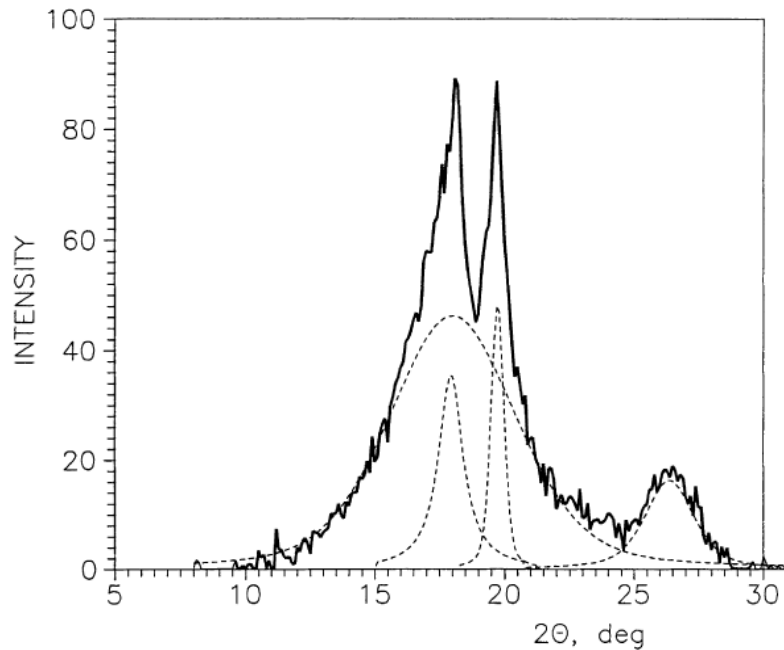


Figure 2.20 WAXS diffractogram of a P(VDF-co-HFP) copolymer showing the resolved crystalline and amorphous peaks (dashed line).

[Reprinted with permission from *Polymer*, Abbrent, S.; Plestil, J.; Hlavata, D.; Lindgren, J.; Tegenfeldt, J.; Wendsjo, A.. 42, 1407, © 2001, Elsevier.]

Chapter 3. Ionic Purity and Percolation of Proton-Conducting Channels in Fluorous-Ionic Diblock Copolymers

3.1 Introduction

The elucidation of fundamental structure-property relationships in proton exchange membranes (PEMs) is currently an active area in fuel cell research.^{106, 159, 182} Specifically, the role of polymer microstructure (i.e., chemical composition, chain architecture, acid content) on the phase segregation of ionic and non-ionic domains, and in turn, on proton transport is a subject of considerable research interest. In this context, model polymers with controlled molecular structures, leading to controlled morphologies, are extensively developed and utilized for investigating relationships between polymer structure, membrane morphology and physicochemical properties.^{5, 106, 159}

It is well-established that block copolymers can self-assemble into a variety of ordered, nano-scaled morphologies through the process of microphase separation.^{186, 187} Microphase separation in block copolymers is driven by the enthalpy of de-mixing of incompatible segments, while further separation into macro-scale domains is prevented by chemical connectivity between segments. The extent of phase separation and the resulting morphology are governed by factors including chemical dissimilarity between blocks, length of each block, their block ratio, and crystallizability. An experimental phase diagram, reported

by Mortensen *et al.*,¹⁸⁸ for a series of poly(styrene-*b*-isoprene) (PS-*b*-PI) diblock copolymers is shown in Figure 3.1. The product χN is the enthalpic-entropic balance and controls the degree of segregation between the block segments (χ is the Flory-Huggins segmental interaction parameter and N is the degree of polymerization). It can be seen that for PS-*b*-PI diblock copolymers possessing sufficiently large χN values (>20), distinct morphologies are obtained depending on the volume fraction of the polyisoprene segment (f_{PI}).

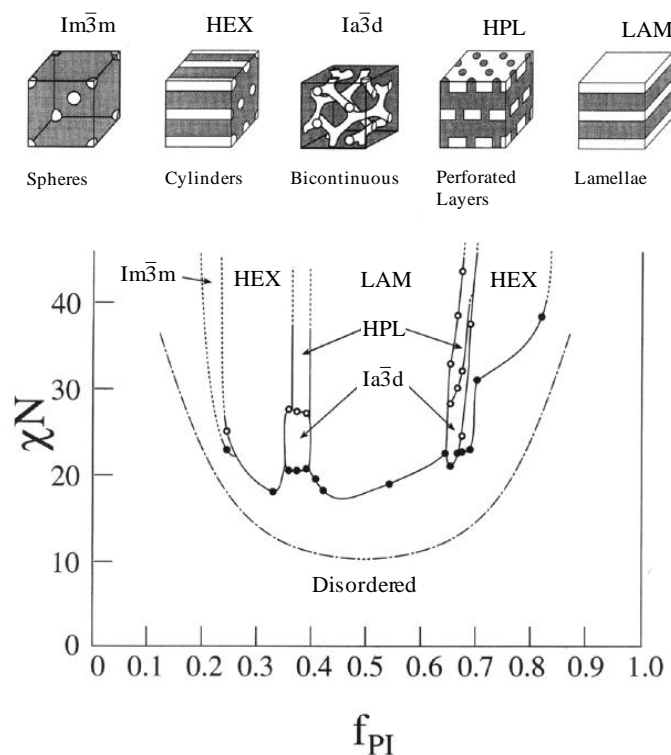


Figure 3.1 Morphological phase diagram for polystyrene-*b*-polyisoprene (PS-*b*-PI) diblock copolymers.

[Reprinted with permission from *Macromolecules*, Khandpur, A. K.; Forster, S.; Bates, F. S.; Hamley, I. W.; Ryan, A. J.; Bras, W.; Almdal, K.; Mortensen, K. 28, 8796, © 1995, American Chemical Society.]

The high-level of morphological control renders ion-containing block copolymers (i.e., block ionomers) potentially useful for studying structure-

property relationships in PEMs, and these are the subject of a recent review by Elabd and Hickner.¹⁸⁹ Block ionomers for PEM materials are typically comprised of an ionic and a non-ionic block. This is often achieved by having constituent blocks to be composed of different chemical units or of units that are chemically identical except that one block is sulfonated and the other is not. Chemical immiscibility of the constituent blocks induces phase separation of ionic and non-ionic domains, in which proton transport is facilitated by the ionic domain while mechanical strength is provided by the other non-ionic domain. Well-defined sulfonated block copolymers can yield highly ordered nanostructures where the morphology and domain size are tunable on the nanoscopic length scale, and thereby, allow for an investigation of the effects of morphology and molecular order on proton transport that are normally difficult to study using randomly sulfonated systems.

The morphology and properties of PEMs based on polystyrene sulfonic acid-containing block ionomers have been extensively studied.⁵⁵⁻⁷⁷ Partially sulfonated poly(styrene-*b*-[ethylene-co-butylene]-*b*-styrene) (S-SEBS), possessing a sequence of ionic/non-ionic/ionic block, have been investigated for examining structure-property relationships as well as the potential application as low-cost membranes in hydrogen PEMFCs.⁵⁵⁻⁶⁹ It is reported that different morphologies can be obtained for S-SEBS when membranes are cast from different solvents, and proton conductivities are highly dependent upon membrane morphologies.^{62, 69} Elabd *et al*⁷¹⁻⁷⁴ examined a similar triblock copolymer, partially sulfonated poly(styrene-*b*-isobutylene-*b*-styrene) (S-SIBS),

which is also found to adopt different morphologies that are dependent upon the casting solvent. Proton conductivity (in-plane direction) is significantly higher in membranes with lamellar structure compared to those with disordered structure. In addition, S-SIBS exhibits a change in morphology with increasing ion contents.⁷⁴ Park and Balsara¹⁹⁰ have recently reported on the effect of alignment of the proton conducting pathways in partially sulfonated poly(styrene-*b*-methylbutylene) (PS-*b*-PMB). Various processing techniques such as solvent casting, pressing, shearing and electric field alignment were used to obtain membranes with different orientation of the ionic lamellar domains, from which the degree of conductivity anisotropy was found to be consistent with the morphological anisotropy observed.¹⁹⁰ More recently, Hillmyer *et al*¹⁹¹ have prepared diblock ionomers of poly([norbornyleneethylstyrene-*r*-styrene]-*b*-styrenesulfonic acid) (PNS-*b*-PSSA) using ATRP. During the solution casting process, the norbornylene groups were cross-linked by ring-opening metathesis polymerization (ROMP). The PNS-*b*-PSSA membranes exhibited a bicontinuous morphology where the PSSA domain sizes were found to be directly proportional to the molecular weight of the PNS-*b*-PSSA copolymer. At fully hydrated conditions, proton conductivity is reported to be independent of PSSA domain size; however, at 90% RH, proton conductivity increases with decreasing PSSA domain size, which is attributed to the capillary condensation effects in smaller ionic domains.

Sulfonated block copolymers possessing fluorinated segments have several advantages including increased thermal and chemical stability, low water

absorptivity and higher resistance to oxidation over hydrocarbon analogues. Furthermore, the hydrophobicity of the fluorocarbon block may lead to a higher degree of hydrophilic/hydrophobic microphase separation.¹⁹² Recently, diblock ionomer systems based on sulfonated poly([vinylidene difluoride-co-hexafluoropropylene]-*b*-styrene) [P(VDF-co-HFP)-*b*-SPS] possessing a hydrophobic fluororous linear segment attached to a hydrophilic sulfonated styrene block have been reported.¹⁹³⁻¹⁹⁵ These were prepared by ATRP of styrene from a fluoropolymer macroinitiator, followed by post-sulfonation (Figure 3.2). This partially fluorinated diblock ionomer system provides great structural control over the lengths of both the fluorinated and the polystyrene segments as well as the ion content via the degree of sulfonation of the PS block. The presence of the fluorinated block is reported to improve phase separation, and thereby enhances proton conductivity compared to random copolymers of styrene and styrenesulfonic acid (PS-*r*-PSSA) as well as to other non-fluorous polystyrene-based block ionomers (i.e., S-SEBS, S-SIBS).¹⁹⁴

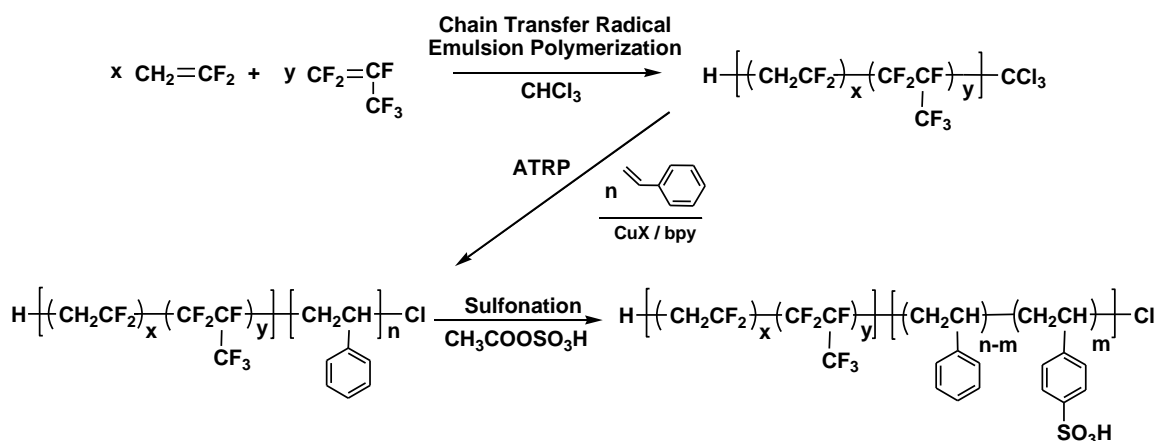
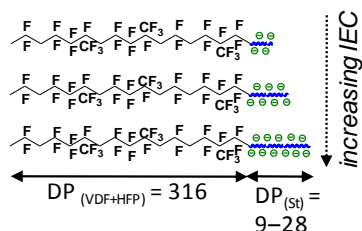


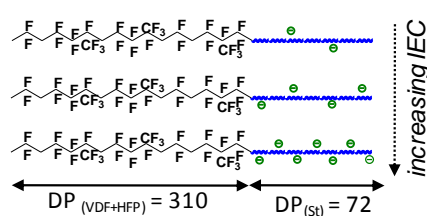
Figure 3.2 Synthetic Scheme for P(VDF-co-HFP)-*b*-SPS.

In this chapter, the P(VDF-*co*-HFP)-*b*-SPS diblock ionomer approach is utilized to elucidate structure-property relationships by preparing several series of diblocks possessing different block ratios (Figure 3.3). Within each membrane series, the ion content was controlled either by varying the length of the fully sulfonated polystyrene (PS) block (Figure 3.3a), or by changing the degree of sulfonation of a fixed PS block (Figure 3.3b and 3.3c). Proton conductivities, proton mobilities, water content, and acid concentration are studied and compared. As anticipated, the membrane morphology plays a profound role on proton transport but surprisingly, the degree of sulfonation of the PS block plays a stronger role as it determines the extent of ionic purity and percolation within the so-called “proton-conducting channels”. A previous neutron scattering study¹⁹⁶ indicated that the ionic channels in these diblock membranes consisted of ionic aggregates of sulfonated polystyrene in a matrix of non-sulfonated polystyrene. Thus, in here, ionic purity is defined as the proportion of sulfonated PS aggregates within the ionic PS domains, and is directly related to the degree of sulfonation of the PS segment. The structure-property relationships reported in this work provide useful insights into the design of next-generation proton-conducting membranes.

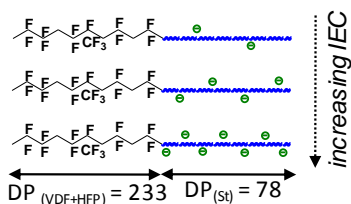
a) 6–17 vol% PS, Fully Sulfonated:



b) 35 vol% PS, Partially Sulfonated:



c) 45 vol% PS, Partially Sulfonated:



d) 50 vol% PS, Partially Sulfonated:

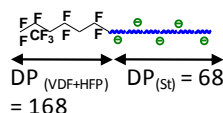


Figure 3.3 Structural relationship between the various series of P(VDF-*co*-HFP)-*b*-SPS membranes.

3.2 Experimental

3.2.1 Materials

Vinylidene difluoride (VDF, SynQuest Laboratory Inc., 99+%), hexafluoropropylene (HFP, Aldrich, 99+%), potassium persulfate (K₂S₂O₈, Allied Chemical, reagent grade), sodium metabisulfite (Na₂S₂O₅, Anachemia, anhydrous, reagent grade), chloroform (Caledon, spectrograde), pentadecafluorooctanoic acid (Aldrich, 96%), copper (I) chloride (CuCl, Aldrich, 99.995+%), 2,2'-bipyridine (bpy, Aldrich, 99+%), 1, 2-dichloroethane (DCE, Caledon, reagent grade), sulfuric acid (Anachemia, 95 – 98%, ACS reagent), and acetic anhydride (Caledon, reagent grade) were used as received. *n*-Butyl acetate (Caledon, reagent grade) was refluxed with small portions of potassium permanganate (KMnO₄), distilled in the presence of calcium hydride (CaH₂)

under reduced pressure, and stored under nitrogen at -20 °C. Styrene (St, Aldrich, 99+%) was washed twice with aqueous 5% sodium hydroxide (NaOH) and twice with water, dried overnight with magnesium sulfate (MgSO₄), distilled in the presence of CaH₂ at 40 °C under reduced pressure, and stored under nitrogen at -20 °C. As received Nafion[®] 117 (Du Pont) membranes were pretreated by boiling sequentially in aqueous 3 v% hydrogen peroxide, 0.5 M sulfuric acid and Milli-Q water (18 MΩ, Millipore Systems) for 2 h and stored in Milli-Q water prior to use.

3.2.2 Synthesis of P(VDF-co-HFP)-*b*-SPS Diblock Ionomers

Diblock ionomers of sulfonated poly([vinylidene difluoride-co-hexafluoropropylene]-*b*-styrene) [P(VDF-co-HFP)-*b*-SPS] were prepared by atom transfer radical polymerization (ATRP) of styrene onto a trichloromethyl- (CCl₃-) terminated fluoropolymer macroinitiator, followed by post-sulfonation (Figure 3.2).^{193, 194}

3.2.2.1 Preparation of P(VDF-co-HFP) Macroinitiator

The CCl₃-terminated P(VDF-co-HFP) macroinitiator was prepared by emulsion copolymerization of vinylidene fluoride (VDF) and hexafluoropropylene (HFP) in the presence of chloroform, which served as a chain transfer agent. A typical procedure for emulsion polymerization is as follows: to an evacuated 160 mL pressure vessel (Parr instruments) equipped with a 600 psi pressure relief valve and a magnetic stir bar, an aqueous solution containing water (100 mL), K₂S₂O₈ (0.80 g), Na₂S₂O₅ (0.58 g), pentadecafluorooctanoic acid (0.04 g), and a

predetermined amount of chloroform was added. An initial monomer mixture of 45 mol% HFP and 55 mol% VDF was introduced into the reactor and the temperature was maintained at 55 °C. A constant pressure of 300 psi was maintained by re-supplying to the vessel a supplemental monomer mixture of 20 mol% HFP and 80 mol% VDF. The polymerization times were varied from 2 to 4 h depending on the amount of chain transfer agent (CHCl₃). The resulting P(VDF-co-HFP) polymer latex was coagulated by freezing, then washed repeatedly with water and ethanol. The crude polymer was purified by dissolution in acetone and precipitation in ethanol, and then dried at 50 °C under vacuum for 24 h. ¹H NMR (500 MHz, d₆-acetone) δ (ppm): 2.8 – 3.5 (head-to-tail VDF sequences, -CF₂-CH₂-CF₂-CH₂*-CF₂-CH₂-), 2.3 – 2.6 (head-to-head or tail-to-tail VDF sequences, -CH₂-CF₂-CF₂-CH₂*-CH₂-CF₂-). ¹⁹F NMR (400 MHz, d₆-acetone) δ (ppm): -71.4 (-CH₂-CF₂-CF(CF₃*)-CF₂-CH₂), -76.0 (-CF₂-CF₂-CF(CF₃*)-CH₂-CF₂), -92.0 to -94.5 (-CF₂-CH₂-CF₂*-CH₂-CF₂), -96.2 (-CF₂-CH₂-CF₂*-CH₂-CH₂), -104.4 (-CF₂-CH₂-CF₂*-CF₂-CF(CF₃)-), -109.7 to -114.5 (-CH₂-CF₂-CF₂*-CH₂-CH₂), -115.5 to -120.0 (-CH₂-CF₂-CF₂*-CF(CF₃)-CH₂), -185.1 (-CF₂-CF*(CF₃)-CF₂- or -CH₂-CF*(CF₃)-CF₂-). The composition of the P(VDF-co-HFP) macroinitiator was estimated by ¹⁹F NMR according to published methods¹⁹⁷ and found to be 16 ± 2 mol% HFP and 84 ± 2 mol% VDF.

3.2.2.2 ATRP of Styrene onto P(VDF-co-HFP) Macroinitiator

Typical procedures for the ATRP reaction were as follows: P(VDF-co-HFP) macroinitiator (0.50 g, M_n = 17 900 Da, 2.8 × 10⁻² mmol), CuCl (0.064 g, 0.65 mmol), 2,2'-bipyridine (0.30 g, 1.9 mmol) and styrene (1.0 mL, 8.7 mmol)

were dissolved in *n*-butyl acetate (3.0 mL) in a dried flask equipped with a rubber septum and a magnetic stir bar. After deoxygenation using three cycles of freeze-pump-thaw, the reaction mixture was heated to 110 °C under a nitrogen blanket for 24 h. The resulting P(VDF-*co*-HFP)-*b*-PS diblock copolymer was purified by dissolving in THF, passing through a column of alumina, precipitating in ethanol and then drying at 50 °C under vacuum for 24 h. ¹H NMR (500 MHz, d₆-acetone) δ (ppm): 6.4 – 7.4 (aryl), 2.8 – 3.5 (methylene, head-to-tail VDF sequences), 2.3 – 2.6 (methylene, head-to-head or tail-to-tail VDF sequence), 1.8 – 2.0 (benzylic), 1.3 – 1.7 (methylene, styrene).

3.2.2.3 Post-sulfonation of Polystyrene Segments

Sulfonation of P(VDF-*co*-HFP)-*b*-PS was carried out in 1,2-dichloroethane according to a procedure reported in the literature,⁵⁶ except a reaction temperature of 40 °C was used. A typical sulfonation reaction is as follows: P(VDF-*co*-HFP)-*b*-PS (0.6 g) and 1,2-dichloroethane (15 mL) were added to a 50 mL three-neck flask equipped with a dropping funnel and condenser. The mixture was heated to 50 °C under nitrogen and stirred until complete dissolution. Acetyl sulfate was prepared by injecting acetic anhydride (1.8 mL) and 1,2-dichloroethane (3.0 mL) into a nitrogen-purged vial. The solution was cooled to ~0 °C in a calcium chloride (CaCl₂, 10 wt%) ice bath after which fuming sulfuric acid (95–97%, 0.6 mL) was injected. The resultant acetyl sulfate was immediately added to the polymer solution at 40 °C. Samples sulfonated to various extents were periodically extracted and precipitated in ethanol/hexanes (50:50, v/v). The precipitate was washed repeatedly with water until the residual

water was pH 7 and then dried under vacuum at 60 °C for 24 h. The ¹H NMR spectra (d₆-acetone) of the sulfonated polymers showed similar signature peaks to that of the pristine polymers, except an additional peak at 7.8 – 7.4 ppm was observed, which is related to aromatic protons adjacent to the sulfonate group.

3.2.3 Membrane Preparation and Characterization

Membranes were prepared by dissolving the sulfonated diblock copolymers in tetrahydrofuran (THF), drop-casting on a levelled Teflon[®] sheet, and immediately covering the film with a petri dish to slow down the solvent evaporation. Polymer membranes were dried at room temperature for 2 h, and then at 60 °C under vacuum for 24 h. The membranes (~100 μm thick) were protonated by immersing in aqueous hydrochloric acid (HCl, 2 M) for 24 h. The protonated membranes were washed several times with Milli-Q water for 30 min periods and stored in water for 24 h to remove excess acid on the surface and the interior of the membranes.

The ion exchange capacities (IEC, mmol/g) were determined by direct titration of the protons released from the membranes in 2 M sodium chloride (NaCl) with standardized sodium hydroxide (NaOH) solutions to the phenolphthalein end-point. The IECs were represented as the millimoles of ionic exchange sites per gram of dry membrane. A detailed description of the method used is presented in Section 2.5.3.

The water uptake was calculated as the percentage increase in mass for a membrane changing from dry to water-saturated state. Water content was

calculated both as a mass and a volume percentage of water in a water-saturated membrane. Water content was also represented as the molar ratio of water to ion exchange sites. This value provided a measure of the average number of water molecules per ion exchange site ($[\text{H}_2\text{O}]/[\text{SO}_3^-]$, referred to as λ value). More detailed descriptions of the above water sorption measurements are given in Section 2.5.2.

The analytical acid concentration was determined as moles of sulfonic acid moieties per unit volume of hydrated membrane, as described in Section 2.5.3.

The *effective* proton mobility (μ_{eff}) was calculated as a normalized proton conductivity where acid concentration effects were removed. A detailed description of the calculation is given in Section 2.5.5.

3.2.4 Instrumentation and Techniques

The molecular weights of the fluororous macroinitiator and the diblock copolymers were estimated by gel permeation chromatography (GPC) using three Waters Styragel HT columns at 25 °C, a Waters 1515 isocratic HPLC pump, THF eluant, a Waters 2414 differential refractometer, and a Waters 2487 dual UV absorbance detector ($\lambda = 254 \text{ nm}$). Polystyrene standards were used for calibration. ^1H NMR spectra (in d_6 -acetone) were recorded on a 500 MHz Varian Inova spectrometer. ^{19}F NMR spectra (in d_6 -acetone) were recorded on a 400 MHz Varian MercuryPlus spectrometer, and chemical shifts were measured with respect to trichlorofluoromethane (CFCl_3).

In-plane and *through*-plane proton conductivities were measured by ac impedance spectroscopy with a Solartron 1260 frequency response analyzer employing a two-electrode configuration, according to a procedure described elsewhere.^{144, 180} A 100 mV sinusoidal ac voltage over a frequency range of 10 MHz to 100 Hz was applied to obtain Nyquist plots. Data was analyzed using commercial Z plot/Z view software (Scribner Associates). A detailed explanation of the method is included in Section 2.5.4. The degree of conductivity anisotropy was calculated as the ratio of in-plane (average of X and Y directions) to through-plane conductivity (Z direction).

Samples for transmission electron microscopy (TEM) were prepared as follows: membranes were stained by immersing in a saturated lead acetate solution for 12 h, then rinsed repeatedly in water, and dried at room temperature under vacuum for 4 h. The stained membranes were embedded in Spurr's epoxy and cured for 6 h at 60 °C. The samples were sectioned to yield slices ~100 nm thick using a Leica UC6 ultramicrotome and picked up on copper grids. Electron micrographs were taken with a Hitachi H7600 TEM using an accelerating voltage of 80 kV.

3.3 Results and Discussion

3.3.1 Synthesis of P(VDF-co-HFP)-*b*-SPS Diblock Ionomers

Diblock ionomers of sulfonated poly([vinylidene difluoride-co-hexafluoropropylene]-*b*-styrene) [P(VDF-co-HFP)-*b*-SPS] were synthesized according to Figure 3.2.^{193, 194} The synthesis involved three steps: 1) preparation

of CCl_3 -terminated fluoropolymer macroinitiator, 2) atom transfer radical polymerization (ATRP) of styrene onto the macroinitiator to yield P(VDF-co-HFP)-*b*-PS diblock copolymers, and 3) post-sulfonation to confer sulfonic acid ($-\text{SO}_3\text{H}$) groups onto the polystyrene segment.^{193, 194} The ionicity, and thus ion exchange capacity (IEC), of the P(VDF-co-HFP)-*b*-SPS diblock copolymers were controlled either by varying the length of a fully sulfonated polystyrene block, or by varying the degree of sulfonation on a fixed polystyrene segment. In the former case, the fully sulfonated polystyrene block was kept relatively short compared to the hydrophobic fluorous block in order to yield water-insoluble diblock copolymers.

The CCl_3 -terminated fluoropolymers of vinylidene difluoride (VDF) and hexafluoropropylene (HFP) were obtained from emulsion copolymerization in the presence of chloroform as the chain transfer agent. The mechanism for the chain transfer polymerization is shown in Figure 3.4. In order to prepare fluorous macroinitiator possessing both H- and CCl_3 -termini, it was desired that monomer polymerization be initiated by CCl_3^\bullet radicals rather than persulfate radicals. This can be achieved, as previously demonstrated by Shi *et al.*,¹⁹³ by having the concentration of CHCl_3 much higher than dissolved monomer so that persulfate radicals, produced by thermolysis, preferentially abstract H atoms from CHCl_3 , forming CCl_3^\bullet . Furthermore, due to the typically low concentration of radicals found in radical polymerization, the concentration of CHCl_3 was intended to be significantly higher than either CCl_3^\bullet or polymer radicals so that propagating

radicals are primarily terminated by H atom abstraction from CHCl_3 rather than by radical-radical coupling.

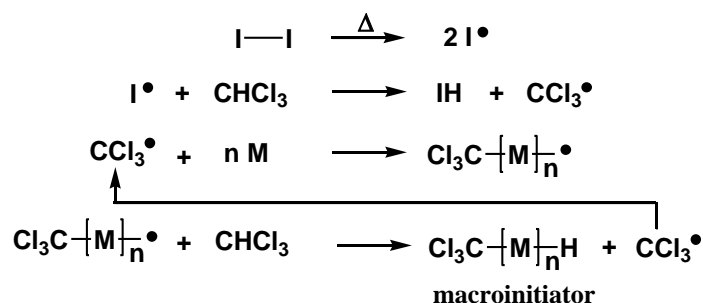


Figure 3.4 Mechanism of chain transfer polymerization initiated by CCl_3^\bullet radicals (I = initiator; M = monomer).

A typical ^1H NMR spectrum of a P(VDF-co-HFP) macroinitiator is shown in Figure 3.5a. Peaks at 2.8 – 3.5 ppm (peak a) correspond to head-to-tail structures of VDF sequences, whereas peaks observed between 2.3 – 2.6 ppm (peak a') are due to head-to-head or tail-to-tail structures.¹⁹³ The presence of the $-\text{CCl}_3$ terminal group on the macroinitiator was also confirmed by ^1H NMR: the small peaks at 3.7 – 3.8 ppm (peak i, see inset) are due to CCl_3 -related structures of $-\text{CH}_2^*-\text{CF}_2-\text{CCl}_3$ or $-\text{CF}_2-\text{CH}_2^*-\text{CCl}_3$; small peaks at 6.2 – 6.4 ppm (peak j) are due to H-terminated chains with structures of $-\text{CF}_2-\text{CH}_2-\text{CF}_2\text{H}^*$ or $-\text{CH}_2-\text{CH}_2-\text{CF}_2\text{H}^*$. The ratio of integrals of peaks i to j provides an estimation of the ratio of CCl_3 - to H-terminated chain ends. This ratio was typically found to be 0.85 ± 0.15 , which suggests that one terminal group is not in large excess of the other. Moreover, no signals related to persulfate-terminus (i.e., $\text{KO-SO}_2\text{-O-CH}_2^*-\text{CF}_2$ -, typically found at 4.5 – 5.0 ppm) were observed. This further indicates that the emulsion polymerization was initiated primarily by CCl_3^\bullet radicals rather than persulfate radicals.

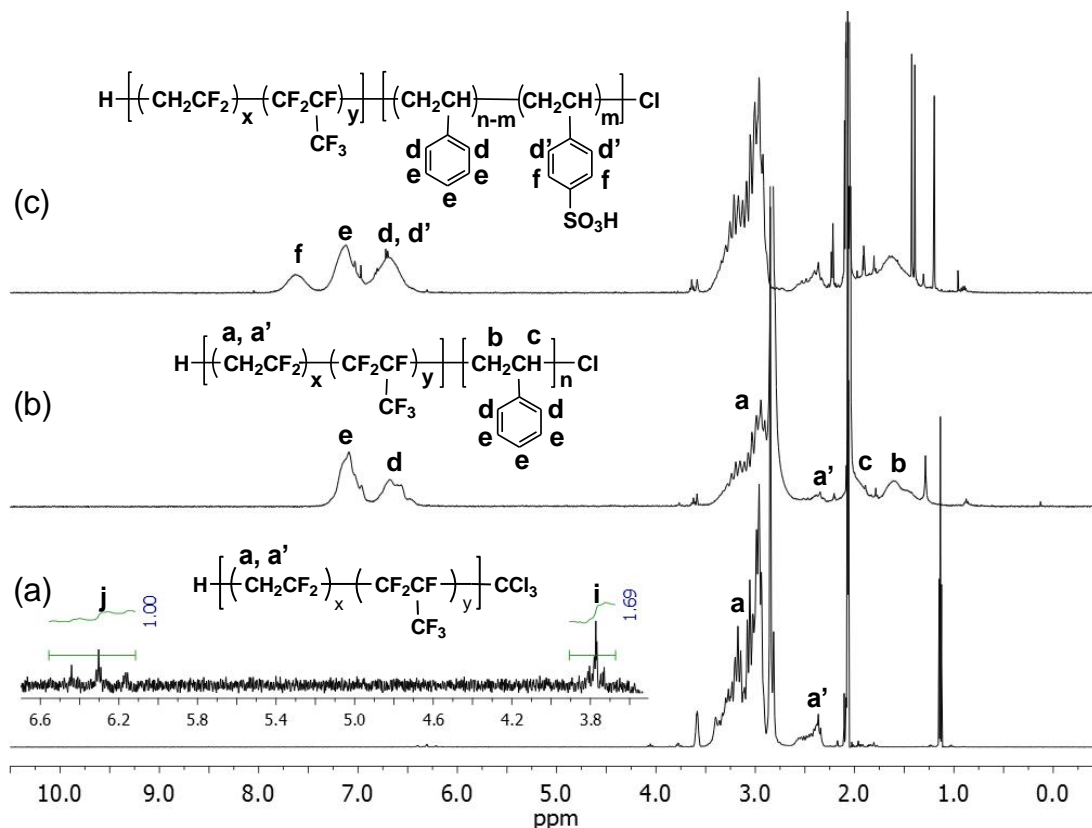


Figure 3.5 ^1H NMR spectra (d_6 -acetone) of (a) P(VDF-co-HFP), (b) P(VDF-co-HFP)-b-PS, and (c) partially sulfonated P(VDF-co-HFP)-b-SPS (DS = 37%).

The compositions of the P(VDF-co-HFP) macroinitiators were determined by ^{19}F NMR spectroscopy (Figure 3.6), as previously described.¹⁹⁷ Peaks at -70 to -80 ppm (peak a) are due to $-\text{CF}_3$ units of HFP, while peaks at -180 to -185 ppm (peak c) are related to $-\text{CF}$ units of HFP. Peaks at -90 to -125 ppm (peak b) are due to the $-\text{CF}_2$ units of both VDF and HFP. The compositions of the P(VDF-co-HFP) macroinitiator were estimated using Equation 3.1:

$$\frac{\text{VDF}}{\text{HFP}} = \frac{B/2 - C}{C} \quad \text{Equation 3.1}$$

where B and C are the integrals of peaks b and c in Figure 3.6, respectively. The monomer compositions of the macroinitiators were typically found to be 84 ± 3

mol% of VDF and 16 ± 2 mol% of HFP. The incorporation of HFP comonomers was intended to disrupt its crystallinity, and thus improve its solubility in common solvents.

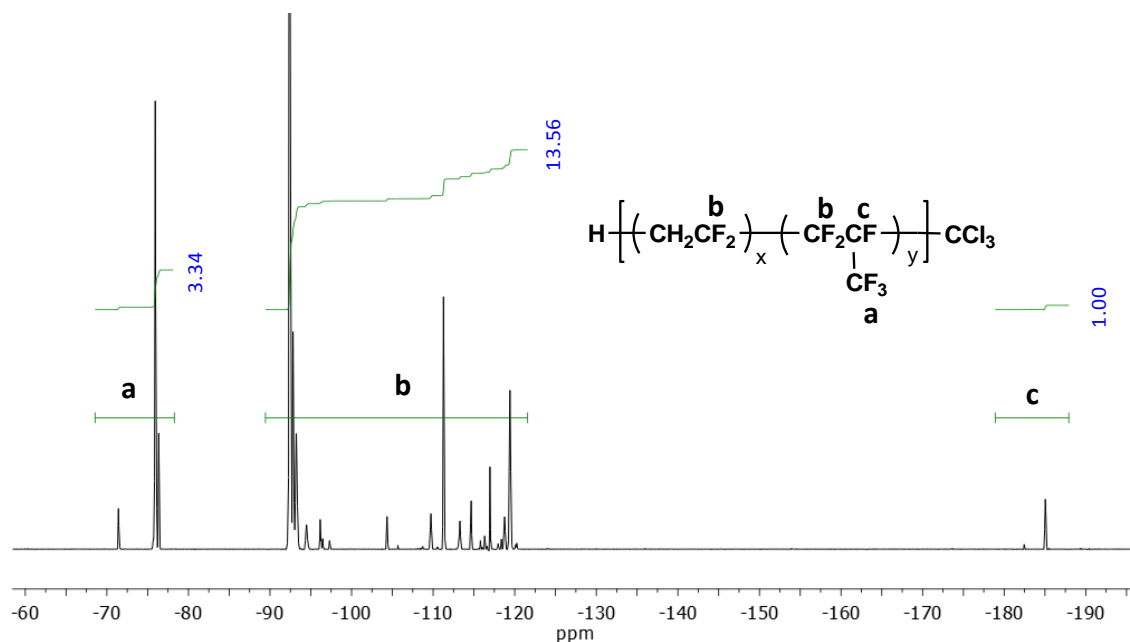


Figure 3.6 ^{19}F NMR spectrum (d_6 -acetone) of P(VDF-co-HFP) macroinitiator.

ATRP of styrene was initiated by the P(VDF-co-HFP) macroinitiator to yield diblock copolymers of P(VDF-co-HFP)-*b*-PS. Gel permeation chromatograms (GPCs) of P(VDF-co-HFP) macroinitiator and its resulting diblock copolymers are shown in Figure 3.7. After ATRP, the peak is shifted to a higher molecular weight, indicating the polymerization of styrene onto the macroinitiator. The unimodal GPC peak of the diblock copolymer indicates that the $-\text{CCl}_3$ terminus of the macroinitiator is a single initiator unit, i.e., no double or triple initiation, which is consistent with previous reports on CCl_3 -terminated macroinitiators.¹⁹⁸⁻²⁰⁰

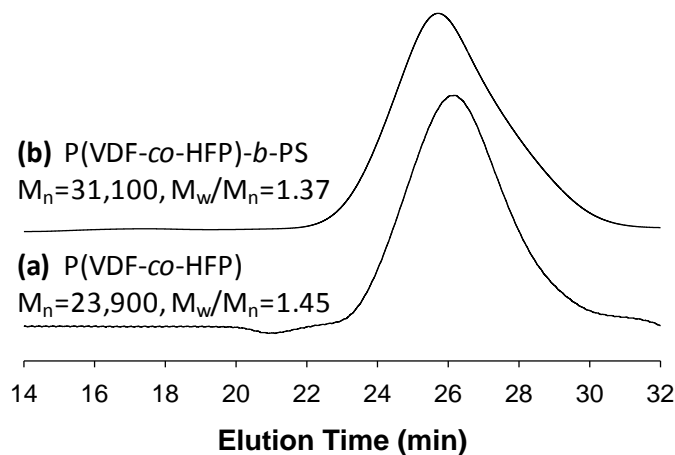


Figure 3.7 GPC traces of (a) P(VDF-co-HFP) macroinitiator, and (b) P(VDF-co-HFP)-b-PS diblock copolymer.

As shown in Figure 3.5b, the ^1H NMR spectrum of the P(VDF-co-HFP)-b-PS diblock copolymer possesses additional peaks at 1.3 – 1.7 ppm (peak b, methylene, 2H), 1.8 – 2.0 ppm (peak c, benzylic, 1H), and 6.4 – 7.4 ppm (peaks d and e, aryl, 5H), which further indicates the successful polymerization of styrene onto the macroinitiator. Quantitative analysis of the styrene units is obtained by the ratio of integrated signals due to the aromatic styrenic protons (peaks d and e) and the methylene protons of VDF (peaks a and a'), as follows:

$$\frac{\text{St}}{\text{VDF}} = \frac{D + E}{A + A'} \times \frac{2}{5} \quad \text{Equation 3.2}$$

where D, E, A and A' are the integrals of peaks d, e, a and a' in Figure 3.5b, respectively. The molecular weights of the diblock estimated from NMR spectroscopy were comparable to those estimated using GPC data, as listed in Table 3.1.

Table 3.1 Chemical Compositions of Macroinitiator, P(VDF-co-HFP)-*b*-PS and Sulfonated P(VDF-co-HFP)-*b*-SPS

Diblock copolymer	P(VDF-co-HFP) macroinitiator		P(VDF-co-HFP)- <i>b</i> -PS					P(VDF-co-HFP)- <i>b</i> -SPS	
	M _{n,GPC} ^a (Da)	DP _(VDF+HFP) ^b	M _{n,GPC} ^a (Da)	M _{n,NMR} ^d (Da)	M _{n,NMR (PS)} ^e (Da)	DP _(St) ^f	Vol% PS ^g	DS (%) ^h	Vol% sulfonated PS ⁱ
1	24 300	316	N/A ^c	25 200	900	9	6	100	8
2	24 300	316	N/A ^c	25 600	1 300	13	8	100	10
3	24 300	316	N/A ^c	26 100	1 800	17	11	100	14
4	24 300	316	N/A ^c	26 400	2 100	20	13	100	16
5	24 300	316	26 200	27 200	2 900	28	17	100	21
6	23 900	310	29 900	31 400	7 500	72	35	16 – 41	36 – 38
7	17 900	233	25 300	26 000	8 100	78	45	12 – 49	46 – 48
8	12 100	168	18 700	19 200	7 100	68	50	35	52

^a Measured by THF-GPC, calibrated with linear PS standards.

^b Combined degree of polymerization of VDF and HFP, calculated using M_{n,GPC} [P(VDF-co-HFP)] and the ratio of VDF/HFP from ¹⁹F-NMR.

^c Increase in molecular weight could not be accurately measured by GPC.

^d Calculated using M_{n,GPC} [P(VDF-co-HFP)] and the ratio of St/VDF from ¹H-NMR.

^e Molecular weight of the polystyrene segment, calculated from the difference between M_{n,NMR} [P(VDF-co-HFP)-*b*-PS] and M_{n,GPC} [P(VDF-co-HFP)].

^f Degree of polymerization of styrene, calculated from M_{n,NMR (PS)}.

^g Volume percentage of polystyrene in the diblock copolymer, calculated according to Eq (3.3).

^h Degree of sulfonation, calculated from ¹H-NMR.

ⁱ Volume percentage of styrenic segment in the sulfonated diblock, calculated by assuming that the incorporation of a -SO₃H group increases the volume of each styrene unit by 30%.

The volumes of the fluororous and the styrenic segments were estimated using their respective density (1.78 g/cm³ for P(VDF-co-HFP) and 1.05 g/cm³ for polystyrene).¹⁹⁶ The volume percentage of polystyrene (vol% PS) was calculated as follows:

$$\text{vol\% PS} = \frac{\frac{M_{n,\text{NMR (PS)}}}{\rho_{\text{PS}}}}{\frac{M_{n,\text{NMR (PS)}}}{\rho_{\text{PS}}} + \frac{M_{n,\text{GPC(P(VDF-co-HFP))}}}{\rho_{\text{P(VDF-co-HFP)}}}} \quad \text{Equation 3.3}$$

where $M_{n,\text{NMR (PS)}}$ and $M_{n,\text{GPC (P(VDF-co-HFP))}}$ are the number-average molecular weights of the polystyrene and the fluororous segments, respectively; ρ_{PS} and $\rho_{\text{P(VDF-co-HFP)}}$ are their respective densities. The estimated volume percentages of polystyrene in the unsulfonated diblock copolymers are listed in Table 3.1. The volume percentages based on sulfonated polystyrene were also considered: Using spacing-filling model software,⁸¹ it was estimated that addition of a sulfonic acid group would increase the volume of a *single* styrene unit by ~30%. For the P(VDF-co-HFP)-*b*-PS diblock copolymers, complete sulfonation of the polystyrene blocks was estimated to increase the volume percentages of the styrenic portion of the entire diblock by 2 – 4 vol% (see last column in Table 3.1). In the case of partial sulfonation of the polystyrene blocks, sulfonation increases the volume percentages by only 1 – 3 vol%. Thus, changes in non-fluorous volume fraction due to the incorporation of –SO₃H groups is very small, and can be neglected.

P(VDF-co-HFP)-*b*-PS parent diblock copolymers, possessing 6, 8, 11, 13, 17, 35, 45 and 50 vol% PS, were systematically prepared and their compositions

described in Table 3.1. For parent diblocks with low PS content (6 – 17 vol%), the polystyrene segments were *fully* sulfonated. Collectively, these yield a series of proton-conducting membranes in which the ionic content is controlled by varying the length of the fully sulfonated polystyrene block, as illustrated in Figure 3.3a. On the other hand, for the parent diblocks with higher polystyrene contents (35, 45 and 50 vol% PS), complete sulfonation of the polystyrene segments leads to water-soluble polymers; thus, these diblocks were *partially* sulfonated to provide membranes with different ionicity, as illustrated in Figure 3.3b and 3.3c. In these membranes series, IEC was controlled by varying the degree of sulfonation on a fixed polystyrene block length. The 50 vol% PS diblock possessed a relatively short fluororous segment ($DP_{(VDF+HFP)} = 168$) compared to the 35 and 45 vol% PS diblocks ($DP_{(VDF+HFP)} \sim 250-300$) in order to yield a high PS content diblock. Only one IEC sample is reported for the 50 vol% PS diblock (Figure 3.3d).

A typical ^1H NMR spectrum of a partially sulfonated diblock copolymer is given in Figure 3.5c. The peak at 6.8 – 7.4 ppm (peak e) is due to *meta*- and *para*- protons on the non-sulfonated styrene units, whereas the peak at 7.4 to 7.8 ppm (peak f) is assigned to aromatic protons adjacent to the sulfonate groups. The degree of polymerization (DS, %) is estimated using the ratio of integrals for peaks e and f, as follows:

$$DS(\%) = \frac{\frac{F}{2}}{\frac{F}{2} + \frac{E}{3}} \times 100\% \quad \text{Equation 3.4}$$

where E and F represent the integrals of peaks e and f in Figure 3.5c, respectively.

The chemical compositions, degrees of sulfonation and IECs for the sulfonated P(VDF-co-HFP)-*b*-SPS membranes are summarized in Table 3.2. For ease of discussion, the membrane series are referred to their PS content: 6 – 17, 35, 45 and 50 vol% PS, and to the degree of sulfonation: *fully* or *partially* sulfonated. Following protonation to their acidic forms, the membranes' nanostructure, water sorption, proton conductivity, and acid concentration were examined; the data are summarized in Table 3.3.

Table 3.2 Chemical Compositions of P(VDF-co-HFP)-*b*-SPS Membranes Studied

Series	Membrane	M_n (fluorous) ^a (Da)	M_n (PS) ^b (Da)	DS ^c (%)	IEC ^d (mmol/g)
6 – 17 vol% PS, fully sulfonated	1 – 1		900		0.34 ± 0.02
	1 – 2		1 300		0.46 ± 0.01
	1 – 3	24 300	1 800	100	0.64 ± 0.02
	1 – 4		2 100		0.70 ± 0.04
	1 – 5		2 900		1.20 ± 0.03
35 vol% PS, partially sulfonated	2 – 1			16 ± 1	0.31 ± 0.02
	2 – 2			21 ± 2	0.42 ± 0.01
	2 – 3	23 900	7 500	27 ± 1	0.52 ± 0.02
	2 – 4			32 ± 2	0.59 ± 0.02
	2 – 5			37 ± 3	0.68 ± 0.02
	2 – 6			41 ± 2	0.73 ± 0.03
45 vol% PS, partially sulfonated	3 – 1			12 ± 2	0.26 ± 0.01
	3 – 2			17 ± 1	0.53 ± 0.02
	3 – 3	17 900	8 100	22 ± 3	0.72 ± 0.05
	3 – 4			32 ± 2	0.89 ± 0.03
	3 – 5			40 ± 3	1.18 ± 0.05
	3 – 6			49 ± 2	1.31 ± 0.05
50 vol% PS, partially sulfonated	4 – 1	12 100	7 100	35 ± 3	1.09 ± 0.05

^a Molecular weight of the fluororous segment, measured by THF-GPC using linear PS standards.

^b Molecular weight of the polystyrene segment, estimated using the ratio of St/VDF from ¹H NMR.

^c Based on ¹H NMR according to Eq 3.12.

^d Measured by acid-base titration.

Table 3.3 Properties of Various Series of P(VDF-co-HFP)-*b*-SPS Diblock Copolymer Membranes

Series	Membrane	IEC ^a (mmol g ⁻¹)	Conductivity ^b (S cm ⁻¹)	Water Content ^c (wt %)	Water Uptake ^c (wt %)	λ	[-SO ₃ H] ^d (M)	X _v (by vol)	$\mu_{eff} \times 10^3$ (cm ² s ⁻¹ V ⁻¹)
6 – 17 vol% PS, fully sulfonated	1 – 1	0.34 ± 0.02	0.001 ± 0.001	19 ± 1	23 ± 1	39 ± 1	0.41 ± 0.02	0.28	0.03
	1 – 2	0.46 ± 0.01	0.006 ± 0.002	20 ± 1	25 ± 2	28 ± 4	0.59 ± 0.03	0.32	0.11
	1 – 3	0.64 ± 0.02	0.023 ± 0.001	27 ± 1	38 ± 2	32 ± 2	0.65 ± 0.02	0.39	0.37
	1 – 4	0.70 ± 0.04	0.028 ± 0.002	33 ± 1	50 ± 2	39 ± 1	0.64 ± 0.03	0.46	0.45
	1 – 5	1.20 ± 0.03	0.11 ± 0.003	61 ± 1	154 ± 3	68 ± 2	0.65 ± 0.03	0.83	1.75
35 vol% PS, partially sulfonated	2 – 1	0.31 ± 0.02	0.002 ± 0.001	5 ± 1	5 ± 1	9 ± 1	0.41 ± 0.01	0.08	0.05
	2 – 2	0.42 ± 0.01	0.009 ± 0.001	8 ± 1	9 ± 1	12 ± 2	0.56 ± 0.03	0.14	0.17
	2 – 3	0.52 ± 0.02	0.023 ± 0.001	12 ± 2	13 ± 3	15 ± 3	0.65 ± 0.02	0.18	0.36
	2 – 4	0.59 ± 0.02	0.042 ± 0.001	21 ± 2	26 ± 2	25 ± 2	0.67 ± 0.02	0.30	0.65
	2 – 5	0.68 ± 0.02	0.049 ± 0.002	33 ± 1	48 ± 1	40 ± 1	0.61 ± 0.02	0.41	0.83
	2 – 6	0.73 ± 0.03	0.036 ± 0.001	40 ± 1	66 ± 1	50 ± 1	0.55 ± 0.02	0.50	0.68
45 vol% PS, partially sulfonated	3 – 1	0.26 ± 0.01	0.001 ± 0.001	1 ± 1	1 ± 1	2 ± 1	0.33 ± 0.03	0.02	0.03
	3 – 2	0.53 ± 0.02	0.003 ± 0.001	2 ± 1	2 ± 1	3 ± 1	0.61 ± 0.02	0.02	0.05
	3 – 3	0.72 ± 0.05	0.016 ± 0.002	12 ± 2	14 ± 3	11 ± 1	0.77 ± 0.03	0.15	0.22
	3 – 4	0.89 ± 0.03	0.055 ± 0.001	28 ± 3	38 ± 3	24 ± 2	0.86 ± 0.10	0.37	0.66
	3 – 5	1.18 ± 0.05	0.080 ± 0.002	47 ± 2	89 ± 7	42 ± 6	0.69 ± 0.04	0.52	1.20
	3 – 6	1.31 ± 0.05	0.076 ± 0.002	80 ± 2	388 ± 10	165 ± 1	0.32 ± 0.03	0.95	2.46
50 vol% PS, partially sulfonated	4 – 1	1.09 ± 0.05	0.050 ± 0.004	36 ± 3	56 ± 7	28 ± 3	0.88 ± 0.03	0.45	0.59

^a Measured by acid-base titration. ^b Measured by AC impedance spectroscopy at room temperature and fully hydrated. ^c At room temperature. ^d Analytical acid concentration in a fully hydrated membrane.

3.3.2 TEM

The nanostructure and morphology of the membranes were investigated using transmission electron microscopy (TEM) on cross-sectional slices (~100 nm) of dry membranes. Membranes were stained with lead acetate prior to imaging, therefore the dark areas in the TEMs correspond to regions of high ionic content. TEM images of selected membranes from the 6 – 17 vol% PS, fully sulfonated series are shown in Figure 3.8 A, B and C. No ion phase separation morphology is observed for the membrane possessing the lowest IEC of 0.07 mmol/g (not shown). With increasing IEC (>0.40 mmol/g), a phase-separated morphology characterized by disordered ionic clusters is observed (Figure 3.8 A, B and C). The size of the ion clusters (dark domains) is found to increase from 6 to 20 nm as IEC increases from 0.40 to 1.13 mmol/g, and is attributed to the increasing length of the fully sulfonated polystyrene segment, which leads to enhanced phase separation and aggregation of larger ionic clusters. Similar trends in ionic domain size have been previously reported by other groups.^{161, 162} Using graft copolymers comprising of polystyrene main chain and ionic polystyrene sulfonic acid graft chains (PS-*g*-PSSA), it is reported that ionic cluster size and the degree of phase separation increases as the length of the PSSA graft chains increase.¹⁶¹

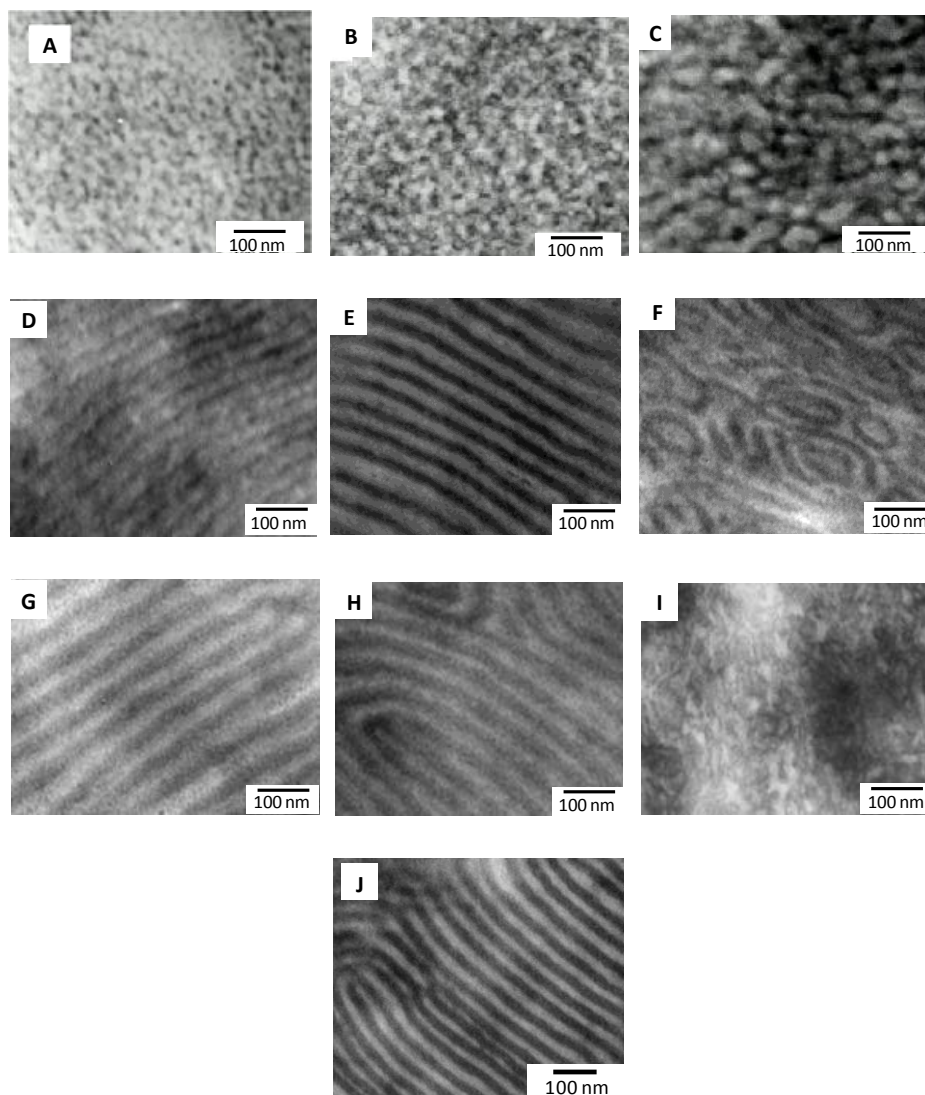


Figure 3.8 TEM images of selected P(VDF-co-HFP)-*b*-SPS membranes from: the 6 – 17 vol% PS series with IECs (mmol/g) of (A) 0.46, (B) 0.70, (C) 1.20; the 35 vol% PS series with IECs of (D) 0.42, (E) 0.68, (F) 0.73; the 45 vol% PS series with IECs of (G) 0.62, (H) 0.89, (I) 1.31; and the 50 vol% PS with IEC of (J) 1.09.

In general, ordered lamellar-like morphologies are observed in partially sulfonated membranes, with low to intermediate IEC, for the 35 (Figure 3.8 D, E), 45 (Figure 3.8 G, H), and 50 vol% PS (Figure 3.8 J) series. These morphologies are consistent with the morphological phase diagram reported for diblock copolymers of poly(styrene-*b*-isoprene) (Figure 3.1), in which pure lamellar structures have been observed for 35 to 65 vol% PS block fractions.^{188, 201} In the

present work, clear signs of phase separation are observed for the 35 vol% PS series even for the lowest IEC sample (0.31 mmol/g, not shown). As IEC increases (from 0.42 to 0.68 mmol/g, Figure 3.8 D and E), phase separation becomes more distinct, and the interface, sharper. The width of the ionic lamellae is ~15 – 20 nm and the inter-domain spacing, ~20 – 40 nm. For higher IEC membranes (e.g., 0.73 mmol/g, DS = 41%, Figure 3.8 F), the morphology becomes disordered. Changes in morphology with sulfonation have been reported in other sulfonated block copolymer systems. For instance, using sulfonated poly(styrene-*b*-isobutylene-*b*-styrene) triblock copolymers (31 wt% PS), Elabd *et al.*⁷⁴ observed a morphological transition from periodic lamellar at IEC < 1.0 mmol/g (DS < 40%) to a non-periodic co-continuous morphology at IECs of 1.1 – 2.0 mmol/g (DS > 40%). The work of Mauritz *et al.*⁶⁸ on sulfonated poly(styrene-*b*-[ethylene-*r*-butylene]-*b*-styrene) revealed morphological transitions from hexagonally packed cylinders to lamellae as the degree of sulfonation on the polystyrene segments increases from 0 to 12%. A few mechanisms have been proposed for the morphological shift with sulfonation in block ionomers.^{68, 74, 202} The presence of strong dipole and electrostatic interactions between the ionic moieties may cause significant changes in the chain conformation of the sulfonated block, leading to shifts in phase behaviour.⁷⁴ Other mechanisms suggested include increased differential solubility parameter and Flory-Huggin segmental interaction parameter (χ) between the sulfonated and unsulfonated blocks,²⁰² as well as increased interfacial surface tension

between the phases leading to a shift toward structures with minimized interfacial surface area.^{68, 203}

TEM micrographs of partially sulfonated membranes for the 45 vol% PS series with IECs of 0.62 and 0.89 mmol/g are shown in Figures 3.8 G and H, respectively. The width of the ionic lamellae phase is found to be 20 – 30 nm, i.e., larger than the 35 vol% PS membranes; but possessing a inter-domain spacing of 20 – 40 nm, which is similar to the 35 vol% PS membranes. A disordered morphology is observed for high IEC membranes (1.31 mmol/g, Figure 3.8 I). For the 50 vol% PS membrane possessing an IEC of 1.09 mmol/g (Figure 3.8 J), the width of the ionic lamellae is found to be 15 – 20 nm with a fluorocarbon inter-domain spacing of 10 – 25 nm. The fluorocarbon and ionic domains are narrower compared to the 35 vol% and 45 vol% PS membranes, due to both the shorter fluororous and ionic segments in the 50 vol% PS membrane.

Although the TEM images shown above are for dry membranes, the morphology is expected to be preserved in the water-swollen membranes, as evidenced in our previous study.¹⁹⁶ Small-angle neutron scattering analysis of P(VDF-co-HFP)-*b*-SPS membranes showed that, upon hydration, the overall morphology of the membranes is maintained, but the dimensions of lamellar spacing vary accordingly.¹⁹⁶

3.3.3 Water Sorption

The water sorption properties of the membranes in the protonic form are expressed both as water content and molar ratio of water to sulfonic acid

($[\text{H}_2\text{O}]/[\text{SO}_3^-]$, λ). Water content and λ versus IEC are plotted in Figure 3.9 (that for Nafion 117, IEC = 0.91 mmol/g, is also plotted for comparison). As expected, water sorption increases with IEC for all membrane series.

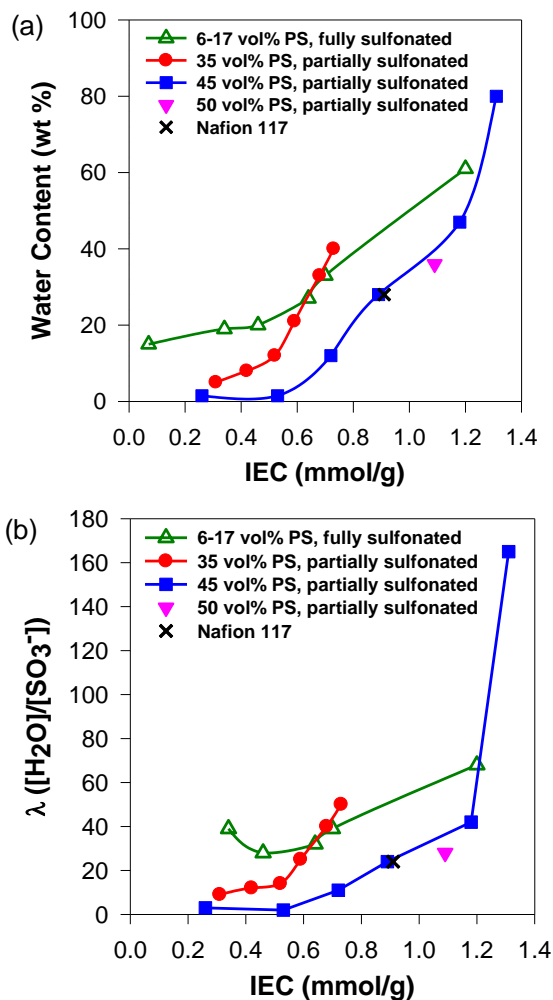


Figure 3.9 (a) Water content vs. IEC and (b) λ vs. IEC for P(VDF-co-HFP)-*b*-SPS membranes with 6 – 17 (Δ), 35 (\bullet), 45 (\blacksquare) and 50 vol% (\blacktriangledown) polystyrene. Note: open symbols represent fully sulfonated membranes; filled symbols, partially sulfonated.

Considerable differences are found in water sorption behaviour between different series of membranes. In the low IEC range (< 0.6 mmol/g), the partially sulfonated membranes (i.e., 35 and 45 vol% PS) absorb significantly less water than the fully sulfonated membranes (6 – 17 vol% PS). For instance, for an IEC

range of 0.3 to 0.6 mmol/g, water contents are found to be 2 – 12 and 5 – 21 wt% for the 35 and 45 vol% PS membranes, respectively; whereas the water content is 19 – 27 wt% for the fully sulfonated 6 – 17 vol% PS membranes. The lower water uptake in the former is attributed to the PS segment being only partially sulfonated. A neutron scattering study¹⁹⁶ on partially sulfonated P(VDF-co-HFP)-*b*-SPS membranes reveals a hierarchical membrane microstructure, involving two levels of phase separation, as illustrated in Figure 3.10. At one level of phase separation (Figure 3.10a), the hydrophobic fluoropolymer segment segregates from the partially sulfonated PS segment forming alternating fluorocarbon and ionic PS domains; but within the ionic PS domain (Figure 3.10b), a sub-level of phase separation exists in which ionic aggregates of PSSA are formed in a matrix of the PS host, similar to that found in randomly sulfonated polystyrene (PS-*r*-PSSA).^{58, 204, 205} The hydrophobic polystyrene matrix opposes water swelling. In contrast, for the 6 – 17 vol% PS membranes, the polystyrene matrix is fully sulfonated and swells considerably for low IEC membranes.

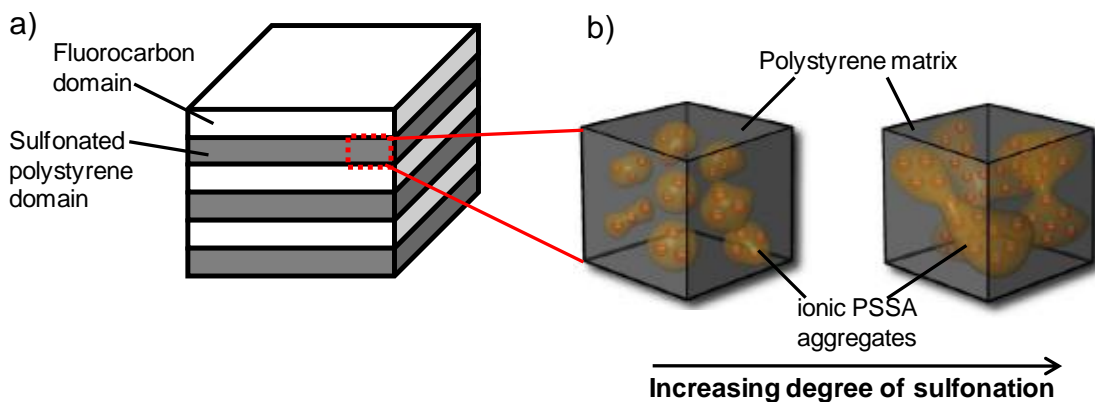


Figure 3.10 Schematic representation of the hierarchical microstructure in P(VDF-co-HFP)-*b*-SPS: a) The large scale morphology consists of stacks of alternating fluorocarbon and sulfonated polystyrene domains. b) Within the sulfonated polystyrene domains, formation of ionic aggregates of sulfonated polystyrene (PSSA) in a matrix of host polystyrene.

As IEC is increased above 0.6 mmol/g, the water sorption of all the membrane series is observed to increase significantly (Figure 3.9). For the partially sulfonated 35 and 45 vol% PS membranes, water sorption shows a slower rate of increase with IEC initially, followed by a sharp increase, indicative of reaching a percolation of ionic domains, as illustrated in Figure 3.10: For low ion contents, or low degrees of sulfonation, the ionic purity within the ionic domains is low – i.e., the ionic PS domains contain mostly of non-sulfonated PS matrix. Both the number and the size of the ionic clusters are small and they remain relatively isolated and thus, water uptake is low. With increasing degrees of sulfonation, the ionic purity and the cluster size increase, leading to increasing amounts of water absorbed; eventually, an interconnected network of ionic clusters is formed for which water uptake increases dramatically. Despite the fully sulfonated 6 – 17 vol% PS membranes exhibiting relatively large water sorption at low IEC ranges, they do not exhibit a threshold effect and water swelling is less sensitive to changes in IEC. This is attributed to the formation of smaller short-range ionic domains (Figure 3.8 A, B and C), which allows for a greater continuity in the hydrophobic fluorocarbon matrix which resists osmotic pressure-driven swelling.

Comparisons between the different series of partially sulfonated membranes reveals that water sorption decreases with increasing PS content in the membranes. For instance, over the IEC range, 0.5 – 0.7 mmol/g, the water content is 12 – 33 and 2 – 12 wt% for 35 and 45 vol% PS membranes, respectively; and for IEC of ~1.1 mmol/g, the water content is 47 and 36 wt% for

the 45 and 50 vol% PS membranes, respectively. That is, for a given IEC, water content decreases in the order of 35 > 45 > 50 vol% PS. To achieve an IEC of ~0.7 mmol/g, the 35 vol% PS polymer membrane requires a degree of sulfonation (DS) of ~40%; whereas the 45 vol% PS membrane requires only ~20% DS (Table 3.2). The higher degree of sulfonation reduces the proportion of hydrophobic PS and allows for closer proximity between the sulfonic acid, which may lead to the formation of larger ionic aggregates and enhanced percolation of ionic cluster networks. Membranes with high PS content require relatively low degrees of sulfonation; thus, the ionic purity within the ionic PS domains is low and the larger distances between sulfonic acid groups restrict the formation of an interconnected ionic cluster network. Simply put, high PS content membranes are less prone to water swelling, which significantly impacts proton transport within them.

3.3.4 Proton Conductivity

In-plane proton conductivities versus IEC for various membrane series are plotted in Figure 3.11a. For the 35 and 45 vol% PS membranes, conductivities increase initially with IEC, and decrease with further increases. A plot of acid concentration in hydrated membranes as a function of IEC is shown in Figure 3.11c. For the partially sulfonated 35 and 45 vol% PS membranes, the $[-\text{SO}_3\text{H}]$ initially increases with IEC but dilution occurs with further increases. These trends are consistent with the water sorption behaviour, as shown in Figure 3.9: For the 35 and 45 vol% PS membranes, water sorption increases sharply above IEC values of 0.5 and 0.7 mmol/g, respectively. Thus, the drop in proton

conductivity observed for high IEC membranes is due to acid dilution caused by excessive water uptake, as reported for other sulfonated polystyrene-based copolymer systems.^{61, 71, 76, 162, 206, 207}

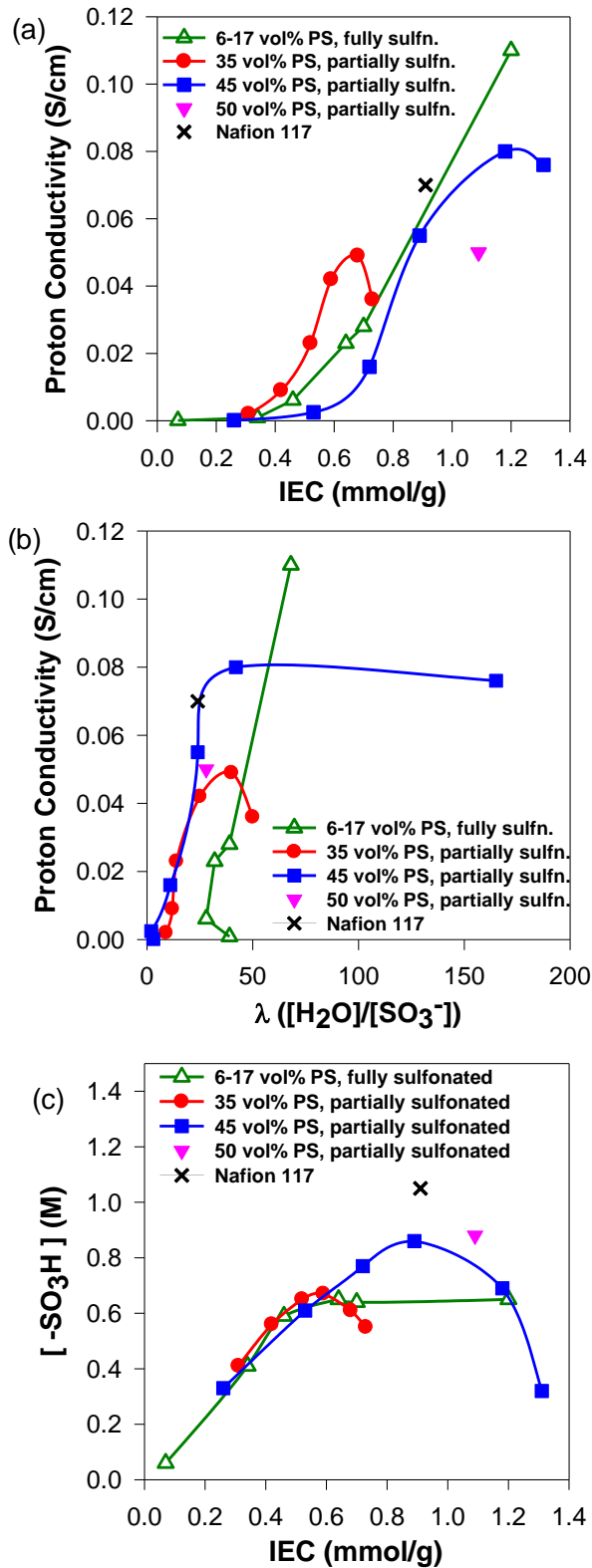


Figure 3.11 (a) Proton conductivity vs. IEC, (b) proton conductivity vs. λ , and (c) $[-SO_3H]$ vs. IEC for P(VDF-co-HFP)-*b*-SPS membranes with 6 – 17 (Δ), 35 (\bullet), 45 (\blacksquare) and 50 vol% (\blacktriangledown) polystyrene. Note: open symbols represent fully sulfonated membranes; filled symbols, partially sulfonated.

The fully sulfonated, 6 – 17 vol% PS membranes exhibit a continuous increase in proton conductivity over the range of IEC studied (Figure 3.11a), and possess a proton conductivity of 0.11 S cm^{-1} at an IEC of 1.20 mmol/g – the highest value observed in this study. Water sorption in the 6 – 17 vol% PS membranes is relatively less sensitive to changes in IEC compared to the other membrane series (Figures 3.9), which enables these membranes to maintain a reasonably high $[-\text{SO}_3\text{H}]$, which remains constant at $\sim 0.6 \text{ M}$ for IECs $> 0.4 \text{ mmol/g}$ (Figure 3.11 c).

Comparisons between partially sulfonated membranes with different PS contents reveal that membranes with lower PS content possess a lower IEC threshold beyond which conductivity increases sharply with IEC (Figure 3.11a). For the 35 and 45 vol% PS membrane series, the threshold is ~ 0.4 and $\sim 0.7 \text{ mmol/g}$, respectively. Over a similar IEC range of 0.3 to 0.7 mmol/g , the 35 vol% PS membranes exhibit higher proton conductivities than the 45 vol% PS membranes. A lower percolation threshold and greater proton conductivity in the 35 vol% PS membranes are due to the relatively higher degree of sulfonation. As discussed previously, a higher degree of sulfonation results in closer spacing, and therefore greater electrostatic attraction, between neighbouring sulfonic acid groups, which in turn, leads to the formation of larger ionic clusters and a more extensive percolated ionic network.

It is reported that perfluorosulfonic acid ionomer membranes show a significant increase in proton conductivity when $\lambda > 6$.²⁰⁸ Figure 3.11b shows the relationship between proton conductivity as a function of water content (λ). For λ

values of 10 – 20, the partially sulfonated, 35 and 45 vol% PS membranes exhibit a similar proton conductivity. However, for λ values between 20 and 40, the ordering of conductivity is $45 > 35 > 6 - 17$ vol% PS. The maximum proton conductivity value occurs when $\lambda \sim 40$ for both the 35 and 45 vol% PS membranes, and conductivity drops with further increases in λ (> 40). Similar observations are reported in other proton conducting block copolymer systems.¹⁸² It is concluded that for sulfonated block copolymer membranes, increasing λ values from 0 to 40 increases the proton conductivity by enhancing proton mobility; however, beyond this, further increases in λ dilute the acid concentration and this effect outweighs any further increase in proton mobility. Such acid dilution does not occur in the fully sulfonated 6 – 17 vol% PS membranes due to their limited water swelling at high IEC, and thus these membranes exhibit a continuous increase in proton conductivity even beyond λ values of 40.

3.3.5 Proton Mobility

The *effective* proton mobility, μ_{eff} – where the effects of acid concentration on conductivity are removed – provides meaningful insights into the combined factors of degree of acid dissociation, ionic channel tortuosity, and spatial proximity between neighbouring acid groups within the ionic domains.¹⁸² Figure 3.12a shows the relationship between μ_{eff} and IEC for the various series of membranes. μ_{eff} generally increases with IEC in these membranes, which is expected, as increasing the IEC leads to increased water sorption and proton mobility. Comparisons between the various partially sulfonated membranes

indicate that proton mobility is higher for membranes with lower PS content. For instance, for IEC values between 0.4 and 0.7 mmol/g, μ_{eff} is $0.17 - 0.83 \times 10^{-3} \text{ cm}^2 \text{ s}^{-1} \text{ V}^{-1}$ for the 35 vol% PS membranes compared to $0.04 - 0.22 \times 10^{-3} \text{ cm}^2 \text{ s}^{-1} \text{ V}^{-1}$ for the 45 vol% PS membranes. The greater proton mobility in the 35 vol% PS membranes is attributed to the relatively higher degree of sulfonation and therefore, closer spatial proximity between acid groups. For example, to obtain an IEC of ~ 0.7 mmol/g, for the 35 vol% PS membranes, a degree of sulfonation of $\sim 40\%$ is required; whereas $\sim 20\%$ is required for the 45 vol % PS membranes (Table 3.2). At this IEC, in the 35 vol% PS membranes, each sulfonic acid group is separated by 1 to 2 non-sulfonated styrene units; whereas for the 45 vol% PS membranes, each sulfonic acid is 5 styrene units apart. The high degree of sulfonation also favors the formation of larger ionic clusters with greater water sorption, which promotes proton dissociation and transport within the ionic channels. It is worth noting that the 35 vol% PS membrane with the highest IEC exhibits a lower proton mobility. This might be explained from the TEM image (Figure 3.8 F), which shows disordered and tortuous ionic channels.

Plots of μ_{eff} versus water volume fraction (X_v) (Figure 3.12b) can be used to gain insights into the degree of tortuosity and connectivity of the ionic domains. The partially sulfonated 35, 45 and 50 vol% PS membranes possess significantly greater μ_{eff} than the fully sulfonated 6 – 17 vol% PS membranes. This suggests that the ionic channels in the partially sulfonated membranes are more contiguous with fewer dead ends, which is consistent with the morphology

revealed in the TEM images (Figure 3.8 D–J). In contrast, the fully sulfonated membranes are characterized as possessing highly encumbered ionic pathways.

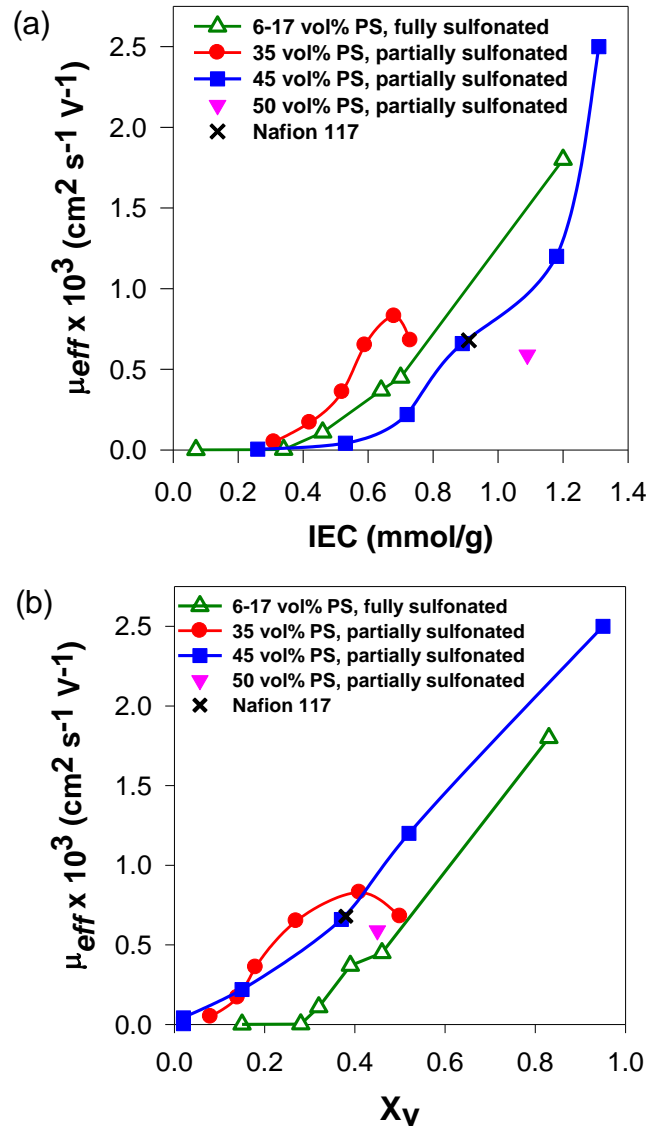


Figure 3.12 (a) Effective proton mobility (μ_{eff}) vs. IEC and (b) μ_{eff} vs. water volume fraction (X_v) for P(VDF-co-HFP)-b-SPS membranes with 6 – 17 (Δ), 35 (\bullet), 45 (\blacksquare) and 50 vol% (\blacktriangledown) polystyrene. Note: open symbols represent fully sulfonated membranes; filled symbols, partially sulfonated.

3.3.6 Conductivity Anisotropy

In an operating PEMFC, proton transport is perpendicular to the plane of the membrane – in the *through-plane* direction; thus, anisotropies in both membrane morphology and proton conductivity are important factors for evaluating PEM materials. Soboleva *et al.*¹⁴⁴ report that the degree of conductivity anisotropy in Nafion is influenced by the casting method: extruded membranes (Nafion 112, 1135, 115 and 117) demonstrate relatively anisotropic conductivity, whereas solution-cast membranes (Nafion 211) exhibit isotropic conductivity; Gebel *et al.*²⁰⁹ reported on the anisotropic proton conductivity in sulfonated polyimide membranes possessing distinct morphological anisotropy.

In order to examine conductivity anisotropy, proton conductivity in the in-plane (both X and Y) and through-plane (Z) directions were measured on selected membranes. Membranes possessing similar water volume fractions of ~0.40 were chosen, that is, IECs of 0.64, 0.68, 0.89 and 1.09 mmol/g for the 6 – 17, 35, 45 and 50 vol% PS membranes, respectively. Conductivity anisotropy ($\sigma_{\parallel/\perp}$), quantified by the ratio of in-plane (σ_{\parallel}) over through-plane (σ_{\perp}) conductivity, are given in Table 3.4. The fully sulfonated 6–17 vol% PS membrane is found to show very similar in-plane and through-plane proton conductivity indicating little anisotropy ($\sigma_{\parallel/\perp} = 0.8$), which is consistent with the randomly distributed ionic cluster morphology, as revealed by TEM (Figure 3.8 A–C).

For the 35, 45 and 50 vol% PS membranes, the in-plane proton conductivity is found to be greater than the through-plane conductivity, indicating a higher degree of anisotropy, and the hydrophilic proton-conducting domains are

oriented along the plane of the membrane in such a way that the alternating hydrophilic and hydrophobic layers are stacked parallel to the membrane's surface. This is consistent with the visualized lamellar morphology observed in the TEM analysis (Figure 3.8 D–J). The conductivity anisotropy of Nafion-117 membranes is found to be 1.2, which is in close agreement to previous reports.¹⁴⁴

Table 3.4 In-plane and Through-plane Conductivity of P(VDF-co-HFP)-*b*-SPS Membranes Possessing Different Morphologies

Membrane	IEC (mmol/g)	X_v	σ_x (S cm ⁻¹)	σ_y (S cm ⁻¹)	σ_z (S cm ⁻¹)	$\sigma_{ \perp}$ ^a
6 – 17 vol% PS, fully sulfonated	0.64	0.39	0.025 ± 0.002	0.021 ± 0.002	0.030 ± 0.004	0.8
35 vol% PS, partially sulfonated	0.68	0.41	0.049 ± 0.002	0.047 ± 0.001	0.016 ± 0.002	3.0
45 vol% PS, partially sulfonated	0.89	0.37	0.054 ± 0.002	0.056 ± 0.001	0.022 ± 0.001	2.5
50 vol% PS, partially sulfonated	1.09	0.45	0.047 ± 0.002	0.048 ± 0.002	0.017 ± 0.003	2.8
Nafion 117	0.91	0.38	0.077 ± 0.001	0.075 ± 0.002	0.069 ± 0.002	1.1

^a Conductivity anisotropy ($\sigma_{||\perp}$) is expressed as the ratio of in-plane ($\sigma_{||}$) to through-plane (σ_{\perp}) conductivity. $\sigma_{||}$ is obtained from the average of σ_x and σ_y ; σ_{\perp} is the σ_z .

3.4 Conclusion

Diblock ionomers of sulfonated poly([vinylidene difluoride-co-hexafluoropropylene]-*b*-styrene) [P(VDF-co-HFP)-*b*-SPS] were prepared for the purpose of studying the role of ionic purity and morphology on the properties of proton exchange membranes. Block ratios were controlled to provide membranes with distinct morphologies. For a given ion exchange capacity (IEC), water

uptake and proton conductivity were shown to be significantly influenced by the degree of sulfonation of the PS block, and, thus, the ionic purity and percolation within the “proton-conducting channels”.

Fully sulfonated membranes with 6 – 17 vol% PS possess disordered ionic clusters (6 – 20 nm in diameter) for which the cluster size increases with the length of the fully sulfonated PS segment. Although these membranes exhibit high water sorption at low IEC, the water sorption and proton conductivity is less sensitive to changes in IEC. Partially sulfonated membranes with 35, 45 and 50 vol% PS displayed lamellar structures. Compared to the fully sulfonated membranes, water contents were found to be lower in the partially sulfonated membranes due to the influence of the hydrophobic non-sulfonated polystyrene matrix surrounding the ionic aggregates. For a given IEC, partially sulfonated membranes with lower PS contents exhibited lower IEC threshold for ionic percolation and enhanced proton conductivity. This is ascribed to the greater degree of sulfonation required, which, in turn, leads to relatively pure and better connected ionic aggregates. Acid dilution effects are more pronounced for the partially sulfonated membranes due to their excessive water uptake at high ion content, leading to drop in proton conductivity for high IEC membranes. Once an ionic percolation threshold is reached in the ionic channels, the lamellar structure of the diblock provides little resistance to swelling. In summary, this work stresses the point that the degree of sulfonation plays a profound role on proton transport as it determines the ionic purity and the extent of percolation of the protogenic aggregates within an ionic channels.

Chapter 4. Nanostructure, Morphology, and Properties of Fluorous Copolymers Bearing Ionic Grafts

[Reprinted in parts with permission from *Macromolecules*, Tsang, E. M. W.; Zhang, Z.; Yang, A. C. C.; Shi, Z., Peckham, T. J.; Narimani, R.; Frisken, B. J.; Holdcroft, S. 42, 9467, © 2009, American Chemical Society.]

4.1 Introduction

Over the past decade, a wide variety of polymer systems have been explored as alternate membrane materials to address the high cost and limited operating conditions of Nafion membranes.^{3, 5, 6, 10-12} Despite numerous efforts, alternate membranes still fail to adequately meet the stringent requirements for high volume fuel cell commercialization. It is argued that a better understanding of fundamental structure-property relationships of PEMs is required for an efficient and rational membrane design.

In Nafion membranes, interconnected, nanometer-sized ionic channels are believed to form due to phase separation between the incompatible hydrophobic polymer backbone and hydrophilic sulfonic acid groups.^{114, 115, 125} Proton conduction occurs through these hydrophilic channels, mediated by water that is either strongly associated with the acidic groups or present as bulk water in the channels.^{14, 115, 116} However, it is still unclear how polymer microstructure influences the aggregation and connectivity of ionic domains and thereby morphology and proton conductivity. Therefore, model polymer systems, in which polymer microstructure can be controlled and systematically studied, are

essential both for elucidating relationships between structure, morphology, and proton conductivity and for obtaining insights into structural preferences for proton exchange membranes.

Zhang and Russell²¹⁰ reported fluorinated/styrenic graft copolymers of poly([vinylidene difluoride-co-chlorotrifluoroethylene]-*g*-styrene) [P(VDF-co-CTFE)-*g*-PS] prepared by graft-atom transfer radical polymerization (*graft*-ATRP) of styrene from commercial P(VDF-co-CTFE). This “grafting-from” approach allows enhanced control of polymer architecture compared to the conventional irradiation-^{211, 212} or ozone-^{213, 214} mediated free-radical polymerization routes. The idea that fluorinated/styrenic block copolymers can readily be converted into proton-conducting polyelectrolytes by postsulfonation of the styrene component provides further impetus for investigating this graft polymer system.

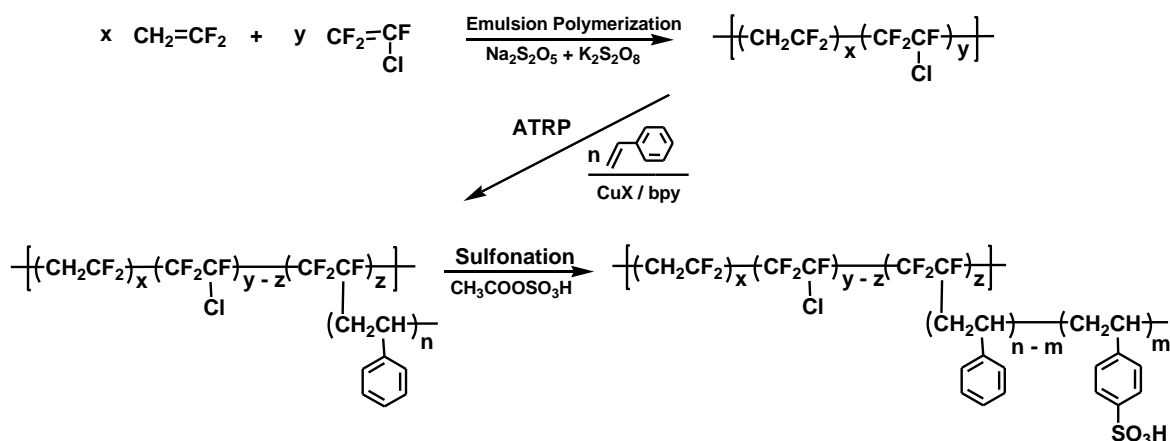


Figure 4.1 Synthetic scheme of partially sulfonated P(VDF-co-CTFE)-*g*-SPS graft copolymers.

The synthesis of proton-conducting partially sulfonated P(VDF-co-CTFE)-*g*-SPS by *graft*-ATRP of styrene from P(VDF-co-CTFE) macroinitiators, followed by postsulfonation has been reported recently (Figure 4.1).¹⁹⁵ This P(VDF-co-CTFE)-*g*-SPS graft system serves as an ideal model system for studying structure-property relationships because their composition and microstructure can be systematically varied by control of graft length, graft density, degree of sulfonation, and ion exchange capacity (IEC). Recently, Chung *et al.*²¹⁵ reported the synthesis of P(VDF-co-CTFE)-*g*-SPS which revealed the effects of polymer microstructures, namely, molecular weight of the polymer backbone and graft density, on membrane properties. It was found that graft copolymers possessing low graft density (0.3 – 0.8 mol%) and long SPS graft length (degree of polymerization of styrene, $DP_{\text{styrene}} = 70 - 120$) formed a morphology with long-range ionic channels (lamellar/cylindrical) imbedded in a highly crystalline fluorocarbon matrix. Although this morphology exhibited a lower percolation threshold and lower activation energy for proton conduction, it also led to increased water swelling and a high sensitivity to humidity. In contrast, graft copolymers with higher graft density (1.4 – 2.4 mol%) and short SPS graft length ($DP_{\text{styrene}} = 10 - 30$) gave rise to a disordered cluster network morphology with small cluster size. This morphology resulted in a higher resistance to water swelling, less sensitivity to humidity, and increased conductivity at higher temperatures. In addition, it was also reported that a high molecular weight P(VDF-co-CTFE) backbone resulted in smaller ionic channel width, lower water

uptake, and enhanced resistance to excessive water swelling at high IEC ranges.²¹⁵

The above studies on P(VDF-*co*-CTFE)-*g*-SPS graft systems warrant further investigation to determine whether a combination of high molecular weight P(VDF-*co*-CTFE) backbone and high graft density leads to membranes with cluster network morphologies that reduce the propensity of water swelling even further, and to determine whether such cluster network morphologies can be further correlated to microstructure. An important question that remains unanswered is the preference for having larger, but widely spaced, ionic clusters or smaller, but closely spaced, ionic clusters imbedded in a hydrophobic fluorocarbon matrix. For the P(VDF-*co*-CTFE)-*g*-SPS system, the length of the sulfonated polystyrene grafts (SPS), in principle, would influence the size of the ionic clusters. In order to manipulate the ionic cluster size without changing the overall cluster network morphology, it is important that the SPS graft length is varied while the graft density is kept constant.

In this chapter, the synthesis of P(VDF-*co*-CTFE)-*g*-SPS for elucidating the effects of SPS graft lengths – *at a fixed graft density*- on membrane morphology and properties is described. As illustrated in Figure 4.2, three parent graft copolymers of P(VDF-*co*-CTFE)-*g*-PS, with similar graft density (~2.5 mol%) but different PS graft length ($DP_{\text{styrene}} = 35, 88, 154$), were prepared from a common fluoropolymer macroinitiator. Each parent P(VDF-*co*-CTFE)-*g*-PS copolymer was subsequently sulfonated to different extents to provide a series of ionic P(VDF-*co*-CTFE)-*g*-SPS, which were cast into membranes to provide

families of membranes with varying IEC. The correlation between graft length, morphology, and properties such as proton conductivity and water sorption reveal interesting trends that are important in the design of next-generation proton conducting membranes.

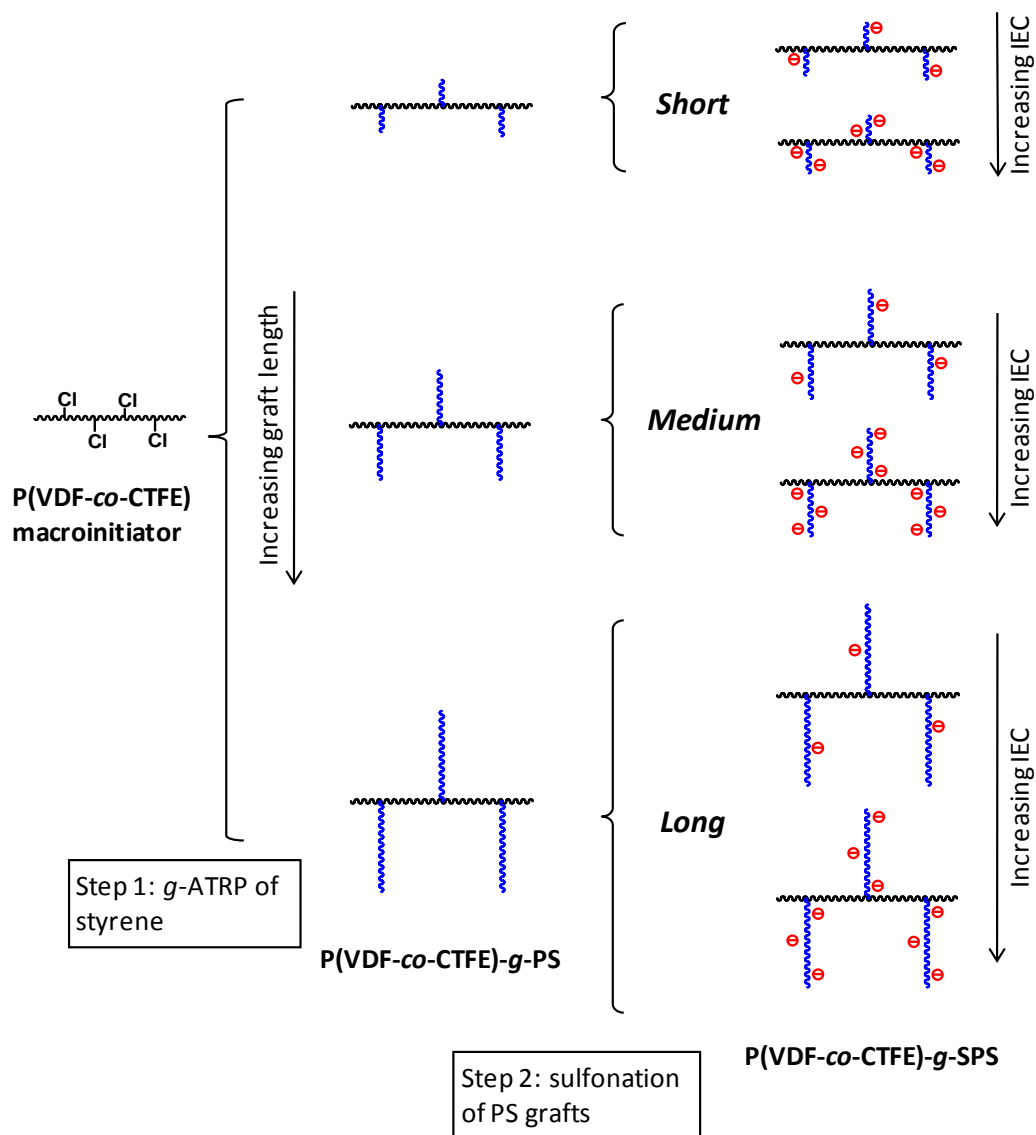


Figure 4.2 Structural relationship between the various series of P(VDF-co-CTFE)-g-SPS.

4.2 Experimental Section

4.2.1 Materials

Vinylidene difluoride (VDF, Aldrich, 99+%), chlorotrifluoroethylene (CTFE, Aldrich, 98%), potassium persulfate ($K_2S_2O_8$, Allied Chemical, reagent grade), sodium metabisulfite ($Na_2S_2O_5$, Anachemia, anhydrous, reagent grade), pentadecafluorooctanoic acid (Aldrich, 96%), copper (I) chloride (CuCl, Aldrich, 99%), copper (II) chloride ($CuCl_2$, Aldrich, 99.999%), 2,2'-bipyridine (bpy, Aldrich, 99+%), 1,2-dichloroethane (Caledon, reagent grade), *N*-methyl-2-pyrrolidone (NMP, Aldrich, anhydrous, 99.5%), *N,N*-dimethylacetamide (DMAc, Aldrich, anhydrous, 99.8%), sulfuric acid (Anachemia, 95 – 98%, ACS reagent), and acetic anhydride (Aldrich, 99.5%) were used as received. Styrene (St, Aldrich, 99+%) was washed repeatedly with aqueous 5 wt% sodium hydroxide and with water, dried with magnesium sulfate, distilled over calcium hydride under reduced pressure, and stored under nitrogen at -20 °C.

4.2.2 Synthesis of Fluorous Macroinitiator [P(VDF-co-CTFE)]

The macroinitiator was prepared by emulsion copolymerization of vinylidene difluoride (VDF) and chlorotrifluoroethylene (CTFE) as follows: to a 160 mL pressure vessel (Parr Instruments) equipped with a 600 psi pressure relief valve and a magnetic stir bar, a mixture of 100 mL of water, 0.40 g of $K_2S_2O_8$, 0.29 g of $Na_2S_2O_5$, 0.04 g of pentadecafluorooctanoic acid was added. A monomer mixture consisting of 80 mol% VDF and 20 mol% CTFE was then introduced into the reactor. The polymerization was carried out for 1 h at 60 °C, and a constant pressure of 300 psi was maintained by re-supplying the vessel

with the monomer mixture. The resulting polymer latex was coagulated by freezing, followed by washing with water and ethanol. The crude fluoropolymer was purified by repeated dissolution in THF and reprecipitation in ethanol. The sample was dried at 80 °C under vacuum for 24h. ¹H NMR (500 MHz, d₆-acetone) δ (ppm): 2.75 – 3.30 (-CF₂-CH₂-CF₂-**CH₂***-CF₂-CH₂-), 2.15 – 2.45 (-CH₂-CF₂-CF₂-**CH₂***-CH₂-CF₂-). ¹⁹F NMR (400 MHz, d₆-acetone) δ (ppm): -90.0 – -94.0 (-CF₂-CH₂-**CF₂***-CH₂-CF₂-), -95.1 (-CF₂-CH₂-**CF₂***-CH₂-CH₂-), -108.7 (-CF₂-CH₂-**CF₂***-CF₂-CFCl-), -114.2 (-CF₂-CH₂-**CF₂***-CF₂-CH₂-), -116.6 (-CH₂-CF₂-**CF₂***-CFCl-CF₂-), -118.5 to -120.0 (-CH₂-CF₂-**CF₂***-CFCl-CH₂-), -120.0 to -121.4 (-CF₂-CF₂-**CF*Cl**-CH₂-CF₂-). The composition of the P(VDF-co-CTFE) macroinitiator was calculated by ¹⁹F NMR according to published methods¹⁹⁷ and found to be 5.8 ± 0.3 mol% CTFE and 94.2 ± 0.3 mol% VDF.

4.2.3 Grafting ATRP of Styrene onto P(VDF-co-CTFE) Macroinitiator

The P(VDF-co-CTFE) macroinitiator (1.0 g, M_n = 3.12 × 10⁵ Da) was dissolved in NMP (40 mL) at 60 °C in a dried flask equipped with a rubber septum and a magnetic stirring bar. After cooling to room temperature, CuCl (0.65 g, 6.5 mmol), CuCl₂ (0.09 g, 0.66 mmol), bpy (3.0 g, 19.2 mmol) and styrene (20 mL, 174.6 mmol) were added. Three freeze-pump-thaw cycles were performed to remove oxygen. The polymerization reaction was carried out at 110 °C under a nitrogen blanket. Polymer samples were periodically removed from the reaction flask using a syringe after 8, 16 and 24 h. The polymer samples were diluted with THF, purified by passing through a column of alumina, and then precipitated into methanol. Homopolymer of polystyrene was removed by

washing repeatedly with cyclohexane. The resulting P(VDF-co-CTFE)-*g*-PS copolymers were dried under vacuum at 60 °C. ¹H NMR (500 MHz, d₆-acetone) δ (ppm): 6.35 – 7.30 (aryl), 2.80 – 3.10 (methylene, head-to-tail VDF sequences), 2.05 – 2.50 (methylene, head-to-head or tail-to-tail VDF sequences), 1.80 – 2.10 (benzylic), 1.10 – 1.80 (methylene, styrene). The ¹⁹F NMR spectrum of P(VDF-co-CTFE)-*g*-PS showed similar signature peaks to that of the fluororous macroinitiator described above, except an additional peak at -165 ppm (–CF₂–CF*[CH₂CH(C₆H₅)]_n–CF₂–).

4.2.4 Sulfonation of Polystyrene Graft Chains

Sulfonation was carried out in 1,2-dichloroethane using a procedure described in the literature,⁵⁵ except a reaction temperature of 40 °C was used. A typical sulfonation reaction is as follows: to a 50 mL three-neck flask equipped with a dropping funnel and condenser, P(VDF-co-CTFE)-*g*-PS (0.6 g) and 1,2-dichloroethane (15 mL) were added. The mixture was heated to 50 °C under nitrogen and stirred until complete dissolution. Acetyl sulfate was prepared by injecting acetic anhydride (1 mL) and 1,2-dichloroethane (3 mL) into a nitrogen-purged vial. The solution was cooled to 0 °C in a calcium chloride ice bath (CaCl₂, 10 wt%) after which fuming sulfuric acid (95 – 97%, 0.3 mL) was added. The resultant acetyl sulfate was immediately added to the polymer solution at 40 °C using a dropping funnel. Samples sulfonated to various degrees were periodically extracted and precipitated in ethanol/hexanes (50/50 v/v). The precipitate was washed repeatedly with water until the residual water was pH 7. The partially sulfonated P(VDF-co-CTFE)-*g*-SPS was dried under vacuum at 60

°C overnight. The ^1H NMR spectrum of P(VDF-*co*-CTFE)-*g*-SPS showed similar signature peaks to that of the pristine P(VDF-*co*-CTFE)-*g*-PS described above, except an additional peak at 7.60 – 7.30 ppm, corresponding to aromatic protons adjacent to the sulfonate group, was observed.

4.2.5 Membrane Preparation and Characterization

Membranes were prepared by dissolving the sulfonated graft copolymers in *N,N*-dimethylacetamide and casting on a levelled Teflon[®] sheet. Polymer films were dried at ambient temperature for 2 days and then at 60 °C under vacuum overnight. The membranes (~100 μm thick) were converted to the protonic form by immersing in aqueous hydrochloric acid (HCl, 2 M) overnight. The protonated membranes were washed several times with deionized water for 30 min periods and placed in water overnight to remove excess acid on the surface and the interior of the membranes.

The ion exchange capacities (IEC, mmol/g) were determined by titrating the protons released from the membranes in 2 M sodium chloride (NaCl) with standardized sodium hydroxide (NaOH) solutions to a phenolphthalein end-point. Control acid-base titrations were also performed on 2 M NaCl solutions with no membranes present to determine the “blank” titration volume. The IECs were represented as the millimoles of ionic exchange sites per gram of dry membrane. A detailed description of the method used is described in Section 2.5.3.

The water uptake was calculated as the percentage increase in mass for a membrane changing from dry state to water-saturated state. Water content was

calculated both as a mass and a volume percentage of water in a water-saturated membrane. Water content is also represented as the ratio of the moles of water to the moles of ion exchange sites. This value provides a measure of the average number of water molecules per ion exchange site ($[\text{H}_2\text{O}]/[\text{SO}_3^-]$, often referred to as λ value). More detailed descriptions of the above water sorption measurements are given in Section 2.5.2.

The analytical acid concentration ($[-\text{SO}_3\text{H}]$, mol/L) was determined as moles of sulfonic acid moieties per unit volume of hydrated membrane, as described in Section 2.5.3.

The *effective* proton mobility (μ_{eff}) in hydrated membranes, calculated using Equation 4.1, is considered as a normalized proton conductivity at which acid concentration effects are removed. A detailed description of the calculation is given in Section 2.5.5.

$$\mu_{eff} = \frac{\sigma}{F [-\text{SO}_3\text{H}]} \quad \text{Equation 4.1}$$

where F is Faraday's constant and σ (S cm^{-1}) is the proton conductivity.

4.2.6 Instrumentation and Techniques

The molecular weight of the macroinitiator and the graft copolymers were estimated by gel permeation chromatography (GPC) using DMF (0.01 M LiBr) eluant, three Waters Styragel HT columns at 50 °C, a Waters 1515 isocratic HPLC pump, a Waters 2414 differential refractometer, and a Waters 2487 dual UV absorbance detector ($\lambda = 254$ nm). Polystyrene standards were used for

calibration. ^1H NMR spectra (in DMSO-d_6) were recorded on a 500 MHz Varian Inova spectrometer; ^{19}F NMR spectra (in DMSO-d_6) were recorded on a 400 MHz Varian MercuryPlus spectrometer, and chemical shifts were measured with respect to trichlorofluoromethane (CFCl_3).

In-plane proton conductivity was measured by ac impedance spectroscopy with a Solartron 1260 frequency response analyzer (FRA) employing a two-electrode configuration, according to the published procedure¹⁸⁰ described in Section 2.5.4. Briefly, a membrane (10 mm x 5 mm) was placed between two Pt electrodes of a conductivity cell, and a 100 mV sinusoidal AC voltage over a frequency range of 10 MHz to 100 Hz was applied. The resulting Nyquist plots were fitted to the standard Randles equivalent circuit to determine the membrane resistance. Proton conductivity (σ) was calculated by

$$\sigma = \frac{L}{R A} \quad \text{Equation 4.2}$$

where L (cm) is the distance between electrodes, R (Ω) is the membrane resistance and A (cm^2) is the cross-sectional area of the membrane. An ESPEC SH-241 temperature/humidity chamber was used for the measurement of membrane conductivity under conditions of variable temperature and humidity. Membranes were equilibrated overnight in the chamber at a pre-determined temperature and relative humidity. Measurements were collected until a constant ionic resistance was obtained. All conductivity values reported were taken as average values of five membrane samples.

Samples for transmission electron microscopy (TEM) were prepared as follows: membranes were stained by soaking in a saturated lead acetate solution overnight, then rinsed in water and dried under vacuum at room temperature for 4 h. The stained membranes were embedded in Spurr's epoxy and cured overnight in an oven at 60 °C. The samples were sectioned to yield slices 60 – 100 nm thick using a Leica UC6 Ultramicrotome, and picked up on copper grids. Electron micrographs were taken with a Hitachi H7600 TEM using an accelerating voltage of 80 kV. The size of the ionic domains was estimated using ImageJ[®] software version 1.41, from National Institutes of Health, USA. The domain sizes were reported as average over ~100 measurements. The cluster number density in 2-dimensions was estimated by counting the number of ionic clusters present in a predetermined area, as follows: a 1 x 1 cm grid was overlaid on the TEM image and the number of clusters present was counted in random sampling areas. The cluster number densities were reported as average over ~30 samples and expressed in terms of number of clusters per 1000 nm².

Wide angle X-ray scattering (WAXS) experiments were performed on a Siemens D-5000 diffractometer. The X-ray unit was operated at 50 kV and 30 mA using a Cu K α source ($\lambda = 0.154$ nm) and a nickel filter. Data were acquired in transmission mode under ambient conditions. A background scattering spectrum was collected on an empty sample holder and subsequently subtracted from the membranes' scattering profiles. Data analysis and fitting were performed using the Origin[®] fit function.

4.3 Results and Discussion

4.3.1 Synthesis of P(VDF-co-CTFE)-*g*-SPS Graft Copolymers

Fluorous-ionic graft copolymers of P(VDF-co-CTFE)-*g*-SPS were prepared via a “grafting from” macroinitiator approach followed by post-sulfonation, as illustrated in Figure 4.1. To obtain the fluorous macroinitiator bearing chlorine sites for subsequent initiation of graft-ATRP, chlorotrifluoroethylene (CTFE) was incorporated into the backbone by its emulsion copolymerization with vinylidene fluoride (VDF). The incorporation of large percentages of CTFE (> 10 mol%) led to cross-linking and gelation during subsequent graft polymerization reaction; it was thus necessary to control and reduce the CTFE content. A P(VDF-co-CTFE) copolymer ($M_{n, \text{GPC}}$ of 312,000 Da), containing 5.8 ± 0.3 mol% of CTFE was prepared. To further inhibit crosslinking during *g*-ATRP, a small amount of a deactivator, CuCl_2 (5 mol% relative to CuCl), was introduced to the CuCl/bpy catalyst system.

GPC traces of the P(VDF-co-CTFE) macroinitiator and its resulting P(VDF-co-CTFE)-*g*-PS graft copolymers at various reaction times are shown in Figure 4.3. It is observed that after graft polymerization, the initial negative RI signal of the macroinitiator transforms to a positive signal. In addition, as the reaction proceeds, the GPC traces shift to a higher molecular weight. These results are indicative of grafting of styrene onto the macroinitiator. The molecular weights of the resulting graft copolymers estimated by GPC ($M_{n, \text{GPC}}$) are listed in Table 4.1. In this graft system, monomer units are grown as side chains from multiple initiating sites along the backbone. Such branching architecture in a graft

copolymer will lead to relatively smaller dynamic volume compared to a linear copolymer of the same molecular weight, thus causing M_n to be underestimated. A more accurate estimate of the graft polymers' molecular weight was obtained by ^1H NMR.

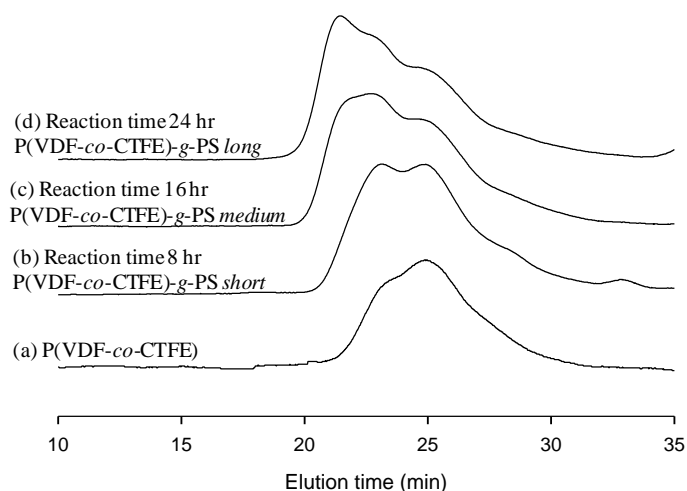


Figure 4.3 GPC traces of (a) P(VDF-co-CTFE) macroinitiator and the resulting P(VDF-co-CTFE)-g-PS graft copolymers at various reaction time: (b) 8 h, (c) 16 h and (d) 24 h (Note: the original negative peak in (a) is inverted for convenience).

Table 4.1 Chemical Compositions of P(VDF-co-CTFE)-g-PS Parent Graft Copolymers

graft copolymer	P(VDF-co-CTFE) ^a		P(VDF-co-CTFE)-g-PS				
	<i>g</i> -ATRP reaction time (h)	$M_{n,GPC}^b$ (Da)	$M_{n,NMR}^c$ (Da)	St/VDF ^d (mole ratio)	% Cl reacted ^e	graft density ^f	graft length ^g
short	8	3.32×10^5	5.76×10^5	80/100	39 ± 2	2.3 ± 0.2	35 ± 3
medium	16	3.95×10^5	13.6×10^5	230/100	44 ± 2	2.6 ± 0.2	88 ± 7
long	24	4.48×10^5	22.0×10^5	415/100	46 ± 3	2.7 ± 0.2	154 ± 11

^a P(VDF-co-CTFE) macroinitiator: $M_{n,GPC} = 3.12 \times 10^5$ Da, 5.8 ± 0.3 mol% CTFE.

^b Measured by DMF-GPC, calibrated with linear PS standards.

^c Calculated using the $M_{n,GPC}$ of P(VDF-co-CTFE) and the ratio of St/VDF from ^1H NMR.

^d Based on ^1H NMR.

^e Based on ^{19}F NMR.

^f Number of PS grafts per 100 units in fluororous backbone, calculated from the mol % of CTFE in P(VDF-co-CTFE) (5.8 mol %) multiplied by the % of Cl reacted during *g*-ATRP.

^g Average number of styrene units in each graft chain, calculated from the St/VDF mole ratio divided by graft density.

¹H NMR spectra of the P(VDF-co-CTFE) macroinitiator and the resulting P(VDF-co-CTFE)-*g*-PS graft copolymers were obtained (Figure 4.4). Peaks between 2.2 and 2.5 ppm (peak a') are due to the head-to-head and tail-to-tail VDF sequences. Peaks at 2.8 – 3.3 ppm (peak a) are due to the head-to-tail VDF sequences. These VDF signature peaks are observed in both the macroinitiator and the resulting graft copolymers. However, additional peaks are found in the graft copolymers (Figure 4.4b). Peaks at 1.10 – 1.80 ppm (peak b) and at 1.80 – 2.10 ppm (peak c) are due to the methylene and the benzylic protons of styrene, respectively. Peaks at 6.35 – 7.30 ppm (peaks d and e) correspond to the aromatic protons of styrene. Quantification of the amount of styrene grafted onto the macroinitiator can be determined from the ratio of integrated signals due to the aromatic styrenic protons (peaks d and e) and the methylene protons of VDF (peaks a and a'), as follows

$$\frac{\text{St}}{\text{VDF}} = \frac{D + E}{A + A'} \times \frac{2}{5} \quad \text{Equation 4.3}$$

where *D*, *E*, *A* and *A'* represent the integrals of peaks d, e, a and a', respectively. As the reaction proceeds, the ratio of styrene to VDF increases. The molecular weights of P(VDF-co-CTFE)-*g*-PS estimated from ¹H NMR (*M_n*, *NMR*) are summarized in Table 4.1.

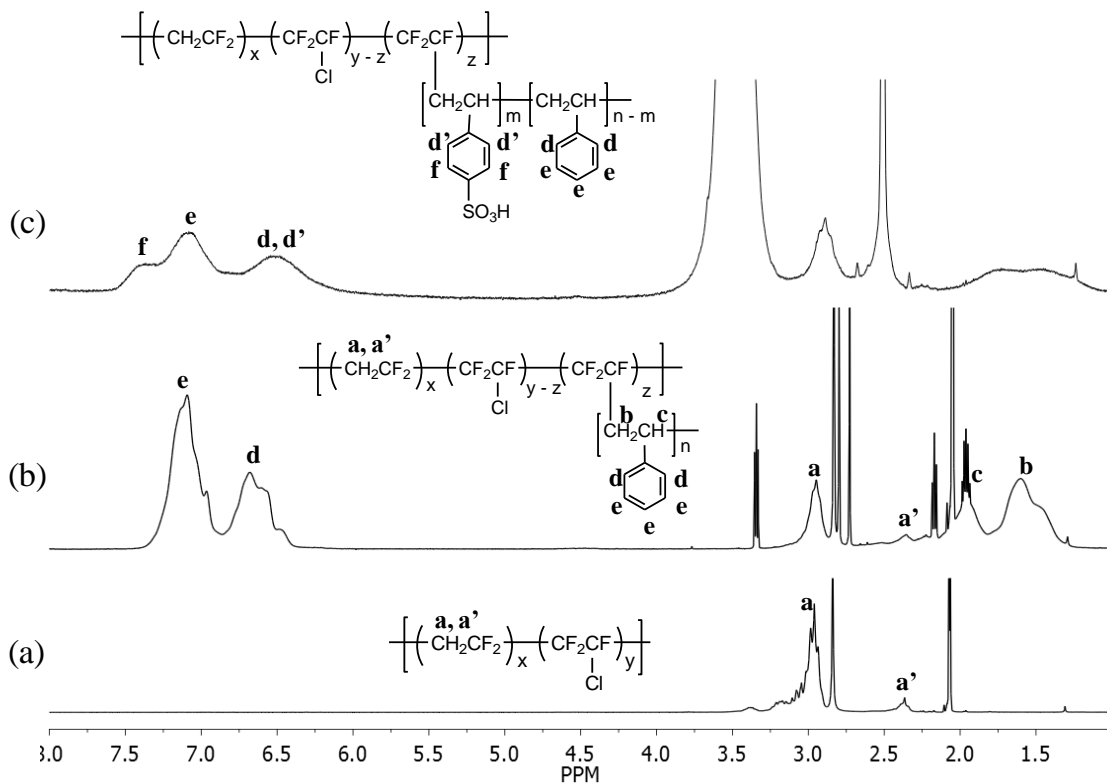


Figure 4.4 ^1H NMR spectra of (a) P(VDF-co-CTFE) macroinitiator (d_6 -acetone), (b) P(VDF-co-CTFE)-g-PS graft copolymer (d_6 -acetone), and (c) partially sulfonated P(VDF-co-CTFE)-g-SPS graft copolymers (d_6 -DMSO).

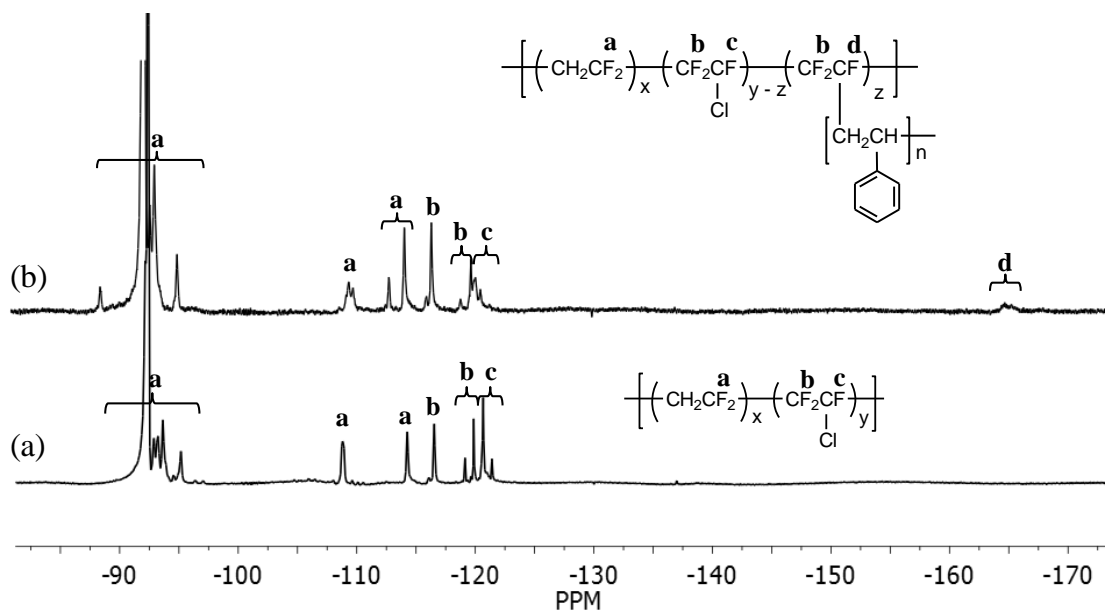


Figure 4.5 ^{19}F NMR spectra of (a) P(VDF-co-CTFE) macroinitiator (d_6 -acetone) and (b) P(VDF-co-CTFE)-g-PS graft copolymer (d_6 -acetone).

In order to estimate the average length of the polystyrene grafts, an estimate of the number density of PS grafts is required. The number of CTFE units involved in the *g*-ATRP reaction directly reflects the graft number density, and this can be determined using ^{19}F NMR (Figure 4.5). It is observed that the resulting graft copolymers possessed similar ^{19}F NMR signature peaks to the macroinitiator, but an additional peak was found at -165 ppm (peak d) due to tertiary fluorine atoms at carbon centers bearing a graft chain ($-\text{CF}_2-\text{CF}^*[\text{CH}_2\text{CH}(\text{C}_6\text{H}_5)]_n-\text{CF}_2-$). Following *g*-ATRP, the peak centered at -121 ppm (peak c), corresponding to $-\text{CF}^*\text{Cl}-$, was reduced in intensity because a portion of the $-\text{CFCl}$ units had reacted. The percentage of Cl sites initiating *g*-ATRP can be quantified by measuring the ratio of integrals for peaks d and c, as given by

$$\% \text{ Cl reacted} = \frac{D}{D+C} \times 100\% \quad \text{Equation 4.4}$$

where *C* and *D* represent the integrals of peaks c and d, respectively. After 8 h it was found that 39 ± 2 % of all Cl groups had reacted. As the reaction time was increased to 16 and 24 h, the number of sites reacted had increased marginally to 44 ± 2 and 46 ± 3 %, respectively. The data represent graft densities of 2.3, 2.6 and 2.7 ± 0.2 mol%, for 8, 16, and 24h reaction times, respectively. Using both the St/VDF ratio estimated from ^1H NMR and the graft number density estimated from ^{19}F NMR, the average degree of polymerization of styrene ($\text{DP}_{\text{styrene}}$) for the 8, 16, 24 h reaction times was estimated to be 35 ± 3 , 88 ± 7 and 154 ± 11 , respectively.

The experimental results and chemical compositions (i.e., M_n , St/VDF, graft number density, graft length, etc.) of the P(VDF-*co*-CTFE)-*g*-PS graft copolymers are listed in Table 4.1. These graft copolymers were synthesized so as to possess very similar graft density (i.e., between 2.3 to 2.7 mol%), but different PS graft length ($DP_{\text{styrene}} = 35$ to 154) in which the graft length was approximately doubled with each series. These are termed *short*, *medium* and *long* graft lengths, respectively.

Each of the three P(VDF-*co*-CTFE)-*g*-PS copolymers was used as parent polymers for subsequent sulfonation. The sulfonation reactions were carried out to different extents to provide three series of partially sulfonated P(VDF-*co*-CTFE)-*g*-SPS polymers. NMR spectroscopy was used to quantify the degree of sulfonation (Figure 4.4c). ^1H NMR spectra of partially sulfonated graft copolymers exhibit a peak at 6.80 – 7.30 ppm (peak e) due to meta and para protons on the non-sulfonated phenyl rings. The peak at 7.30 – 7.60 ppm (peak f) is assigned to aromatic protons adjacent to the sulfonate group on the sulfonated phenyl rings. The degree of sulfonation, represented as DS (%), was quantified using the ratio of integrals for peaks e and f, as follows

$$DS(\%) = \frac{F/2}{F/2 + E/3} \times 100\% \quad \text{Equation 4.5}$$

where E and F represent the integrals of peaks e and f, respectively.

The macromolecular structural relationships between the three series of P(VDF-*co*-CTFE)-*g*-SPS polymers are illustrated in Figure 4.2. From these polymers, three series of membranes, processing similar graft number density,

varying graft chain length and varying ion exchange capacity (IEC) were prepared, which allowed the opportunity to systematically investigate the effects of graft chain lengths on membrane properties and morphology, as discussed in the following sections. Compositional data and properties for these membranes are summarized in Table 4.2 and 4.3, respectively.

Table 4.2 Chemical Compositions of P(VDF-co-CTFE)-*g*-SPS Graft Membranes

Series	Membrane	Graft density	Graft length	DS (%) ^a	measured IEC ^b (mmol/g)
Short	S-1	2.3 ± 0.2	35 ± 3	13 ± 2	0.64 ± 0.02
	S-2			21 ± 2	1.03 ± 0.03
	S-3			26 ± 3	1.22 ± 0.02
	S-4			34 ± 2	1.59 ± 0.02
	S-5			44 ± 3	1.98 ± 0.05
	S-6			59 ± 4	2.48 ± 0.03
Medium	M-1	2.6 ± 0.2	88 ± 7	10 ± 1	0.73 ± 0.01
	M-2			15 ± 2	1.02 ± 0.03
	M-3			18 ± 2	1.22 ± 0.01
	M-4			21 ± 3	1.40 ± 0.04
	M-5			26 ± 2	1.67 ± 0.02
	M-6			34 ± 3	2.10 ± 0.02
	M-7			41 ± 3	2.46 ± 0.05
Long	L-1	2.7 ± 0.2	154 ± 11	9 ± 2	0.73 ± 0.02
	L-2			11 ± 1	0.92 ± 0.03
	L-3			15 ± 2	1.23 ± 0.03
	L-4			18 ± 2	1.45 ± 0.05
	L-5			22 ± 3	1.72 ± 0.03
	L-6			25 ± 2	1.93 ± 0.05
	L-7			30 ± 3	2.24 ± 0.01
	L-8			33 ± 4	2.53 ± 0.03

^a Degree of sulfonation, calculated from ¹H NMR data. ^b Measured by acid-base titration.

Table 4.3 Properties of P(VDF-co-CTFE)-g-SPS Membranes

Membrane	Measured IEC ^a (mmol g ⁻¹)	Conductivity ^b (S cm ⁻¹)	Water content ^c (wt %)	Water uptake ^c (wt %)	λ	[H ⁺] (M)	X _v (by vol)	$\mu_{eff} \times 10^3$ (cm ² s ⁻¹ V ⁻¹)
S-1	0.64 ± 0.02	0.002 ± 0.001	8 ± 1	9 ± 1	7 ± 1	0.62 ± 0.02	0.07	0.03
S-2	1.03 ± 0.04	0.010 ± 0.003	17 ± 1	21 ± 2	11 ± 1	0.82 ± 0.02	0.18	0.15
S-3	1.22 ± 0.02	0.040 ± 0.002	22 ± 1	28 ± 1	13 ± 1	1.01 ± 0.01	0.24	0.41
S-4	1.59 ± 0.02	0.075 ± 0.006	47 ± 3	89 ± 5	31 ± 2	0.89 ± 0.03	0.48	0.92
S-5	1.98 ± 0.05	0.083 ± 0.002	63 ± 1	176 ± 5	53 ± 3	0.73 ± 0.01	0.68	1.18
S-6	2.48 ± 0.06	0.065 ± 0.001	78 ± 1	358 ± 17	80 ± 3	0.52 ± 0.01	0.80	1.30
M-1	0.73 ± 0.01	0.003 ± 0.001	9 ± 1	10 ± 1	7 ± 1	0.66 ± 0.01	0.09	0.05
M-2	1.02 ± 0.03	0.006 ± 0.002	11 ± 1	12 ± 2	7 ± 1	0.93 ± 0.05	0.13	0.07
M-3	1.22 ± 0.01	0.014 ± 0.004	16 ± 1	18 ± 1	8 ± 1	1.04 ± 0.02	0.15	0.13
M-4	1.40 ± 0.04	0.023 ± 0.004	20 ± 1	24 ± 1	10 ± 1	1.17 ± 0.02	0.21	0.20
M-5	1.67 ± 0.02	0.066 ± 0.003	31 ± 2	42 ± 2	14 ± 1	1.22 ± 0.04	0.31	0.51
M-6	2.10 ± 0.02	0.090 ± 0.001	60 ± 2	143 ± 4	37 ± 2	0.87 ± 0.02	0.60	1.07
M-7	2.46 ± 0.05	0.057 ± 0.001	83 ± 1	495 ± 20	110 ± 5	0.46 ± 0.02	0.85	1.28
L-1	0.73 ± 0.02	0.002 ± 0.001	9 ± 1	10 ± 1	8 ± 1	0.70 ± 0.01	0.08	0.03
L-2	0.92 ± 0.03	0.005 ± 0.001	11 ± 1	12 ± 1	8 ± 1	0.84 ± 0.01	0.10	0.06
L-3	1.23 ± 0.03	0.015 ± 0.001	20 ± 1	24 ± 2	11 ± 1	1.03 ± 0.05	0.21	0.15
L-4	1.45 ± 0.05	0.025 ± 0.002	24 ± 1	30 ± 3	12 ± 1	1.16 ± 0.02	0.24	0.22
L-5	1.72 ± 0.03	0.049 ± 0.001	31 ± 2	44 ± 3	15 ± 1	1.25 ± 0.01	0.30	0.42
L-6	1.93 ± 0.05	0.082 ± 0.003	45 ± 3	79 ± 3	22 ± 2	1.16 ± 0.02	0.46	0.73
L-7	2.24 ± 0.01	0.095 ± 0.005	67 ± 2	207 ± 16	55 ± 2	0.80 ± 0.04	0.67	1.30
L-8	2.53 ± 0.03	0.045 ± 0.003	87 ± 1	680 ± 46	154 ± 8	0.33 ± 0.01	0.94	1.40

^a Measured by acid-base titration. ^b Measured by AC impedance spectroscopy at room temperature and fully hydrated. ^c At room temperature. ^d Analytical acid concentration in a fully hydrated membrane. ^e Water volume fraction at room temperature.

4.3.2 TEM

Transmission electron micrographs (TEMs) of selected membranes prepared from the *short*, *medium*, and *long* graft length polymers are shown in Figure 4.6. To investigate phase separation and ionic aggregation, membranes were stained with lead acetate, thus, dark areas correspond to regions of high ionicity; brighter areas, hydrophobic regions. It was observed that all three series of the dry graft membranes possessed a phase-separated morphology characterized by small, 2 – 4 nm ionic clusters interconnected by narrow ionic channels. This morphology is very similar to that of Nafion[®], which possesses a “cluster-network” comprising of 5 - 10 nm ionic clusters, but the dimensions are much smaller.^{126, 127, 129, 131}

In all three series of graft membranes, the ion content was observed to play an important role on phase separation and ionic aggregation. For each graft length series, membranes with lower IEC exhibit less distinctive phase separation wherein the interface between the ionic domains and the hydrophobic matrix is less sharp (i.e., Figure 4.6 A, C and E). On the other hand, in membranes with higher IEC, a more distinct phase-separated morphology with sharply visible ionic clusters is observed (i.e., Figure 4.6 B, D and F). In addition, the size of the ionic clusters increases with increasing IEC, which is explained on the basis of an increasing proportion of sulfonic acid (-SO₃H) groups present. Histograms showing the distribution of ionic cluster sizes in the membranes are presented in Figure 4.7, and the averaged data are summarized in Table 4.4.

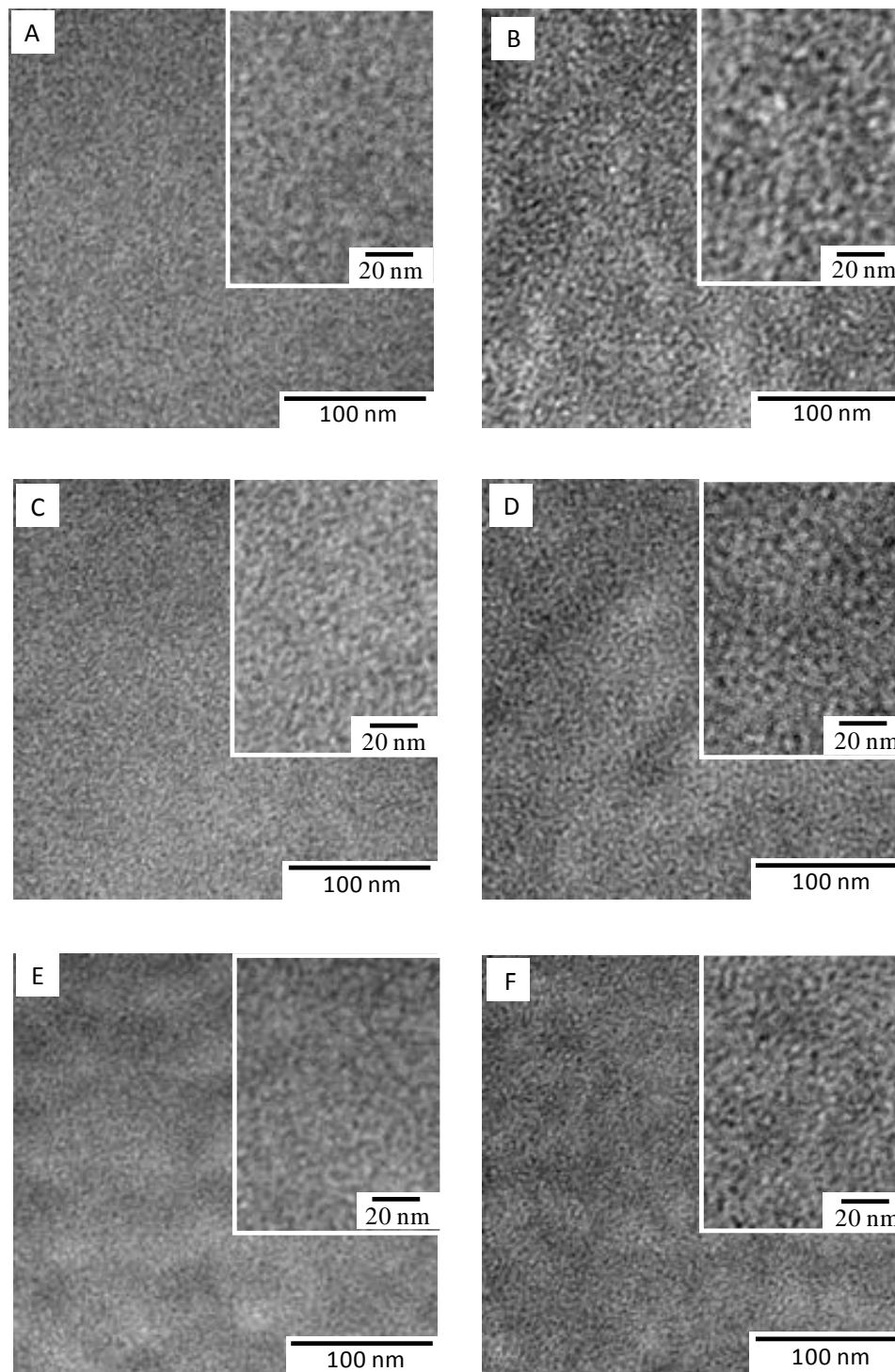


Figure 4.6 TEM images of selected P(VDF-co-CTFE)-g-SPS membranes from the short series with IECs (mmol/g) of 0.64 (A) and 2.48 (B); the medium series with IECs of 0.73 (C) and 2.46 (D) mmol/g; and the long series with IECs of 0.73 (E) and 2.53 (F) mmol/g.

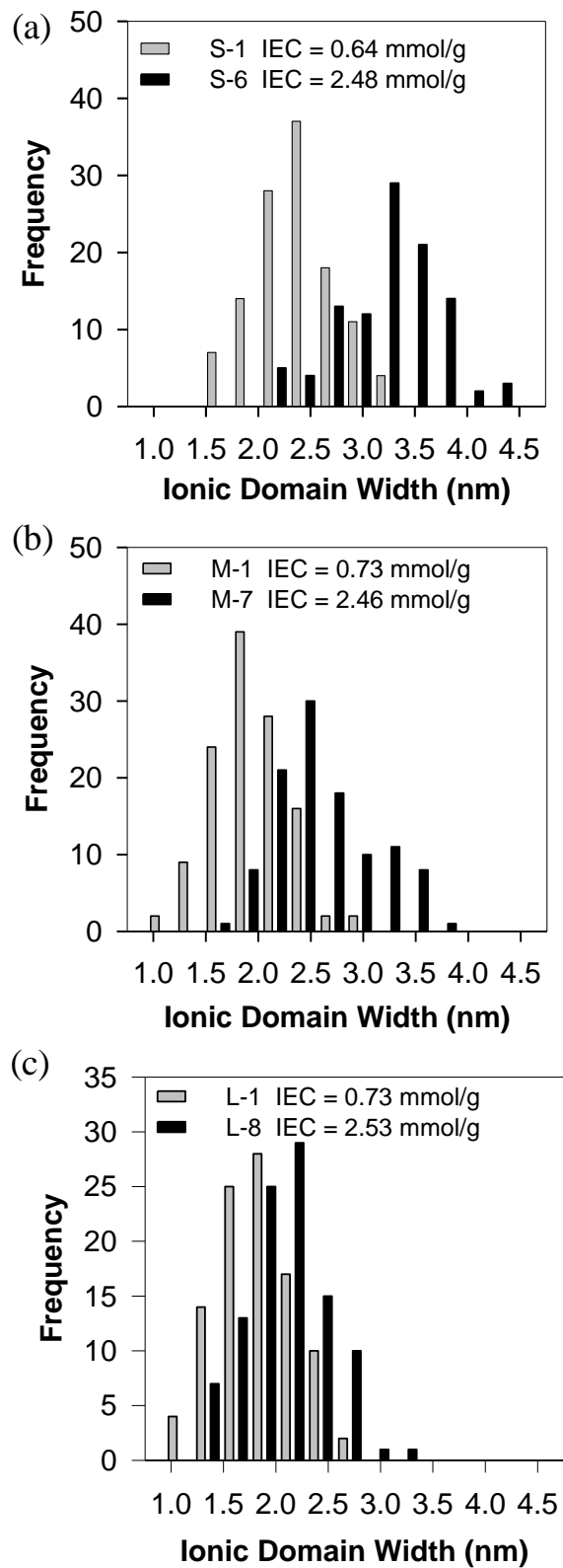


Figure 4.7 Distributions of the ionic cluster sizes in selected membranes from (a) short, (b) medium, and (c) long graft copolymer series.

Table 4.4 Ionic Cluster Size and Number Density

membrane	IEC (mmol/g)	ionic cluster width (nm)	2-D cluster number density (per 1000 nm ²)
S – 1	0.64	2.2 ± 0.4	21 ± 2
S – 6	2.48	3.3 ± 0.4	19 ± 2
M – 1	0.73	1.9 ± 0.3	26 ± 3
M – 7	2.46	2.6 ± 0.4	28 ± 2
L – 1	0.73	1.8 ± 0.3	25 ± 3
L – 8	2.53	2.1 ± 0.3	35 ± 3

The average ionic cluster size increases from 2.2 to 3.3, 1.9 to 2.6 and 1.8 to 2.1 nm over a similar IEC range of ~0.7 to ~2.5 mmol/g for membranes prepared from short, medium and long graft length polymers, respectively. Moreover, the ionic cluster size shows a substantially larger increase with IEC for membranes prepared from the short graft length series. For instance, as IEC increases from ~0.7 to ~2.5 mmol/g, the ionic cluster size increases by 50% for the short graft series, whereas an increase of only 17% is observed for the long graft series. Furthermore, the number density of the ionic clusters is also influenced by the ion content of the membranes, as summarized in Table 4.4. For the short graft membranes, the cluster number densities (measured in 2-dimensions) are estimated to be 21 and 19 ± 3 ionic clusters per 1000 nm² for the 0.7 and 2.5 mmol/g IEC samples, respectively. The cluster number density increases more significantly, from 25 to 35 ± 3 ionic clusters per 1000 nm², over a similar IEC range for the long graft membranes. The medium graft membranes show intermediate increases in number density upon increasing IEC. Thus, differences in the percolated ionic networks formed from polymers with different

graft lengths are small but significant. Pictorially, these differences are depicted in Figure 4.8. For the short graft series, as IEC increases, the ionic cluster size increases while the number of ionic clusters remains approximately the same (Figure 4.8a). In contrast, for the long graft series, as the ion content increases, the number of ionic clusters increases but the ionic cluster size remains nearly constant (Figure 4.8b).

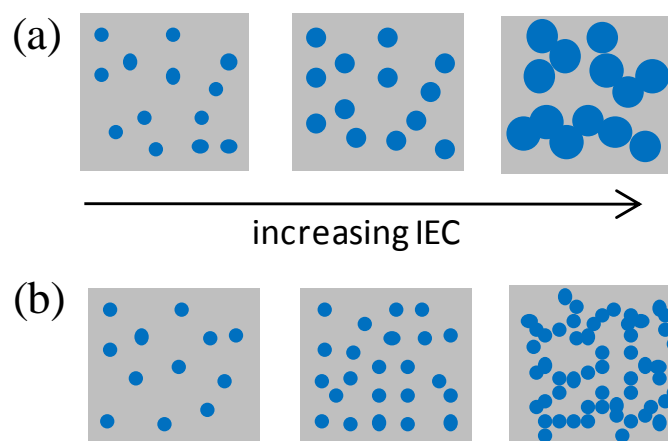


Figure 4.8 Schematic representation for the formation of a percolated ionic network: (a) increasing ionic cluster size but constant number of ionic clusters and (b) increasing number of ionic clusters but constant ionic cluster size.

Intuitively, the ionic cluster size is expected to increase with increasing PS graft length. However, as shown in Figure 4.7, the inverse is found to be true – membranes prepared from the shortest graft length series possessed larger ionic domains and, as graft length increases, the size of the ionic clusters decreases. This trend is accentuated for membranes possessing higher IEC. As summarized in Table 4.4, for membranes possessing IEC ~ 2.5 mmol/g, the average ionic cluster size decreases from 3.3 to 2.6 to 2.1 nm as the graft length transverses the series: short, medium, long. This is believed to be due to differences in the

degree of sulfonation (DS) of the PS side chain: for a given IEC, a higher degree of sulfonation is required for the short graft copolymers because they inherently contain a lower styrene content. For instance, to achieve an IEC of ~ 2.5 mmol/g, the short graft copolymers require a DS of 59%, whereas the long graft copolymers require only 33% (Table 4.2). A higher degree of sulfonation of the PS chains leads to a closer proximity between sulfonic acid groups along the graft chains. For example, for short graft copolymers possessing an IEC of 2.48 mmol/g (DS = 59%), every other styrene unit along the PS graft is sulfonated; in contrast, long graft copolymers, of IEC of 2.53 mmol/g (DS = 33%), possess polystyrene sulfonic acid groups that are separated by two non-sulfonated styrene units, on average. The closer proximity of the sulfonic acid groups in the short graft copolymers relieves steric hindrance imposed from the intervening PS chain and allows stronger electrostatic attractions between the sulfonic acid groups to be formed; thus, leading to larger and purer ionic aggregates.²⁰⁴ By inference, if the ionic clusters are more ionically pure, the surrounding hydrophobic polymer in which they are embedded is more hydrophobically pure. In the case of the long graft copolymers, as more ions are introduced to the polymer, additional ionic clusters are formed (increase in the cluster number density). This is attributed to the relatively greater distances between the sulfonic acid groups and subsequent reduced electrostatic interactions, i.e., the formation of larger clusters is inhibited. The differences in ionic domain size, domain purity, and domain continuity have a strong influence on the membrane's water sorption behavior, and hence proton conductivity, as will be shown later.

4.3.3 Water Sorption

Water sorption properties of the membranes are measured and expressed in terms of water content and molar ratio of water molecules to sulfonic acid group ($[\text{H}_2\text{O}]/[\text{SO}_3^-]$, often referred to as λ). Plots of water content versus IEC for the various series of P(VDF-co-CTFE)-*g*-SPS membranes are shown in Figure - 4.9a. As expected, within each graft length series, water content increases with ion content. A similar trend is observed in the plot of λ vs IEC as shown in Figure 4.9b. The water content and water uptake of Nafion 117 were measured to be 23 and 29 wt%, respectively. For a similar IEC to Nafion 117 (IEC = 0.91 mmol/g), water sorption by the graft membranes (11 – 16 wt%) was significantly less.

Water content and water uptake are important parameters that provide insights into the continuity of the hydrophobic domains and the ability of the fluoropolymer matrix to resist osmotic pressure forces. Lower values of λ indicate stronger elastic forces of the fluoropolymer matrix, and thus a greater ability to oppose osmotic pressure-driven swelling. When the osmotic pressure force exceeds the elastic forces of the matrix, dissolution occurs. The observation that the graft copolymer membranes absorb less water than Nafion reveals that the hydrophobic regions in the graft copolymers are well-interconnected and form a continuous network that allow exceedingly high IEC vinylic polymers to remain insoluble. A design feature found from this work is thus: continuous hydrophobic domains, facilitated by the formation of a high density of small nano-sized ionic clusters, enhance the elastic forces in the matrix and limit excessive swelling of

the membranes - allowing them to remain insoluble in water, even when the IEC is high.

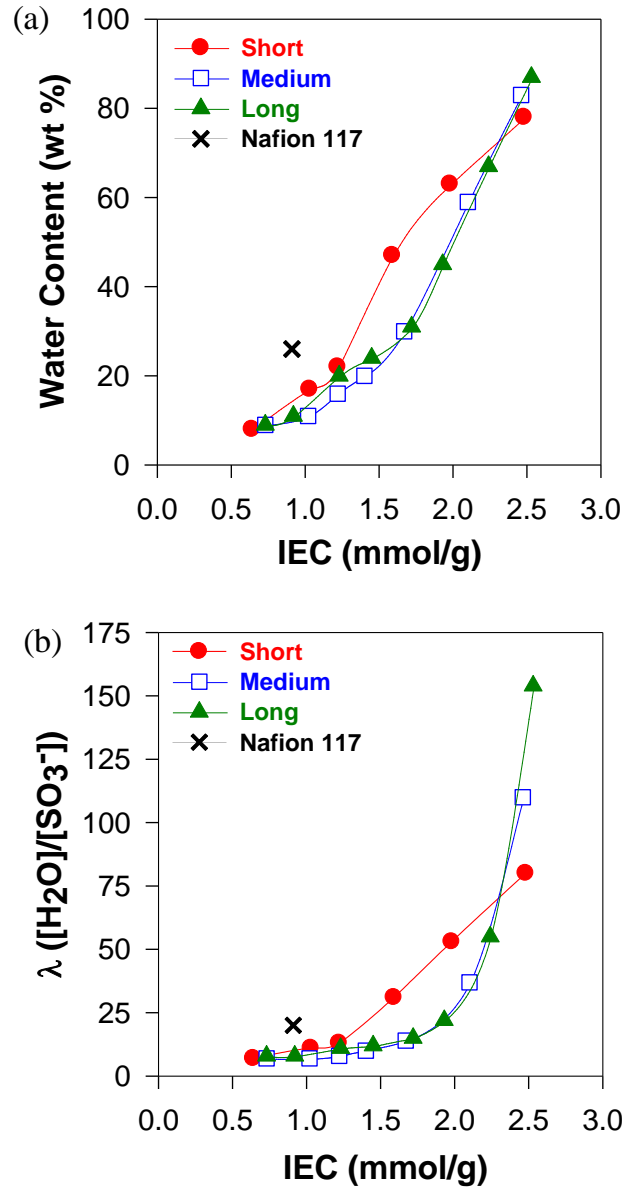


Figure 4.9 (a) Water content (wt %) vs. IEC and (b) λ vs. IEC for P(VDF-co-CTFE)-g-SPS having short (●), medium (□), and long (▲) graft chains.

To investigate the effects of graft chain length – and hence cluster size – on water sorption, membranes of similar IEC values but from different graft length

series are compared. As shown in Figures 4.9a and 4.9b, distinctive water sorption behaviours are observed which can be correlated to their graft lengths. For low IEC membranes (0.6 – 1.0 mmol/g), all three series absorb a similar amount of water regardless of the graft chain length. However, when IEC is increased beyond 1.0 mmol/g, the rate of increase of λ with IEC is considerably different for the three membrane series. For IECs ranging from 1.0 – 2.0 mmol/g, the short graft length series possesses a much sharper increase in λ while the medium and the long series increase more steadily and are indistinguishable within experimental error. Furthermore, the IEC threshold - beyond which water sorption increases sharply - is considerably lower for the short series (~1.20 mmol/g) than for the medium and the long series (~1.75 mmol/g). These results indicate that for intermediate IECs, membranes with longer graft chain lengths are less vulnerable to swelling; but in the high IEC regime, i.e., where proton conductivity is high, membranes prepared from the shorter graft lengths are less susceptible to swelling. The molecular and morphological bases for these phenomena are discussed below.

According to Eisenberg, Hird, and Moore,²⁰⁴ the morphology of random ionomers is characterized by formation of small ionic aggregates consisting of several ion pairs; these ionic aggregates are distributed randomly in a matrix of the host polymer. The formation of ionic aggregates is influenced by several factors including: the strength of the electrostatic interactions between ion pairs, the spatial proximity of the ion pairs, the chain flexibility of the host polymer, and steric hindrances. Because the partially sulfonated polystyrene graft chains in

P(VDF-co-CTFE)-*g*-SPS are essentially random ionomers, the model of Eisenberg *et al.*²⁰⁴ can be used to explain the differences observed in the swelling behavior. As shown previously by TEM (Figure 4.6), short graft membranes possess larger ionic cluster size than longer graft membranes. This is rationalized as being due to differences in the degree of sulfonation and the proximity of sulfonic acid groups. Proposed ionic aggregation for the short and long graft copolymers are schematically illustrated in Figure 4.10. In the short graft copolymers, the relatively higher degree of sulfonation and closer proximity of the sulfonic acid groups along the PS grafts increase electrostatic attractions among acid groups, resulting in larger ionic aggregates and more ionically pure domains, as illustrated in Figure 4.10a (left side). Furthermore, the lower styrene content results in the formation of a thinner shell of hydrophobic polystyrene matrix around the ionic aggregates, leading to a higher degree of water swelling in the low to intermediate IEC regime. In contrast, the long graft membranes possess smaller ionic aggregates due to a lower degree of sulfonation and wider spacing between acid groups. As the long graft copolymers possess higher styrene content, these ionic aggregates are surrounded by a thicker shell of polystyrene matrix, as illustrated in Figure 4.10b (left side). At low to intermediate IEC, it is postulated that the thicker polystyrene shell provides additional opposition to water swelling.

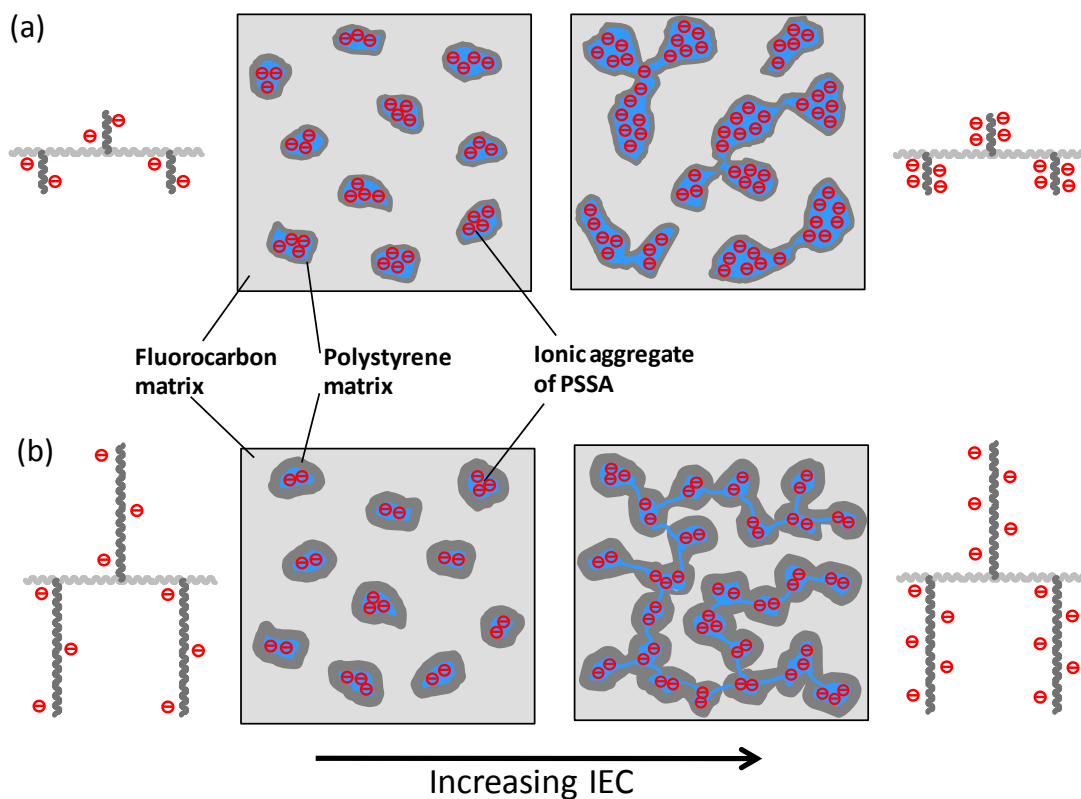


Figure 4.10 Schematic representation of the postulated ionic aggregation in P(VDF-co-CTFE)-g-SPS membranes with (a) short and (b) long graft length at different ion contents.

However, at high IEC (~ 2.50 mmol/g), the trend in water swelling is reversed. The short graft membranes exhibit significantly less swelling compared to the longer graft membranes. TEM analysis revealed that as IEC increases, the short graft membranes exhibit increasing ionic cluster size, but the number density of ionic clusters remains similar; thus, the ionic domains remain comparatively isolated, as shown pictorially in Figure 4.10a (right side). This allows a more contiguous fluorocarbon matrix and, therefore, reduced water swelling in the high IEC regime. In contrast, as IEC increases, membranes from the long graft series show an increase in the number of ionic clusters, although the size of ionic cluster remains nearly constant. The increase in the density of

ionic clusters leads to a smaller distance between ionic clusters and a more extensive percolation of ionic domains, as shown in Figure 4.10b (right side). This in turn might lead to greater water swelling in the long graft membrane at IEC of 2.50 mmol/g.

4.3.4 Wide-Angle X-ray Scattering^a

For Nafion[®] membranes, it is reported that increasing the crystallinity can lead to lower water swelling due to an increase in the elastic energy of the polymer matrix.^{216, 217} In the present work, wide-angle X-ray scattering (WAXS) was performed to probe the structure at molecular length scales and to determine the degree of crystallinity in the membranes.^a The fluorinated backbone in the P(VDF-co-CTFE)-*g*-PS graft copolymers consists of vinylidene difluoride (VDF) copolymerized with 5.8 mol% of chlorotrifluoroethylene (CTFE). Homopolymers of PVDF are highly crystalline polymers with poor solubility in common solvents.²¹⁸ Incorporation of the Cl atoms along the PVDF backbone perturbs the microstructural regularity, reduces crystallization, and results in improved solubility in common solvents. The WAXS spectra of membranes prepared from the P(VDF-co-CTFE) macroinitiator and the P(VDF-co-CTFE)-*g*-PS graft copolymers possessing various graft lengths are shown in Figure 4.11a. In the WAXS spectrum of the macroinitiator, the broad peak at a scattering wavevector q of 1.3 \AA^{-1} , corresponding to a feature size of 4.8 \AA , is associated with correlation distances between fluorinated polymer chains in the amorphous

^a WAXS data were collected and analyzed by Rasoul Narimani of Department of Physics, Simon Fraser University.

phase. A relatively sharp crystalline peak is observed on this broad peak, indicating the presence of crystallinity. Two Gaussian peaks were fitted to the data to distinguish the crystalline peak from the broad amorphous peak (Figure 4.11b) and the percent of crystallinity, x_{cr} , was quantified using the ratio of scattering from the crystalline domains to the overall scattering, as follows:²¹⁹

$$x_{cr} = \frac{I_{cr}}{I_{cr} + I_{am}} \times 100\% \quad \text{Equation 4.6}$$

where I_{cr} and I_{am} are the integrated signals of the crystalline and the amorphous peak, respectively. It was calculated that the percent of crystallinity in the P(VDF-co-CTFE) macroinitiator is $12 \pm 1\%$.

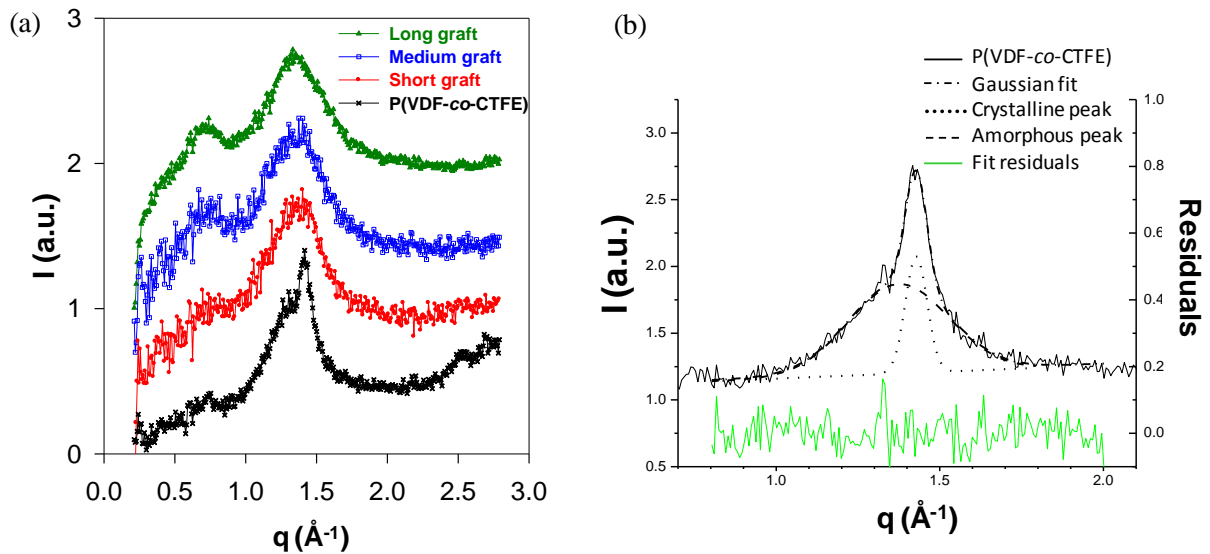


Figure 4.11 (a) WAXS spectra for membranes of P(VDF-co-CTFE) macroinitiator and P(VDF-co-CTFE)-g-PS of various graft lengths (measured under ambient conditions, intensity scale is in arbitrary units). (b) Fitting of the scattering data with two Gaussians for identifying of the amorphous peak and the crystalline peak (note: lower curve shows the residuals from the fit).^b

^b WAXS data were collected and analyzed by Rasoul Narimani of Department of Physics, Simon Fraser University.

In the WAXS spectra of the resultant P(VDF-co-CTFE)-*g*-PS graft copolymers (Figure 4.11a), a broad peak is observed at a similar q -range, however, the crystalline peak is either dramatically reduced or virtually absent. The percent of crystallinity is estimated to be 4 ± 2 , 2 ± 1 and ~ 0 % for the short, medium, and long graft membranes, respectively. The reduction in crystallinity is attributed to steric hinderance of the polystyrene side chains which inhibits the crystallization of the fluorinated backbone. Since all three graft copolymers possessed poor crystallinity, the differences in water swelling between membranes with different graft lengths is unlikely to be due to differences in crystallinity. An additional broad peak at $q \sim 0.7 \text{ \AA}^{-1}$, corresponding to a feature size of 9 \AA , is observed in the WAXS spectra of the graft copolymer membranes. It is postulated that this peak is associated with the correlation distances between polystyrene chains since its intensity is increasing with increasing PS graft length.

The effect of sulfonation on crystallinity was also investigated. The WAXS spectra of the *short* graft membranes with various degrees of sulfonation are shown in Figure 4.12. The percent of crystallinity was found to remain nearly constant (~ 4 %) with increasing sulfonation. Similar observations (not shown) were found in membranes from the longer graft series. These results indicate that incorporation of sulfonic acid groups does not influence the crystallinity of the membranes, which is inherently low.

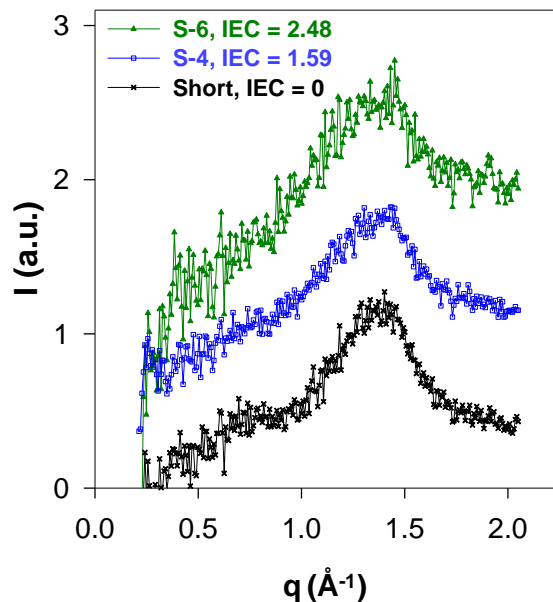


Figure 4.12 WAXS spectra for short graft membranes of various degrees of sulfonation (measured under ambient conditions, intensity scale is in arbitrary units).^c

4.3.5 Proton Conductivity

In Figure 4.13a, proton conductivity is plotted as a function of IEC for the various series of P(VDF-co-CTFE)-*g*-SPS membranes. As expected, within each series, proton conductivity generally increases with IEC. The critical IEC beyond which proton conductivity increases sharply with ion content is very similar for each series and occurs between 0.9 and 1.0 mmol/g.

^c WAXS data were collected and analyzed by Rasoul Narimani of Department of Physics, Simon Fraser University.

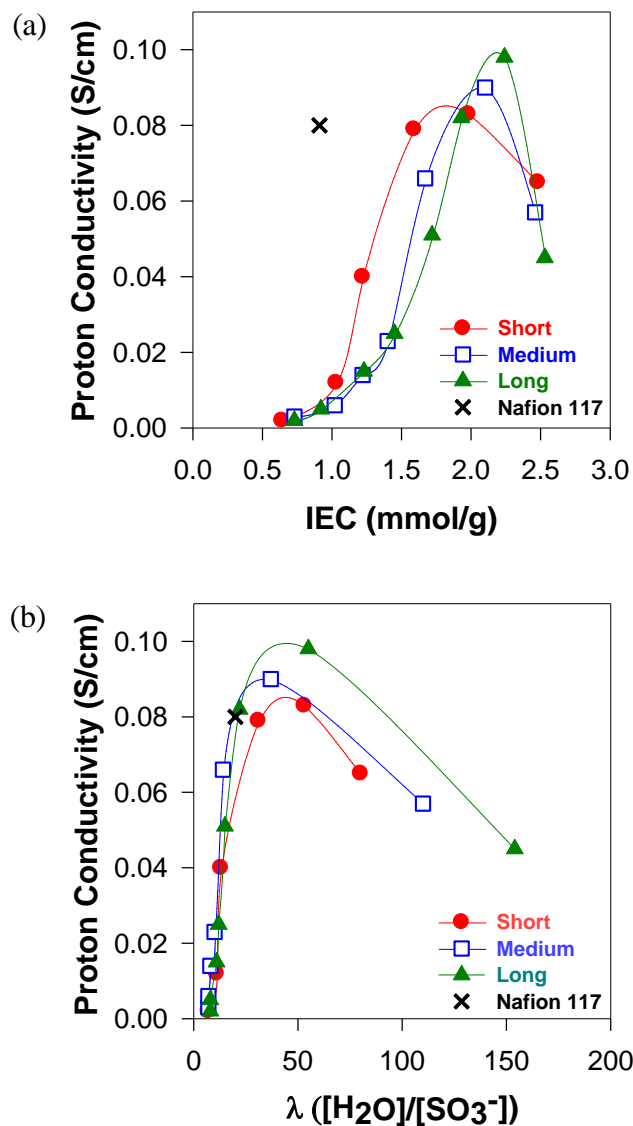


Figure 4.13 (a) Proton conductivity vs. IEC and (b) proton conductivity vs λ for P(VDF-co-CTFE)-g-SPS membranes having short (●), medium (□), and long (▲) graft lengths.

For intermediate IECs (1.0 – 1.5 mmol/g), the short graft membranes show a sharper increase in proton conductivity with IEC (Figure 4.13a). At high ion contents (IEC > 2.0 mmol/g), proton conductivities for all three series are observed to reach a maximum or even drop with further increase in IEC. This is due to the proportionally larger amounts of water absorbed at high ion contents,

which leads to acid dilution. In Figure 4.14a, acid concentration in hydrated membranes is plotted as a function of IEC. It is observed that membranes prepared from short graft polymers show a decrease in acid concentration as IEC increases above 1.20 mmol/g, because these membranes swell to a greater extent in this IEC regime (Figure 4.9). The highest proton conductivity obtained in this work was observed in membrane from the long series (L – 7: 0.095 S/cm at 2.24 mmol/g IEC), however the “window” of IEC over which the long graft chain membranes exhibit relatively high proton conductivity is quite narrow because at low IEC they absorb too little water while at high IEC they absorb too much. In contrast, the IEC “window” of high conductivity increases for the medium and short series. For the very high IEC membranes (~2.50 mmol/g), it is the shorter graft chain polymers that provide the higher conductivity because in this region, the water content is relatively lower and the acid concentration, higher.

A deeper understanding of the observed trends in proton conductivity can be obtained by studying proton conductivity as a function of λ (Figure 4.13b). It is reported that the proton conductivity of perfluorosulfonic acid membranes increases significantly when λ values are > 6 .²⁰⁸ Proton conductivity values for all three series are similar for λ values ranging between 10 – 15. At $\lambda > 20$, it can be seen that the ordering of conductivity is *long* $>$ *medium* $>$ *short*. The maximum conductivity values were observed in the region of $\lambda = 40 – 50$, which is similar to that observed for other polymer systems,¹⁸² and serve as an empirical guideline in the design of proton conducting membranes.

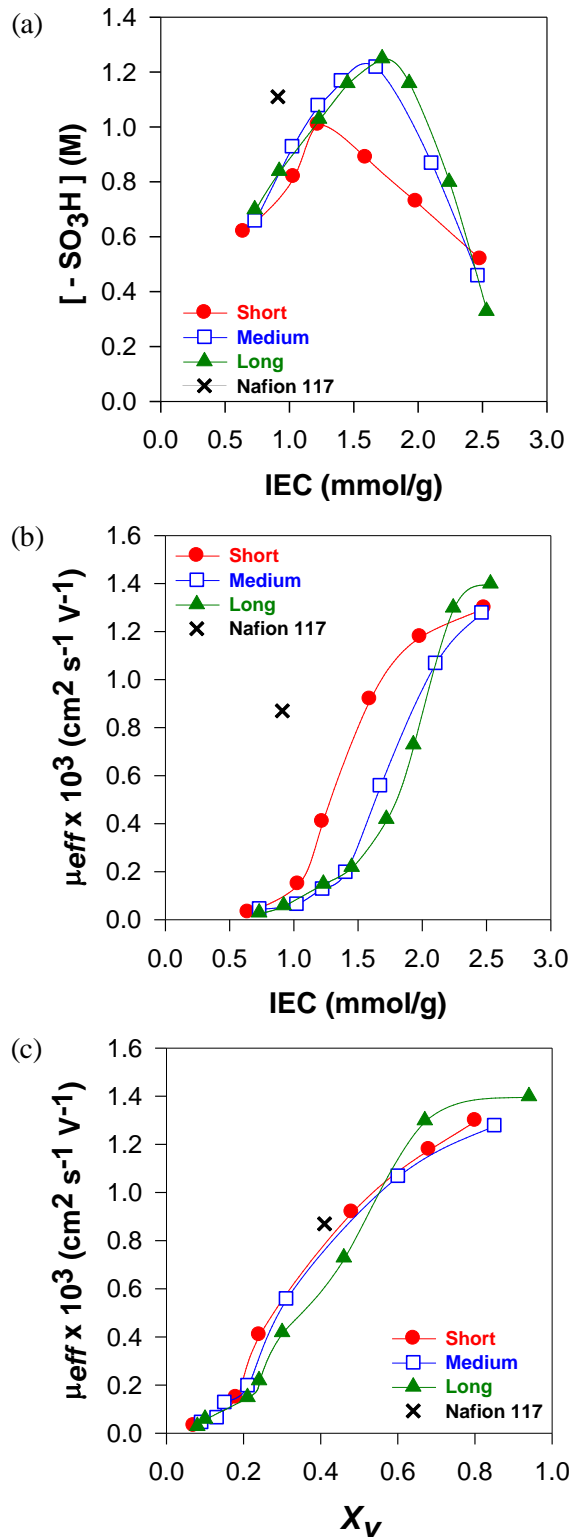


Figure 4.14 (a) Analytical $[-SO_3H]$ in hydrated membranes vs. IEC, (b) effective proton mobility (μ_{eff}) vs. IEC and (c) μ_{eff} vs. water volume fraction (X_v) for P(VDF-co-CTFE)-g-SPS membranes having short (\bullet), medium (\square), and long (\blacktriangle) graft lengths.

The *effective* proton mobility, μ_{eff} , allows the “normalized” proton conductivity to be determined, i.e., the effects of acid concentration on conductivity are removed. *Effective* proton mobilities provide useful insights into the extent of acid dissociation, ionic channel tortuosity and spatial proximity of neighboring acid groups.¹⁸² A plot of μ_{eff} versus IEC is shown in Figure 4.14b. Membranes prepared from *short* graft polymers possessed significantly greater proton mobility because these membranes possess higher water contents, which promote the dissociation of protons from the tethered sulfonic groups and form a more contiguous path for protons. A plot of μ_{eff} versus water volume fraction (X_v) is illustrated in Figure 4.14c. Proton mobilities appear to be independent of graft length but simply increase with water volume fraction until maximum value is reached. To remove the effects of the different acid strengths, the μ_{eff} was calculated at $X_v = 1.0$ by performing linear regressions, and the results are summarized in Table 4.5. The μ_{eff} at $X_v = 1.0$ are 1.75 , 1.65 and $1.66 \times 10^{-3} \text{ cm}^2 \text{ s}^{-1} \text{ V}^{-1}$ for short, medium and long graft membranes, respectively. These mobility values are significantly lower than the theoretical mobility of a free proton in water at infinite dilution ($3.63 \times 10^{-3} \text{ cm}^2 \text{ s}^{-1} \text{ V}^{-1}$ at $25 \text{ }^\circ\text{C}$).²²⁰ This may be a result of the tortuosity of the ionic pathways and the tethered $-\text{SO}_3^-$ groups. It is interesting to note that these μ_{eff} at $X_v = 1.0$ values are comparable to those of other PEM systems, i.e., 1.6 , 2.3 and $2.6 \times 10^{-3} \text{ cm}^2 \text{ s}^{-1} \text{ V}^{-1}$ for BAM[®], Nafion[®] and poly(ethylene-co-tetrafluoroethylene)-*g*-poly(styrene sulfonic acid) [ETFE-*g*-PSSA], respectively.¹⁸³

Table 4.5 Extrapolated Proton Mobility Values at Infinite Dilution ($X_v = 1.0$)

Polymers	μ_{eff} at $X_v = 1.0$ ($\times 10^{-3} \text{ cm}^2 \text{ s}^{-1} \text{ V}^{-1}$)	reference
Short graft	1.75	this work
Medium graft	1.65	this work
Long graft	1.66	this work
BAM [®]	1.6	183
Nafion [®]	2.3	183
ETFE- <i>g</i> -PSSA	2.6	183

4.3.6 Conductivity as a Function of Temperature and Humidity

Proton conductivity of polymer electrolyte membranes is known to be dependent upon both temperature and water content,⁶ and thus investigating how external conditions influence the conductivity is important for identifying the limitations of operation. Generally, for a given humidity, proton conductivity increases with temperature, and this is attributed to the activation barrier for proton motion, for which absorbed water is a highly influential factor. For example, the conductivity of Nafion 117 under 100 % RH increases from 0.1 to 0.2 S/cm when the temperature is raised from 30 to 85 °C.¹³ However, at higher temperature (> 90 °C), dehydration becomes a predominant factor, and adversely affects proton conductivity. Furthermore, at a constant temperature, conductivity decreases as RH is decreased. In the case of Nafion 117, at 30 °C the conductivity decreases from 0.066 to 0.00014 S/cm as RH decreases from 100% to 34%.²²¹

The effects of temperature and humidity on proton conductivity was investigated using membranes from the long grafts series with high IEC values

(i.e., L-5, L-6, L-7 possessing IECs of 1.72, 1.93 and 2.24, respectively). At ambient temperature and humidity, these membranes exhibit high proton conductivity (0.051 – 0.098 S/cm) and intermediate swelling ($\lambda = 15 - 55$) and high acid concentration (1.25 – 0.8 mol/L). It is therefore worthwhile to investigate their conductivity under various environmental conditions. As shown in Figure 4.15a, at a constant temperature of 30 °C, proton conductivity increases with relative humidity, and since water sorption is directly related to the humidity, these data represent a change in conductivity with water content. At low RH (< 65%), dehydration of the membranes reduces the fraction of liquid-like water, leading to low conductivity (< 0.01 S/cm). Conductivity increases more sharply with RH for membranes possessing higher IEC. For instance, as RH increases from 75 to 95 %, the conductivity increases from 0.016 to 0.089 S/cm for membrane L-7 (IEC = 2.24 mmol/g), whereas the conductivity increases steadily from 0.011 to 0.022 S/cm for membrane L-5 (IEC = 1.72 mol/g). This can be explained by the change in water uptake with relative humidity, as shown in Figure 4.15b. As expected, all three graft membranes, as well as Nafion[®] 117, exhibit a substantial increase in water sorption with RH. However, the rate of increase in water uptake is significantly greater for membranes with higher IEC. For instance, for the RH range 75 – 95%, water uptake increases from 15 to 44% and from 10 to 25% for membranes L-7 and L-5, respectively. The dramatic increase in the water uptake of membrane L-7 is likely the cause of the sharp increase in proton conductivity with RH.

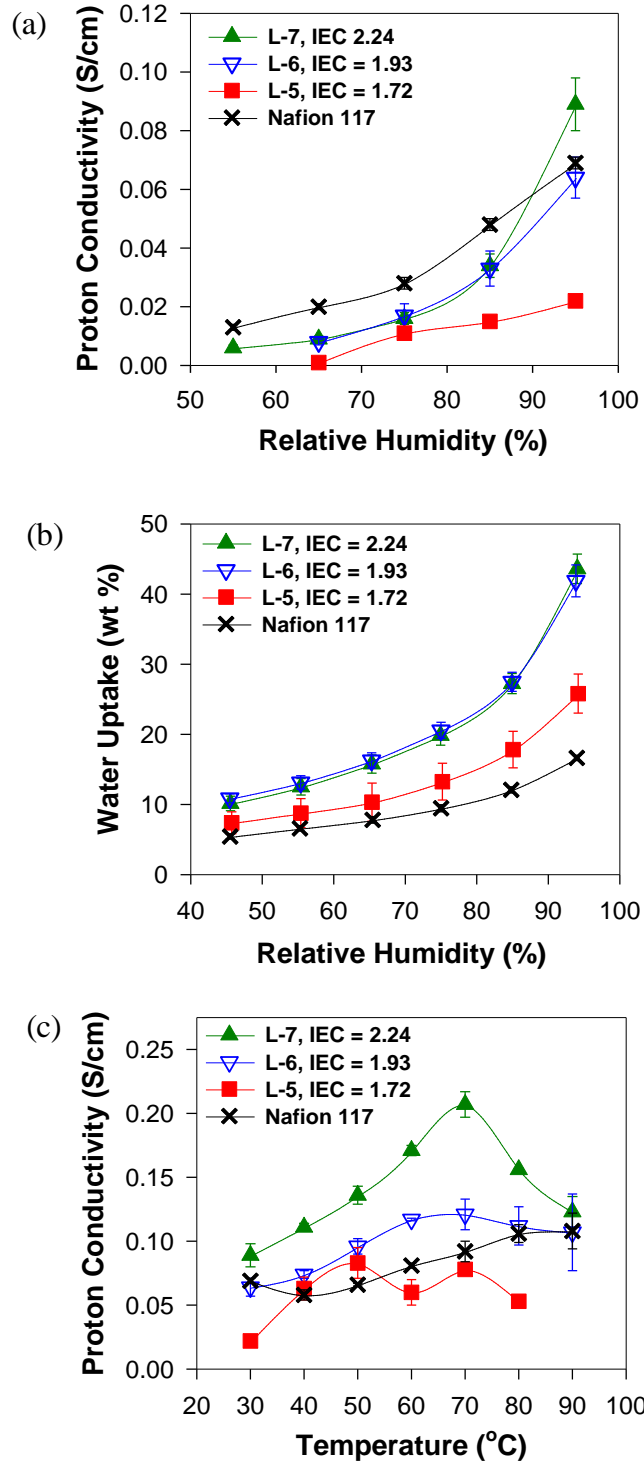


Figure 4.15 (a) Proton conductivity vs. relative humidity, at 30 °C; (b) water uptake vs. relative humidity, at 25 °C; and (c) proton conductivity vs. temperature, at 95 % RH, for selected P(VDF-co-CTFE)-*g*-SPS membranes from long graft series and Nafion® 117.

The relationship between proton conductivity and temperature for selected long graft membranes, under a constant RH of 95%, is shown in Figure 4.15c. The conductivity of the graft membranes (L-5, L-6, L-7) increases with temperature to a maximum value, after which conductivity drops with further increase in temperature. The temperature at the maximum conductivity increases as the ion content increases. For instance, the maximum conductivity is observed at 50 °C, 60 °C and 70 °C for membranes with IEC of 1.72, 1.93 and 2.24 mmol/g, respectively. This indicates that graft membranes possessing higher ion content are less susceptible to dehydration, and therefore exhibit a more continuous increase in conductivity over a greater temperature range. The drop in proton conductivity at temperatures > 70 °C is due to excessive swelling and acid dilution.

From Arrhenius plots (i.e., natural logarithm of conductivity vs $1000/T$), as shown in Figure 4.16, the activation energy for proton transport are found to be 27.5, 17.3, and 18.3 kJ/mol for the graft membranes possessing IECs of 1.72, 1.93, and 2.24 mmol/g, respectively. These values are comparable with that found for Nafion 117, 14.1 kJ/mol (reported values are 7.8,²²² 9.6,¹³ and 13.5²²³ kJ/mol), and with the reported values of 12.9 kJ/mol for P(VDF)-*g*-SPS by Zhang *et al.*²¹⁵ The activation energies for proton conduction through P(VDF-*co*-CTFE)-*g*-SPS membranes show decreasing values (from 27.5 to 18.3 kJ/mol) as IEC increases. This observation agrees with the experimental data for P(VDF-*co*-HFP)-*b*-SPS diblock copolymer membranes where the activation energy is reported to fall from 25.7 to 17.1 kJ/mol as IEC increases from 0.72 to 1.18

mmol/g.¹⁹⁴ As shown previously in the TEM images (Figure 4.6), membranes with lower IEC form smaller, more isolated ionic clusters; thus, the energy barrier for both water swelling and proton motion are greater.

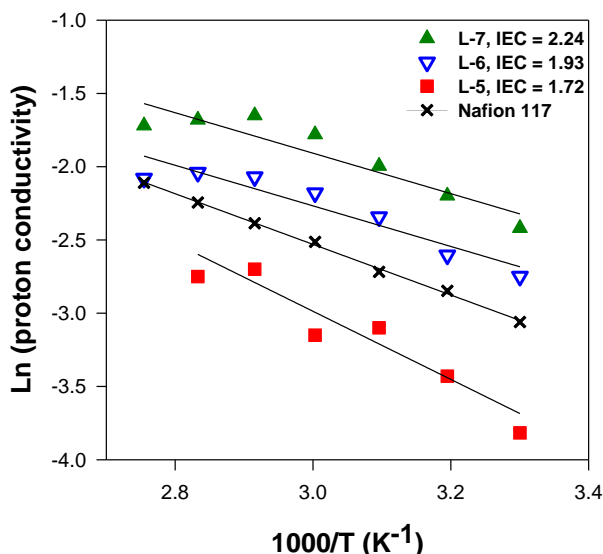


Figure 4.16 Plots of natural logarithm of proton conductivity vs $1000/T$ (K^{-1}) for P(VDF-co-CTFE)-g-SPS membranes and Nafion[®] 117.

4.4 Conclusion

Graft copolymers of partially sulfonated poly([vinylidene difluoride-co-chlorotrifluoroethylene]-g-styrene) [P(VDF-co-CTFE)-g-SPS] were devised and synthesized for a systematic study of the effects of graft chain length on PEM membrane properties. Three parent copolymers of P(VDF-co-CTFE)-g-PS were synthesized possessing similar graft density but different graft chains. Each of the three P(VDF-co-CTFE)-g-PS parent copolymers were sulfonated to different extents to provide three series of P(VDF-co-CTFE)-g-SPS membranes with various ion contents. The shorter graft length copolymer provided membranes with larger ionic clusters although the cluster size in all the membranes was

unusually small (2 – 4 nm) – much smaller than those found for Nafion (5 – 10 nm). The extent of sulfonation and the proximity of sulfonic acid groups along the polystyrene grafts are found to influence the cluster size, and by inference, the ionic purity of the clusters. The formation of larger ionic clusters in the short graft series led to a greater water uptake in the low to intermediate IEC regime, but the reverse for high IEC membranes. The lower degree of sulfonation and smaller ionic clusters found for long graft membranes led to a high fraction of hydrophobic polystyrene surrounding the ionic clusters, leading to lower swelling and higher acid concentration; although proton mobility was lower because of the lower extent of hydration. The smaller ionic cluster in the long graft membranes also allowed them to retain more water at low humidity conditions (2–3 times greater than that of Nafion[®]), and maintain proton conduction at temperatures > 70 °C and over wide humidity ranges.

Research on the synthesis and characterization of fluorosulfonic-ionic graft copolymers with varied graft number density, and the effect on proton conductivity and morphology, is underway to further examine the structure-property relationships for this system. While it is recognized that sulfonated polystyrene-based systems may not be sufficiently stable under fuel cell operating conditions, this work clearly demonstrates that polymer microstructure, particularly graft length and sulfonic acid proximity, can be manipulated further to play a profound role in determining membrane morphology and ionic conductivity. These concepts should provide valuable insights into the design of PEMs for fuel cell applications.

Chapter 5. Fluorous-Ionic Copolymers: Diblocks versus Grafts

[Reprinted in parts with permission from *Journal of the American Chemical Society*, Tsang, E. M. W.; Zhang, Z.; Shi, Z.; Soboleva, T.; Holdcroft, S. 129. 15106, © 2007, American Chemical Society.]

5.1 Introduction

The nanostructure and morphology of a membrane are believed to play a profound role on its proton conduction.^{106, 107} Using various scattering techniques, the nanostructure of Nafion membranes has been characterized as a network of ionic aggregates embedded in a hydrophobic perfluorinated polymer matrix.^{115-118, 125} In the presence of water, the ionic clusters swell to provide continuous ionic channels for proton transport.^{14, 115, 116} However, there is not yet a comprehensive understanding of how polymer architecture influences ionic aggregation and morphology of the membrane, and in turn, influences physicochemical properties such as proton transport and water sorption. Questions concerning the preference of diblock, multiblock, graft, or random ionic copolymers for proton conducting media are relatively unexplored.^{106, 107} Thus, there exists a need to develop and investigate model polymer systems, with systematically controlled chemical composition and polymer architecture, to facilitate elucidation of fundamental structure-property relationships in PEMs and thereby, gain insights into membrane design and preferred structures.

Ding *et al.*^{160, 162} studied structure-property relationships in PEMs using model graft polymers comprising of styrene main chain and sulfonated styrene graft chains (PS-*g*-PSSA). These amphiphilic graft copolymers form ionic aggregates in a hydrophobic matrix. Compared to random copolymers of styrene and sulfonated styrene (PS-*r*-PSSA), the more structurally ordered PS-*g*-PSSA provided significantly higher proton conductivity. Through TEM analysis, it was observed that PS-*g*-PSSA membranes exhibited nanophase-separated morphologies consisting of a continuous network of ionic channels, whereas PS-*r*-PSSA exhibited no sign of phase separation. These results suggested that directing acid groups onto particular segment(s) in a polymer promotes microphase separation and thereby, enhances proton transport.^{160, 162}

Hickner *et al.*¹⁶⁸ reported the preparation of midblock-sulfonated triblock copolymers to investigate how the location of the sulfonated block as well as the composition and properties of the unsulfonated blocks influence proton transport properties. ABA triblock with an ionic center block provided higher proton transport over a wide range of RH values. Another study on structure-property relationships in PEM was reported by Okamoto *et al.*²²⁴ using sulfonated polyimides. It was reported that improvements in microphase separation and proton conductivity could be achieved by separating the sulfonic acid group from the polymer backbone by means of a short graft chain. A similar study by Watanabe *et al.*²²⁵ revealed that polyimides with sulfonic acid bearing side chains provide enhanced proton transport.

In Chapters 3 and 4, the syntheses and characterization of model diblock and graft copolymers containing both fluorinated and sulfonated polystyrene segments have been described. Diblock copolymers of partially sulfonated poly([vinylidene difluoride-*co*-hexafluoropropylene]-*b*-styrene) [P(VDF-*co*-HFP)-*b*-SPS]^{193, 194} possessed a hydrophobic fluorinated segment linearly connected to an ionic sulfonated styrenic segment (Figure 5.1a); whilst graft copolymers of partially sulfonated poly([vinylidene difluoride-*co*-chlorotrifluoroethylene)-*g*-styrene) [P(VDF-*co*-CTFE)-*g*-SPS]²⁰⁷ consisted of a hydrophobic fluorinated backbone with ionic sulfonated styrenic side chains (Figure 5.1b). In this chapter, a direct comparison between these two related model polymer systems for investigating the role of polymer architecture on membrane morphology and properties is described. The diblock and the graft copolymers used for this study contain a similar ratio of fluorinated to styrene components, and similar chemical compositions, but distinct macromolecular architecture. Both copolymers were sulfonated to different degrees to provide two series of ionic copolymers, which were cast into membranes possessing varying ion exchange capacity (IEC). Comparison between these two series of chemically-related but architecturally-distinct membranes reveal that polymer architecture significantly affects the morphology of the membranes, and in turn, their respective properties.

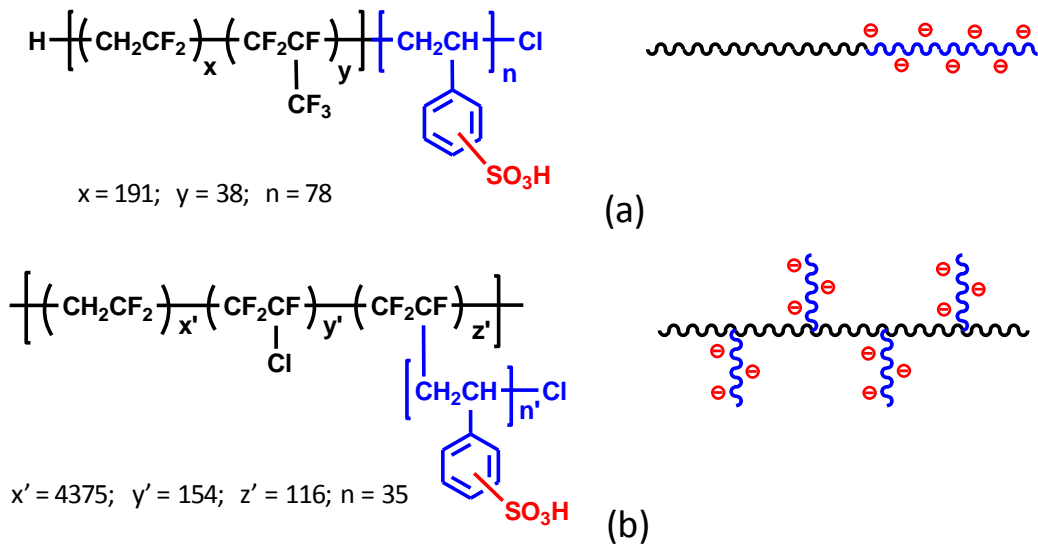


Figure 5.1 Chemical structures of (a) P(VDF-*co*-HFP)-*b*-SPS diblock and (b) P(VDF-*co*-CTFE)-*g*-SPS graft copolymers.

5.2 Experimental Section

5.2.1 Materials

Diblock copolymers of partially sulfonated poly([vinylidene difluoride-*co*-hexafluoroisopropylidene]-*b*-styrene) [P(VDF-*co*-HFP)-*b*-SPS] were synthesized according to a procedure reported by Shi *et al.*^{193, 194} The synthesis involved the atom transfer radical polymerization (ATRP) of styrene initiated by a trichloromethyl-terminated fluoropolymer macroinitiator, P(VDF-*co*-HFP), followed by post-sulfonation. A detailed procedure for this synthesis is previously described in Section 3.2.2. Graft copolymers of partially sulfonated poly([vinylidene difluoride-*co*-chlorotrifluoroethylene]-*g*-styrene) [P(VDF-*co*-CTFE)-*g*-SPS] were synthesized by *graft*-ATRP of styrene from a fluoropolymer macroinitiator, P(VDF-*co*-CTFE), followed by post-sulfonation.²⁰⁷ The experimental procedure of this synthesis is given in Sections 4.2.2 – 4.2.4. For

both the diblock and the graft copolymers, post-sulfonation reactions using acetyl sulfate were carried out to various degrees to provide a series of ionic copolymers of different ion content.

As received Nafion[®] 117 (Du Pont) membranes were pretreated by boiling sequentially in 3 vol% hydrogen peroxide, 0.5 M sulfuric acid, and Milli-Q water (18 M Ω , Millipore Systems) for 2 h period, and stored in Milli-Q water prior to use.

5.2.2 Membrane Preparation and Characterization

Membranes were prepared by dissolving the sulfonated polymers in their respective solvents (P(VDF-*co*-HFP)-*b*-SPS in THF and P(VDF-*co*-CTFE)-*g*-SPS in *N,N*-dimethylacetamide) and casting on a levelled Teflon[®] sheet. Polymer films were dried at ambient temperature for 24 h and then at 60 °C under vacuum for 24 h. The membranes (~100 μ m thick) were converted to the protonic form by immersing in aqueous hydrochloric acid (HCl, 2 M) for 24 h. The protonated membranes were washed repeatedly with Milli-Q water for 30 min periods and placed in water overnight to remove excess acid on the surface and the interior of the membranes.

The ion exchange capacities (IEC, mmol/g) were determined by direct titration of the protons released from the membranes in 2 M sodium chloride (NaCl) with standardized sodium hydroxide (NaOH) solutions. The IECs were represented as the millimoles of ionic exchange sites per gram of dry membrane. A detailed description of the method used is given in Section 2.5.3.

The water uptake was calculated as the percentage increase in mass for a membrane changing from dry state to water-saturated state. Water content was calculated both as a mass and a volume percentage of water in a fully hydrated membrane. Water content is also represented as the ratio of the moles of water to the moles of ion exchange sites. This value provides a measure of the average number of water molecules per ion exchange site ($[\text{H}_2\text{O}]/[\text{SO}_3^-]$, often referred to as λ value). Detailed descriptions of the above water sorption measurements are given in Section 2.5.2.

The analytical acid concentration was determined as moles of sulfonic acid moieties per unit volume of hydrated membrane, as described in Section 2.5.3 .

The *effective* proton mobility (μ_{eff}) was calculated as a normalized proton conductivity where acid concentration effects were removed (Equation 5.1). A detailed description of the calculation is given in Section 2.5.5.

$$\mu_{eff} = \frac{\sigma}{F [-\text{SO}_3\text{H}]} \quad \text{Equation 5.1}$$

where F is Faraday's constant and σ (S cm^{-1}) is the proton conductivity.

5.2.3 Instrumentation and Techniques

The molecular weight of the macroinitiators and the resulting copolymers were estimated by gel permeation chromatography (GPC) using three Waters Styragel HT columns, a Waters 1515 isocratic HPLC pump, a Waters 2414 differential refractometer, and a Waters 2487 dual UV absorbance detector ($\lambda=$

254). For P(VDF-co-HFP)-*b*-PS diblock copolymers, THF eluant with a column temperature of 25 °C was employed; whereas for P(VDF-co-CTFE)-*g*-PS graft copolymers, DMF (0.01 M LiBr) eluant at 50 °C was used. Polystyrene standards were used for calibration. ¹H NMR spectra were obtained on a 500 MHz Varian Inova spectrometer. ¹⁹F NMR spectra were recorded on a 400 MHz Varian MercuryPlus spectrometer, and chemical shifts were measured with respect to trichlorofluoromethane (CFCl₃).

In-plane and *through-plane* proton conductivities were measured by ac impedance spectroscopy with a Solartron 1260 frequency response analyzer employing a two-electrode configuration, according to a procedure described elsewhere.^{144, 180} A 100 mV sinusoidal ac voltage over a frequency range of 10 MHz to 100 Hz was applied to obtain Nyquist plots. Data was analyzed using commercial Z plot/Z view software (Scribner Associates). A detailed explanation of the method is included in Section 2.5.4. The degree of conductivity anisotropy was calculated as the ratio of in-plane (average of X and Y directions) to through-plane conductivity (Z direction).

Samples for transmission electron microscopy (TEM) were prepared as follows: membranes were stained by soaking in a saturated lead acetate solution for 24 h, then rinsed with water, and dried under vacuum at room temperature for 4 h. The stained membranes were embedded in Spurr's epoxy and cured for 8 h at 60 °C. The samples were sectioned to yield slices 60 – 100 nm thick using Leica UC6 ultramicrotome and picked up on copper grid. Electron micrographs were taken with a Hitachi H7600 TEM using an accelerating voltage of 80 kV.

5.3 Results and Discussion

5.3.1 Preparation of Diblock and Graft Ionic Copolymers

Diblock copolymers of partially sulfonated poly([vinylidene difluoride-co-hexafluoropropylene]-*b*-styrene) [P(VDF-co-HFP)-*b*-SPS] were prepared by the atom transfer radical polymerization (ATRP) of styrene onto a CCl₃-terminated fluoropolymer macroinitiator [P(VDF-co-HFP), $M_{n, GPC} = 17\,900$ g/mol, 84 ± 2 mol% VDF and 16 ± 2 mol% HFP], followed by post-sulfonation.^{193, 194} The synthetic scheme is previously demonstrated in Figure 3.2. Gel permeation chromatography (GPC) and NMR spectroscopy were employed to verify each reaction step and to determine the molecular weights of the block segments. A detailed description of the characterization method is described previously in Section 3.3.1. The number-average molecular weight (M_n) of the fluororous and the styrene segments were estimated to be 17 900 g/mol and 10 400 g/mol, respectively.

Graft copolymers of partially sulfonated poly([vinylidene difluoride-co-chlorotrifluoroethylene]-*g*-styrene) [P(VDF-co-CTFE)-*g*-SPS] were prepared via graft-ATRP of styrene onto a fluoropolymer macroinitiator synthesized with controlled Cl content [P(VDF-co-CTFE), $M_{n, GPC} = 312\,000$ g/mol, 6 ± 1 mol% CTFE], followed by postsulfonation. The synthetic scheme is illustrated previously in Figure 4.1. The fluoropolymer macroinitiator and the resulting graft copolymers were characterized by GPC and NMR spectroscopy. The details of the characterization method are described in Section 4.3.1. The fluororous backbone possessed a $M_{n, GPC}$ of 312 000 g/mol. The combined molecular weight

of all styrene graft chains was estimated to be 212 000 g/mol by ^1H NMR spectroscopy.

The chemical compositions of the diblock and the graft copolymers are summarized in Table 5.1. These two model polymer systems were synthesized so as to contain similar chemical compositions and similar polystyrene content (~40 wt% polystyrene). However, they possessed distinct macromolecular architectures, as previously illustrated in Figure 5.1: P(VDF-*co*-HFP)-*b*-SPS diblock copolymers possessed a hydrophobic fluoruous segment linearly attached to an ionic sulfonated styrenic segment, whereas P(VDF-*co*-CTFE)-*g*-SPS graft copolymers consisted of a hydrophobic fluoruous backbone with ionic sulfonated styrene side chains. Both the diblock and the graft copolymers were sulfonated to different degrees to provide two series of copolymers, which were cast into membranes possessing varying ion exchange capacity (IEC), as summarized in Table 5.2. A direct comparison between these two series of chemically-related but architecturally-distinct copolymers allows an investigation of structure-property relationships in proton exchange membranes. Specifically, the effect of polymer architecture on membrane morphology and properties are examined. The measured IEC, proton conductivities and water sorptions of the membranes are also listed in Table 5.2.

Table 5.1 Chemical Compositions of P(VDF-co-HFP)-*b*-PS Diblock and P(VDF-co-HFP)-*g*-PS Graft Copolymers

Copolymer	$M_{n,GPC}^a$ of Fluoropolymer (g/mol)	$M_{n,GPC}^b$ of PS (g/mol)	$M_{n,NMR}^c$ of PS (g/mol)	Wt % of PS ^d
Diblock	17 900	8 700	10 400	37
Graft	312 000	136 000 ^e	212 000 ^e	40

^a Measured by gel permeation chromatography (GPC), calibrated with linear PS standards.

^b Calculated from GPC, using difference between M_n of the resulting copolymer and M_n of fluoropolymer macroinitiator.

^c Based on ¹H NMR using mole ratio of Styrene:VDF.

^d Based on the molecular weights estimated from NMR data.

^e Combined molecular weight of all polystyrene graft chains.

Table 5.2 Properties of P(VDF-co-HFP)-*b*-SPS Diblock and P(VDF-co-CTFE)-*g*-SPS Graft Copolymer Membranes

Membrane ^a	DS ^b (%)	IEC ^c (mmol g ⁻¹)	Proton Conductivity ^d (S cm ⁻¹)	Water Content ^e (wt %)	λ ^e	[-SO ₃ H] ^f (M)	χ_v ^g	$\mu_{eff} \times 10^3$ (cm ² s ⁻¹ V ⁻¹)
D1	12 ± 2	0.26 ± 0.01	0.0002 ± 0.0001	2 ± 1	3 ± 1	0.33 ± 0.03	0.02	0.01
D2	17 ± 2	0.53 ± 0.02	0.0025 ± 0.0002	2 ± 1	2 ± 1	0.61 ± 0.02	0.02	0.04
D3	22 ± 3	0.72 ± 0.08	0.016 ± 0.002	12 ± 2	11 ± 1	0.77 ± 0.03	0.15	0.22
D4	32 ± 2	0.89 ± 0.03	0.055 ± 0.001	28 ± 3	24 ± 2	0.86 ± 0.10	0.37	0.66
D5	40 ± 3	1.18 ± 0.09	0.080 ± 0.002	47 ± 2	42 ± 6	0.69 ± 0.04	0.52	1.20
D6	49 ± 2	1.31	0.076	80	165	0.32	0.95	2.46
G1	13 ± 2	0.64 ± 0.02	0.002 ± 0.001	8 ± 1	7 ± 1	0.62 ± 0.02	0.07	0.03
G2	21 ± 2	1.03 ± 0.04	0.010 ± 0.003	17 ± 1	11 ± 1	0.82 ± 0.02	0.18	0.15
G3	26 ± 3	1.22 ± 0.02	0.040 ± 0.002	22 ± 1	13 ± 1	1.01 ± 0.01	0.24	0.41
G4	34 ± 2	1.59 ± 0.02	0.075 ± 0.006	47 ± 3	31 ± 2	0.89 ± 0.03	0.48	0.92
G5	44 ± 3	1.98 ± 0.05	0.083 ± 0.002	63 ± 1	53 ± 3	0.73 ± 0.02	0.68	1.18
G6	59 ± 4	2.48 ± 0.06	0.065 ± 0.001	78 ± 2	80 ± 3	0.52 ± 0.02	0.80	1.30

^a D = diblock copolymers and G = graft copolymers.

^b Degree of sulfonation, estimated by ¹H NMR.

^c Measured by acid-base titration.

^d Measured by AC impedance spectroscopy, at room temperature, fully hydrated condition.

^e At room temperature.

^f Analytical acid concentration in fully hydrated membranes.

^g Water volume fraction at room temperature.

5.3.2 TEM

TEM analyses were performed on ~100 nm-thick cross-sectional slices of dehydrated membranes, which were stained with lead acetate prior to imaging; thus, the dark areas represent ionic domains whereas brighter areas, hydrophobic domains. As shown in Figure 5.2a, the diblock membranes (IEC = 0.72 mmol/g) possess well-segregated morphologies of ionic-rich lamellar structures. These ionic channels are ~8 to 15 nm in width with a fluorous interdomain spacings of 20 to 40 nm. In stark contrast, the morphologies of the graft membranes (IEC = 1.03 mmol/g) are characterized by an interconnected network of small ionic clusters of 2 to 3 nm in size, as shown in Figure 5.2b. This morphology is very similar to the archetypical proton conducting membrane, Nafion, in which a “cluster-network” composed of 5 to 10 nm ionic clusters interconnected by narrow ionic channels is reported;¹²⁴ however, the ionic clusters found in the graft membranes (2 to 3 nm) are much smaller. The differences in morphological structure between the diblock and the graft membranes have important implications on their water sorption and proton conductivity behaviour.

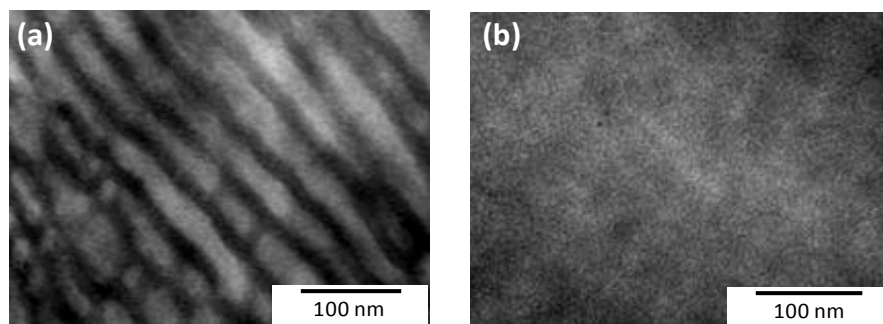


Figure 5.2 TEM micrographs of (a) P(VDF-co-HFP)-*b*-SPS diblock (IEC = 0.72 mmol/g) and (b) P(VDF-co-CTFE)-*g*-SPS Graft (IEC = 1.03 mmol/g) membranes.

5.3.3 Water Sorption

Water sorption of the membranes in their protonic form were expressed as both water content (weight percent of water in a fully hydrated membrane) and λ (average number of water molecules associated with each sulfonic acid site). Plots of water sorption against IEC for the diblock and the graft membranes are shown in Figure 5.3. As expected, for both membrane series, water content increases continuously with ion content. Increasing ion content increases the hydrophilicity of the membranes, and hence promotes the uptake of a larger amount of water. Interestingly, the diblock membranes exhibit a much more substantial increase in water content with increasing IEC. Diblock membranes possessing IEC > 1.31 mmol/g (not shown) swell excessively in water, are gelatinous, and exhibit poor mechanical properties. Greater water swelling in diblock membranes is attributed to their long-range lamellar-like membrane morphology, and the inability of the fluorinated matrix to prevent excessive expansion in the direction perpendicular to the lamellae.²²⁶ Anisotropic water swelling in lamellar membranes has been previously reported.²²⁷

In contrast, the graft membranes uptake significantly less water for similar IECs, and their λ value remains moderately low even for IECs as high as 2.22 mmol/g. The small ionic cluster morphology is believed to be responsible for the lower water sorption: the formation of small ionic clusters allows for a more continuous and cohesive hydrophobic matrix that opposes the increasing osmotic pressure induced by increasing ionicity. Consequently, graft copolymers possessing very high ion contents remain insoluble in water. Wide angle X-ray

scattering (WAXS) analysis (not shown) revealed that the fluororous domains in both the graft and the diblock membranes were amorphous, indicating that differences in water sorption are not a result of differences in crystallinity.

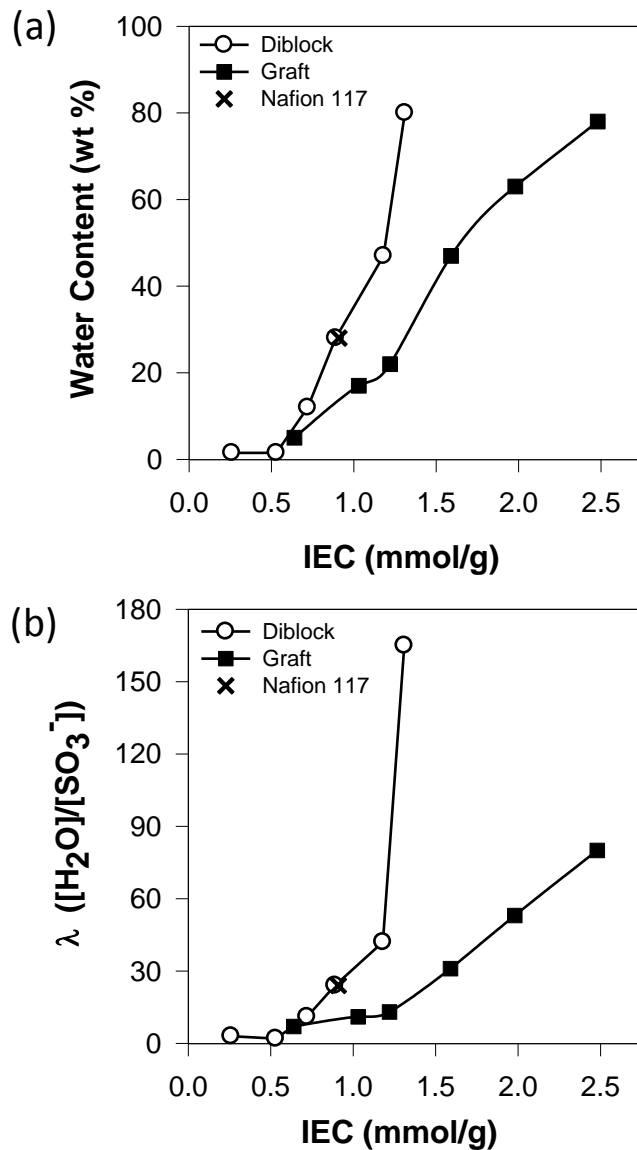


Figure 5.3 (a) Water content vs. IEC and (b) λ vs. IEC of P(VDF-co-HFP)-*b*-SPS diblock (○) and P(VDF-co-CTFE)-*g*-SPS graft (■) membranes.

5.3.4 Proton Conductivity

Proton conductivities of the membranes in fully hydrated conditions were measured by ac impedance spectroscopy. In-plane proton conductivity data are listed in Table 5.2 and plotted as a function of IEC in Figure 5.4a. Generally, proton conductivity increases with increasing IEC because conductivity depends on both the ion content and the water content of the membrane. For both the diblock and the graft membranes, proton conductivity initially increases incrementally with IEC; however, at certain critical IEC values, both membranes show a sharp increase in conductivity with IEC. These observations can be correlated to the water content of the membranes. At low IEC ranges, the membranes absorb very little water, and thus the volume of the hydrophilic regions is insufficient to form a percolated network of ionic domains. With increasing IEC, the membranes absorb increasing amounts of water and eventually, a percolation threshold is reached at which an interconnected network of ionic domains is formed and proton conductivity increases sharply. As shown in Figure 5.4a, the graft membranes possess a significantly higher percolation threshold than the diblock membranes, ~ 1.0 mmol/g for grafts and ~ 0.5 mmol/g for the diblocks. These results are consistent with their different water sorption behaviours, as previously shown in Figure 5.3. For the graft membranes, excessive water swelling occurs at an IEC value of ~ 1.0 mmol/g, whereas diblock membranes, ~ 0.5 mmol/g.

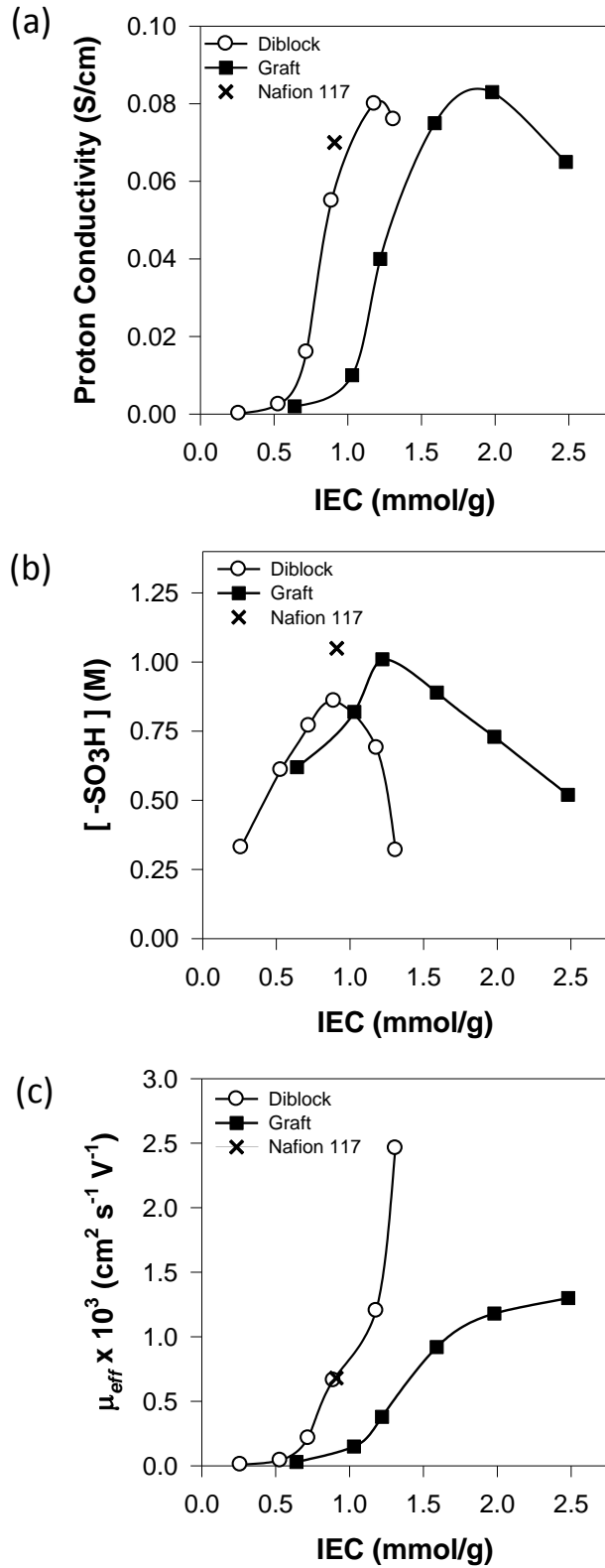


Figure 5.4 (a) In-plane proton conductivity vs. IEC, (b) analytical [-SO₃H] vs. IEC, and (c) effective proton mobility (μ_{eff}) vs. IEC of P(VDF-co-HFP)-*b*-SPS diblock (○) and P(VDF-co-CTFE)-*g*-SPS graft (■) membranes.

At high IEC ranges, for both the diblock and the graft membranes, proton conductivities show a peak and then drop with further increase in IEC (Figure 5.4a). This might seem counter-intuitive as one might expect proton conductivity to increase continuously with ion content due to the increasing amount of charge-carrier available. However, the effect of increasing ion content on water sorption and in turn, on proton concentration must also be considered. Proton conductivity is a direct function of proton mobility and proton concentration. Notice that *acid* concentration, instead of actual free *proton* concentration, is the parameter being measured by acid-base titration; hence, the proton mobility, calculated here from the proton conductivity and the analytical acid concentration, is an *effective* proton mobility (μ_{eff}), which incorporates uncertainty in acid dissociation. Figure 5.4b and c show plots of analytical acid concentration and μ_{eff} versus IEC, respectively. The μ_{eff} is much lower for the graft membranes, but their analytical acid concentration is much higher. This can be explained on the basis of their relatively lower water sorption, as previously observed in Figure 5.3. In contrast, the μ_{eff} is generally much higher for the diblock membranes, and increases at a much lower IEC threshold, with the commensurate increase in water uptake. However, as a result of the excessive water sorption and relatively lower IEC, acid concentration is relatively low and in fact decreases for membranes possessing IEC > ~1 mmol/g to the extent that acid concentration for diblock membranes possessing IECs of 0.26 and 1.31 mmol/g are similar (Figure 5.4b). Acid dilution due to excessive water swelling can lead to drop in proton conductivity at high IEC ranges. Such acid dilution effects are observed in both

the diblock and the graft membranes; however, the dilution effect is more pronounced (i.e., occurring at relatively lower IEC values) in the diblock membranes due to their much greater water sorption.

Under the assumption that protons travel through the aqueous domains of the membrane, a plot of μ_{eff} versus water volume fraction provides insights into the degree of tortuosity and connectivity of the ionic networks within a membrane. Such a plot is shown in Figure 5.5, which reveals that, for a given water volume, the diblock membranes possess relatively higher proton mobility. This suggests that the diblock membranes provide a less encumbered pathway, from which it can be inferred that the ionic domains are more linear and well-interconnected. This highly linear and interconnected nature of the ionic channels is also supported by the TEM images shown previously in Figure 5.2.

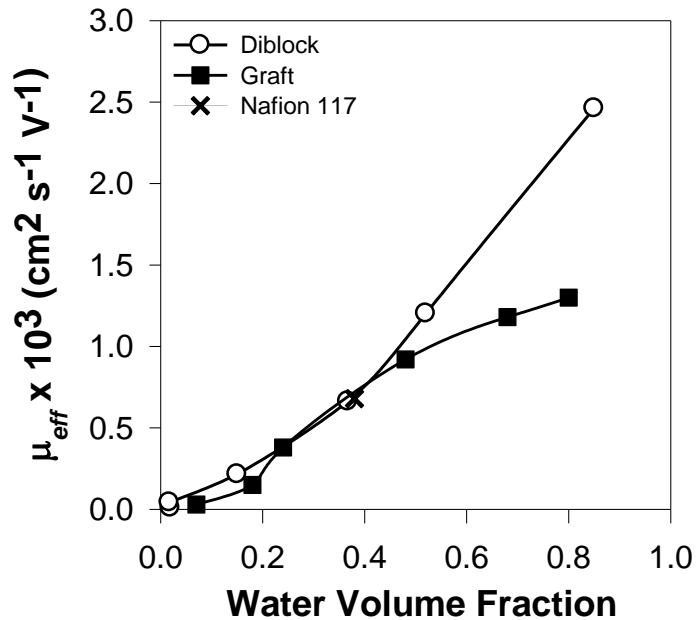


Figure 5.5 Effective proton mobility (μ_{eff}) vs. water volume fraction of P(VDF-co-HFP)-*b*-SPS diblock (○) and P(VDF-co-CTFE)-*g*-SPS graft (■) membranes.

5.3.5 Conductivity Anisotropy

Inducing ionic groups in a morphologically organized manner has anisotropic implications. To examine the anisotropic nature of proton conductivity, both *in-plane* and *through-plane* conductivity values were measured for the diblock and the graft membranes possessing similar water volume fractions of ~0.40, that is, IECs of 0.89 and 1.59 mmol/g, respectively. Conductivity anisotropy ($\sigma_{\parallel/\perp}$) is defined as the ratio of in-plane (σ_{\parallel} , average of X and Y directions) over through-plane (σ_{\perp} , Z direction) conductivity. The proton conductivity in the X, Y, Z directions and the calculated anisotropy are summarized in Table 5.3. In the diblock membranes, the in-plane proton conductivity is found to be greater than the through-plane conductivity by a factor of ~2.5, indicating a mild degree of anisotropy. In contrast, the graft membranes were found to possess very similar in-plane and through-plane conductivity indicating a nearly isotropic conductivity ($\sigma_{\parallel/\perp} = 0.95$). The conductivity anisotropy in the diblock membranes is consistent with the morphology previously observed by TEM (Figure 5.2), which reveals alternating layers of ionic and hydrophobic domains. Based on the anisotropic proton conductivity in the diblock membranes, it can be concluded that the alternating ionic and hydrophobic lamellae are stacked parallel to the membrane's surface. Such orientation of ionic domains makes proton conductivity much more difficult in the through-plane direction. As a point of reference, the conductivity anisotropy of Nafion 112 membranes is found to be ~1.3, which is in close agreement to previous reports.¹⁴⁴

Table 5.3 Proton Conductivity Anisotropy ($\sigma_{\parallel/\perp}$) of Selected P(VDF-co-HFP)-*b*-SPS Diblock and P(VDF-co-CTFE)-*g*-SPS Graft Membranes

Membrane	Water Volume Fraction	IEC (mmol g ⁻¹)	σ_{\parallel} (x-direction) ^a (S cm ⁻¹)	σ_{\parallel} (y-direction) ^a (S cm ⁻¹)	σ_{\perp} (z-direction) ^a (S cm ⁻¹)	$\sigma_{\parallel/\perp}$ ^b
D4	0.37	0.89	0.054 ± 0.002	0.056 ± 0.001	0.022 ± 0.001	2.5
G4	0.48	1.59	0.080 ± 0.002	0.075 ± 0.002	0.081 ± 0.003	0.95
Nafion 112	0.38	0.91	0.078 ± 0.003	0.076 ± 0.002	0.061 ± 0.002	1.3

^a Fully hydrated membranes at room temperature.

^b Conductivity anisotropy ($\sigma_{\parallel/\perp}$) is expressed as the ratio of in-plane (σ_{\parallel}) to through-plane (σ_{\perp}) conductivity, where σ_{\parallel} is calculated as the average of the x- and y-directions, and σ_{\perp} is the z-direction.

5.4 Conclusion

Two chemically-related but architecturally-distinct model polymer systems were synthesized and characterized for investigating structure-property relationships in proton exchange membranes. Diblock copolymers of partially sulfonated poly([vinylidene difluoride-co-hexafluoropropylene]-*b*-styrene) [P(VDF-co-HFP)-*b*-SPS] possess a hydrophobic fluorous segment linearly attached to an ionic sulfonated styrenic segment. On the other hand, graft copolymers of partially sulfonated poly([vinylidene difluoride-co-chlorotrifluoroethylene]-*g*-styrene) [P(VDF-co-CTFE)-*g*-SPS] consist of a hydrophobic fluorous backbone with ionic sulfonated styrenic side chains. Both model polymers are sulfonated to various extents to provide two series of membranes possessing different ion content. Comparison between the diblock and the graft membrane series clearly demonstrate that polymer architecture plays an important role on the morphology

of the membrane and on properties such as proton conductivity, proton mobility, and water content.

The diblock copolymers yield membranes that are characterized by alternating layers of hydrophobic and ionic domains with a higher degree of long-range ionic order. This leads to membranes that swell excessively in water at low IEC, thereby diluting the proton concentration, and limiting the IEC attainable ($IEC < 1.3$ mmol/g). Conductivity anisotropy is observed in the diblock membranes in which proton conductivity in the through-plane direction is lower than that in the in-plane direction by a factor of 2.5; it is through-plane that is relevant to proton conduction in fuel cells. Thus, conductivity anisotropy effects must be carefully considered in the design of novel membranes possessing morphological anisotropy.

On the other hand, the graft copolymers yield membranes with an interconnected network of small ionic clusters (2 – 3 nm in size) embedded in a fluorocarbon matrix. Due to the more continuous nature of the fluorocarbon matrix, these membranes can tolerate much higher ionic contents ($IEC > 2.0$ mmol/g) without excessive swelling and dissolution. The lower water swelling leads to membranes with highly concentrated isotropically connected ionic domains. Nearly isotropic conductivity is observed in the graft membranes as expected from the isotropic morphology observed in TEM. This work suggested that the formation of small-scale ionic domains is advantageous in PEMs due to the greater resistance to water swelling, which mitigates acid dilution effects and allows for enhanced proton conductivity in membranes at high ion contents.

Chapter 6. Research Summary and Outlook

The elucidation of structure-property relationships in proton exchange membranes is the focus of this thesis work. In particular, the role of polymer microstructure – i.e., polymer architecture, chemical composition and ion content – on ionic aggregation and morphological formation, and in turn, on the physicochemical properties of a membrane are investigated. This is achieved by developing model polymer systems in which the polymer microstructures can be controlled and systematically varied, leading to membranes with controlled nanophase-separated morphologies. The correlations between polymer microstructure, morphology and proton conductivity were carefully studied to obtain insights into structural preferences for membrane design.

In Chapter 3, a model polymer system based on diblock ionomers of sulfonated poly([vinylidene difluoride-*co*-hexafluoropropylene]-*b*-styrene) [P(VDF-*co*-HFP)-*b*-SPS] was utilized for investigating the role of sulfonation degree and morphology on membrane properties. By varying the ratio of the constituent blocks and the extent of sulfonation, membranes with different nanophase-separated morphology were obtained, from which properties such as water swelling, proton conductivity and mobility were observed to be strongly influenced by the resulting membrane's nanostructure.

One of the key findings of the diblock work is that the constituent polymer's degree of sulfonation exerts an essential role in determining the

resulting membrane's morphology and properties. The spatial proximity of sulfonic acid groups along the polystyrene segments, as dictated by the degree of sulfonation, greatly influences the aggregation of sulfonic acid groups and the connectivity and purity of the ionic domains. P(VDF-co-HFP)-*b*-SPS diblock copolymers with a lower content of the polystyrene block provided enhanced proton conductivity at low IEC ranges. This is attributed to the relatively high degree of sulfonation required and therefore, closer spacing between the sulfonic acid groups, which allows for the formation of larger-scale and purer ionic clusters. This in turn, leads to enhanced percolation of the ionic aggregates within a "proton-conducting channel" and thus, higher proton conductivity at a given IEC. However, one must bear in mind that when the degree of sulfonation is exceedingly high, the depletion of the hydrophobic polystyrene matrix surrounding the ionic clusters might lead to excessive water swelling and loss of mechanical properties. Thus, when designing proton-conducting membranes based on block architectures, the ratio of the acid-bearing polymer block to the non-ionic polymer block must be carefully controlled. A lower content of the acid-bearing polymer block is advantageous due to the relatively high degree of sulfonation and closer proximity of the acid groups, which promote the formation of better percolated ionic network for proton conduction.

In Chapter 4, the synthesis of graft copolymers of partially sulfonated poly([vinylidene difluoride-co-chlorotrifluoroethylene]-*g*-styrene) [P(VDF-co-CTFE)-*g*-SPS] for a systematic study of the effects of graft chain length on membrane properties is described. Interestingly, the trend between ionic cluster

size and ionic graft length was found to be counter-intuitive, that is, ionic cluster size was observed to increase with decreasing graft length. These results further confirm the importance of the degree of sulfonation in determining membrane morphology and properties, as observed in Chapter 3 using diblock copolymers. The higher degree of sulfonation found in the short graft copolymer allows for closer spatial proximity and greater ionic interaction between the sulfonic acid groups, leading to the formation of relatively larger ionic domains. For the P(VDF-co-CTFE)-*g*-SPS system, the density of the sulfonated polystyrene grafts, in principle, would influence the density of the ionic clusters. Hence, future work on this graft copolymer system may involve an investigation of the effects of graft density on membrane properties. In particular, graft copolymers with a lower density of graft chains are of interest due to the anticipated increase in membrane crystallinity which may provide lower water uptake and greater mechanical strength.

In Chapter 5, the diblock and the graft model systems were directly compared to each other for the elucidation of preferred structural design for proton-conducting membranes. It was found that diblock copolymers, possessing a higher degree of long-range ionic order, gave higher proton mobility; however, the formation of long-range ionic domains caused excessive water uptake leading to acid dilution and limits the IEC attainable. In contrast, graft copolymers exhibited a morphology characterized by randomly distributed small ionic clusters (2 – 3 nm in width), which are much smaller in dimension compared to the archetypical Nafion membrane (5 – 10 nm in width). The formation of tiny ionic

clusters allows greater continuity in the hydrophobic fluoropolymer matrix, giving rise to reduced water swelling and higher proton concentration. In addition, smaller ionic clusters allowed for improved water retention at low humidity conditions and greater proton conduction over wide temperature and humidity ranges, as observed in Chapter 4. For future membrane design, it is suggested that a membrane morphology consisting of a high density of small-scale ionic domains may be preferable for enhanced water retention and proton transport at low humidity and high temperature conditions.

During PEM fuel cell operation, protons are transported in the through-plane direction, thus the orientation of the ionic domains is particularly important in polymers with anisotropic morphologies such as those adopting lamellar or cylindrical structures. In Chapter 3 and Chapter 5, significant conductivity anisotropy was observed in diblock membranes with lamellar structures, in which proton conductivity in the through-plane direction was found to be significantly lower than that in the in-plane direction. The orientation of the ionic domains has been reported to be related to the method of membrane casting and processing – i.e., solvent effects, annealing, electric-field alignment and shear forces;¹⁹⁰ thus, more work needs to be undertaken to control the orientation of ionic domains within a membrane to provide more effective proton conduction pathways.

This thesis work is mainly focused on the effects of morphology and nanostructure on the proton conductivity and water sorption properties of PEMs. While these two properties are critical to the performance of a PEM fuel cell, future work on structure-property relationships of PEMs may be extended to

include other crucial properties such as chemical stability, mechanical strength, and water transport. A better understanding of the relationships between chemical structure, morphology and these other membrane properties will aid the design of membranes with an optimized set of properties. Furthermore, in this thesis research, diblock and graft copolymer systems were studied; however, more complex block copolymer systems (i.e., star-block, multiblock, triblock, etc) would be of interest since they may provide a wider variety of morphological structures. For instance, A-B-C triblock copolymer systems may lead to the formation of three-phase morphologies in which each phase can be designed to promote a particular desirable property. This would require ongoing research effort into the development of synthetic methodologies to obtain polymers with complex structures.

The knowledge gained from this research should provide useful insights into the structure-property relationships in PEMs, and therefore, facilitate a more effective development of future membranes that fulfill the requirements for a mass commercialization of PEM fuel cells.

References

1. Vielstich, W.; Lamm, A.; Gasteiger, H. A. *Handbook of Fuel Cells-Fundamentals, Technology and Applications*. Wiley: New York, 2003.
2. Larminie, J.; Dicks, A. *Fuel Cell Systems Explained*. John Wiley & Sons Ltd.: New York, 2003.
3. Smitha, B.; Sridhar, S.; Khan, A. A. *Journal of Membrane Science* **2005**, *259*, 10-26.
4. Barbir, F. *PEM Fuel Cells: Theory and Practice*. Elsevier Academic Press: New York, 2005.
5. Hickner, M. A.; Ghassemi, H.; Kim, Y. S.; Einsla, B. R.; McGrath, J. E. *Chemical Reviews* **2004**, *104*, 4587-4611.
6. Rikukawa, M.; Sanui, K. *Progress in Polymer Science* **2000**, *25*, 1463-1502.
7. Yu, J. R.; Yi, B. L.; Xing, D. M.; Liu, F. Q.; Shao, Z. G.; Fu, Y. Z. *Physical Chemistry Chemical Physics* **2003**, *5*, 611-615.
8. Guo, Q. H.; Pintauro, P. N.; Tang, H.; O'Connor, S. *Journal of Membrane Science* **1999**, *154*, 175-181.
9. Ibrahim, S. M.; Price, E. H.; Smith, R. A. *Proceedings of the Electrochemical Society* **1983**, 83-86.
10. Hamrock, S. J.; Yandrasits, M. A. *Polymer Reviews* **2006**, *46*, 219-244.
11. Li, Q.; He, R.; Jensen, J. O.; Bjerrum, N. J. *Chemistry of Materials* **2003**, *15*, 4896-4915.
12. Miyatake, K.; Watanabe, M. *Electrochemistry (Japan)* **2005**, *73*, 12-19.
13. Ma, C. S.; Zhang, L.; Mukerjee, S.; Ofer, D.; Nair, B. D. *Journal of Membrane Science* **2003**, *219*, 123-136.
14. Mauritz, K. A.; Moore, R. B. *Chemical Reviews* **2004**, *104*, 4535-4585.
15. Eisman, G. A. *Journal of Power Sources* **1990**, *29*, 389-398.
16. Prater, K. *Journal of Power Sources* **1990**, *29*, 239-250.
17. Paddison, S. J.; Elliott, J. A. *Physical Chemistry Chemical Physics* **2006**, *8*, 2193-2203.
18. Arcella, V.; Ghielmi, A.; Tommasi, G. *Advanced Membrane Technology*, Li, N. N.; Drioli, E.; Ho, W. S. W.; Lipscomb, G. G., Eds. New York Acad Sciences: New York, 2003; Vol. 984, p 226-244.

19. Rivard, L. M.; Pierpont, D.; Freemeyer, H. T.; Thaler, A.; Hamrock, S. J., Development of a new electrolyte membrane for PEM fuel cells. In *Fuel Cell Seminar*, Miami Beach, FL, 2003.
20. Hoshi, N.; Uematsu, N.; Saito, H.; Hattori, M.; Aoyagi, T.; Ikeda, M. U.S. Patent, 2 005 130 006, 2005.
21. Savett, S. C.; Atkins, J. R.; Sides, C. R.; Harris, J. L.; Thomas, B. H.; Creager, S. E.; Pennington, W. T.; DesMarteau, D. D. *Journal of the Electrochemical Society* **2002**, *149*, A1527-A1532.
22. Perpall, M. W.; Smith, D. W.; DesMarteau, D. D.; Creager, S. E. *Polymer Reviews* **2006**, *46*, 297-313.
23. Atkins, J. R.; Sides, C. R.; Creager, S. E.; Harris, J. L.; Pennington, W. T.; Thomas, B. H.; DesMarteau, D. D. *Journal of New Materials for Electrochemical Systems* **2003**, *6*, 9-15.
24. Steck, A. E. In First International Symposium of New Materials for Fuel Cell Systems, Montreal, July 9-13, **1995**.
25. Wei, J.; Stone, C.; Steck, A. E. U.S. Patent, 5 422 411, 1995.
26. Dargaville, T. R.; George, G. A.; Hill, D. J. T.; Whittaker, A. K. *Progress in Polymer Science* **2003**, *28*, 1355-1376.
27. Nasef, M. M.; Hegazy, E. S. A. *Progress in Polymer Science* **2004**, *29*, 499-561.
28. Gubler, L.; Gursel, S. A.; Scherer, G. G. *Fuel Cells* **2005**, *5*, 317-335.
29. Guzmangarcia, A. G.; Pintauro, P. N.; Verbrugge, M. W.; Schneider, E. W. *Journal of Applied Electrochemistry* **1992**, *22*, 204-214.
30. Nasef, M. M. *Polymer Degradation and Stability* **2000**, *68*, 231-238.
31. Nasef, M. M.; Saidi, H.; Dessouki, A. M.; El-Nesr, E. M. *Polymer International* **2000**, *49*, 399-406.
32. Nasef, M. M.; Saidi, H.; Nor, H. M.; Yarmo, M. A. *Journal of Applied Polymer Science* **2000**, *76*, 336-349.
33. Liang, G. Z.; Lu, T. L.; Ma, X. Y.; Yan, H. X.; Gong, Z. H. *Polymer International* **2003**, *52*, 1300-1308.
34. Holmberg, S.; Lehtinen, T.; Nasman, J.; Ostrovskii, D.; Paronen, M.; Serimaa, R.; Sundholm, F.; Sundholm, G.; Torell, L.; Torkkeli, M. *Journal of Materials Chemistry* **1996**, *6*, 1309-1317.
35. Flint, S. D.; Slade, R. C. T. *Solid State Ionics* **1997**, *97*, 299-307.
36. Hietala, S.; Holmberg, S.; Karjalainen, M.; Nasman, J.; Paronen, M.; Serimaa, R.; Sundholm, F.; Vahvaselka, S. *Journal of Materials Chemistry* **1997**, *7*, 721-726.
37. Danks, T. N.; Slade, R. C. T.; Varcoe, J. R. *Journal of Materials Chemistry* **2002**, *12*, 3371-3373.

38. Danks, T. N.; Slade, R. C. T.; Varcoe, J. R. *Journal of Materials Chemistry* **2003**, *13*, 712-721.
39. Nasef, M. M.; Saidi, H.; Nor, H. M.; Dahlan, K. Z. M.; Hashim, K. *Journal of Applied Polymer Science* **1999**, *73*, 2095-2102.
40. Nasef, M. M.; Saidi, H.; Nor, H. M. *Journal of Applied Polymer Science* **2000**, *77*, 1877-1885.
41. Nasef, M. M.; Saidi, H.; Nor, H. M.; Foo, O. M. *Journal of Applied Polymer Science* **2000**, *76*, 1-11.
42. Nasef, M. M.; Saidi, H.; Yarmo, M. A. *Journal of Applied Polymer Science* **2000**, *77*, 2455-2463.
43. Horsfall, J. A.; Lovell, K. V. *Fuel Cells* **2001**, *1*, 186-191.
44. Herman, H.; Slade, R. C. T.; Varcoe, J. R. *Journal of Membrane Science* **2003**, *218*, 147-163.
45. Nasef, M. M.; Saidi, H.; Nor, H. M. *Journal of Applied Polymer Science* **2000**, *76*, 220-227.
46. Rouilly, M. V.; Kotz, E. R.; Haas, O.; Scherer, G. G.; Chapiro, A. *Journal of Membrane Science* **1993**, *81*, 89-95.
47. Stone, C.; Steck, A. E.; Choudhury, B. U.S. Patent, 0 137 806, 2002.
48. Buchi, F. N.; Gupta, B.; Haas, O.; Scherer, G. G. *Electrochimica Acta* **1995**, *40*, 345-353.
49. Gupta, B.; Anjum, N.; Jain, R.; Revagade, N.; Singh, H. *Journal of Macromolecular Science-Polymer Reviews* **2004**, *C44*, 275-309.
50. Buchi, F. N.; Gupta, B.; Haas, O.; Scherer, G. G. *Journal of the Electrochemical Society* **1995**, *142*, 3044-3048.
51. Yu, J.; Yi, B.; Xing, D.; Liu, F.; Shao, Z.; Fu, Y.; Zhang, H. *Physical Chemistry Chemical Physics* **2003**, *5*, 611-615.
52. Pozio, A.; Silva, R. F.; De Francesco, M.; Giorgi, L. *Electrochimica Acta* **2003**, *48*, 1543-1549.
53. Assink, R. A.; Arnold Jr, C.; Hollandsworth, R. P. *Journal of Membrane Science* **1991**, *56*, 143-151.
54. Hubner, G.; Roduner, E. *Journal of Materials Chemistry* **1999**, *9*, 409-418.
55. Weiss, R. A.; Sen, A.; Pottick, L. A.; Willis, C. L. *Polymer* **1991**, *32*, 2785-2792.
56. Weiss, R. A.; Sen, A.; Willis, C. L.; Pottick, L. A. *Polymer* **1991**, *32*, 1867-1874.
57. Lu, X. Y.; Steckle, W. P.; Weiss, R. A. *Macromolecules* **1993**, *26*, 6525-6530.

58. Lu, X. Y.; Steckle, W. P.; Weiss, R. A. *Macromolecules* **1993**, *26*, 5876-5884.
59. Lu, X. Y.; Steckle, W. P.; Hsiao, B.; Weiss, R. A. *Macromolecules* **1995**, *28*, 2831-2839.
60. Edmondson, C. A.; Fontanella, J. J.; Chung, S. H.; Greenbaum, S. G.; Wnek, G. E. *Electrochimica Acta* **2001**, *46*, 1623-1628.
61. Kim, J.; Kim, B.; Jung, B. *Journal of Membrane Science* **2002**, *207*, 129-137.
62. Kim, J.; Kim, B.; Jung, B.; Kang, Y. S.; Ha, H. Y.; Oh, I. H.; Ihn, K. J. *Macromolecular Rapid Communications* **2002**, *23*, 753-756.
63. Mauritz, K. A.; Storey, R. F.; Mountz, D. A.; Reuschle, D. A. *Polymer* **2002**, *43*, 4315-4323.
64. Mauritz, K. A.; Storey, R. F.; Reuschle, D. A.; Tan, N. B. *Polymer* **2002**, *43*, 5949-5958.
65. Lee, W. J.; Jung, H. R.; Lee, M. S.; Kim, J. H.; Yang, K. S. *Solid State Ionics* **2003**, *164*, 65-72.
66. Won, J.; Choi, S. W.; Kang, Y. S.; Ha, H. Y.; Oh, I. H.; Kim, H. S.; Kim, K. T.; Jo, W. H. *Journal of Membrane Science* **2003**, *214*, 245-257.
67. Won, J.; Kang, Y. S. *Macromolecular Symposia* **2003**, *204*, 79-91.
68. Mauritz, K. A.; Blackwell, R. I.; Beyer, F. L. *Polymer* **2004**, *45*, 3001-3016.
69. Kim, B.; Kim, J.; Jung, B. *Journal of Membrane Science* **2005**, *250*, 175-182.
70. Storey, R. F.; Chisholm, B. J.; Masse, M. A. *Polymer* **1996**, *37*, 2925-2938.
71. Elabd, Y. A.; Napadensky, E.; Sloan, J. M.; Crawford, D. M.; Walker, C. W. *Journal of Membrane Science* **2003**, *217*, 227-242.
72. Elabd, Y. A.; Walker, C. W.; Beyer, F. L. *Journal of Membrane Science* **2004**, *231*, 181-188.
73. Elabd, Y. A.; Napadensky, E. *Polymer* **2004**, *45*, 3037-3043.
74. Elabd, Y. A.; Napadensky, E.; Walker, C. W.; Winey, K. I. *Macromolecules* **2006**, *39*, 399-407.
75. Mokrini, A.; Acosta, J. L. *Polymer* **2001**, *42*, 9-15.
76. Mokrini, A.; Del Rio, C.; Acosta, J. L. *Solid State Ionics* **2004**, *166*, 375-381.
77. Mani, S.; Weiss, R. A.; Williams, C. E.; Hahn, S. F. *Macromolecules* **1999**, *32*, 3663-3670.
78. Zhang, G. Z.; Liu, L.; Wang, H. M.; Jiang, M. *European Polymer Journal* **2000**, *36*, 61-68.

79. Roziere, J.; Jones, D. J. *Annual Review of Materials Research* **2003**, *33*, 503-555.
80. Ogawa, T.; Marvel, C. S. *Journal of Polymer Science Part A-Polymer Chemistry* **1985**, *23*, 1231-1241.
81. Bishop, M. T.; Karasz, F. E.; Russo, P. S.; Langley, K. H. *Macromolecules* **1985**, *18*, 86-93.
82. Genies, C.; Mercier, R.; Sillion, B.; Cornet, N.; Gebel, G.; Pineri, M. *Polymer* **2001**, *42*, 359-373.
83. Wang, F.; Hickner, M.; Ji, Q.; Harrison, W.; Mecham, J.; Zawodzinski, T. A.; McGrath, J. E. *Macromolecular Symposia* **2001**, *175*, 387-395.
84. Asensio, J. A.; Borros, S.; Gomez-Romero, P. *Journal of Polymer Science Part A-Polymer Chemistry* **2002**, *40*, 3703-3710.
85. Guo, X. X.; Fang, J. H.; Watari, T.; Tanaka, K.; Kita, H.; Okamoto, K. I. *Macromolecules* **2002**, *35*, 6707-6713.
86. Wang, F.; Hickner, M.; Kim, Y. S.; Zawodzinski, T. A.; McGrath, J. E. *Journal of Membrane Science* **2002**, *197*, 231-242.
87. Harrison, W. L.; Wang, F.; Mecham, J. B.; Bhanu, V. A.; Hill, M.; Kim, Y. S.; McGrath, J. E. *Journal of Polymer Science Part A-Polymer Chemistry* **2003**, *41*, 2264-2276.
88. Yin, Y.; Fang, J. H.; Cui, Y. F.; Tanaka, K.; Kita, H.; Okamoto, K. *Polymer* **2003**, *44*, 4509-4518.
89. Einsla, B. R.; Hong, Y. T.; Kim, Y. S.; Wang, F.; Gunduz, N.; McGrath, J. E. *Journal of Polymer Science Part A-Polymer Chemistry* **2004**, *42*, 862-874.
90. Xing, P. X.; Robertson, G. P.; Guiver, M. D.; Mikhailenko, S. D.; Kaliaguine, S. *Macromolecules* **2004**, *37*, 7960-7967.
91. Gao, Y.; Robertson, G. P.; Guiver, M. D.; Mikhailenko, S. D.; Li, X.; Kaliaguine, S. *Macromolecules* **2005**, *38*, 3237-3245.
92. Xing, P. X.; Robertson, G. P.; Guiver, M. D.; Mikhailenko, S. D.; Kaliaguine, S. *Polymer* **2005**, *46*, 3257-3263.
93. Ghassemi, H.; McGrath, J. E. *Polymer* **2004**, *45*, 5847-5854.
94. Lin, J. C.; Ouyang, M.; Fenton, J. M.; Kunz, H. R.; Koberstein, J. T.; Cutlip, M. B. *Journal of Applied Polymer Science* **1998**, *70*, 121-127.
95. Bottino, A.; Capannelli, G.; Monticelli, O.; Piaggio, P. *Journal of Membrane Science* **2000**, *166*, 23-29.
96. Jung, B.; Kim, B.; Yang, J. M. *Journal of Membrane Science* **2004**, *245*, 61-69.
97. Choi, J.; Kim, I. T.; Kim, S. C.; Hong, Y. T. *Macromolecular Research* **2005**, *13*, 514-520.

98. Kerres, J. A. *Fuel Cells* **2005**, 5, 230-247.
99. Kerres, J.; Cui, W.; Disson, R.; Neubrand, W. *Journal of Membrane Science* **1998**, 139, 211-225.
100. Kerres, J.; Ullrich, A.; Meier, F.; Haring, T. *Solid State Ionics* **1999**, 125, 243-249.
101. Jorissen, L.; Gogel, V.; Kerres, J.; Garche, J. *Journal of Power Sources* **2002**, 105, 267-273.
102. Schuster, M. E.; Meyer, W. H. *Annual Review of Materials Research* **2003**, 33, 233-261.
103. Savadogo, O. *Journal of Power Sources* **2004**, 127, 135-161.
104. Herring, A. M. *Polymer Reviews* **2006**, 46, 245-296.
105. Bonnet, B.; Jones, D. J.; Roziere, J.; Tchicaya, L.; Alberti, G.; Casciola, M.; Massinelli, L.; Bauer, B.; Peraio, A.; Ramunni, E. *Journal of New Materials for Electrochemical Systems* **2000**, 3, 87-92.
106. Yang, Y.; Holdcroft, S. *Fuel Cells* **2005**, 5, 171-186.
107. Kreuer, K. D. *Journal of Membrane Science* **2001**, 185, 29-39.
108. Kreuer, K.-D.; Paddison, S. J.; Spohr, E.; Schuster, M. *Chemical Reviews* **2004**, 104, 4637-4678.
109. Choi, P.; Jalani, N. H.; Thampan, T. M.; Datta, R. *Journal of Polymer Science Part B-Polymer Physics* **2006**, 44, 2183-2200.
110. Tuckerman, M.; Laasonen, K.; Sprik, M.; Parrinello, M. *Journal of Chemical Physics* **1995**, 103, 150-161.
111. Tuckerman, M. E.; Marx, D.; Klein, M. L.; Parrinello, M. *Science* **1997**, 275, 817-820.
112. Agmon, N. *Chemical Physics Letters* **1995**, 244, 456-462.
113. Eikerling, M.; Kornyshev, A. A. *Journal of Electroanalytical Chemistry* **2001**, 502, 1-14.
114. Zawodzinski, T. A.; Springer, T. E.; Uribe, F.; Gottesfeld, S. *Solid State Ionics* **1993**, 60, 199-211.
115. Gebel, G. *Polymer* **2000**, 41, 5829-5838.
116. Rollet, A. L.; Diat, O.; Gebel, G. *Journal of Physical Chemistry B* **2002**, 106, 3033-3036.
117. Gebel, G.; Aldebert, P.; Pineri, M. *Polymer* **1993**, 34, 333-339.
118. Gebel, G.; Lambard, J. *Macromolecules* **1997**, 30, 7914-7920.
119. Fujimura, M.; Hashimoto, T.; Kawai, H. *Macromolecules* **1982**, 15, 136-144.

120. Hsu, W. Y.; Gierke, T. D. *Journal of Membrane Science* **1983**, *13*, 307-326.
121. Dreyfus, B.; Gebel, G.; Aldebert, P.; Pineri, M.; Escoubes, M.; Thomas, M. *Journal De Physique* **1990**, *51*, 1341-1354.
122. Litt, M. H. *Polymer Preprints* **1997**, *38*, 80-81.
123. Haubold, H. G.; Vad, T.; Jungbluth, H.; Hiller, P. *Electrochimica Acta* **2001**, *46*, 1559-1563.
124. Rubatat, L.; Rollet, A. L.; Gebel, G.; Diat, O. *Macromolecules* **2002**, *35*, 4050-4055.
125. Schmidt-Rohr, K.; Chen, Q. *Nature Materials* **2008**, *7*, 75-83.
126. Ceynowa, J. *Polymer* **1978**, *19*, 73-76.
127. Rieberer, S.; Norian, K. H. *Ultramicroscopy* **1992**, *41*, 225-233.
128. Fujimura, M.; Hashimoto, T.; Kawai, H. *Macromolecules* **1982**, *15*, 136-144.
129. Xue, T.; Trent, J. S.; Osseasare, K. *Journal of Membrane Science* **1989**, *45*, 261-271.
130. Porat, Z.; Fryer, J. R.; Huxham, M.; Rubinstein, I. *Journal of Physical Chemistry* **1995**, *99*, 4667-4671.
131. Cheng, X.; Yi, B.; Han, M.; Zhang, J.; Qiao, Y.; Yu, J. *Journal of Power Sources* **1999**, *79*, 75-81.
132. Gierke, T. D.; Munn, G. E.; Wilson, F. C. *Journal of Polymer Science Part B-Polymer Physics* **1981**, *19*, 1687-1704.
133. McLean, R. S.; Doyle, M.; Sauer, B. B. *Macromolecules* **2000**, *33*, 6541-6550.
134. Morrison, F. A.; Winter, H. H. *Macromolecules* **1989**, *22*, 3533-3540.
135. Kotaka, T.; Okamoto, M.; Kojima, A.; Kwon, Y. K.; Nojima, S. *Polymer* **2001**, *42*, 3223-3231.
136. Stevens, M. P. *Polymer Chemistry: an Introduction*. 3rd ed.; Oxford University Press: New York, 1999; p 63.
137. Brinkmann, S.; Stadler, R.; Thomas, E. L. *Macromolecules* **1998**, *31*, 6566-6572.
138. Funaki, Y.; Kumano, K.; Nakao, T.; Jinnai, H.; Yoshida, H.; Kimishima, K.; Tsutsumi, K.; Hirokawa, Y.; Hashimoto, T. *Polymer* **1999**, *40*, 7147-7156.
139. Kim, G.; Libera, M. *Macromolecules* **1998**, *31*, 2569-2577.
140. Heck, B.; Arends, P.; Ganter, M.; Kressler, J.; Stuhn, B. *Macromolecules* **1997**, *30*, 4559-4566.
141. Zaluski, C.; Xu, G. *Macromolecules* **1994**, *27*, 6750-6754.

142. Gardner, C. L.; Anantaraman, A. V. *Journal of Electroanalytical Chemistry* **1995**, 395, 67-73.
143. Gardner, C. L.; Anantaraman, A. V. *Journal of Electroanalytical Chemistry* **1998**, 449, 209-214.
144. Soboleva, T. Y.; Xie, Z.; Shi, Z. Q.; Tsang, E.; Navessin, T. C.; Holdcroft, S. *Journal of Electroanalytical Chemistry* **2008**, 622, 145-152.
145. Alberti, G.; Casciola, M.; Massinelli, L.; Bauer, B. *Journal of Membrane Science* **2001**, 185, 73-81.
146. Jannasch, P. *Current Opinion in Colloid & Interface Science* **2003**, 8, 96-102.
147. Shao, Y.; Yin, G.; Wang, Z.; Gao, Y. *Journal of Power Sources* **2007**, 167, 235-242.
148. Steele, B. C. H.; Heinzl, A. *Nature* **2001**, 414, 345-352.
149. Brandon, N. P.; Skinner, S.; Steele, B. C. H. *Annual Review of Materials Research* **2003**, 33, 183-213.
150. Paddison, S. J. *Annual Review of Materials Research* **2003**, 33, 289-319.
151. Licoccia, S.; Traversa, E. *Journal of Power Sources* **2006**, 159, 12-20.
152. Zhang, J. L.; Xie, Z.; Zhang, J. J.; Tanga, Y. H.; Song, C. J.; Navessin, T.; Shi, Z. Q.; Song, D. T.; Wang, H. J.; Wilkinson, D. P.; Liu, Z. S.; Holdcroft, S. *Journal of Power Sources* **2006**, 160, 872-891.
153. Jagur-Grodzinski, J. *Polymers for Advanced Technologies* **2007**, 18, 785-799.
154. Neburchilov, V.; Martin, J.; Wang, H. J.; Zhang, J. J. *Journal of Power Sources* **2007**, 169, 221-238.
155. Devanathan, R. *Energy & Environmental Science* **2008**, 1, 101-119.
156. Chanda, M. *Advanced Polymer Chemistry: A Problem Solving Guide*. Marcel Dekker, Inc.: New York, 2000.
157. Noshay, A.; McGrath, J. E. *Block Copolymers: Overview and Critical Survey*. Academic Press Inc: New York, 1977; p 12.
158. Peckham, T. J.; Holdcroft, S. *Advanced Materials* **2010**, 22, 4667-4690.
159. Yang, Y.; Siu, A.; Peckham, T. J.; Holdcroft, S. *Advances in Polymer Science* **2008**, 215, 55-126.
160. Ding, J. F.; Chuy, C.; Holdcroft, S. *Chemistry of Materials* **2001**, 13, 2231-2233.
161. Ding, J. F.; Chuy, C.; Holdcroft, S. *Advanced Functional Materials* **2002**, 12, 389-394.
162. Ding, J. F.; Chuy, C.; Holdcroft, S. *Macromolecules* **2002**, 35, 1348-1355.

163. Bae, B.; Miyatake, K.; Watanabe, M. *Macromolecules* **2009**, *42*, 1873-1880.
164. Miyatake, K.; Shimura, T.; Mikami, T.; Watanabe, M. *Chemical Communications* **2009**, 6403-6405.
165. Mikami, T.; Miyatake, K.; Watanabe, M. *ACS Applied Materials & Interfaces* **2010**, *2*, 1714-1721.
166. Shimura, T.; Miyatake, K.; Watanabe, M. *Bulletin of the Chemical Society of Japan* **2010**, *83*, 960-968.
167. Mikami, T.; Miyatake, K.; Watanabe, M. *Journal of Polymer Science Part A-Polymer Chemistry* **2011**, *49*, 452-464.
168. Saito, T.; Moore, H. D.; Hickner, M. A. *Macromolecules* **2010**, *43*, 599-601.
169. Matyjaszewski, K. *Controlled Radical Polymerization*. American Chemical Society: Washington, DC, 1998.
170. Quirk, R. P.; Lee, B. *Polymer International* **1992**, *27*, 359-367.
171. Greszta, D.; Mardare, D.; Matyjaszewski, K. *Macromolecules* **1994**, *27*, 638-644.
172. Goto, A.; Fukuda, T. *Progress in Polymer Science* **2004**, *29*, 329-385.
173. Braunecker, W. A.; Matyjaszewski, K. *Progress in Polymer Science* **2007**, *32*, 93-146.
174. Wang, J. S.; Matyjaszewski, K. *Journal of the American Chemical Society* **1995**, *117*, 5614-5615.
175. Patten, T. E.; Matyjaszewski, K. *Advanced Materials* **1998**, *10*, 901-915.
176. Matyjaszewski, K.; Xia, J. H. *Chemical Reviews* **2001**, *101*, 2921-2990.
177. Kamigaito, M.; Ando, T.; Sawamoto, M. *Chemical Reviews* **2001**, *101*, 3689-3745.
178. Matyjaszewski, K.; Coca, S.; Gaynor, S. G.; Nakagawa, Y.; Jo, S. M. U.S. Patent, 5 789 487, 1998.
179. Kucera, F.; Jancar, J. *Polymer Engineering and Science* **1998**, *38*, 783-792.
180. Xie, Z.; Song, C. J.; Andreaus, B.; Navessin, T.; Shi, Z. Q.; Zhang, J. J.; Holdcroft, S. *Journal of the Electrochemical Society* **2006**, *153*, E173-E178.
181. Atkins, P. *Physical Chemistry*. 6th ed.; Oxford University Press: New York, 1999; p 723-760.
182. Peckham, T. J.; Schmeisser, J.; Rodgers, M.; Holdcroft, S. *Journal of Materials Chemistry* **2007**, *17*, 3255-3268.
183. Peckham, T. J.; Schmeisser, J.; Holdcroft, S. *Journal of Physical Chemistry B* **2008**, *112*, 2848-2858.

184. Alexander, L. E. *X-ray diffraction methods in polymer science*. Wiley-Interscience: New York, 1969.
185. Abbrent, S.; Plestil, J.; Hlavata, D.; Lindgren, J.; Tegenfeldt, J.; Wendsjö, Å. *Polymer* **2001**, *42*, 1407-1416.
186. Bates, F. S.; Fredrickson, G. H. *Annual Review of Physical Chemistry* **1990**, *41*, 525-557.
187. Bates, F. S.; Schulz, M. F.; Khandpur, A. K.; Forster, S.; Rosedale, J. H.; Almdal, K.; Mortensen, K. *Faraday Discussions* **1994**, *98*, 7-18.
188. Khandpur, A. K.; Forster, S.; Bates, F. S.; Hamley, I. W.; Ryan, A. J.; Bras, W.; Almdal, K.; Mortensen, K. *Macromolecules* **1995**, *28*, 8796-8806.
189. Elabd, Y. A.; Hickner, M. A. *Macromolecules* **2011**, *44*, 1-11.
190. Park, M. J.; Balsara, N. P. *Macromolecules* **2010**, *43*, 292-298.
191. Chen, L.; Hallinan, D. T.; Elabd, Y. A.; Hillmyer, M. A. *Macromolecules* **2009**, *42*, 6075-6085.
192. Trabelsi, H.; Szonyi, S.; Gaysinski, M.; Cambon, A.; Watzke, H. J. *Langmuir* **1993**, *9*, 1201-1205.
193. Shi, Z. Q.; Holdcroft, S. *Macromolecules* **2004**, *37*, 2084-2089.
194. Shi, Z. Q.; Holdcroft, S. *Macromolecules* **2005**, *38*, 4193-4201.
195. Tsang, E. M. W.; Zhang, Z.; Shi, Z.; Soboleva, T.; Holdcroft, S. *Journal of the American Chemical Society* **2007**, *129*, 15106-15107.
196. Rubatat, L.; Shi, Z. Q.; Diat, O.; Holdcroft, S.; Frisken, B. J. *Macromolecules* **2006**, *39*, 720-730.
197. Isbester, P. K.; Brandt, J. L.; Kestner, T. A.; Munson, E. J. *Macromolecules* **1998**, *31*, 8192-8200.
198. Kotani, Y.; Kato, M.; Kamigaito, M.; Sawamoto, M. *Macromolecules* **1996**, *29*, 6979-6982.
199. Destarac, M.; Matyjaszewski, K.; Silverman, E.; Ameduri, B.; Boutevin, B. *Macromolecules* **2000**, *33*, 4613-4615.
200. Semsarzadeh, M. A.; Mirzaei, A.; Vasheghani-Farahani, E.; Haghghi, M. N. *European Polymer Journal* **2003**, *39*, 2193-2201.
201. Matsen, M. W.; Bates, F. S. *Macromolecules* **1996**, *29*, 1091-1098.
202. Park, M. J.; Balsara, N. P. *Macromolecules* **2008**, *41*, 3678-3687.
203. Lu, X. Y.; Weiss, R. A. *Macromolecules* **1996**, *29*, 1216-1221.
204. Eisenberg, A.; Hird, B.; Moore, R. B. *Macromolecules* **1990**, *23*, 4098-4107.
205. Yarusso, D. J.; Cooper, S. L. *Macromolecules* **1983**, *16*, 1871-1880.

206. Won, J.; Park, H. H.; Kim, Y. J.; Choi, S. W.; Ha, H. Y.; Oh, I. H.; Kim, H. S.; Kang, Y. S.; Ihn, K. J. *Macromolecules* **2003**, *36*, 3228-3234.
207. Tsang, E. M. W.; Zhang, Z. B.; Yang, A. C. C.; Shi, Z. Q.; Peckham, T. J.; Narimani, R.; Frisken, B. J.; Holdcroft, S. *Macromolecules* **2009**, *42*, 9467-9480.
208. Gavach, C.; Pamboutzoglou, G.; Nedyalkov, M.; Pourcelly, G. *Journal of Membrane Science* **1989**, *45*, 37-53.
209. Blachot, J. F.; Diat, O.; Putaux, J. L.; Rollet, A. L.; Rubatat, L.; Vallois, C.; Muller, M.; Gebel, G. *Journal of Membrane Science* **2003**, *214*, 31-42.
210. Zhang, M. F.; Russell, T. P. *Macromolecules* **2006**, *39*, 3531-3539.
211. Gupta, B.; Scherer, G. G. *Angewandte Makromolekulare Chemie* **1993**, *210*, 151-164.
212. Flint, S. D.; Slade, R. C. T. *Solid State Ionics* **1997**, *97*, 299-307.
213. Zhai, G. Q.; Kang, E. T.; Neoh, K. G. *Journal of Membrane Science* **2003**, *217*, 243-259.
214. Zhai, G. Q.; Ying, L.; Kang, E. T.; Neoh, K. G. *Macromolecules* **2002**, *35*, 9653-9656.
215. Zhang, Z. C.; Chalkova, E.; Fedkin, M.; Wang, C. M.; Lvov, S. N.; Komarneni, S.; Chung, T. C. M. *Macromolecules* **2008**, *41*, 9130-9139.
216. Park, Y. S.; Yamazaki, Y. *Polymer Bulletin* **2005**, *53*, 181-192.
217. Sacca, A.; Carbone, A.; Pedicini, R.; Portale, G.; D'Ilario, L.; Longo, A.; Martorana, A.; Passalacqua, E. *Journal of Membrane Science* **2006**, *278*, 105-113.
218. Abbrent, S.; Plestil, J.; Hlavata, D.; Lindgren, J.; Tegenfeldt, J.; Wendsjo, A. *Polymer* **2001**, *42*, 1407-1416.
219. Kasai, N.; Kakudo, M. *X-ray Diffraction by Macromolecules*. Kodansa Ltd.: Tokyo, 2005.
220. Adamson, A. A. *A Textbook of Physical Chemistry*. Academic Press, Inc.: New York, 1973.
221. Anantaraman, A. V.; Gardner, C. L. *Journal of Electroanalytical Chemistry* **1996**, *414*, 115-120.
222. Kopitzke, R. W.; Linkous, C. A.; Anderson, H. R.; Nelson, G. L. *Journal of the Electrochemical Society* **2000**, *147*, 1677-1681.
223. Halim, J.; Buchi, F. N.; Haas, O.; Stamm, M.; Scherer, G. G. *Electrochim. Acta* **1994**, *39*, 1303-1307.
224. Yin, Y.; Fang, J. H.; Watari, T.; Tanaka, K.; Kita, H.; Okamoto, K. *Journal of Materials Chemistry* **2004**, *14*, 1062-1070.

225. Asano, N.; Aoki, M.; Suzuki, S.; Miyatake, K.; Uchida, H.; Watanabe, M. *Journal of the American Chemical Society* **2006**, *128*, 1762-1769.
226. Albalak, R. J.; Capel, M. S.; Thomas, E. L. *Polymer* **1998**, *39*, 1647-1656.
227. Folkes, M. J.; Keller, A. *Journal of Polymer Science Part B-Polymer Physics* **1976**, *14*, 833-843.